UNIVERSITY OF SOUTHAMPTON

FACULTY OF ENGINEERING AND THE ENVIRONMENT

Fluid Structure Interactions Research Group

Bio-inspired energy harvesting for sensors from unsteady fluid flow

By

Andreas Mathikolonis

Thesis for the degree of Doctor of Philosophy

February 2018

UNIVERSITY OF SOUTHAMPTON

ABSTRACT

FACULTY OF ENGINEERING AND THE ENVIRONMENT

FLUID STRUCTURE INTERACTION GROUP

Doctor of Philosophy

BIO-INSPIRED ENERGY HARVESTING FOR SENSORS
FROM UNSTEADY FLUID FLOW

By Andreas Mathikolonis

This thesis investigates the development of a bio-inspired method of recovering energy from unsteady flow with the specific application of powering sensors in remote areas. It has long been understood that fish, through altering their mode of swimming to interact with naturally produced vortices, conserving energy and in certain instances extracting energy from the flow. The current study examines the interaction that exists between vortices shed from a bluff body and a flexible cylinder tethered downstream. It has been found that it is possible to synchronise the motion of the flexible cylinder with the unsteady flow and exhibit a motion similar to that of a trout swimming with a Von Kármán gait. Vibrational characteristics of the flexible cylinder were examined and verified using theoretical, experimental and computational approaches. An extensive discussion concerning all the experimental and computational analysis is included. The first significant output from this research is the three-dimensional, two-way coupled, fluid-structure interactions model which provides detailed insight into the behaviour of both the fluid and structural response. The second is an in-house manufactured piezoelectric device integrated into the flexible cylinder. It was found that there is the potential to harvest energy from this fluid-structure interaction system. In cases where the energy is of a very small magnitude, the system has shown that it can behave as a sensor, able to give characteristics of the flow through interaction with the flexible cylinder.

[This page intentionally left blank]

Dedication

To my parents, who have raised me to be the person I am today. You have been with me every step of the way, through good times and bad. Thank you for all the unconditional love, guidance and support that you have given me, helping me to succeed! Thank you for everything!

To my beloved sister who has always supported and motivated me to finish this research.

[This page intentionally left blank]

Contents

List of Figures

List of Tables

List of Equations

[This page intentionally left blank]

Academic Thesis: Declaration of Authorship

I, Andreas Mathikolonis declare that this thesis and the work presented in it are my own and has been generated by me as the result of my own original research.

Title: Bio-inspired energy harvesting for sensors from unsteady fluid flow.

I confirm that:

1. This work was done wholly or mainly while in candidature for a research degree at this University;

2. Where any part of this thesis has previously been submitted for a degree or any other qualification at this University or any other institution, this has been clearly stated;

3. Where I have consulted the published work of others, this is always clearly attributed;

4. Where I have quoted from the work of others, the source is always given. With the exception of such quotations, this thesis is entirely my own work;

5. I have acknowledged all main sources of help;

6. Where the thesis is based on work done by myself jointly with others, I have made clear exactly what was done by others and what I have contributed myself;

7. None of this work has been published before submission.

Signed: .....

Date: 1st November 2019

[This page intentionally left blank]

Acknowledgments

I am very grateful to my supervisor Associate Professor Stephen Boyd for all his guidance and support throughout the project. I would like to express my deepest gratitude for all the time and effort he spent helping me overcome all the obstacles I have come across, without which any of this would have been possible. I wish everyone had a supervisor like him!

My dearest Alina Berezovskaya, thank you for always being there for me when needed, your unconditional love and support throughout my PhD research years. Thank you for lifting me up when down, thank you for encouraging me to complete this research and get through the darkest years of my life.

I would also like to thank the following:

My line manager and Director of ECS Teaching Facilities Mr David Oakley, for employing me for the past few years, while giving me valuable guidance and work experience.

Prof Steve Beeby for his contribution during the project whenever was required.

Dr Toru Tsuzaki and Mr Karl Scammell for their help and assistance in setting up the experiments at the Armfield Water Channel, as well as for its maintenance.

Dr Monika Glanc-Gostkiewicz for her support and advices while manufacturing the PZT films.

Mr Lishan for helping me overcome any difficulties I faced while working on the models in ANSYS®, as well as for his contribution when needed.

Mr Barry Bailey for his assistance and constructive thinking and more specifically when manufacturing the experimental apparatus for the energy harvesting used in this research.

My fellow PhD researchers for the constructive discussions and advices.

My close friends for all the support and encouragement. Thank you for believing in me when I mostly needed it.

And last, but by no means least, to me, for deciding to stick with this research through some of my darkest times, it was a battle that has been won and I am a better and stronger person for sticking with it and completing this work.

[This page intentionally left blank]

Nomenclature

Symbols	Description	Units (SI)
A_c :	Water channel cross-sectional area	m^2
A_r :	Aspect ratio, width over channel depth	-
B :	Log-law integration constant	-
B_{force} :	Force of buoyancy	N
C_D :	Average steady state drag coefficient	-
d:	Grid dimension	3
d_{PZT}:	Thickness of piezoelectric film	µ
d_{33} :	Piezoelectric charge coefficient	C/N
$D_{channel}$:	Depth of water channel	m
D_{bb} :	Diameter of the bluff body	m
D_{fc} :	Diameter of flexible cylinder	m
E:	Electric field	V/m
EI :	Structural rigidity	N/m^2
e_a^{21} :	GCI extrapolated relative error	-
f_{factor} :	Friction factor from Blasius	-
f_{fc} :	Flexible cylinder oscillation frequency	Hz
f_{shed} :	Vortex shedding frequency	Hz
GCI_{fine}^{21} :	Grid Convergence Index	
G_{force} :	gravitational force	N
g :	gravitational constant	m/s^2
h :	Height of the cones from their base	m
k :	Von Kármán constant equals to 0.41	-
k_s:	Height of the roughness (particle size)	mm
$L_{entrance}$:	Open channel entrance length	m
L_{fc} :	Total length of flexible cylinder	m
$L_{formation}$:	Formation region length	m
$L_{loading}$:	Distance from support to load	m
$L_{casting}$:	Length of casting body	m
$L_{channel}$:	Length of the water channel	m
m :	Strouhal number calculation coefficient	-
n_{el1} :	Number of elements in the finer mesh	-

n_{el2} :	Number of elements in the coarser mesh	-
p :	Formal order of accuracy	-
$\hat{p}$:	Observed order of accuracy	-
$R_{channel}$:	Open channel Reynolds number	-
R_h :	Hydraulic radius	m
R_L :	Electrical resistive load	Ω
R_{inner} :	Flexible cylinder inner radius	m
R_{outer} :	Flexible cylinder outer radius	m
P_{wet} :	Water channel wetted perimeter	m
Q :	Flow rate	m^3/s
Re :	Reynolds number	-
$Re_{channel}$:	Open channel Reynolds number	-
Re_L :	Boundary layer Reynolds number	-
r :	Refinement factor	-
St :	Strouhal Number	-
St^* :	Strouhal number calc. coefficient	-
U_* :	Shear velocity	m/s
U_{actual} :	Flow velocity with constrains	m/s
U_{max} :	Maximum dip velocity	m/s
U_{avg} :	Nominal flow velocity	m/s
V :	Applied voltage	V
V_{fc} :	Volume of flexible cylinder	m^3
V_{outer} :	Flex. cylinder volume with outer radius	m^3
$W_{channel}$:	Width of the water channel	m
y_h :	Distance from the channel bed	m
y_0 :	No-slip distance from bed	m
y^+ :	Dimensionless wall distance	-
y_1 :	First cell height in CFD	m
α :	Velocity profile improvement parameter	-
θ :	Angle between adjacent radial grid lines	Radians
μ:	Mass per unit length	Kg/m
ν_{water} :	Kinematic viscosity of water	m^2/s
ξ :	Dimensionless distance from bed	-
ξ_{dip} :	Location of dip-phenomenon (U_{max})	m
Π :	Coles' wake function parameter	-

$\boldsymbol{\rho_{fc}}$ **:**	Flexible cylinder density	Kg/m^3
$\boldsymbol{\rho_{water}}$ **:**	Density of water	Kg/m^3
$\boldsymbol{\tau_w}$ **:**	Shear stress	Pa
$\boldsymbol{\omega}$ **:**	Corresponding frequency	rad/s
$\boldsymbol{\eth}$ **:**	Difference between circle and polygon	-
$\boldsymbol{\Phi_{ext}^{21}}$ **:**	GCI extrapolated value	-

[This page intentionally left blank]

Chapter 1

Introduction

For the last few decades, oceans have received a great deal of attention regarding environmental issues, resources, as well as scientific and military tasks. Consequently, there have been numerous research and development activities worldwide in developing self-sustainable sensing systems, in order to overcome scientific and engineering challenges caused by the oceans' environment. Sensors deployed at several locations in the oceans or even rivers, enable the monitoring and the collection of data regarding pollution, exploration, marine life, upcoming disasters, as well as assisting with navigation and tactical surveillance applications [1]. Nowadays, thanks to the rapid development of new materials, the theoretical advancements in combination with advanced computing and sensory technology, the research and development activities in the marine community have been boosted. However, this is just the beginning as more advanced, more reliable and practical sensing systems are still needed [2] [3].

Currently, the ability of sensors to undertake long-term missions is limited by their ability to receive energy or properly manage it during their mission. Assuming that the energy management can be controlled, the problem is narrowed down to whether the sensors will be able to produce or receive extra energy to extend their mission length. By carefully looking at the case of the fish that holds station in unsteady fluid flow whilst migrating upstream to spawn, it can be observed that fish take advantage of its environment to minimise energy expenditure. From the latter, it can be assumed that by using the fluid flow due to tidal streams or forward velocity as an energy source, energy could be extracted. A methodology could be applied to extract energy from the environment and charge the sensors. The requirement of returning the system to the surface or sending specialised divers in the ocean to replace the batteries would be reduced, except in the case of unavoidable maintenance. This would be very time and cost beneficial and could also expand the range of potential sensing applications.

Such methodology could also be implemented at a different fluid, in air. Taking as example the complex HVAC duct network at enterprise buildings, there are sensors to control and monitor the temperature, pressure and humidity. Having energy harvesting devices exploiting the airflow round the clock producing power, which in turn is stored and accumulated over time at power banks, can dramatically increase the lifespan of such monitoring systems. Sometimes, the devices themselves operate as sensors and energy harvesters at the same time, being able to partly or fully cover their power requirements.

From an engineering perspective, there has always been a fascination with the way nature operates. Engineers often try to imitate natural processes and behaviour. For example, marine animals can instinctively harvest fluid-mechanical principles in a way engineers and biologists are only just beginning to understand. Nature has evolved with time to develop capabilities of speed, body manoeuvrability and efficiency, characteristics very desirable for energy harvesting and sensing application.

This research will investigate whether an inanimate object, subjected to unsteady flow, can enable energy to be extracted from its motion utilising the same physical phenomena as fish. This will require a mechanical structure that is coupled to the fluid flow in such a way that it captures the kinetic energy enabling it to be converted into electrical energy. Examples of such kind of devices have been demonstrated in airflows [4] and the electric eel work developed for use in the water [5]. In order to achieve a successful energy harvester, the mechanical structure has to be designed to maximise the coupling to the fluid flow, the energy harvesting mechanism must be well coupled to the structure and the power conditioning electronics must be carefully considered to maximise conversion efficiency.

1.1 Thesis Aims and Objectives

This research has two key challenges. Firstly, to explore whether an inanimate object can be tuned to respond to an unsteady flow field. Secondly, whether the motion of the inanimate object is sufficient to act as an energy harvesting device.

In order to accomplish the aforementioned challenges and demonstrate that a suitably tuned inanimate body can harvest energy from an unsteady underwater fluid flow, the following objectives were set:

1) Through experimental analysis, to investigate the response of a silicone flexible cylinder tethered behind a bluff body, a recirculating water channel was utilised in which the flow velocity and water levels can be controlled.

2) To determine the amplitude and frequency tuning of an inanimate object to a specific, or series, of unsteady flow regimes. Using a customised Matlab® code, it has been possible to identify the two parameters at different flow regimes, experimentally.

3) To design and validate a computational model incorporating a fully coupled computational fluid dynamics/finite element model, using the ANSYS® suite. The model provided detailed insight into both the fluid and structural response of the system, with the potential for being used in the future to predict scenarios at different flow velocities and possibly different inanimate body geometries.

4) To develop a method of piezoelectric material insertion into the flexible cylinder.

5) To investigate the energy harvesting limitations of the piezo-system through experimental means utilising materials characterisation facilities.

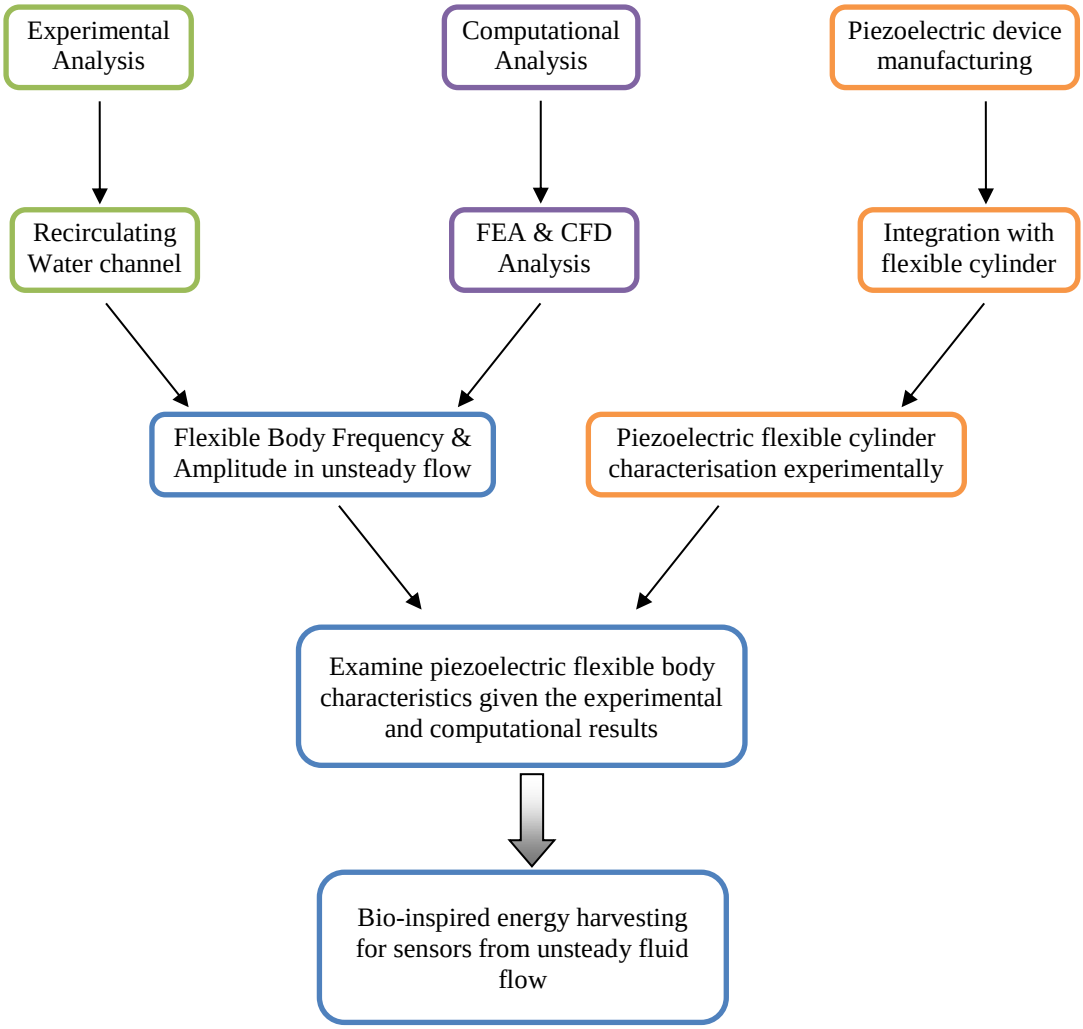

Figure 1. Research plan.

1.2 Thesis Outline

In Chapter 1, a brief overview of the problem statement, the objectives and the research methodology are outlined.

In Chapter 2, background literature related to turbulent flow is discussed and relevant research activities relevant to the current research are investigated. Furthermore, the related physics of a flow in a narrow open channel and passed a bluff body are discussed. An introduction to piezoelectric materials and CFD turbulence models is also presented.

Chapter 3 contains the experimental approach of the project. Three methodologies are presented; a method for creating unsteady flow, a method for designing a flexible cylinder and a method for manufacturing a flexible cylinder. Furthermore, analysis of the experimental data is defined using a video processing tool, followed by any possible limitations that might occur from this assessment.

Chapter 4 includes post video processing in different flow cases where the behaviour of the flexible cylinder while interacting with the flow is analysed and discussed. The natural frequencies and amplitudes of the flexible cylinder are found and compared with theoretical calculations. Overall discussion and assessment of the results is included as well as comparison with work done by other authors. Finally, the tests have been repeated at different flow velocities, where the frequencies and amplitudes were found for each case and presented accordingly.

Chapter 5 provides a guided design and validation process towards designing and creating a coupled computational model. Initially, a two dimensional model is designed in detail and then validated using experimental data from the literature. Mesh independence study has reassured the quality and convergence of the models and expected flow phenomena were identified. Having confidence in the quality of the results, the two-dimensional model has been extruded into a three-dimensional model, preparing a coupled mesh design model to be investigated in the next chapter.

Chapter 6 presents the method of creating a fully coupled three-dimensional computational model, followed by qualitative and quantitative validation of the model. Investigating the model, expected flow phenomena were identified and the flow development is qualitatively investigated to reassure that vortices reach the inanimate flexible cylinder

located downstream the bluff body. In the end, this chapter has provided a fully coupled computational model, which enables the study of the behaviour of a fluid past a bluff body in different velocities and Reynold regimes, and the physical characteristics of flexible bodies undergoing stress from shed vortices. The model will serve as a design tool for future related research.

Chapter 7 presents the experimental approach of the research related to energy harvesting. Initially, two methodologies are presented; a method to manufacture a piezoelectric device, including the poling and characterisation processes and a method for integrating the piezoelectric device into the flexible cylinder. Then, an experimental investigation of the response of the piezoelectric device at different frequencies and amplitudes is conducted. It is believed that the system can serve as sensor at its current state, as well as an energy harvesting device, with enhancement in specific areas, as discussed in the further work section.

Chapter 8 draws conclusions on the work carried out under the present research. It focuses on the objectives of the project and how they have been achieved throughout the thesis.

Chapter 9 discusses potential work and areas for improvement regarding the research work done.

Chapter 2

Background and Literature Review

In this chapter the fundamental theory of the governing laws for fluid flow is introduced. The governing equations of fluid flow are called the Navier-Stokes equations. These equations have been derived based on the governing equations of fluid dynamics, called the continuity, the momentum and the energy equations, which represent the conservation laws of physics.

Moreover, discussion on flows occurring behind a circular object is included. The flow is sensitive to the changes of Reynolds number, a dimensionless parameter representing the ratio of inertia to viscous forces in the flow. There has been a strong impetus over the last decade to understand vortex dynamics in wake flows which are important not only for our understanding of fundamental flow physics, but also for the many applications of bluff body flows in technology. Experimentally, this is achieved by placing a bluff body in a water tank under controlled flow.

Using published work, the equations for the distribution of shear stress and velocity in open channels is used to recreate the vertical velocity profile of the fluid in the experimental channel.

A discussion related to the computational models available to compute the physics of the open channel and around the bluff body is included. It is explained why the SST k-ω RANS model is used compared to other well-established models in the field.

Finally, an introduction to energy harvesting gives an initial idea of the use of piezoelectric material in similar projects.

2.1 Governing Laws of Fluid Flow

Fluid dynamics is the investigation of the interactive motion of a larger number of individual particles. Even an infinitesimally small element of the fluid, still contains a sufficient number of particles, for which the mean velocity and mean kinetic energy can be specified. In this way, velocity, pressure, temperature, density, and other important quantities at each point of the fluid can be defined.

The derivation of the principal equations of fluid dynamics is based on the dynamical behaviour of a fluid, determined by the following conservation laws, namely:

i) The conservation of mass, which expresses that the mass cannot be created nor can disappear. How much enters and leaves a control volume can be ascertained. This is known as the continuity equation.

ii) The conservation of momentum, based on Newton's second law which states that the variation of momentum is caused by the net force acting on a mass element.

iii) The conservation of energy, based on the first law of thermodynamics. The law states that any changes in time of the total energy inside the fluid volume are caused by the rate of work of forces acting on the volume and the net heat flux into it. The total energy per unit mass of a fluid is obtained by adding its internal energy per unit mass, to its kinetic energy per unit mass.

The conservation of a certain flow quantity means that its total variation inside an arbitrary volume can be expressed as the net effect of the amount of the quantity being transported across the boundary, of any internal forces and sources, and of external forces acting on the volume [6].

In the mid-18th century, the French engineer Claude Navier and the English mathematician George Stokes derived the well-known equations of fluid motion, known as the Navier-Stokes equations. These equations of motion provide a complete mathematical description of the flow of incompressible Newtonian fluids which have been derived based on the fundamental governing equations of fluid dynamics described above [7]. These equations have extensively been used to create the computational turbulence models currently used in Computational Fluid Dynamics (CFD) applications. Further discussion on the computational models is found in section 2.4 of this chapter.

2.2 Unsteady Flow Due to a Bluff Body

Flow past a circular cylinder has been the subject of both experimental and numerical studies for decades. This flow is very sensitive to the changes of Reynolds number, a dimensionless parameter representing the ratio of inertia force to viscous force in a flow. Work in this chapter aims to give a conceptual overview of the flow past a circular cylinder, representing the bluff body in the experimental chapter 3. The flow characteristics around the circular cylinder such as the Strouhal number, vortex shedding, formation region and the Von Kármán vortex street are introduced.

The flow past a circular cylinder tends to follow the shape of the body provided that the velocity of the flow is very slow, this is known as laminar flow. Flow at the inner part of the boundary layers travels more slowly than the flow near to the free stream. As the speed of the flow increases, separation of flow occurs at some point along the circular cylinder due to the occurrence of adverse pressure gradient regions. Flow separation tends to roll up the flow into swirling eddies, resulting in alternate shedding of vortices in the wake region of the body known as the Von Kármán vortex street.

2.2.1 Formation Region

The formation or suction region is the region directly behind the bluff body where the separated flow layers have not rolled into vortices. Even if a detailed description of the mechanics of the formation region will not be given in this report, it is important to note that there is a drop in pressure associated with the formation region. As well noted in the literature, a fish can use this drop of pressure in the formation to effectively be sucked upstream, in other words to entrain [8] just behind the bluff body. It has also been noted that the length of the formation region in a low turbulence free stream was larger than the formation region in a turbulent free stream and that increasing the aspect ratio of the bluff body decreases the formation region length [9]. In other words, as the Reynolds number increases, the length of the formation region decreases. For the need of this research, it is sufficient to know that the suction region has a shorter length than the $2D_{bb}$ (bluff body diameter) where the flexible cylinder is tethered downstream. Therefore, any experiments conducted are outside the formation region, allowing the flexible cylinder to oscillate at its maximum amplitude.

2.2.2 Reynolds Number

Reynolds number is a dimensionless number which describes the ratio of inertial to viscous forces and is defined as,

$$Re = \frac{inertial\ forces}{viscous\ forces} = \frac{\rho \times U_{actual} \times Length\ of\ object}{Dynamic\ viscosity} = \frac{U_{actual} \times Length\ of\ object}{\nu}$$

Equation 1. Reynolds Number equation.

Observing Figure 2 below, at very low Reynolds numbers ($Re_{bb} < 5$), when the viscous forces are dominant, laminar flow occurs and it is characterised by constant and smooth fluid motion.

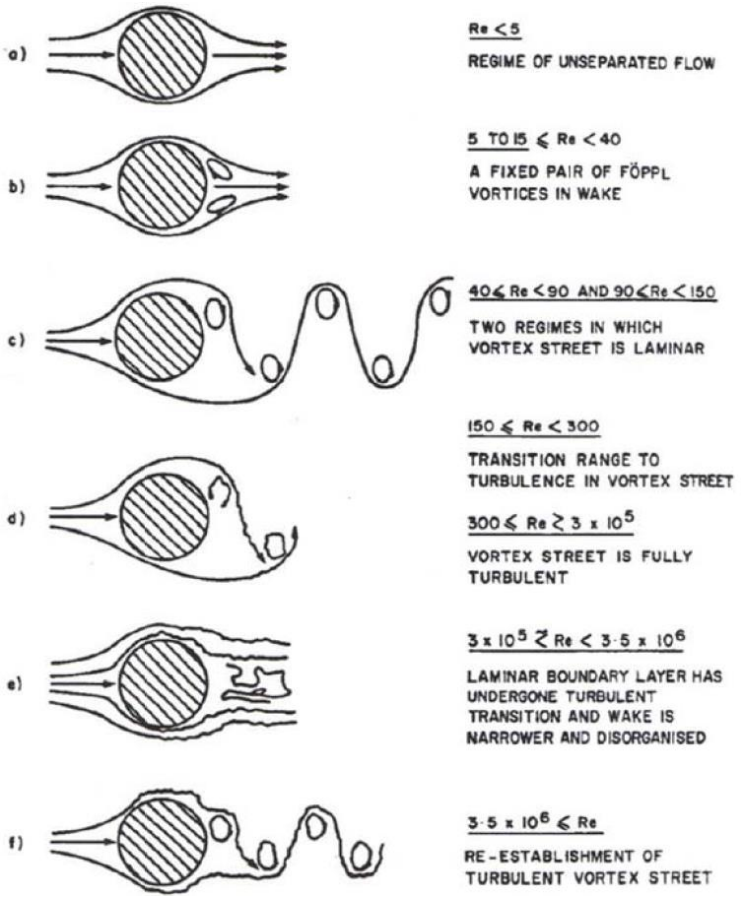

Figure 2. The flow regime at varying Re around a static cylinder (adapted from [10]).

As the flow velocity increases, the flow separates from the bluff body to form a pair of Föppl vortices ($Re_{bb} < 40$). With further increase of the flow velocity, a laminar vortex street is formed, which consists of vortices shed off at both sides of the bluff body ($Re_{bb} < 150$). At high Reynolds numbers, where the inertial forces are dominant, turbulent flow

occurs, which produces chaotic vortices and is replaced by a disorganised wake ($3 \times 10^5 < Re_{bb} < 3.5 \times 10^6$).

2.2.3 Strouhal Number

The frequency of the vortices, in other words, how often the vortices are shed from the bluff body, is characterized by the Strouhal number (St) which, on the assumption that the flow is not constricted, is defined as,

$$St = \frac{f_{shed} D_{bb}}{U_{avg}}$$

Equation 2. Strouhal number equation without flow constrains.

where f_{shed} is the frequency of vortex formation, $D_{bb}$is the width (diameter) of the bluff body, and U_{avg} is the nominal flow velocity (free stream).

In the case where the flow is constricted due to the presence of the bluff body in combination with the channel width, the formula will change to,

$$St = \frac{f_{shed} D_{bb}}{U_{actual}}$$

Equation 3. Strouhal number equation with constricted flow.

where, $U_{actual} = U_{avg} \times (\frac{W_{channel}}{W_{channel} - D_{bb}})$

Equation 4. Constricted flow speed.

and $W_{channel}$ is the width of the flow channel. The same approach is observed in similar research [11].

The Strouhal number is a function of Reynolds number but it remains relatively constant at a value of approximately 0.2 for a wide range of Reynolds number ($10^2 - 10^5$) [12] [13].

To understand the relationship between the dimensionless Strouhal number and the flow regime in which it is occurring, numerous investigations have taken place. A general relationship between Strouhal and Reynolds numbers is presented in [14] of the form,

$$S_t = A - \frac{B}{Re} + CRe^2$$

Equation 5. Quadratic function for Strouhal number estimation.

Where, A, B and C are constants related to different flow regimes. Studies have proposed different values for the constants A, B and C, according to the Reynolds number value, the roughness of the cylinder and the level of flow turbulence, at given fluid. A brief discussion can be found in [14]. In general, as [14] suggests, the majority of the coefficients give good approximations of the Strouhal number in low Reynolds number flow (Re<300) compared to higher Reynolds number. In most cases, coefficient C is zero, therefore Equation 5 is re-written in the simplified form,

$$S_t = A \times (1 - \frac{B/A}{Re})$$

Equation 6. Simplified form of Strouhal number quadratic function estimation.

In this work, three possible St–Re relationships are discussed which seem to be the most applicable given the characteristics of the experimental system. These have been chosen by examining the Reynolds number, the aspect ratio of the cylinder length to the diameter ($\frac{L_{bb}}{D_{bb}}$) and supporting data from the literature. According to [15], the Strouhal number can be expressed as a function of the Reynolds number in the form shown in Equation 7,

$$S_t = St^* + \frac{m}{\sqrt{Re}}$$

Equation 7. Strouhal number function of Reynolds number.

where St^* and m are coefficients obtained experimentally, as shown in Table 1 [15]:

Re Range	St^*	m
47 < Re < 180	0.2684	-1.0356
180 < Re < 230	0.2437	-0.8607
230 < Re < 240	0.4291	-3.6735
240 < Re < 360	Dependant on boundary conditions	
360 < Re < 1300	0.2257	-0.4402
1300 < Re < 5000	0.2040	0.3364
5000 < Re < 2.00× 10^5	0.1776	2.2023

Table 1. St* and m coefficients for the respective Reynolds Numbers.

To derive the values in Table 1, experiments were conducted from the beginning of the vortex shedding at Re ≈ 47 up to the upper end of the subcritical regime, at Re ≈ 2×10^5. The upper limit of the empirical function is higher than the Reynolds number of the flow in this research making the function suitable. However, in [15] it is suggested that Equation 7 is only valid for bluff body aspect ratios ($\frac{L_{bb}}{D_{bb}}$) of 15 or greater, as this was the smallest aspect ratio of the experimental work used to determine the equation. The current experimental set-up has an aspect ratio of approximately four. This brings into question whether Equation 7 is valid for the present research, however, there does not appear to be any evidence in the literature to support this.

Equation 8 [16] can also be used to determine Strouhal number, however it is only valid for 300 < Re < 2000. In practice, it is often also applied for higher Reynolds numbers, still giving a good approximation to estimate Strouhal number, however, it should not be used for Re > 5000, since there is a stronger decrease in Strouhal number than predicted by Equation 7. The author of Equation 8, stated in his report that for higher Reynolds numbers, the maximum error is 4%, relative to the best-fit line, within the suggested regime, which is still an approximation of the experimental measurements [16]. That means the uncertainty will be higher than 4% at a higher Reynolds number.

$$St = 0.212 \left(1 - \frac{12.7}{Re}\right)$$

Equation 8. Roshko's formula for Strouhal number approximation.

Equation 9 is very common in the literature [17] [18] [19] [20]. It is applicable for 250 < Re < 2×10^5 and that the experiments were of a high aspect ratio around 20000, given other published work.

$$St = 0.198 \left(1 - \frac{19.7}{Re}\right)$$

Equation 9. Strouhal number estimation formula at high aspect ratio.

The problem of bluff body flow has been under investigation for many decades. There have been literally hundreds of papers, in part due to its engineering significance, and in part due to the tempting simplicity in setting up such an arrangement in an experimental or computational laboratory.

In fact, the surge of activity on wakes over the past decades from experiments [21] [22] [23] [24] [25], numerical simulations [26] [27] [28], and extensive data analysis has yielded a wealth of new understandings. Although our knowledge of this flow is great, the problem of bluff body flow remains almost entirely in the empirical, descriptive realm of knowledge. The fluid mechanics literature has not been entirely clear in defining the exact values and the experimental uncertainties of lift, drag and vortex frequency measurements for circular cylinders. Certain sets of data are traditionally accepted, although improved data exist. Many sets of data conflict and the variability of results is often overlooked. An example of such case is Figure 3 [21], published in 1966. The author of the figure summarised and evaluated the available data in that time, in an attempt to improve the situation and to provide ready access to previously scattered information. To date, Figure 3 is still generally accepted; it can be said that the Strouhal number at Reynolds numbers between 10^2 – 10^5 remains constant at about 0.2, before rising sharply to a maximum of about 0.4 as the Reynolds number increases beyond the upper range [12].

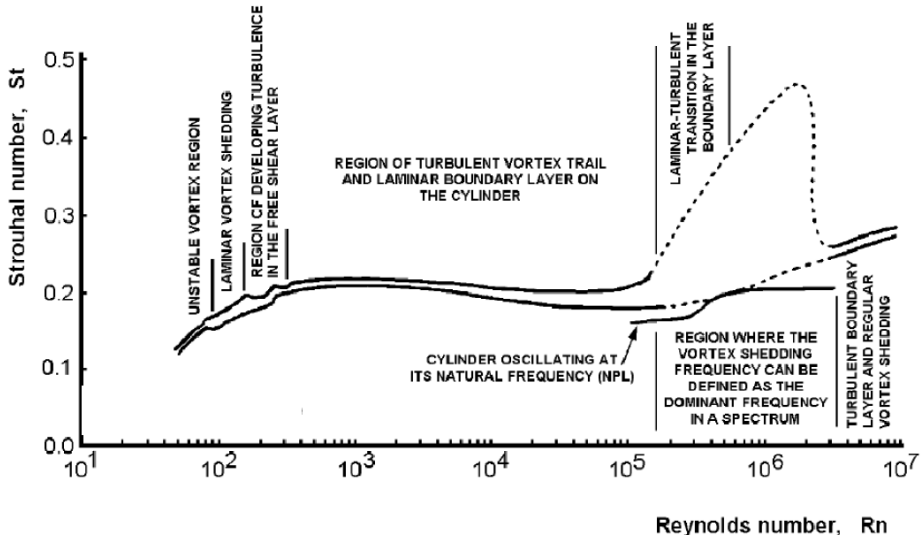

Figure 3. Strouhal and Reynolds numbers variation (adapted from [21] [12]).

Since it is in the interest of this research to use one of the empirical equations to predict an approximation of the Strouhal number at a Reynolds number of 5.14×10^4, a better look is necessary within this region of the data.

Work done in [21] allows one to investigate the scattered data, as seen in Figure 4.

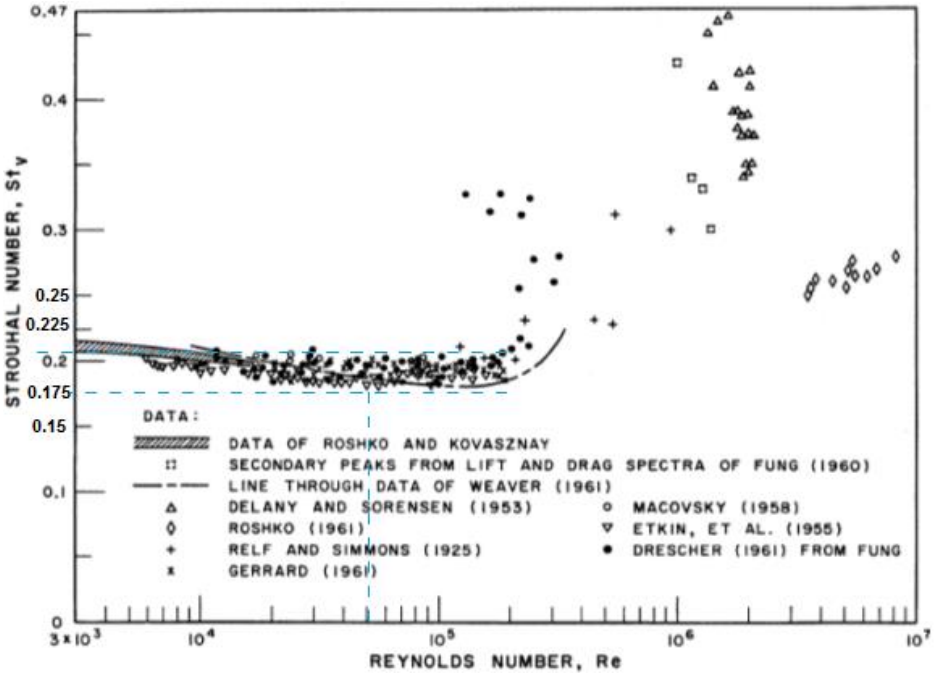

Figure 4. St-Re numbers data for circular cylinders: 3 x 10^3 < Re < 10^7 (adapted from [21]).

For a Reynolds number of approximately 5 × 10^4, the Strouhal numbers range from 0.18 to 0.21. It is also stated by the investigators that the Strouhal number is accurate within ±5% over most Reynolds numbers [21].

From further investigation into the presented envelope of data, it was found that more factors affect the flow, such as the freestream turbulence and the surface roughness of the cylinder. These are all included in the scattered data. In the experiments of this project, the turbulence of the flow has not been measured, therefore no further discussion will take place on this. With regards to surface roughness, the investigators of the presented data have used three levels of relative roughness. They have estimated the average particle size from sandpaper which uses the roughness height and calculates the relative roughness $\frac{k_s}{D_{bb}}$, where k_s is the height of the roughness (particle size) and D_{bb} the diameter of the cylinder. This is referred to as the Nikuradse sand-grain roughness, who extensively investigated the field [29].

The non-dimensional relative roughness for a smooth cylinder is of the level 10^{-5}, for a medium rough cylinder, 10^{-4} and of a rough cylinder 10^{-3}. In the experiments for this research, a 0.11m diameter PVC pipe has been used as the bluff body. A pipe database provides the roughness for a PVC, glass and other drawn tubing to be 0.0015mm [30].

Therefore, the relative roughness for the cylinder used as bluff body is $\frac{k_s}{D_{bb}} = \frac{0.0015}{110} = 1.3\times10^{-5}$, which classifies the pipe as a smooth cylinder.

In general, it is customary to regard a surface as smooth when it is so even that no roughness or points are perceptible to the touch. It is known, however, that an examination of such a surface under a microscope would reveal the presence of small excrescences and undulations that the surface would appear "rough". The smoothness (or roughness) of a surface is therefore a relative quantity. In problems on fluid motion the surface of a body can be regarded as smooth when the excrescences and undulations are small and of such a character that they do not affect, to any measurable extent, the flow characteristics of the body. Some of the essential differences between the aerodynamical behaviour of surfaces classified as "smooth " and "rough," can be gathered from extensive work of other authors [31].

The experimental data in Figure 4 varies greatly since different methods, measuring scales, flow turbulence levels and roughnesses have been used. However, in general, it has been shown that there is a trend connecting the Reynolds and Strouhal numbers, all enclosed within the envelope. In Figure 3, the top line of the envelope represents data from a smooth cylinder and the bottom data from a rough cylinder.

Understandably, the limitations identified will bring a certain amount of error to the Strouhal prediction calculations, however, this will be discussed later. Section 4.5 provides an analysis of the Strouhal number empirical equations, which will be used to assess the quality of the computational model results.

2.2.4 Von Kármán Vortex Street

The Von Kármán vortex street has been investigated by many people, undertaking experiments with very positive and promising results for future work. Vortex shedding is very common in engineering applications. Since this project has been inspired by the behaviour of the fish behind a bluff body, this section will explain the concept of the Von Kármán vortex street by presenting existing work done in the field related to fish. The fish can easily be compared to the flexible cylinder that will be used to undertake the experiments in this research and similar behaviour and physics should be expected.

Taking a look at the anatomy of a flow around a bluff body, and in this case around a circular cylinder, the behaviour of the fish can be divided into four areas. As shown in Figure 5(a), a fish is swimming in a steady free stream flow. The fish exhibits muscle activity to stay in position. When the steady flow encounters the bluff body, it becomes unsteady, creating a high-pressure region upstream of the bluff body commonly known as stagnation point where the fluid velocity is Figure 5(b) [8]. Exhibiting very little body undulation, the fish is holding station in the reduced-flow region of the bow wake. Similarly, at the low-pressure suction region, Figure 5(c), the fish 'entrains' near the low-pressure suction region of the cylinder [9]. It balances the drag and thrust forces to hold station without making any regular axial swimming motions [8] [32], by making only fine-scale corrections using its fins and by positioning the head really close to the bluff body, but without touching it. This can be clearly observed from the pattern diagrams which present the body movement of the fish. Moving downstream, the fish will seek and maintain position in the flow, a few body lengths further from the bluff body, Figure 5(d), an area where the frequency of the shed vortices from the bluff body, generate a wake known as the Von Kármán vortex Street [10], within the range of Reynolds number between 300 and 150000 [33]. As well identified, this unique pattern of motion is characterised by lower tail-beat frequency and larger lateral body amplitudes and curvatures than for swimming in a uniform flow [34]. The distinctive pattern can be seen in Figure 5(d) when looking at the body lines diagram.

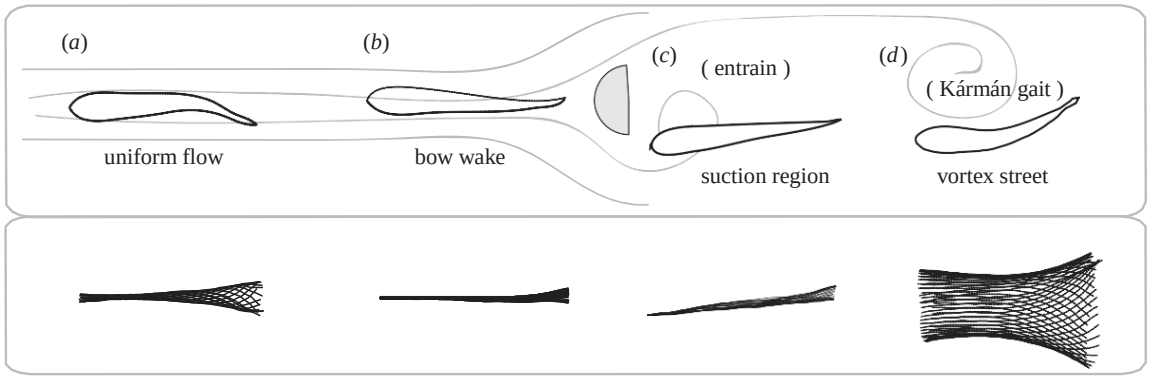

Figure 5. Fish positioning around a circular bluff body (adapted from [6]).

By changing the flow velocity and the cylinder diameter, it is possible to systematically alter the frequency at which vortices are shed, as well as the downstream spacing between successive vortices (i.e. wake wavelength). In this way, consistent, repeatable and controlled hydrodynamic perturbations are generated. The fish, while swimming to the Von Kármán vortex street at point d, adapts its swimming mode to interact with the shed

vortices, where effectively it reduces the energy expended to maintain position in the flow [8]. Similarly, in this project, the aim is to match the natural frequency of an inanimate flexible body to the shedding frequency. This will allow the flexible body to have larger body amplitude and more energy could be potentially harvested through means that will be explored at a later stage.

This great interest started back in 1912, when Theodore Von Kármán studied and analysed the stability of the different vortex configurations and managed to establish a theoretical link between the vortex street structure and the drag on the body, the well know Von Kármán vortex street [35]. Von Kármán vortex street is the flow created when passing a stationary body, which is primarily consisted by regions of discrete, periodical shed vortices flowing downstream and having alternate senses of rotation, which give the impression of positive (clockwise) and negative (anticlockwise) vortices [34].

A very remarkable contribution was made when it was demonstrated that a fish prefers to adopt a Von Kármán gait than other modes of swimming such as entraining at a slower flow velocity or in front of the bluff body [34]. In the study, it is stated that the fish, while swimming a few body lengths behind the cylinder, adopted a distinctive pattern of movement, where the only movement done was by the anterior axial muscles for station keeping, and it was synchronized with the shedding frequency of the cylinder used during the experiment. Therefore, the fish preferred to alter its body kinematics and to synchronize with the shed vortices by having larger body amplitudes and curvatures exhibiting the Von Kármán gait than having a lower body wave speeds and tail-beat amplitudes. This implies that the Von Kármán gait is more energetically favourable region for the fish.

Further experimental work has advanced the conclusions of the previous experiments. It has been shown that a dead fish, tied by a string, in the wake of a bluff body, it could adopt the Von Kármán gait. The dead fish overcame its own drag, by extracting sufficient energy from the flow and consequently it could be seen that it was ‘swimming’ upstream without any energy input of their own [11]. During the experiments, it was also demonstrated that a passive, high aspect ratio, foil could extract sufficient energy from the turbulent eddies by employing a similar flow energy extraction mechanism and effectively propel itself upstream.

A more detailed study has shown that a dead fish exhibited signs of moving upstream only before rigor mortis set in [8]. In other words, once the trout has reached the state of rigor

mortis, and consequently becomes stiff, no upstream movement was achieved. This clearly indicates that the flexibility of a body is crucial in determining its ability to move upstream or hold station.

It is important to note that, in the above experiments, the fish were placed at a distance downstream of the bluff body at about four times the diameter (D_{bb}) of the bluff body. This is very important as it shows that the fish were outside the suction region which is estimated at $1.75D_{bb}$ [11] created immediately behind the bluff body [9] and therefore the fish were not entraining.

In order to describe the thrust production mechanism, a review by other eminent authors in the field will be used, where the mechanism is outlined perfectly and therefore the description will be preserved in its entirely. By observing Figure 6, the flow velocity is represented by the direction and the length of the black arrows, where it is assumed that the muscle activity of the fish is playing a role in controlling the body posture and compliance rather than generating propulsive body movements.

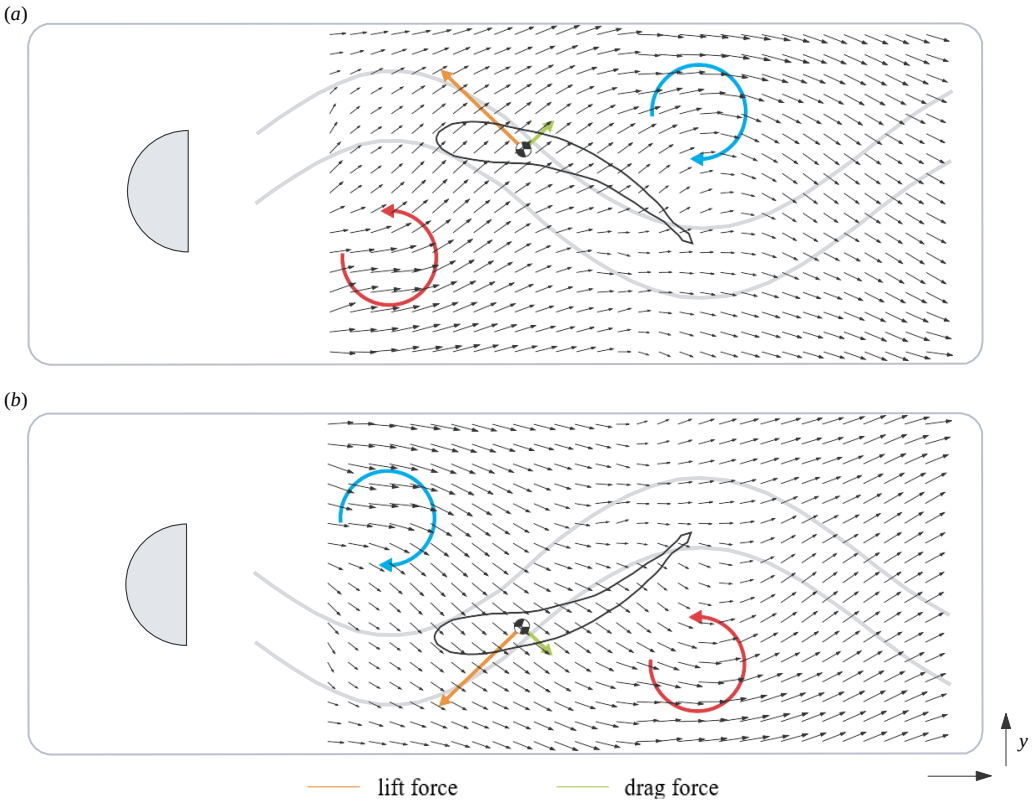

Figure 6. Vortex Street captured by a fish (adapted from [8]).

Looking at Figure 6(a), a low-pressure, counter-clockwise vortex (red circle) is shed from the cylinder and approaches the head of the swimming trout, causing the incident flow to be directed at an angle to the body. The relatively large angle of attack of the body produces a lift force (orange arrow) normal to the path of the incident flow and a drag force (green arrow) parallel to the flow. The region of average reduced flow behind the cylinder is approximated by the grey sinusoidal lines.

After a certain period of time, at Figure 6(b), the flow of the Von Kármán vortex street translates the fish back towards the midline of the wake such that the fish will then encounter a clockwise vortex (blue circle). Force vectors in the bottom diagram are the same as in the top diagram, only flipped in the y- direction. Owing to vorticity decay, the upstream vortex has a lower pressure than the downstream vortex, which may facilitate holding position in a certain region along the x-axis of the wake [8].

Summing up, the Von Kármán vortex street consists of a passive lift-based mechanism that relies on the interaction of a flexible body with the local flow velocities surrounding shed vortices [13]. In this research, it will be shown that these methods used by the fish to exploit vortices for energy extraction and conservation, can be applied to a flexible inanimate object to potentially harvest energy.

2.2.5 Vortex Induced Vibrations (VIV) Examples

Vortex Induced Vibrations (VIV) are self-limiting dynamic fluid-structure interactions caused by forces due to vortex shedding. When an object undergoes VIV, it experiences vortex shedding as a result of flow across its body profile. If the shedding frequency approaches the natural frequency of the object, large amplitude motions occur [36] [37]. Structures from mooring cables to spar buoys experience this and the resulting large amplitude motions can impact their fatigue life and the general operation of these structures.

The study of Vortex Induced Vibrations can be attributed to a large number of real-life scenarios such as the fluid flow in a heat exchanger, the vibration of structures, the vibrations of both riser pipes and offshore structures, and more. In the past, the effects of VIV have always proved detrimental. An example of this is the collapse of the Tacoma

Narrows Bridge in Washington in 1940. When a fluid flows over a bluff body, like a cylinder, due to viscous effects, a separation of fluid from the surface takes place. This separation of fluid causes an alternate shedding of vortices in the downstream region of the bluff body. These shedding of vortices cause alternate forces to develop on the surface. These forces can be large enough for the structures to vibrate, ultimately resulting in failure. As a result, understanding the fundamental nature of VIV from a design point of view, to avoid engineering failures has become very important. Many researchers [36] [38] [39] [22] [40] have thus tried to reduce the VIV of structures, specifically VIV for a flow over circular cylinders. The study of the complex fluid-structure interaction has been a topic of interest for many researchers for decades.

In the present study, a vortex street is intentionally created by placing a bluff body in a water channel and a flexible cylinder is tethered behind it. Although VIV is concerned with the shed frequency matching the natural frequency of the bluff body creating the vortex shedding, the goal of this study is to match or closely match the natural frequency of the downstream inanimate object, with the frequency of the vortices shed from the bluff body. This will enable the system to resonate and provide the potential for energy harvesting from the induced vibrations and mode shapes of the flexible cylinder due to its deformation.

2.3 Open Channel Velocity Profile Modelling

This section aims to present some of the background literature necessary to understand the fluid flow dynamics on which this project is based.

Flows in closed conduits or channels, like pipes or air ducts, are entirely in contact with rigid boundaries. Open channel flows, on the other hand, are those whose boundaries are not entirely a solid and rigid material. A part of the boundaries may be another fluid, as is the case in this research, where the top of the water channel is open, and the water is in contact with air, instead of a solid boundary. The surface of the flow thus formed is called a free surface, because that flow boundary is freely deformable, in contrast to the solid boundaries. The boundary conditions at the free surface of an open channel flow are always that both the pressure and the shear stress are zero everywhere. It is possible to have a free surface but not be an open channel flow. Closed conduit flows that consist of two

immiscible fluid phases of differing density in contact with each other along some bounding surface are not open channel flows, because they are nowhere in contact with open space, but they do have a freely deformable boundary within them.

Using published work by other authors, the equations for the distribution of shear stress and velocity in open channels will be used to recreate the vertical velocity profile of the fluid in the experimental channel used in this project. In most cases, the equations presented will not be fully derived but presented in a suitable form for the needs of the project and explained. At a later stage in this research, the velocity profile graph produced from the experimental data will be compared with the velocity profile extracted from the computational model and conclusions will be drawn.

2.3.1 Laminar and Turbulent Flow

Laminar flow is characterised by smooth, predictable streamlines (the paths of single fluid particles). In turbulent flow, the streamlines are erratic and unpredictable. Turbulent flow is characterized by the formation of eddies within the flow, resulting in continuous mixing throughout the section. Eddies result in varying velocity directions as well as magnitudes. At times, the eddies contribute to the velocity of a given particle in the direction of flow, and at other times detract from it. The result is that velocity distributions captured at different times will be quite different from one another, and will be far more chaotic than the velocity distribution of a laminar flow section. By strict interpretation, the changing velocities in turbulent flow would cause it to be classified as unsteady flow. Over time, however, the average velocity at any given point within the section is essentially constant, so the flow is assumed to be steady [7] [41].

The velocity at any given point within the turbulent section will be closer to the mean velocity of the entire section than with laminar flow conditions. As shown in Figure 7, turbulent flow velocities are closer to the mean velocity because of the continuous mixing of flow, particularly the mixing of low-velocity flow near the channel walls with the higher-velocity flow toward the centre.

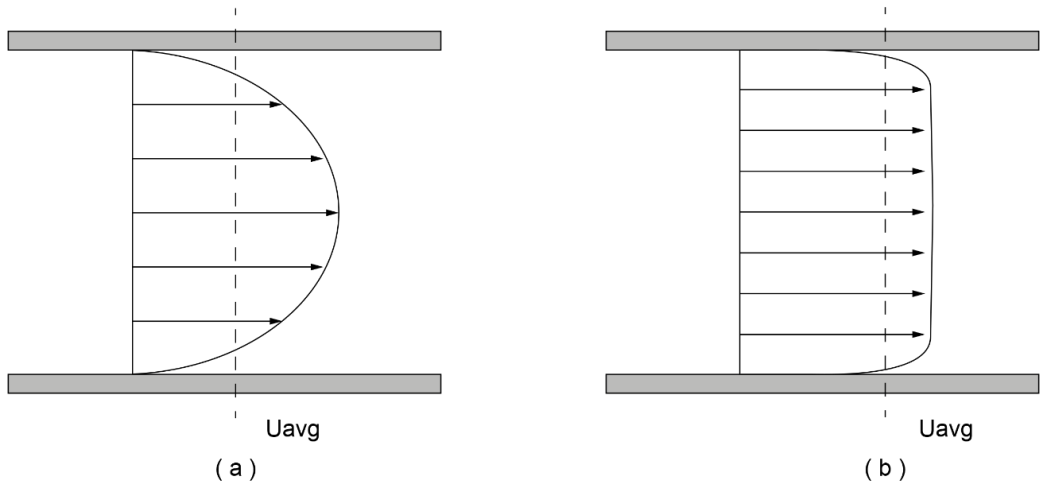

Figure 7. Laminar (a) and turbulent (b) velocity profile.

Figure 8 shows a comparison of velocity profiles, in both pipes and channels, between laminar and turbulent flows arranged to have the same discharge. It is clear that the turbulent-flow velocity profiles are much more uniform over most of the flow but show a much sharper change in velocity near the boundary, where the no-slip condition means the velocity has to go to zero [7] [42].

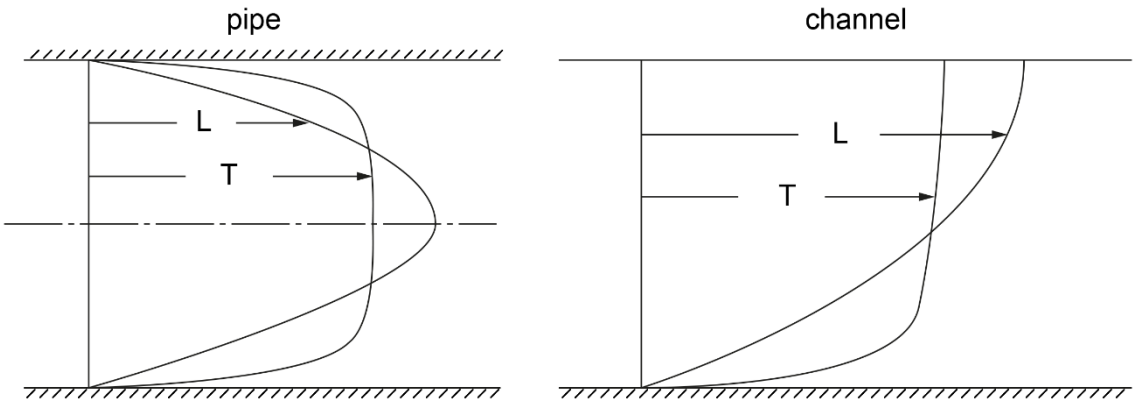

Figure 8. Laminar and turbulent flow velocity profile comparison.

2.3.2 Vertical Organisation of Flow Structure in a Channel

Through the years, considerable information concerning turbulent velocity profiles have been obtained using dimensional analysis, experimentation, numerical simulations, and semi empirical theoretical efforts.

As shown in Figure 9, the vertical velocity profile can be divided into two regions, characterised by their distances from the wall; the inner region near the bed of the channel, and the outer region near the free surface.

The inner region is divided into the viscous sublayer (laminar sublayer) adjacent to the wall, an intermediate area of transition (buffer layer) and the fully turbulent region (logarithmic region - Figure 9). The viscous sublayer, is a thin layer of flow next to the boundary (channel bed) in which viscous shear stress predominates over turbulent shear stress which in contrary dominates in the outer region, where considerable mixing and flow randomness exists [7].

The buffer layer is a zone outside the viscous sublayer where both viscous and turbulent effects are present in the flow. The fully turbulent region is also called the overlap region or the logarithmic region. Since the outer region does not satisfy the no-slip condition at the boundary and at the same time the inner region does satisfy the no-slip condition, the overlap layer serves as a mean to correctly asymptote the inner to the outer region.

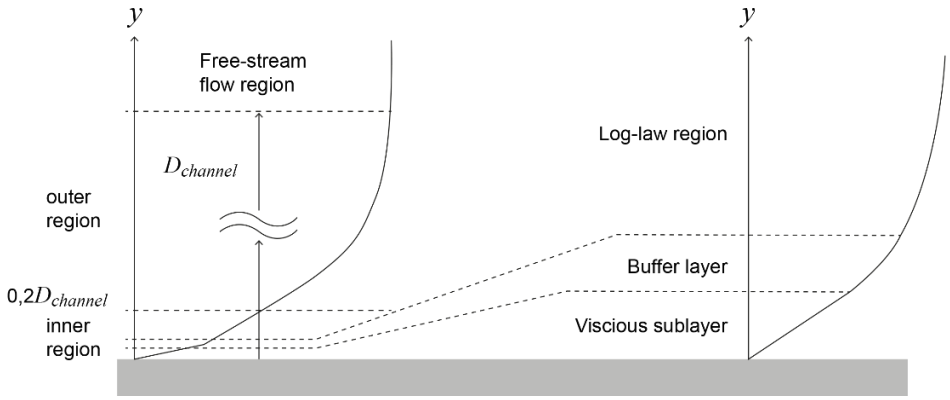

Figure 9. Vertical velocity profile distribution in open water channel.

The flow in the inner region is affected by the roughness of the channel bed. The influence of boundary texture on the velocity profile has been studied by gluing uniform sand grains to the bed of the flume and the velocity profile over the bed at different flow speeds has been measured [43] [44] [45]. It was found that when the surface texture is smaller than

the viscous sublayer, then the flow above does not feel the surface texture, at a condition $y_0 = \frac{\nu}{9U_*}$. y_0 is the distance from the boundary at which the idealized velocity given by the law of the wall goes to zero [46] [47]. This is referred to as a smooth surface. Otherwise, when the bed surface is rough, it does affect the region and this has to be taken into consideration when fitting the respective equations. In this project, the bottom of the water channel is smooth, therefore no discussion will be provided related to rough surface bed and the respective equations.

Numerous studies, by a careful use of dimensional analysis arguments for the flow and by matching the results in the common layers, presented various semi-empirical equations giving very good velocity profile approximation of a fully developed turbulent flow. There have been an extensive number of corrections and additions to these equations aiming to have a more accurate fitting to the experimental results. Below, the most accepted basic forms of equations are presented for a channel with a smooth bed.

First, in 1930, Theodore von Kármán published the law of the wall [48], stating that the average velocity of a turbulent flow at a certain point is proportional to the distance from that point to the wall, or the boundary of the fluid region. In the case of viscous sublayer, the boundary distribution is written as:

$$\frac{U_{avg}}{U_*} = \frac{y_h U_*}{\nu}$$

Equation 10. Viscous Sublayer velocity profile fitting equation.

Where, U_{avg} is the average velocity at a distance y_h from the bottom of the channel. U_* is the shear (friction) velocity. Equation 10 is valid very near the smooth wall for $0 \leq \frac{y_h U^*}{\nu} \leq 5$. Derivation of the law of the wall can be found in [49]. Further discussion follows in section 5.4.2, introducing the dimensional form of the law.

From the experiments of Nikuradse, it has been found that in the overlap region, the vertical distribution of the velocity should vary as the logarithm of y_h. Therefore, the logarithmic law [50] has been proposed:

$$\frac{U_{avg}}{U_*} = \frac{1}{k} ln \frac{y_h U_*}{\nu} + B$$

Equation 11. The logarithmic law.

Where, k is the Von Kármán constant and B is an integration constant, found experimentally. Various researchers have studied these parameters. The value of $k = 0.41$ is a universal constant irrespective of flow configuration [51]. In contrast, the constant B may depend on flow properties. Table 2 summarises the values for constant B obtained from various studies.

Reference	***B***
Nikuradse [50]	5.50
Bradshaw *et al.* [52]	5.20
Stefler *et al.* [53]	5.50
Nezu and Rodi [54]	5.29
Cardoso *et al.* [55]	5.10
Kirkgöz and Ardiclioglou [56]	5.50

Table 2. Integration constant (B) proposed values for the logarithmic law.

The quantity $U_* = \sqrt{\frac{\tau_w}{\rho}}$ is termed the friction or shear velocity because it has dimension m/s, although it is not actually a flow velocity and can be written as $\tau_w = \rho U_*^2$. Further explanation as well as the physics behind can be found in [7]. Darcy - Weisbach related the pressure drop in the flow to the shear stress and proposed formulas involving the friction factor with the shear stress. Then, Prandtl derived an expression where Reynolds number was associated with friction factor. Finally, Blasius proposed a simplification of the previous work in the area with the following formula [57] [58],

$$f_{factor} = (100 Re_{channel})^{-1/4}$$

Equation 12. Blasius friction factor formula.

Combining Darcy – Weisbach work and Equation 12, an expression relating the maximum velocity with the average velocity and the friction factor is derived [57] [58],

$$U_{max} = U_{avg}(1 + 1.33\sqrt{f_{factor}})$$

Equation 13. Maximum velocity expression.

Generally, there are many empirical equations with a good correlation with experimental data such as the Power law, the Wake law, Binary law etc. All give a good representation of the inner region, however, in this research, the outer region is the one of interest. This

is because the flexible cylinder is tethered at a height of $0.3m$ from the bottom of the water channel. According to Cebeci, the inner region is about 20% of the entire boundary thickness (water depth) [59]. That equates to 0.094m from the channel bed.

2.3.2.1 Velocity Models in the Outer Region

The vertical velocity profile is well described by the classical logarithmic law in the inner region $\xi < 0.2$, where $\xi = \frac{y_h}{D_{channel}}$ is the ratio of the distance from the bed to flow depth [54] [55] [60] [61]. However, the log law deviates from experimental data in the outer region $\xi > 0.2$ and and fails to predict the maximum velocity just under the water surface. Coles introduced the wake function taking into account this deviation [62] [63].

Nezu and Rodi proposed that the open channel flows could be classified into two categories, two or three-dimensional. This refers to the number of space coordinates required to describe the flow. Any physical flow is generally three-dimensional, however since there is an increased difficulty to calculate, this can be achieved by ignoring changes of the flow in any of the directions, thus reducing the complexity [64].

In two-dimensional open channel flows, where the aspect ratio $A_r > 5$, in addition to the simple power law [65] [66], Coles' log-wake law appears to be the most reasonable extension of the log law [60] [62]. However, in narrow open channels like the Armfield water channel used during this project, with an aspect ratio $A_r < 5$, the maximum velocity appears below the free surface producing the velocity-dip-phenomenon as shown schematically in Figure 10, where maximum velocity occurs below the water surface. This phenomenon, which was reported more than a century ago [67] [68], involves a deviation from the log-wake law. Coles' function is unable to represent the secondary currents generated in the three-dimensional open channel flows. It predicts a velocity which increases with distance from the channel bed [69] and a maximum velocity located on the water surface [69]. Coles' wake function is valid for both smooth and rough surfaces and it is defined as:

$$w(\xi) = \frac{2\Pi}{k} sin^2(\frac{\pi}{2}\xi)$$

Equation 14. Coles' wake function.

Where, k is the Von Kármán constant, ξ is the dimensionless distance from the bed and Π is the function parameter [69]. Many researchers [54] [70] [55] have checked the validity of this law for the inner and outer regions of the boundary layer and they have proposed different values for the parameter Π. In order to fit their experimental results with this law, Nezu and Rodi had to decrease the value proposed by Coles ($\Pi = 0.55$) and they proposed a value of $\Pi = 0.2$ for Reynolds numbers higher than 10^5 [54]. Kirkgöz needed to lower that parameter to $\Pi = 0.10$ [56]. In this project, since the Reynolds number of the channel is in the order of 10^5, the value of the function parameter is chosen to be $\Pi = 0.2$.

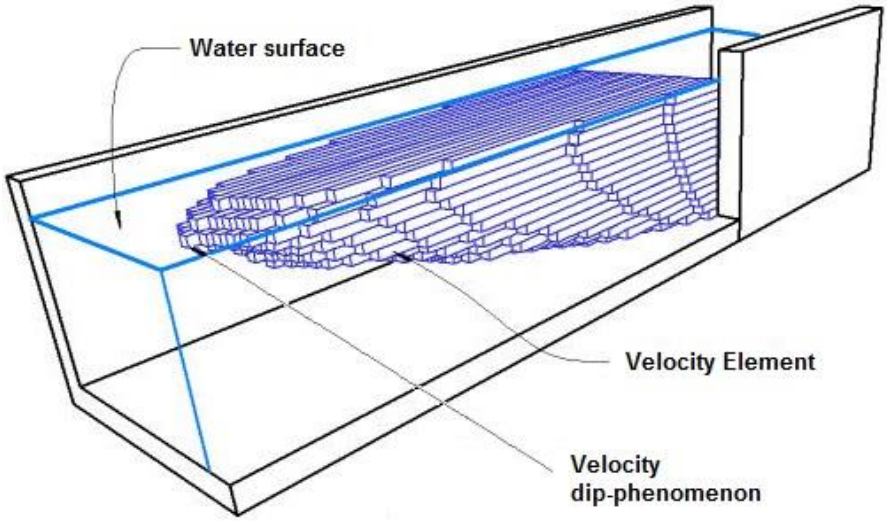

Figure 10. Illustration of a typical velocity profile development in a rectangular open channel (adapted from [71]).

Coles' wake function is an additive correction to the log-law, therefore the semi-empirical equation for the outer region is shaped as [69],

$$\frac{U_{avg}}{U_*} = \frac{1}{k} ln \frac{y_h U_*}{\nu} + B + w(\xi)$$

Equation 15. Log-law with Coles' wake function.

The last decade, several analytical or empirical equations were proposed to predict the velocity profile for narrow channels, usually a modification of the log-law and Coles' wake function, aiming to characterise the velocity-dip-phenomenon in the outer region. Substantial review can be found in the literature [72] [73] [74] [75].

For the needs of this project, the 'simple dip-modified log-wake' law has been applied. It is created by adding both the Coles' wake function and the term linearly proportional to the logarithmic distance from the free surface [73] to the log-law, formed as,

$$\frac{U_{avg}}{U_*} = \frac{1}{k}\left[ln\left(\frac{y_h}{y_0}\right) + 2\Pi\, sin^2\left(\frac{\pi}{2}\xi\right) + \propto ln(1-\xi)\right]$$

Equation 16. Simple dip-modified log-wake law.

Where, $\propto = 1.3e^{\left(\frac{W_{ch}}{2D_{ch}}\right)}$ is the velocity profile improvement parameter [74].

The location of the maximum velocity (dip-phenomenon), can be found using established equations from the literature. According to [75] [76], the location of the dip phenomenon can be found by,

$$\xi_{\text{dip}} = \frac{1}{1 + 1.3e^{\left(\frac{-A_r}{2}\right)}}$$

Equation 17. Dip-phenomenon dimensionless location.

Where, A_r is the aspect ratio of width to depth of the channel. As it can be observed, the equation does not require any experimental data to provide the answer, therefore it is expected to give an accurate approximation of the dip location. Further discussion follows in section 2.3.3 of this chapter, where the fitting process of the semi-empirical equations is described.

2.3.2.2 Open Channel Reynolds Number

As already discussed, Reynolds number is the ratio of inertial to viscous forces and characterises the level of turbulence in the flow. The value of Reynolds number varies for different geometries and flow conditions. Compared to the circular bluff body discussed earlier, for flow through a water channel, the Reynolds number is based on the hydraulic radius R_h defined as,

$$Rh = \frac{A_C}{P_{wet}}$$

Equation 18. Hydraulic radius of open channel.

where A_c is the cross-sectional area of the water channel and P_{wet} is the wetted perimeter. Therefore, the Reynolds number of the open channel is,

$$Re_{channel} = \frac{U_{avg} \times R_h}{\nu}$$

Equation 19. Reynolds number of open channel.

This definition of Reynolds number (open channel) will be used at a later stage to calculate parameters necessary to create the vertical velocity profile of the experimental water channel. The turbulence of the water channel will not be characterised as it falls outside the scope of this research but discussion follows in chapter 3.

2.3.2.3 Entrance Length

Consider a fluid entering an open channel at a uniform velocity. Because of the no-slip condition, the fluid particles in the layer in contact with the walls of the channel come to a complete stop. This layer also causes the fluid particles in the adjacent layers to slow down gradually as a result of friction. To make up for this velocity reduction, the velocity of the fluid at the midsection of the channel has to increase to keep the mass flow rate through the channel constant. As discussed in section 2.1, this is the law of conversation of mass.

As a result, a velocity gradient develops along the channel. The region of the flow in which the effects of the viscous shearing forces caused by fluid viscosity are felt is called the boundary layer. The hypothetical boundary surface divides the flow in the channel into two regions: the boundary layer region, in which the viscous effects and the velocity changes are significant, and the irrotational flow region, in which the frictional effects are negligible and the velocity remains essentially constant in the radial direction [7].

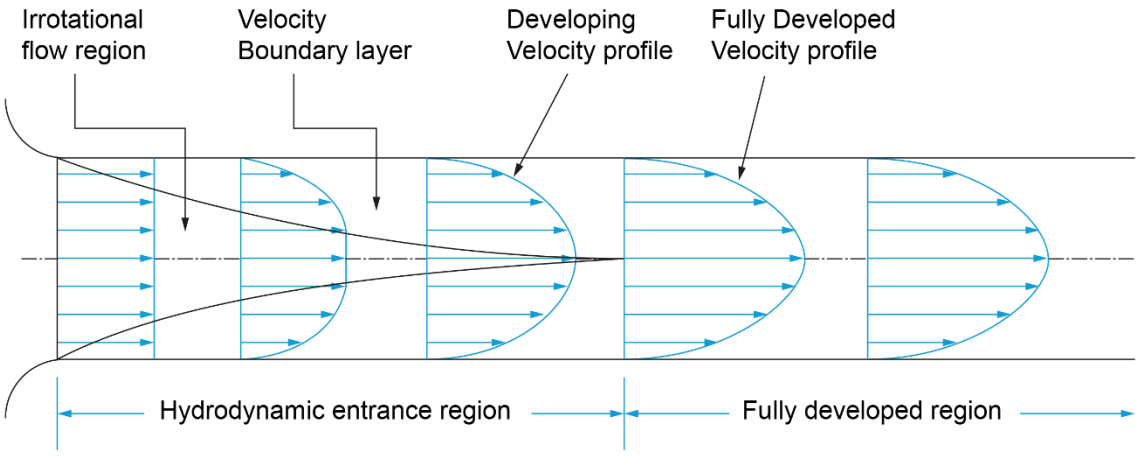

Figure 11. Entrance length plan view of open channel (adapted from [51]).

The thickness of this boundary layer increases in the flow direction until the boundary layer reaches the channel centre and thus fills the entire channel, as shown in Figure 11. The region from the channel inlet to the point at which the boundary layer merges at the centreline is called the hydrodynamic entrance region, and the length of this region is called the hydrodynamic entrance length. Flow in the entrance region is called hydro-dynamically developing flow since this is the region where the velocity profile develops. The region beyond the entrance region in which the velocity profile is fully developed and remains unchanged is called the hydro-dynamically fully developed region. The flow is said to be fully developed when the velocity profile 'shape' remains unchanged. The velocity profile in the fully developed region is parabolic in laminar flow and somewhat flatter (or fuller) in turbulent flow due to eddy motion and more vigorous mixing in the radial direction [7].

The entry lengths vary according to the turbulence level (laminar or turbulent) and the geometry of the conduit. It has been shown in [7] and [77] that the entrance length for turbulent flow in open channels is found by,

$$L_{entrance} = 4.4Re_{channel}^{1/6}$$

Equation 20. Entrance length for rectangular open channels.

According to Equation 20, the distance which the flow needs to travel in the present research to become fully developed is 30.89m. As it will be discussed later, the experimental channel available has a maximum length of 23m. Therefore, the profile of the flow will not be fully developed.

It is also important to highlight that the velocity of the flow measured experimentally, initially using a lightweight ball as described in section 3.1.1 and later verified using an Acoustic Doppler Velocimetry (ADV), as presented in section 4.4, despite that the measurements are of a good agreement, the author believes that further flow investigation would add more value and create more substantial base of data to work with during the experimental and computational work, presented later. For example, the level of turbulence has not been assessed which could have been used as an input to the computational model. Also, the effect of the pump in the flow has not been investigated, which would have given a more precise understanding of the velocity, turbulence levels and development of the velocity profile. Despite this, as it will be shown later, the results both experimentally and computationally sufficiently satisfy this scope of this research.

2.3.2.4 Velocity Profile Fitting Process

As previously discussed, there has been an extensive body of work conducted over the years recreating the velocity profile of open channels. Each law with their respective equations require a set of known parameters to enable their implementation, usually either found through experiments or using already established formulas in the field.

Similarly, in this project, in order to be able to use the semi-empirical equations and plot the velocity profile, it is necessary to find a set of parameters. Since the only parameter found experimentally is the average velocity, the rest will be determined using already established formulas from the literature. For the needs of the project, three semi-empirical equations will be plotted, namely; the logarithmic law in a smooth wall, Coles' wake function which is an extension of the Log-law and the 'simple dip-modified log-wake' law, a modification of a combination of the previous two laws.

For all laws, Equation 11 (logarithmic law), Equation 15 (Coles' wake function) and Equation 16 (simple dip-modified log-wake function), the shear velocity U_* is the missing parameter which cannot be directly quantified from the current experimental data and characteristics of the water channel. In order to find the value of the shear velocity, a combination of equations has been used, directly obtained from the literature. These equations are a simplification of more complex formulas, which will not be discussed in this project as their derivation can be found at the relevant references.

A graphical representation of the fitting process can be found in Figure 12 below. Using the width and the depth of the water channel, the hydraulic radius is found which is then used to calculate the Reynolds number of the open channel. Worth mentioning again $Re_{channel}$ is different from the Reynolds number around the bluff body and in this project, it will only be used once, to find the missing parameter for the velocity profile fitting. Any reference to Reynolds number, unless otherwise specified, it will be towards the Reynolds number of the bluff body. Finding the Reynolds number of the open channel, the friction factor is then calculated, which in turn allows the shear velocity U_*, to be found. Finally, shear velocity is used as an input parameter in every velocity profile equation, alongside with the related law constants. In Appendix A.5.1, a spreadsheet is included where the calculation and values of the parameters can be found. Further discussion will follow in chapter 4, where the experimental data are used to plot the velocity profile.

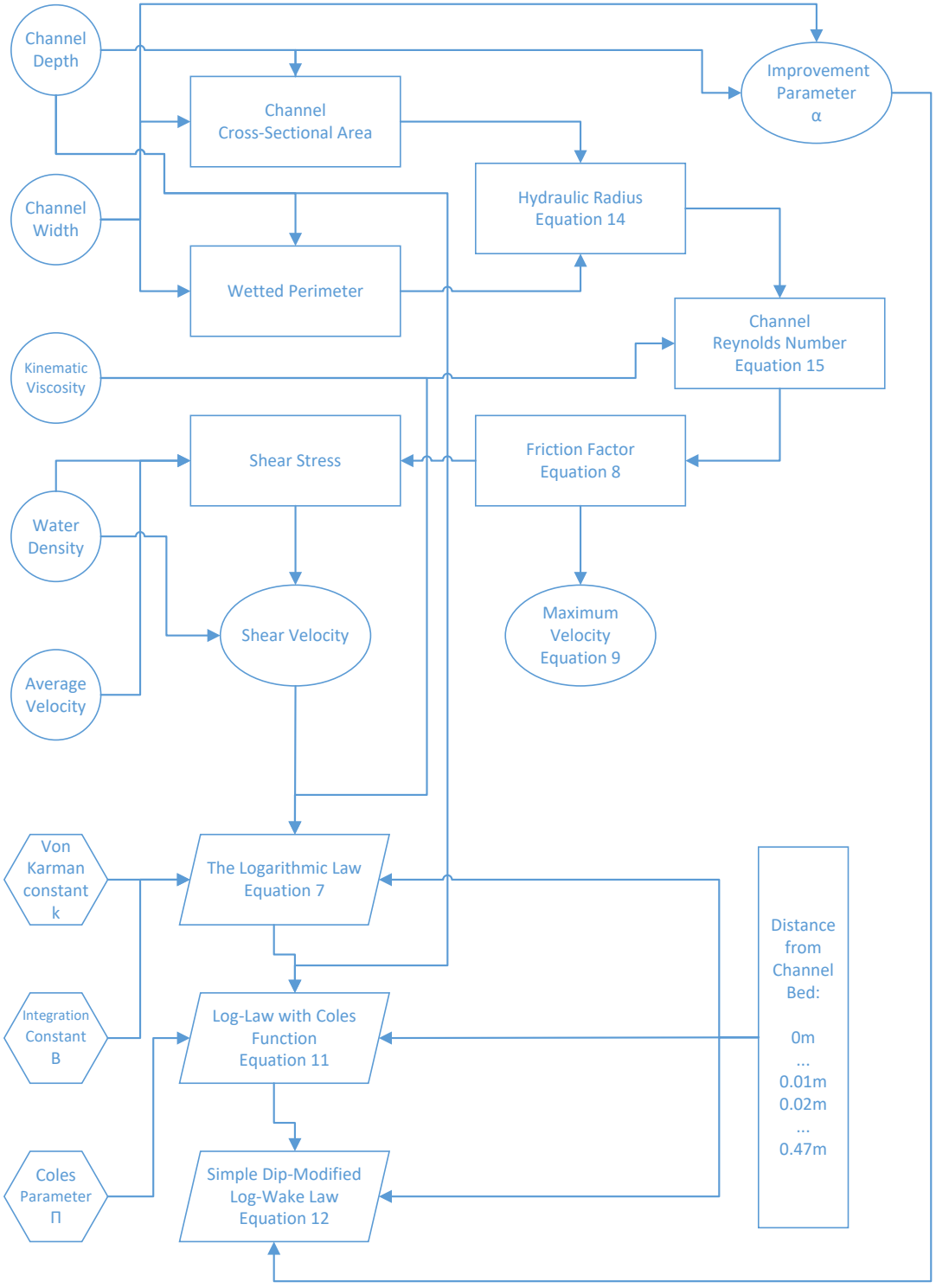

Figure 12. Velocity profile fitting process diagram.

2.4 Computational Modelling of Flow Field

Computationally, turbulent flows may be evaluated using several different approaches. Either by solving the Reynolds-averaged Navier- Stokes equations with suitable models for turbulent quantities or by computing them directly. The main approaches are summarised below.

Turbulent flows are characterized by velocity fields which fluctuate rapidly both in space and time. Since these fluctuations occur over several orders of magnitude it is computationally very expensive to construct a grid which directly simulates both the small scale and high frequency fluctuations for problems of practical engineering significance. Two methods can be used to eliminate the need to resolve these small scales and high frequencies: Filtering and Time averaging [78].

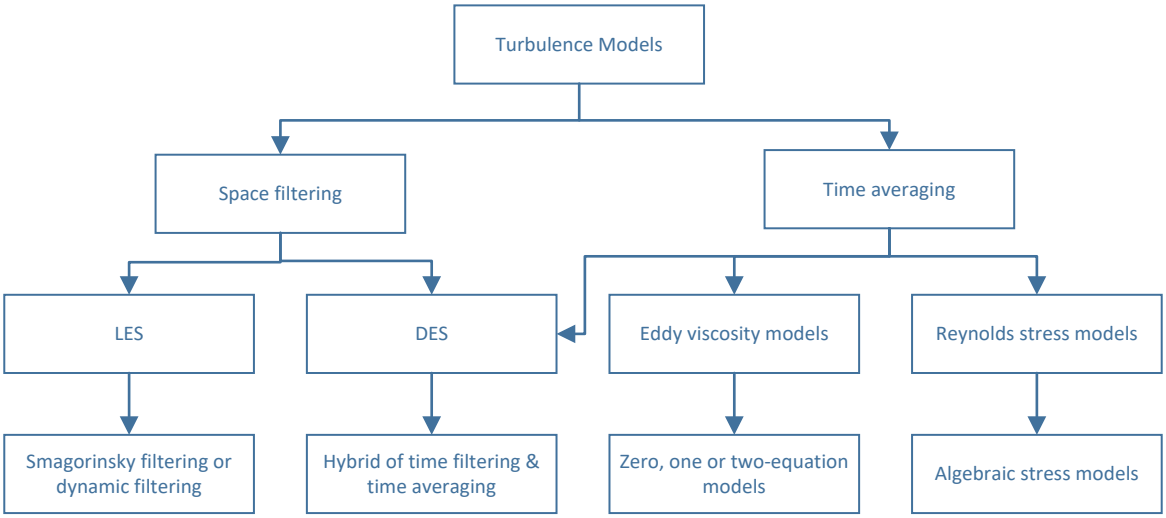

Figure 13. Turbulence models classification.

Figure 13 presents the overview of turbulence models commonly available in CFD, just for the information of the reader. Generally, simulations of flow can be done by filtering or averaging the Navier-Stokes equations (RANS). Filtering in the context of large eddy simulation (LES) and Detached Eddie Simulation (DES), is a mathematical operation intended to remove a range of small scales from the solution to the Navier-Stokes equations. Because the principal difficulty in simulating turbulent flows comes from the wide range of length and time scales, this operation makes turbulent flow simulation cheaper by reducing the range of scales that must be resolved. The LES filter operation is low-pass, meaning it filters out the scales associated with high frequencies [79].

In the time averaging or Reynolds averaging approach all flow variables are divided into a mean component and a rapidly fluctuating component and then all equations are time averaged to remove the rapidly fluctuating components. In the Navier-Stokes equation the time averaging introduces new terms which involve mean values of products of rapidly varying quantities. These new terms are known as the Reynolds Stresses, and solution of the equations initially involves the construction of suitable models to represent these Reynolds Stresses [80]. Figure 14 presents the turbulence models available in Fluent, ANSYS®, categorised according to their computational cost.

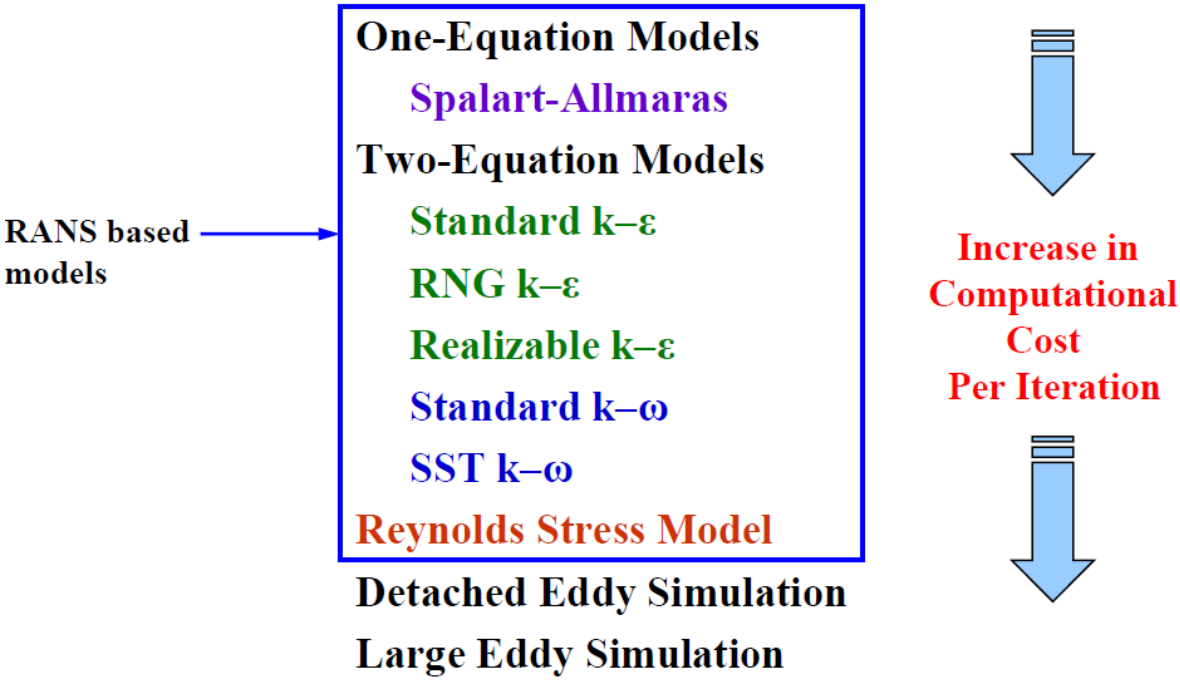

Figure 14. Fluent turbulence models categorised according to computational cost (taken from [81]).

An example of time averaging model is the widely used k-ε model, part of the RANS family. Due to its popularity a short summary of its functionalities is presented:

The k-ε turbulence model is a sophisticated and general turbulence model that is used in Computational Fluid Dynamics (CFD) that allows for the effect of transport of turbulence properties by convection and diffusion and for production and destruction of turbulence. It is a two equation model that gives description of turbulence by means of two transport equations (PDEs), one for the turbulent kinetic energy, k , and the other one for the rate of dissipation of turbulent kinetic energy, ε. The principal assumption of this turbulence model is that the turbulent viscosity is isotropic, which means that the ratio between Reynolds stress and mean rate of deformation is the same in all directions [82]. However,

this assumption fails in many complex flows where it leads to inaccurate predictions. The summary of the performance assessment for the standard k-ε is listed as follows:

- Advantages
    - The simplest turbulence model since boundary layer conditions do not need to be specified.
    - Gives excellent performance in many industrially relevant flows.
    - Well established.
    - The most widely validated turbulence model.
- Disadvantages
    - It can be computationally costly compared with the other turbulence model such as mixing length model.
    - Gives poor performance in a variety of important cases such as:
        - Unconfined flows.
        - Flows with large extra strains (e.g. swirling flows, curved boundary layers).
        - Rotating flows.
        - Flows driven by anisotropy of normal Reynolds stresses (e.g. fully developed flows in non-circular ducts).

In general, the standard two-equation k-ε model is unable to predict secondary currents and the related velocity dip-phenomenon where the maximum velocity appears below the free surface producing the velocity-dip-phenomenon, since it assumes isotropic turbulence. Accurate predictions of velocity-dip-phenomena therefore require more sophisticated models.

Another popular two-equation model pairs k with the specific rate of dissipation of kinetic energy, or omega (ω). The aim of the standard k-ω model is to model near-wall interactions more accurately than k-ε models. However, the k-ω model can over-predict shear stresses of adverse pressure gradient boundary layers and that the model has issues with free stream flows. The model is also very sensitive to inlet boundary conditions, which is a disadvantage not seen in k-ε [83].

The Shear Stress Transport (SST) k-ω model is an enhancement of the original k-ω model and addresses some specific flaws of the base model, such as the sensitivity to freestream

turbulence levels. It has the advantage that it can be applied to the viscous-affected region without further modification, which is one reason it has become a popular choice in aerospace applications where the flow is deemed too complex for Spalart-Allmaras. The SST k-ω accounts for cross-diffusion which better marries the k-epsilon and k-omega models. Using a blended function based on wall distance, engineers can include cross-diffusion when away from the wall but not near it. In other words, using the wall distance as a switch, SST works like k-ε in the far field and k- ω near the target geometry [83]. Authors who use the SST k-ω model often merit it for its good behaviour in adverse pressure gradients and separating flow. The SST k-ω model does produce a bit too large turbulence levels in regions with large normal strain, like stagnation regions and regions with strong acceleration. This tendency is much less pronounced than with a normal k-ε model though [84].

RANS models simulate all scales of turbulence and resolve none. Models which use the filtering approach like, Large-eddy simulation (LES) and detached-eddy simulation (DES), resolve the largest scales of turbulence and model the rest by use of sub-grid turbulence models or by blending with a RANS model. It means that the small scales of the transport equation solution are taken out by applying low-pass filtering. The models are used to predict large turbulent eddy structures when solving a CFD model system with a fine mesh. However, since turbulent scales are small near the wall, the model is unable to predict these regions with accuracy. The biggest limitations with both the LES and DES models are their high computational costs.

As there is not one-model-fits-all cases, one should consider some of the following points whilst deciding which model to use. First of all, the accuracy when used in their original scope, thus to make sure that the model can actually resolve the physics of the problem under study. The ability to produce appropriate results in applications that will not be useful towards the primary goal of the study. Finally, but very important, the computational cost of the turbulence model and its ability to produce quick preliminary results. This always depends on the available computational power.

Following the work done by other authors, as well as some initial computational modelling, it has been decided that SST k- ω model will be used for all the computational work in this project. The major decision factor was the available computational power to the author and

the licence restrictions related to HPC, two-way coupling within the University of Southampton ANSYS® academic license provided.

No further discussion will take place regarding the computational models as it falls outside the scope of this project.

To create a computational domain representing the experimental open channel, it is necessary to define correctly the boundary conditions of the domain. Looking at other published work, three different approaches are used to create the concept of the open channel in ANSYS®. The first approach is using the Volume of Fluid (VOF) condition, where the solver knows that one surface of the model is in contact with another fluid (air). Three out of the four sides of the domain are declared as 'wall', and the forth one (top side), acts as the surface of the channel. VOF is usually used when the study requires to investigate the surface of the channel, such as wave interaction with a structure. The second and third approaches is to declare the same top side of the computational domain as 'symmetry' or 'zero shear'. The 'symmetry' boundary is often used in cases where it is known that the model under investigation will behave identically around an axis. Therefore, the model can be halved and save significant time in computation. It is understandable that there might be some loses of the characteristics of the surface or just under the surface, however the area of interest is in the region of 30cm measured from the bottom of the water channel. That is the area where the flexible cylinder is tethered and expected to move. In general, VOF is computationally expensive and it is usually used for studies related to the free surface of the fluid, for example a semi-submerged object in the water, therefore not the best fit for the needs of this research. Further discussion will take place in chapter 5.

2.5 Piezoelectricity and Energy Harvesting Devices

Piezoelectricity was discovered by two brothers Jacques and Pierre Curie in 1880 [85]. The name "piezo" was derived from the Greek, meaning ‘to press’, hence, piezoelectricity is the generation of electricity as a result of a mechanical pressure. The discovery of piezoelectricity has led researchers to employ it in applications such as sensing, actuating and energy harvesting. This section provides a brief summary of the mechanisms behind the concept of piezoelectricity and presents some related work done by other authors.

2.5.1 Piezoelectric Concept

To understand the concept of a piezoelectric material the piezoelectric effect must first be examined. The piezoelectric effect is the effect of generating electric charge by a material once it is subjected to mechanical stress and this effect is irreversible. A rubber band produces heat when it is subjected to a series of extensions and the reasoning behind the piezoelectric material is the same only that now the material produces electricity, not heat [86]. In this respect, piezoelectric materials can be defined as materials that can show a piezoelectric effect, meaning to generate electric charge in response to applied stress.

These materials can either be natural or manmade. Flexible piezoelectric materials with applications in low frequency are those that catch mechanical stress of low frequencies. They are mostly crystalline materials like quartz but can also be ceramic or polymer. They are made up of ions which contain both positive and negative charges. Once a piezoelectric material is subjected to a mechanical force, there is shifting of positive and negative charges inside the material causing polarisation and in turn an external electric field is created. The strength of electric field created or the degree of polarisation depends highly on the amount of mechanical force. The materials are sensitive to stress as well as to electric fields. When a stress is applied on them, they convert the mechanical energy into electrical signals. This is called the direct piezoelectric effect and was discovered by the Curie brothers. When they are exposed to electric fields, the opposite happens and they convert the electrical signals into mechanical energy [87]. This is called the inverse piezoelectric effect and was discovered by Lippmann in 1881 [88].

Initially, most piezoelectric materials were made of ceramic but they have the disadvantage of not being able to withstand much strain. Conversely, electro active polymers (EAPs) are able to withstand a lot of strain and they show changes in size and shape when put into an electric field. There are different types of the EAPs. First there are the dielectric EAPs, with a high level of flexibility by withstanding high strain levels. They produce high electric volts and use very little power. Secondly, the ferroelectric polymer such as polyvinylidene fluoride (PVDF) which has the ability of holding a permanent electric polarization. Thirdly, the electrostrictive graft polymer which contains flexible chains, with a backbone chain that branches into side chains. Ionic polymers are polymers that show actuation through the displacement of ions inside the material [89].

Nowadays, most piezoelectric materials are ferroelectrics (e.g. lead zirconate titanate PZT) except quartz. Quartz possesses a natural spontaneous polarisation without applying an external field [90]. For ferroelectric material, the dipoles of the molecules are aligned in the direction of the applied electric field and a net polarisation is generated [91]. Figure 15, illustrates the orientation of the dipoles before, during and after the poling process. The poling process is further discussed in section 7.2, when used in this research.

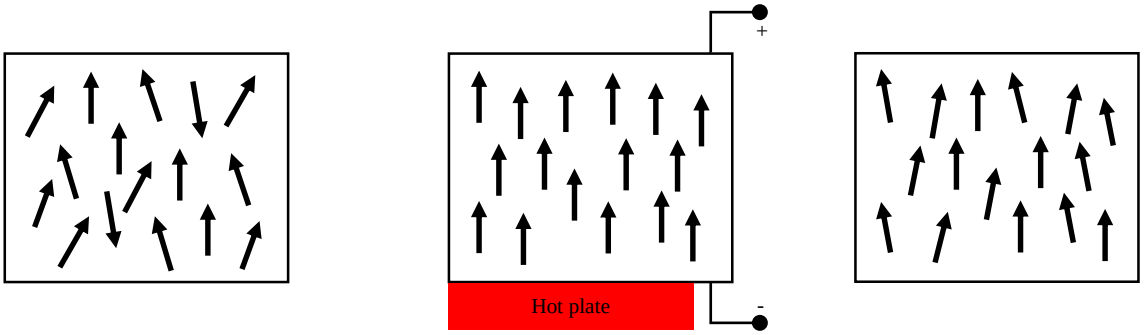

(a) Before Poling (b) During Poling (c) After Poling

Figure 15. The effect of poling on the dipoles of a ferroelectric material.

The direction of the external electric field, the polarisation force applied on the element and the charge extractions are all interrelated parameters and can be described using the piezoelectric coefficients. These coefficients reflect how piezoelectric a material is. The higher the piezoelectric property, the higher electrical power that could be harvested. The most commonly cited coefficient is the piezoelectric charge coefficient (d) which is defined as the electric charge generated per unit area when a force is applied (C/N) [92]. It can also be defined as the resultant strain when an electric field is applied. A second piezoelectric

coefficient is the piezoelectric voltage coefficient (g). It is defined as the open- circuit electric field generated when a mechanical stress (N/m^2) is applied.

Piezoelectric coefficients with double subscripts link electrical and mechanical quantities. The first subscript gives the direction of the externally applied electrical field. The second subscript gives the direction of mechanical stress or strain applied to the material [92]. To identify directions in a piezoelectric element, the three principle axes are defined, as shown in Figure 16(a).

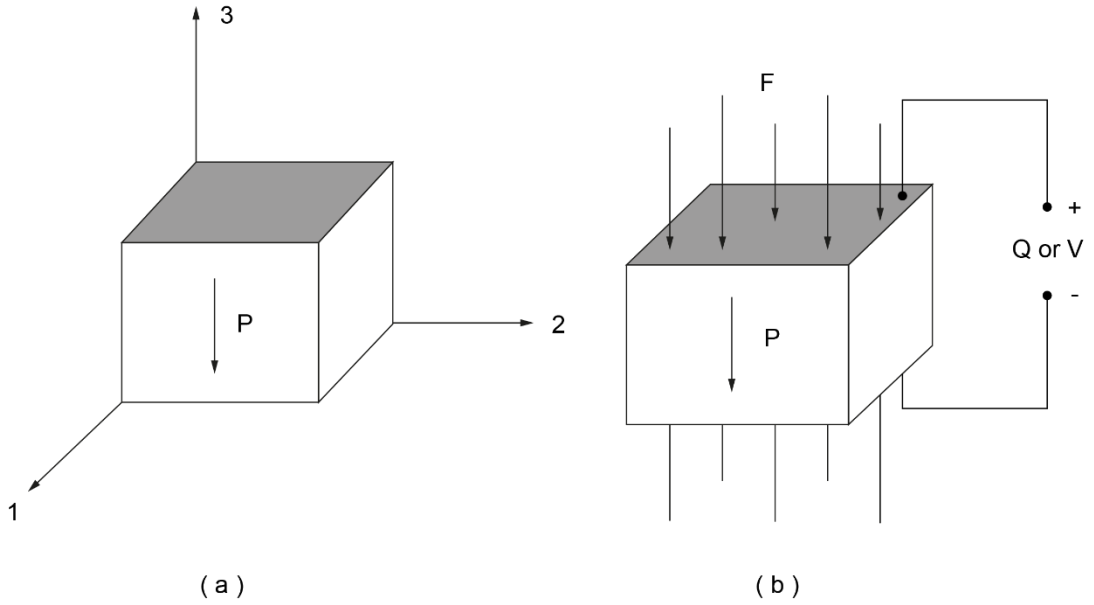

Figure 16. Directions in a piezoelectric element (a) and d_{33} coefficient poling direction (b).

Material properties along the 1 and 2 axes are identical to each other and in the plane of the piezoelectric material. The properties in the 3 direction, are different to those in the 1 and 2 directions. For simplicity, references in the literature are mostly made only to the 3 and 1 directions. The poling or 3-axis is invariably taken parallel to the direction of polarisation within piezoelectric layer. The polarisation vector P is represented by an arrow pointing from the positive to the negative poling electrode. In this research, the longitudinal piezoelectric charge coefficient d_{33} is used when the applied force and the generated charge are in the same direction of the polarisation, which is the 3-direction as shown in Figure 16(b). If the force were to be applied on the 2-direction, the transverse piezoelectric charge coefficient d_{31} would have been used. The piezoelectric charge coefficient is a measure of the amount of generated charge (Q) when 1N of force is applied to the piezoelectric element. Thus, units can be expressed in Coulombs per square meter, over Newton's per square meter, resulting to Coulombs over Newton's (C/N).

2.5.2 Energy Harvesting Using Piezoelectric Material

This section attempts to introduce energy harvesting devices using piezoelectric material arrangements to harvest energy.

Harvesting energy using piezoelectricity is not a new concept. Due to its increasing demand and attention, the power generation from such applications have been increasing. One of the first innovative types of piezoelectric wind generators was a windmill with ten piezoelectric bimorphs in a cantilever form. The wind could rotate a table fan which was generating a torque turning the windmill. The transducers were oscillating between stoppers as seen in Figure 17. The research proved a 7.5mW power generation at a wind speed of 4.5 m/s, across an optimum load of 6.7kΩ [93].

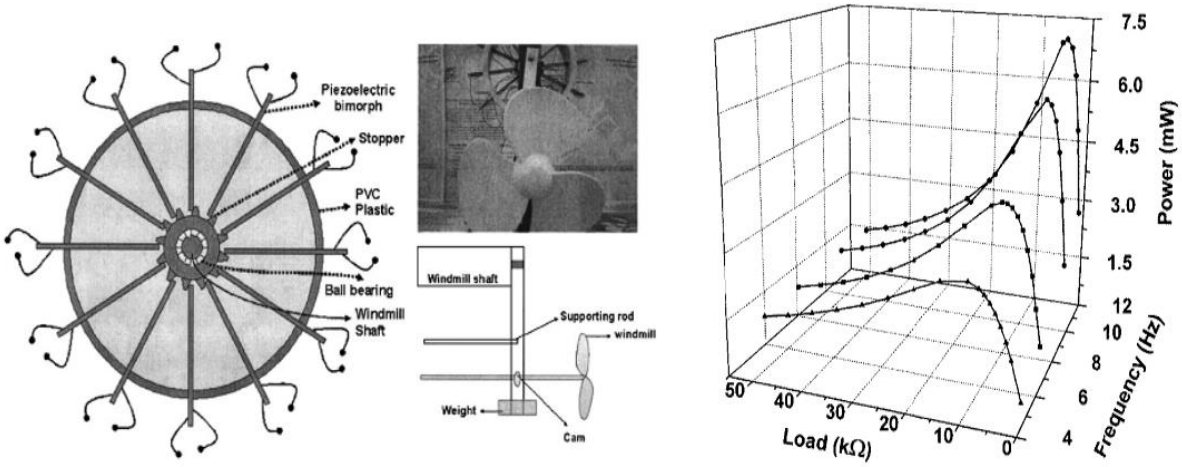

Figure 17. Schematic of piezoelectric windmill (left), variation of power with respect to frequency and load (right) (adapted from [93]).

Another example is the work done in energy harvesting applications from wind using flag-like membranes [94]. The flapping of the membrane caused by the wind induces bending stresses, which generate voltage across the surface of the material with its respective piezoelectric properties. In this research, a simple homemade suction wind tunnel and a bimorph PVDF. The bimorph consisted of two piezoelectric layers, one on the top surface of the non-active core and one on the bottom surface. Each PVDF sheet is electrically in parallel, therefore the capacitance of each individual sheet can be summed together to give a total capacitance 'C' of the bimorph. It was possible to generate an output power of 1mW at a wind speed of 5m/s using a resistive load matched to the capacitive source impedance.

A researcher at the University of Southampton has created a miniature energy harvester using air as the source of mechanical energy applied on a flapping cantilevered piezoelectric film, shown in Figure 18. In this case, the bluff body was an airfoil that was simulated using ANSYS® CFX and assessed for different angles of attack, lengths of cantilevered beam as well to estimate the lift force the wing would experience. After performing wind tunnel tests, it was able to generate power output in the order of few μW with a maximum open-circuit voltage of 1.32V [95].

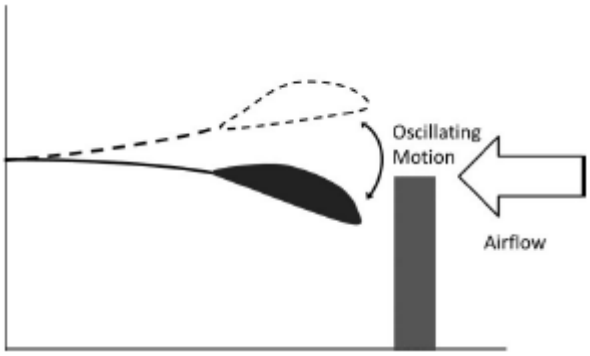

Figure 18. Flapping generator schematic.

Despite the vast amount of research that has been undertaken into the swimming abilities of fish, very few cases have found their way into practical engineering solutions such that it would be possible to generate energy with piezoelectric material. In related research by other authors, it has been seen that they investigated the area with theoretical examples as well as computational, but only few of them have tried to implement their research and validate their work experimentally. Also, those who did, they have done these experimental in small scale, thus not making them viable energy harvesters.

Few attempts of making devices to extract energy from unsteady flow using fish inspired mechanisms are the following. A device has been designed that could extract energy from unsteady flow using a flapping foil [11]. By placing the flapping foil behind a cylindrical bluff body, it is possible to harnessing the power of the oncoming vortices, provided forward thrust at propulsive efficiencies greater than 100% [96]. As the leading edge of the foil intercepts with the vortices, vortices shed off the foil act to cancel out the oppositely spinning vortices from the bluff body, resulting to the net cancellation of the vorticity with large amount of thrust. The concept of the devices is very similar to the way that fish intercept with the oncoming vortices and is a development of the Katzmayr effect, named

after an engineer who first investigated how to extract energy from unsteady flow using a stationary foil [97].

In other work, a piezoelectric eel, fixed vertically behind the bluff body was developed. The shed vortices created a motion in the piezoelectric membrane fitted in to the skin of the flexible cylinder. The eel systems investigated have the potential to generate power from milli-watts to many watts depending on system size and flow velocity, however a power-generating eel has not been demonstrated yet [5] [98].

More recently, it has been demonstrated that it is possible to extract energy by means of piezoelectric material cantilevered to a cylinder placed in a uniform flow. It was observed that when the resulting wake was interacting with the cantilevered material, flexing would result into charge generation [99]. Despite the positive outcome, it is noted that the piezoelectric material has one main drawback. If the material vibrates in a mode other than its first resonant one, this will lead to an inflection point in the beam which considerably reduces the voltage output due to charge cancelation taking place. Therefore, in order for the piezoelectric material to be a viable option, the arrangement might be consisted of a cantilevered beam having a number of unconnected piezoelectric segments running along its length.

For this research, a flexible piezoelectric device has been manufactured and integrated into the flexible cylinder. Further discussion can be found in chapter 7, related to the energy harvesting element of this research.

Chapter 3

Experimental Approach

The following section details the steps taken in determining the dimensions and form of an experiment designed to investigate the dynamics of a flexible cylinder behind a bluff body in a periodic unsteady wake. A methodology is provided with which one can measure the frequency and amplitude of a flexible cylinder and the shedding frequency of a bluff body in unsteady flow. This will allow one to test flexible bodies and bluff bodies with different geometries in order to tune the system to vibrate in a manner that will enable energy to be extracted from the flexible body's vibration mode shapes.

As discussed in the literature review, the experimental methodology is inspired by a similar mechanism used by fish to extract energy from unsteady flow. The fish, depending on their body length, will adopt a novel gait when stationed behind a cylinder, such that they synchronize their body motions to the vortex shedding frequency across different combinations of cylinder and flow regimes [8]. The fish, adapts its swimming mode to interact with the shed vortices coming from the bluff body, where effectively it reduces the energy expended to maintain station in the flow. By matching or closely matching the natural frequency of an inanimate object with the frequency of the vortices shed from the bluff body, the system will resonate and provide the potential for energy to be harvested from the induced resonance. As discussed in the literature review, the flexible body will mimic passive fish swimming behaviour behind a bluff body commonly known as Von Kármán gait. This, in turn, will suggest that the possible station holding behaviour of the flexible body is a result of the wake dynamics rather than of an active process such as muscle activity and propulsive swimming like entraining. To achieve this, a balance between drag and thrust needs to be established. Resonance of the body due to frequency matching does not guarantee station holding behaviour. However, as discussed, in the literature review, there is potential for net forward thrust due to Von Kármán gait [8]. If this net forward thrust is equal to the drag of the body, then station holding will occur. This phenomenon will be assessed within this experimental methodology. Observations on the

cylinder's motion will take place with the use of a digital camera mounted above the towed flexible cylinder. Then with the aid of a pre-built Matlab® code, the videos will be analysed in order to define the experimental dimensions and the form of the induced vibration.

3.1 Experimental Design

The aim of this section is to size a system where the natural frequency of a flexible body matches that of the vortex shedding frequency behind a bluff body.

A methodology for creating unsteady flow will be presented where the shedding frequency and other flow characteristics from different cases will be measured. A discussion regarding the calculation and prediction of the natural frequency of flexible cylinders, is presented. The manufacturing procedure of the flexible cylinder is presented and explained how neutral buoyancy has been achieved such that the flexible body is moving in plane representing constant depth.

During the experiments, there will be sufficient downstream distance between the bluff and the flexible body to make sure that the flexible body is outside the suction region, which is estimated at 1.75 times the diameter of the bluff body D_{bb} [11] created immediately behind the bluff body [9]. Therefore, any upstream movement or station hold behaviour noted during the experiments, it should not be a result of entraining but wake dynamics from the Von Kármán vortex street. Similar investigations will be used as a basis and will provide a form of validation for the present research [13] [35] [97].

3.1.1 Method for Creating Unsteady Flow

The unsteady flow will be generated at the Armfield Water Channel located at Chilworth Science Park at the University of Southampton, with the following characteristics as provided in Table 3:

Parameters	Value	Units	Comments
Length [$L_{channel}$] =	23	m	
Width [$W_{channel}$] =	1.37	m	
Depth [$D_{channel}$] =	0.6	m	(max)
Flow rate [Q] =	0.8	m^3/s	(max)
Kinematic viscosity [ν_{water}] =	1.14×10^{-6}	m^2/s	assumes ν at 15°C (fresh water)

Table 3. Armfield Water Channel Characteristics.

A simple experimental apparatus is used during the experiments, as depicted in Figure 19. A rigid circular cylinder of 0.11m diameter (D_{bb}) is vertically lowered in the centre of the flume's width, perpendicular to the oncoming uniform flow $U_{nominal}$, in a fixed position, 7.5m away from the inlet valves of the channel. Coaxially to the bottom end of the circular cylinder in the water, a concentric thin disc has been fitted, having a diameter 1.45 times larger than that of the cylinder to which it is fixed. By doing so, a bottom end condition conducive to parallel vortex shedding is created, which increases the local flow velocity at the bottom of the cylinder. This is done because over the course of this research, emphasis shall be placed on experiments where the vortex shedding is parallel to the bluff body axis. Thus, in order to allow parallel shedding to transpire over oblique shedding, the end plate is introduced. At the free surface end of the cylinder, it can be assumed that such boundary is particularly effective in allowing parallel vortex shedding. Such measures are in accordance to those taken in [100].

A flexible cylinder is tethered with the aid of a very thin rope from the bluff body, with characteristics as shown in Table 9. This should help to minimize the influence such a tether can have on the flow, as well as to prevent the flexible cylinder from rotating about its own axis. By having the length of the tether adjustable, allows the increase or decrease of the distance between the bluff body and the flexible cylinder. The tether is secured on the bluff body at approximately 0.30m from the bottom of the channel. This distance will ensure that the flexible cylinder is approximately equidistant between the free surface and

the channel floor to minimise the influence of any shear vortices or hydrostatic pressure on the flexible body, found at the bottom of the channel. Finally, an overhead camera has been placed at the top of the channel, in a position such that the transverse movement of the flexible body is captured which will be used for later post-processing to extract the desired experimental results, e.g. frequency and amplitude of vibration.

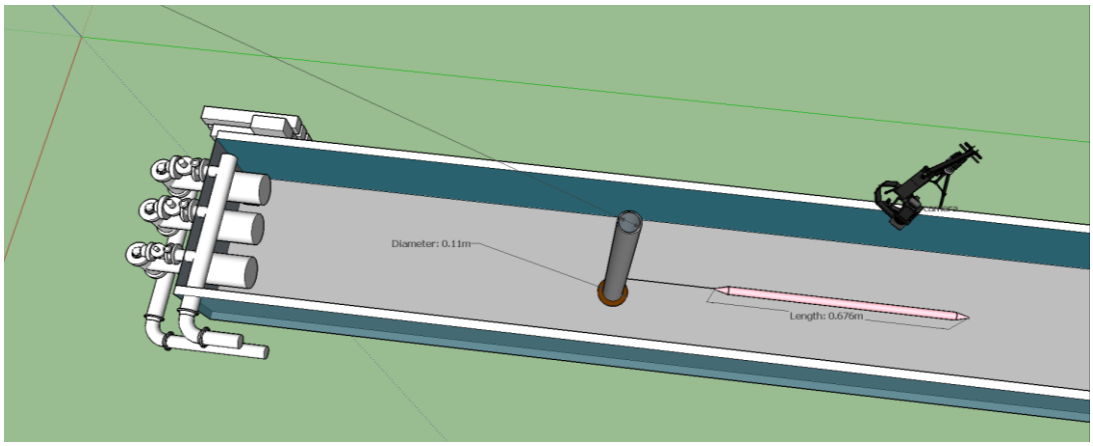

Figure 19. Apparatus Top-Perspective View (not in scale).

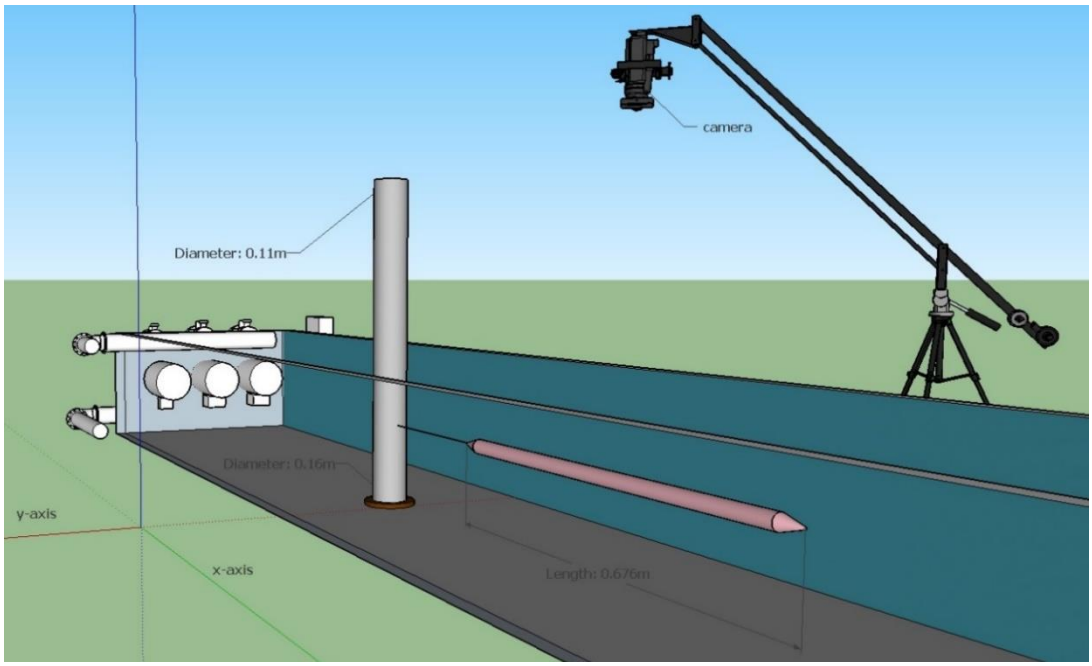

Figure 20. Apparatus Side-Perspective View (not in scale).

To create the desired flow conditions with the appropriate water height and fluid velocity, a combination of three pumps, three water outlet valves and the channel bridge need to be controlled. The water pumps control the pressure of the water, the outlet valves control the flow rate of the water and the channel bridge controls water height and velocity through an exit flow rate.

Initially, the working space was defined by deciding the height of the water. The bridge of the channel was raised such that the flexible cylinder is approximately equidistant between the free surface and the bottom of the channel. The flow velocities were created by combining the pressure from the three available pumps, and the opening of the three water outlet pipes recirculating the water in the channel. After several tests, it was decided to keep pumps one and three on with their respective pipes fully opened. This resulted in some good flow velocities having Reynolds numbers at the desired region. The different flow tests can be found in Table 4.

	Case				
Configuration	**#1**	**#2**	**#3**	**#4**	**Units**
Pump 1	Old/On	On	On	On	On/Off
Pump 2	Off	Off	Off	Off	On/Off
Pump 3	Off	On	On	On	On/Off
Valve 1	1	1	1	1	0, ½, 1
Valve 2	0	½	½	½	0, ½, 1
Valve 3	0	½	1	0	0, ½, 1
Water height	0.5	0.48	0.47	0.48	m
ν_{water}	1.054×10^{-6}	1.054×10^{-6}	1.054×10^{-6}	1.054×10^{-6}	m^3/s
Velocity	0.29	0.469	0.453	0.474	m/s

Table 4. Flow velocities in different pumps and water valves combinations.

The three pumps available at the Armfield Water Channel have different powers. However, the larger and most powerful pump has been out of order during the initial experiments, leaving only the two small and less powerful pumps available. This has resulted in increased difficulty in achieving the desired flow velocities, effectively limiting the range of the available velocities that could have been useful for this study and consequently reducing the amount of suitable data. Also, it had a significant negative impact on the time spent doing different arrangements to achieve the desired flow speed. This shows the importance of being able to create the desired flow velocities with precision.

During the preliminary tests, it was observed that a significant amount of bubbles were present in the flow, where the water was coming out of the outlet valves. These bubbles would travel a short distance downstream before imploding, resulting in a pressure shock, and leading to turbulence. Therefore, in order to eliminate the effect of this undesired

turbulence, the arrangement was set-up around in the middle of the channel where there was no presence of bubbles, while at the same time avoiding the recirculation region generated by the channel bridge which adjusts the height of the water. In order to create a number of flow cases, the water depth and nominal velocity values were measured during the experiments. To calculate the flow velocity ($U_{nominal}$), a very small lightweight ball has been used which was left freely to flow down the flume in a predefined distance. By measuring the time needed to travel this distance using a stopwatch and averaging 10 measurements, the final flow velocity was found. In order to measure the height of the water, a ruler was attached on the sidewalls of the flume. To calculate the real velocity of the flow, Equation 4 takes into consideration the constriction effects from the bluff body in the flow. It is assumed that the width of the obstruction is given by the diameter of the bluff body. As a consequence of these constrictions, the vortex shedding frequency, f_{shed}, is also expected to be adjusted to include the U_{actual} term rather than the free stream velocity as it will be described later and it is calculated by re-arranging Equation 3. To predict the approximation of the Strouhal number, Equation 7 is used. Firstly, because the Reynolds numbers of the flow cases as presented in Table 5 fall within the equation's limits. Secondly, the aspect ratio of Equation 7 is closest to the one used in the current experimental work compared to the other equations. To calculate the vortex shedding frequency, Equation 2 has been rearranged in respects to shed frequency in order to identify which flow Case shed frequency is closest to the natural frequency of the flexible cylinder. Table 5 provides the details of the unsteady flow cases that will be investigated in association with the flexible body natural frequency. The flow velocity further measured and verified using Acoustic Doppler Velocimetry (ADV). More detailed analysis of the velocity measurements can be found in section 4.4.

	Case				
	#1	**#2**	**#3**	**#4**	**Units**
Water depth [$D_{channel}$] =	0.5	0.48	0.47	0.48	m
Nominal flow velocity [$U_{nominal}$] =	0.29	0.469	0.453	0.473	m/s
Actual flow velocity [U_{actual}] =	0.315	0.510	0.493	0.515	m/s
Bluff Body Reynolds Number [Re_{bb}] =	3.29×10^4	5.32×10^4	5.14×10^4	5.37×10^4	-
Strouhal Number [St] =	0.1897	0.1871	0.1873	0.1871	-
Vortex shedding frequency [f_{shed}] =	0.544	0.868	0.839	0.876	Hz

Table 5. Flow measurements including blockage correction.

Finally, once again, it is important to highlight that this research is not going to look into the effects of turbulence in the flow and how this affects the excitation of the flexible cylinder, since this is outside the scope of the research. It is imperative though that any future work with this research as its base, should assess the level of turbulence in the flow.

The method used to measure turbulence depends on the application, the available budget and resources, but usually Particle Image Velocimetry (PIV) is used. It is an optical method for flow visualisation which uses a laser to track particles (seeded into the flow) and produces instantaneous 2D or even 3D vector fields. Hotwire anemometry and Laser Doppler Velocimetry (LDV) are other methods but only measure the flow at one point whereas PIV measures a 2D plane or even the entire flowfield when properly implemented in the flow.

Knowing the level of turbulence, can give a better understanding of the flow development, the flow dynamics around and downstream the bluff body. As it will be discussed later, the experimental arrangement was successful and it was able to capture the displacement of the flexible cylinder, which in turn has been compared with that observed at the computational model, alongside frequency of oscillation and shed frequency. Knowing the levels of turbulence at different locations in the experimental water channel, it would be possible to replicate this in the computational model, creating a more robust model, adding not only more confidence to the results but also giving the opportunity to investigate the effect of the turbulence on the flexible cylinder in more detail, since the computational model is able to provide significant visualisation without the need of experiments.

3.1.2 Method for Flexible Cylinder Design

In order to conduct this experiment and get any meaningful results, the flexible cylinder had to fulfil two requirements. Firstly, the experiments need to be conducted on the premise that the flexible cylinder will be oscillating on a 2-D plane, forward-backwards (x-axis) and left-right (y-axis), looking from the top. Therefore, in order to assure that the third dimension is eliminated without having any motion on the z-axis it was necessary for it to be neutrally buoyant. This, theoretically, will make the body to move in the x-y plane. The reason for adopting this approach is because of the limitation in the measurement system being 2-D and therefore the flexible cylinder design aims to be operated only in 2-D.

Secondly, the natural frequency of the flexible cylinder had to match or being as close as possible to the frequency of the vortices shed from the bluff body, outlined in Table 5.

The design of the geometry of the flexible cylinder has been conducted via the use of Archimedes Principle. It indicates that the upward buoyant force that is exerted on a body immersed in a fluid, whether fully or partially submerged, is equal to the weight of the fluid that the body displaces [101]. Therefore, in order to see whether a body is neutrally buoyant, the buoyancy and gravitational forces must be calculated and be equal. If the force of buoyancy is greater than the force of gravity, the object will float. If the force of gravity is greater, it will sink. If they are equal, the object is said to be neutrally buoyant.

The calculation of the forces occurred as follows. Since the body is completely submerged, the whole volume of the flexible cylinder was calculated taking into account only the outer diameter since it is sealed. Then, the buoyancy force was calculated using:

$$B_{force} = V_{outer} \times \rho_{water} \times g$$

Equation 21. Buoyancy force calculation

where ρ_{water} is the density of fresh water 1000 Kg/ m^3, g the gravitational force and

$$V_{outer} = \pi {R^2}_{outer} L_{fc},$$

Equation 22. Flexible cylinder volume using only the outer radius

where R_{outer} is the outer radius of the flexible cylinder. Then, the gravitational force was calculated by,

$$G_{force} = m_{fc} \times g = \rho_{fc} \times V_{fc} \times g$$

Equation 23. Gravitational force calculation

where, m_{fc} is the mass of the flexible cylinder calculated using the density (ρ_{fc}) of the material multiplied by its volume and g the gravitational constant.

$$V_{fc} = \pi L_{fc} ({R^2}_{outer} - {R^2}_{inner})$$

Equation 24. Flexible cylinder real volume taking into account both radii,

where, R_{inner} is the inner radius of the flexible cylinder.

This allowed for altering the main variables of the flexible body named, length (L_{fc}), inner (R_{inner}) and outer (R_{outer}) radius (Figure 21), providing a method that could be used to design neutrally buoyant flexible cylinders with different geometries.

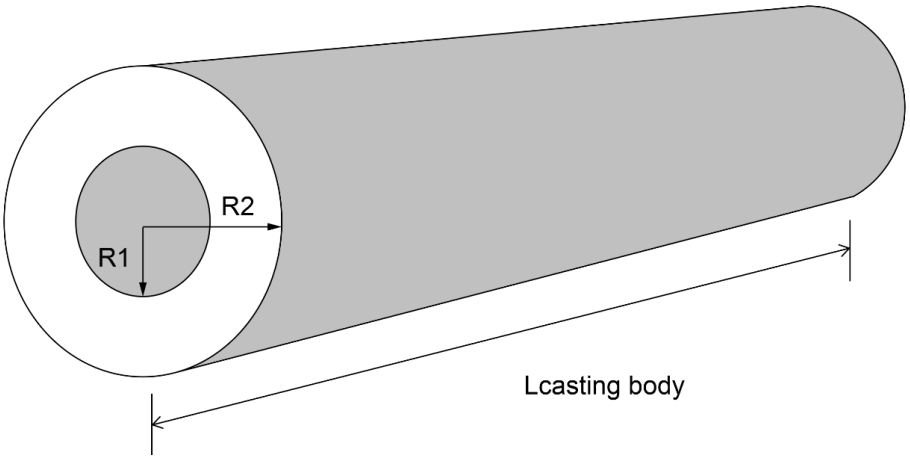

Figure 21. Inner (R1) and outer (R2) diameters of the casting body.

In order to calculate the natural frequency of the flexible cylinder, a review of literature revealed an extensive analysis on the different available forms of the equations of motion. Many attempts have been done by various authors in publishing different forms of the equations of motion and a lot of literature related to slender bodies submerged in a fluid.

The equation of motion for a slender flexible cylinder in a uniform axial flow was firstly described through work towards the 'Dracone Barge', a long flexible tube with tapering ends which is designed to carry oil and other liquids lighter than water [102]. However, few years later, work done by other authors is more notably remembered and has been the basis for future work in the field with experiments on a cylinder free to translate laterally and axially. A general theory was presented to account for the small, free, lateral motions of a flexible, slender, cylindrical body immersed in fluid flowing parallel to the position of rest of its axis [103].

A more recent contribution, deduced a non-linear form of the linear equations of motion presented by previous authors, where the results of the experiments using a non-linear model were qualitatively similar to those of a linear model [104]. Additionally, it is worth noting that the linear model has some shortcomings which have been long understood but never really improved due to the complexity of doing so. Discussion of the latter is beyond the scope of this investigation, however, some possible improvements can be found in the literature [105] [106].

The non-linear form of the equation will be used to identify the flexible cylinder's natural frequency where some constraints will be applied at some of the hydrodynamic effects acting on the cylinder. Firstly, it will be assumed that any natural frequencies and associated principal mode shapes will be determined in a flow having a simple harmonic motion. Secondly, the mass per unit length and the flexibility of the cylinder will be taken as constant along the cylinder.

Based on the above conditions, the analytical solution to Euler's Beam theory takes the form as shown in Equation 25 below:

$$v(x) = C_1 Cos(\beta x) + C_2 \sin(\beta x) + C_3 \cosh(\beta x) + C_4 \sinh(\beta x)$$

Equation 25. Analytical Solution of Euler's Beam Theory.

where, $v(x)$ is the transverse displacement and $\beta^4 = \frac{\omega^2 \mu}{EI}$, where, ω is the corresponding natural frequency (rad/s), μ is the mass per unit length (Kg/m) EI is the structural rigidity (N/m^2) and $C1, C2, C3, C4$ are the constants depending on the boundary conditions. Given that the experimental setup consists of a flexible cylinder tethered to a bluff body, which was allowed to move about a short radius in relation to the bluff body, the determination of the boundary conditions was based on the possibility that at any point in time, the tethered condition results, in either of the two constrains. In reality, the tethered end was free to move unconstrained or alternatively to slide, while the other end was free to move at all times. A full derivation of this equation can be found in Blevins' book alongside the boundary conditions [107].

In order to calculate the natural frequency of the flexible cylinder f_{fc} in vacuum, the following equation can be used as an outcome of the derivation of Equation 25 as found in [107]:

$$f_{fc/vacuum} = \frac{(\beta_n)^2}{2\pi {L_{casting}}^2} \sqrt{\frac{EI}{\mu}}$$

Equation 26. Flexible Cylinder natural frequency calculation

where, β_n determines the roots of the equation of motion (eigenvalues). None of the boundary conditions described for the solution to this equation perfectly describe the boundary conditions of the flexible cylinder tethered with a rope. For comparison with

numerical solution later a simple free-free boundary condition for the tail and nose: $\beta_n L_{casting} = \frac{(2n+1)\pi}{4}$, where there is no geometric restraint on the flexible cylinder. Therefore, the cylinder can move freely in any direction. The solution of Equation 25 is exact only for vibrations in a vacuum. Therefore, Equation 26 is limited to the fact that any external forces and structural added mass effects accounting for the inertia of the fluid, entrained by the accelerating structure, are not included.

In order to meaningfully account for the conical ends during the calculation of the natural frequencies of the flexible cylinder, it is assumed that the height of the cones (h) from their respective base, satisfy the condition that the height of the cone is much smaller than the length of the cylinder ($h \ll L_{fc}$) so that they can be accumulated and thought of just being an extension of the uniform cylinder. However, at the same time, the height of the cones must be large enough to permit the use of slender-body approximations. Furthermore, the ends are assumed to be rigid so that their motion is determined solely by the values of displacement and velocity at their respective base. In doing so, and given that we are only looking for the general characteristics of the dynamical problem, the forces acting on the non-cylindrical ends are lumped and incorporated in the boundary conditions [35]. There are almost endless combinations of inner radius and length that could potentially lead to a neutrally buoyant body, however, only few bodies can have a natural frequency matching or being very close to a shedding frequency from the flow cases in Table 5.

Table 6 shows four flexible cylinder case studies that have been assessed for their neutral buoyancy.

	Case				
	#1	**#2**	**#3**	**#4**	**Units**
Inner Radius [R_{inner}] =	0.005	0.012	0.013	0.005	m
Outer Radius [R_{outer}] =	0.01	0.03	0.015	0.011	m
Length [$L_{casting\ body}$] =	0.4	0.5	0.6	0.586	m
Mass per unit length [μ] =	0.28981	2.92130	0.21639	0.3709	Kg/m
Density [ρ_{fc}] =	1230	1230	1230	1230	Kg/m^3
Buoyancy – Gravity [$F_{buoyand} - F_{gravity}$] =	+0.1516	-0.4043	+2.9430	+0.1440	N

Table 6. Flexible Cylinder case studies characteristics.

3.1.3 Method for Flexible Cylinder Manufacturing

For casting the flexible cylinder, a high quality two component room temperature condensation curing silicone compound has been used. The cured product gives an exceptionally flexible rubber with very high mechanical properties and good shelf life stability. Consulting the datasheet [108], the specific gravity of the silicone is 1.23, therefore, any solid geometry made from it would be negatively buoyant. The Young's Modulus is 0.79MPa. The silicone has similar properties to the one used in the literature [97] [35]. Consequently, it can be deduced that similar characteristics are expected from the flexible cylinders of this project.

Figure 22 depicts the casting procedure. The mould is secured vertically with the aid of a clamp. The bottom end is sealed with hard polystyrene which also helps to secure the threaded rod in the middle of the casting tube. The mixing ratio of the silicone (Part A) and the catalyst (Part B) is 20:1 and the curing starts to be noticeable 15 minutes after mixing, when the mixture becomes more viscous. This gives a very short time window to pour the mixture inside the very narrow nozzle of the casting tube, where the threaded rod is also present. To mix the two parts, an electronic precision scale has been used which allowed accurate measurement of the two parts. The overall curing procedure lasts for seven to eight hours. Step by step manufacturing process is found in Table 7.

Figure 22. Casting apparatus and the two-part silicone compound.

Steps	Description
1	Prepare the mould by cutting the foam cylinder into a length few centimetres longer than the length of the flexible body needed.
2	On a level surface, draw the dimensions of the mould and at the centre secure the threaded rod.
3	Place the mould on the level surface such as the rod is inside the mould, on the centre.
4	Secure the mould on the level surface and seal the sides to avoid any silicone leakage.
5	At the mould's open surface, make sure the rod is in the centre. Secure the rod to avoid any movement during moulding.
6	Mix Part A and Part B of silicone at a 20:1 ratio and steer well until a uniform mixture is created.
7	Pour the mixture into the moulding tub.
8	Wait for 8 hours to cure, remove the moulding and threaded rod.
9	Secure the tether, nose, tail with hot glue.
10	Paint the body as described in section 3.1.3. Hang the flexible body vertically and let it dry for 48 hours.
11	Place in a water bucket to check buoyancy.

Table 7. Step by step moulding process.

Initially, an attempt was made to build a flexible cylinder using the aforementioned compound where a straight plastic water tube with diameter D_{fc}=0.3m was used as a mould and a threated rod 0f 0.026m. Once cured, the threaded rod was unscrewed, allowing air to replace the gap decreasing the mass of the cylinder. This would help to manufacture a body close to neutral buoyancy. Then, the tail and nose ends were glued, sealing the cylinder, avoiding any water to penetrate into the cylinder during the experiments.

With the aid of the buoyancy equations as previously defined, the correct length for the body of the flexible cylinder was found which should allow the body to be approximately neutrally buoyant. Unfortunately, when tested, the flexible cylinder was sinking and it was not lying in the x-y plane as seen in Figure 23. The flexible cylinder was then weighed and found that its weight was more than the theoretical value. This was most likely because of the additional weight caused by the 11 tape stripes and the glue used to secure the nose and tail in place.

Figure 23. Flexible cylinder sinking due to negative buoyancy.

Thus, in order to increase the accuracy of the manufacturing and allow having a cylinder that is neutrally buoyant including any extra appendage mass, it was decided to design a cylinder which would be positively buoyant by a few grams, therefore, any additional mass caused by the tape stripes and glue, would not cause any negative buoyancy. This would also allow for the addition of additional mass to ensure the flexible cylinder was as close to neutral buoyancy as possible. The second attempt to manufacture a neutrally buoyant flexible cylinder was made with the aid of the equations in order to be able to manufacture a cylinder with positive buoyancy. This time, a foam pipe insulation tube with a smaller diameter ($D_{fc} = 0.22m$) has been used as a mould. Different combinations of inner radius, R_{inner} (threaded rod diameter) and length were investigated. The manufactured flexible body has characteristics as outlined in Case#4 in Table 6.

For the nose and tail of the flexible cylinder, two conical ends made from very lightweight foam have been chosen, following the work done in [13] regarding the different flexible cylinder end forms. It was concluded that between the slender-slender, slender-blunt and blunt-blunt configurations, the slender-slender configuration is the one showing qualitative agreement, exhibiting similar motions to those predicted by the theory. Therefore, it was decided to use the slender-slender end forms for the flexible cylinder as shown in Figure 24. The same end forms have been used by [35] but without any justification.

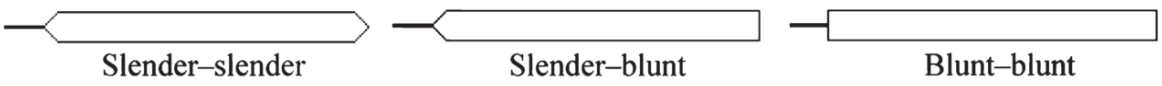

Figure 24. Flexible cylinder end forms.

The characteristics of the nose and tail are presented in Table 8 below and measured experimentally:

Parameters	Value	Units
Nose height $[h]$ =	37.00	mm
Nose weight =	0.000823	Kg
Tail height $[h]$ =	37.00	mm
Tail weight =	0.000823	Kg

Table 8. Nose and Tail geometrical and physical properties.

3.1.4 Flexible Cylinder Characteristics

As discussed in section 3.1.1, there are an infinite number of different flow velocities producing different shedding frequencies. The same applies with the different possible geometries of the flexible cylinder as described in section 3.1.2. Each cylinder has its own natural frequencies at the different boundary conditions and mode shapes. The aim is to excite the flexible cylinder using the shedding frequency from the bluff body. To achieve this by matching the two frequencies, there are two possible methodologies. Firstly, to choose a flow arrangement and manufacture a flexible cylinder that has a natural frequency the same or close to the shedding frequency of that specific flow. Secondly, to create a flexible cylinder with a known natural frequency at the respective boundary conditions and adjust the flow velocity and bluff body to create a flow that has a shedding frequency the same or close to that of the flexible body. The second route was chosen because manufacturing a flexible cylinder is time consuming. By having a flexible cylinder with fixed characteristics and properties will make things simpler since in order to change the flow velocity only a combination of the three pumps and water outlet valves is needed. However, in reality this cannot be achieved as it is impossible to control the flow characteristics of the natural environment, therefore, the flexible cylinder must be designed to meet specific range of flow characteristics with the respective shedding frequencies. Given the moulding tube sizes and threaded rods available, case #4 from Table 6 has been manufactured, having characteristics as presented in Table 9:

Flexible Cylinder			
Length [L_{fc}] =	0.676	M	Including nose and tail
L_{fc} without $2xh$ =	0.586	M	Excluding nose and tail
Diameter [D_{fc}] =	0.022	M	
Young's Modulus [E_{fc}] =	0.79	MPa	Material datasheet
Mass per unit length [μ] =	0.3709	Kg/m	
Tether			
Diameter [D_{rope}] =	0.002	M	
Young's Modulus [E_{rope}] =	3	GPa	

Table 9. Physical characteristics of the flexible cylinder and rope.

It has been observed from the experimental testing, to be discussed later, that the flexible cylinder has either a half or full sinewave shape corresponding to the first two mode shapes of oscillation. The natural frequency of the flexible cylinder for the free-free boundary condition, has been calculated using Equation 26, as shown in Table 10.

		Mode shapes			
Boundary conditions		0	1	2	Hz
Free – Free Natural Freq. [$f_{fc,ff}$] =	$\frac{(2n+1)\pi}{2}$	0	1.5861	4.3722	Hz

Table 10. Natural frequencies in vacuum.

Using Blevins equation, it is known that the solution is exact only for vibrations in a vacuum. Thus, the solution is limited to the fact that any external forces and structural added mass effects are not included. Additionally, the presence of the rope is not taken into account either when using Equation 26. Therefore, since Blevins equation does not represent the physical boundary conditions of the system, further assessment of the flexible cylinder natural frequency has taken place, using finite element analysis.

The finite element analysis method is a numerical procedure that can be used to obtain solutions to a large class of engineering problems involving stress analysis, heat transfer, electromagnetism and fluid flow.

In the investigation of this thesis, modal analysis has been used as part of the FEA analysis to determine the vibration characteristics of the modelled flexible cylinder. Similar to Blevins equation, the results are exact only for vibrations in a vacuum. This method is

attractive because the response of a multi-degree-of-freedom (MDF) system is expressed as the superposition of modal responses, each modal response is determined from the dynamic analysis of a single-degree-of-freedom (SDF) system, and these dynamic analyses need to be implemented only for those modes with significant contribution to the response [109].

The flexible cylinder built for this analysis has dimensions as presented in Table 9, same as the flexible cylinder used in the experimental analysis. Two models have been created; one with free-free boundaries as seen in Figure 25, and one where the flexible cylinder is tethered by a fixed rope (Figure 26) and it is free to have six degrees of freedom (DoF). According to the specifications of the project, the body is expected to move only in four DoF, excluding any vertical motion as it is supposed to move only on the x-y plane. However, as it has been observed experimentally, the system is not ideal. Therefore, it was decided to use a six DoF system and observe the results. When needed, single axis movement was extracted from the total deformation.

Table 11 summarises the ANSYS® Mechanical settings. Any other settings have been left at their default values or under 'Program Controlled' function. Further details can be found in section 6.1, where the flexible cylinder design is introduced as a coupled model.

Solution Setup	**Configuration**
Mesh	
Elements	48356
Nodes	226312
Relevance	80
Size Function	Proximity and Curvature
Relevance Centre	Medium
Smoothing	Medium
Transition	Fast
Span Angle Centre	Medium
Analysis Settings	
Maximum modes to Find	9
Solver Type	Program Controlled

Fixed Support	
Fixed Support	Applied on the rope's free end
Solution	
Total Deformation	Modes 1- 10
Directional Deformations	x- axis, y- axis, z- axis

Table 11. ANSYS Transient Structural - modal analysis simulation settings.

The values for the frequency obtained from modal analysis are characteristically repetitive. By investigating a bit further, it has been found that modal analysis gives the resonance frequency for all the axis of oscillation and not per modal shape, thus the repetitive results. Result #1 represents a rigid body motion in the vertical y-plane, as identified in Figure 25. Similarly for result #2. Result #3 gives a rigid body oscillation on the x-plane. Result #4 represents an 'enlargement' and 'shrinkage' of the cylinder. Results #5 and #6 represent a rigid motion of the cylinder moving between planes. Result #7, gives a shape that resembles of that of the first real mode of oscillation, as seen in Figure 28. As expected, result #8 gives the same oscillation, but on a different plane. Results #9 and #10 give the second mode of oscillation each at a different plane. Similar representation of results can be found in [110] where they present their results as torsional and extension mode, instead of 'enlargement' and 'shrinkage'.

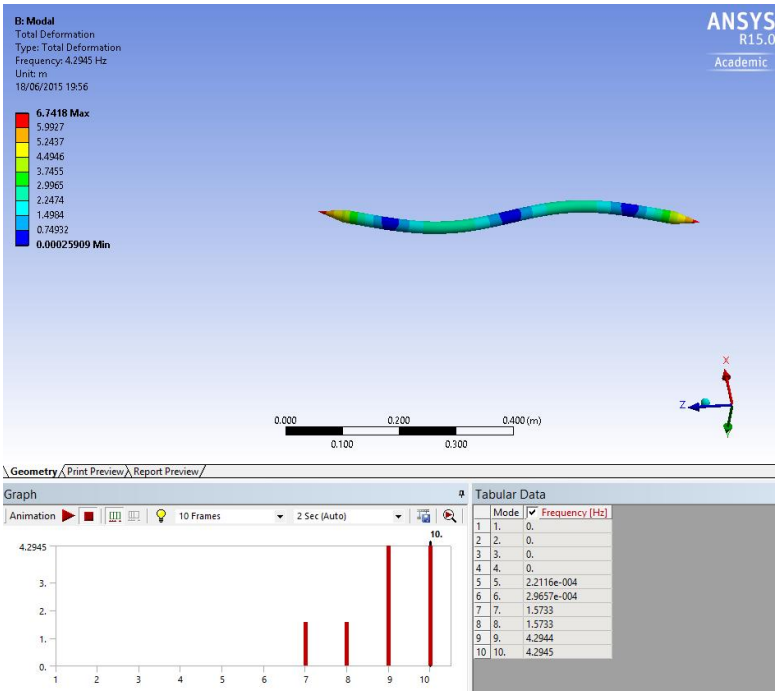

Figure 25. Flexible cylinder modal analysis with the free- free boundary conditions.

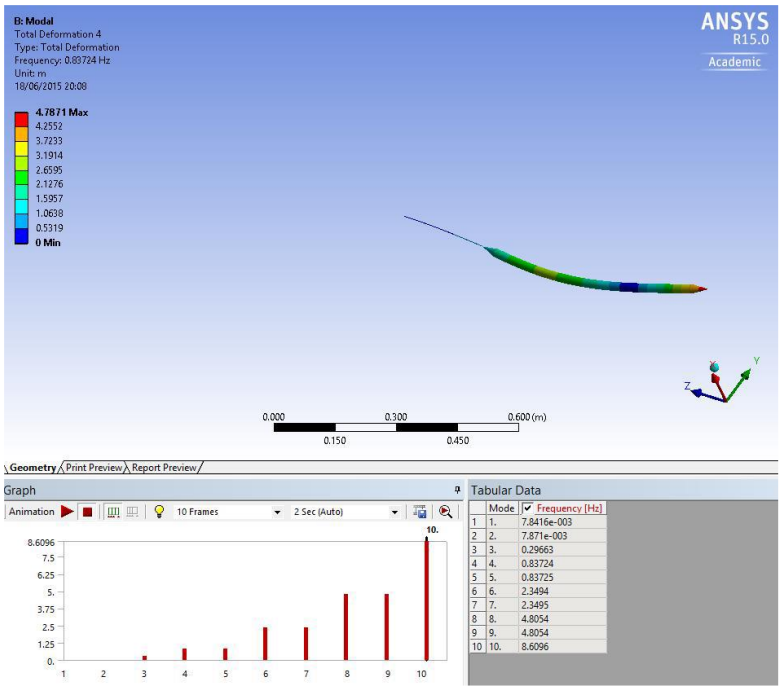

Figure 26. Modal analysis of the flexible cylinder tethered on a fixed rope.

Looking at the results of interest, it can be seen that the modal analysis gives a zero value for the 0^{th} mode shape, 1.573 for the 1^{st} mode shape and 4.294 for the 2^{nd} mode shape. The results are nominally the same to those presented in Table 10, found using Blevins equation at the same boundary condition, free-free. This gives confidence that the numerical modal analysis is giving results as expected from the empirical solution. The analysis is repeated with the more realistic boundary condition of being tethered with a rope. As shown in Figure 27, results 5 and 7 represent the expected shape of vibration as observed in the experimental tests. These have natural frequencies of 0.837 and 2.349 Hz respectively. This clearly indicates that the presence of the realistic boundary condition has a damping effect on the system.

It is important to note that the amplitude values obtained from the deformation in modal analysis are arbitrary and cannot be accounted as real values. That is because modal analysis ignores any applied forces on the model and just gives what modes of vibration could occur and at what frequencies, not what modes will occur [111]. This also explains the difference in 'modes' between the theory and the computational modes which are essentially the results of the simulation, instead of actual mode shapes. In order to be able to find the amplitude of the body, the input energy must be known.

Since the frequency, the wavelength and velocity are independent to the amplitude of the flexible cylinder, the input energy cannot be found from these known characteristics. As

the amplitudes of vibration are important to this research an alternative to modal analysis must be used. For this to be achieved, the force or pressure acting on the cylinder must be taken into consideration since the amplitude depends on the applied force from the upcoming vortex. In order to achieve this, a 3D coupled model has been designed, including the bluff body, the rope and the flexible cylinder. As it will be discussed in section 5.4.4, the force data are obtained from the 3D fluid model and imported in transient analysis, where the frequency and respective amplitudes are found. Nevertheless, the investigation has given confidence towards the numerical model of the flexible cylinder and it is now possible to use this geometry for further analysis. Thus, it will be possible to attempt to match the flow shed frequency to natural frequency of the flexible cylinder to produce resonance.

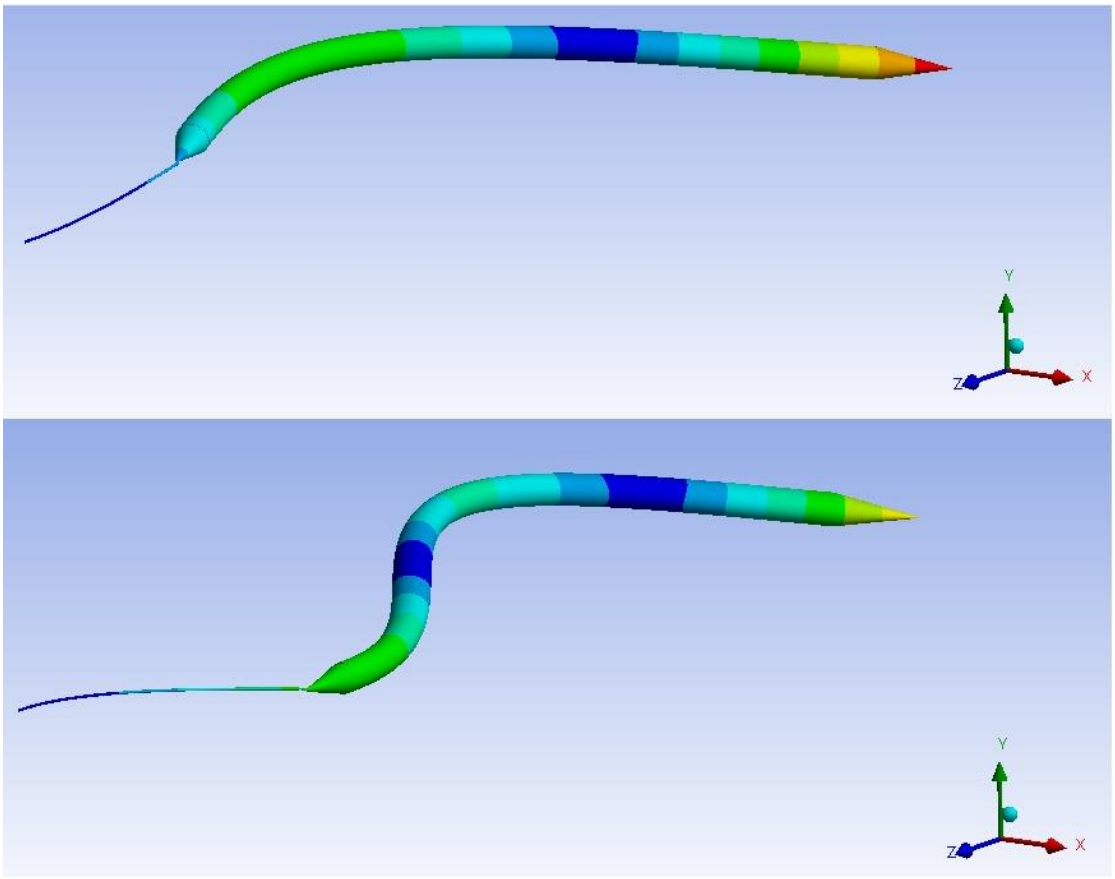

Figure 27. Modal mode shapes free-free with rope. From the top: Mode 5, Mode 7.

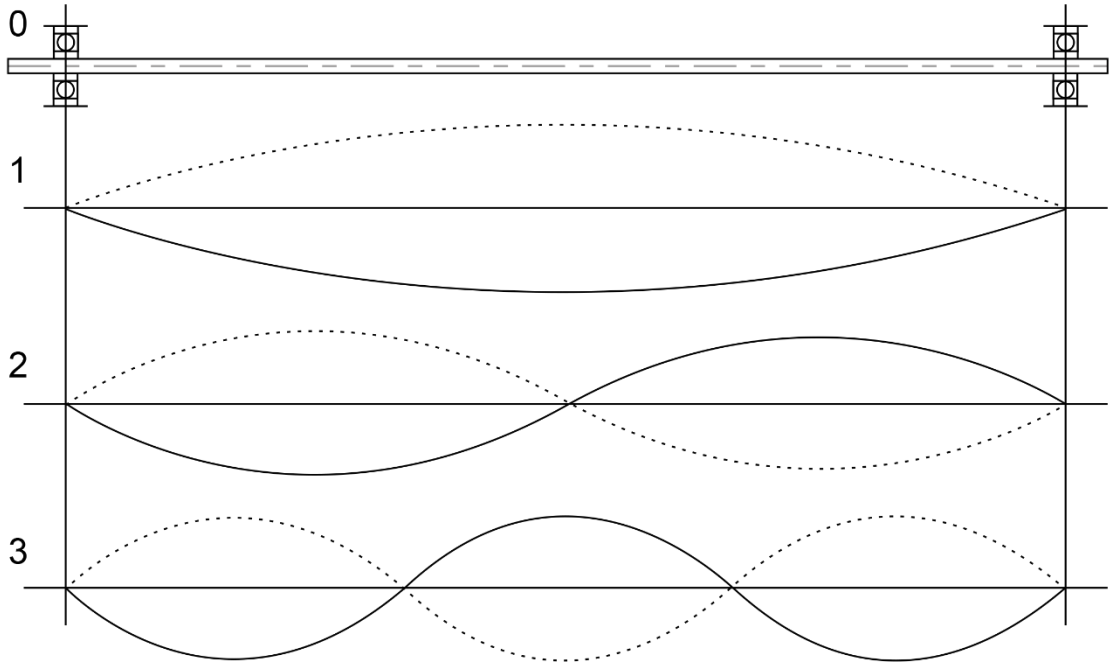

Figure 28. Modes of oscillation.

3.2 Experimental Assessment of Flexible Body Motion

The experimental set-up has been described in section 3.1.1 and shown schematically in Figure 19. The measurements acquired are used to describe the nature of the flexible cylinder behind a bluff body in unsteady flow.

3.2.1 Video Processing

To analyse the videos with the flexible cylinder movement, a pre-built Matlab® code was used which can be found as an open source [112]. It was initially built to identify vehicle plate numbers and altered by the author in [35] to read and detect the flexible cylinder in the flow in such way that the results can be used in the benefit of the project.

As described by the author of the code, the Matlab® programme runs a sequence of image data processing operations on a number of predefined frames. The code compares each pixel intensity value to a threshold intensity value and subsequently creates a binary image (Figure 29), for all the pixels that meet the imposed user criteria [35]. Therefore, the successful implementation of the code will lead to a considerable amount of quantifiable fluid-structure interaction characteristics such us velocity, frequency and amplitude.

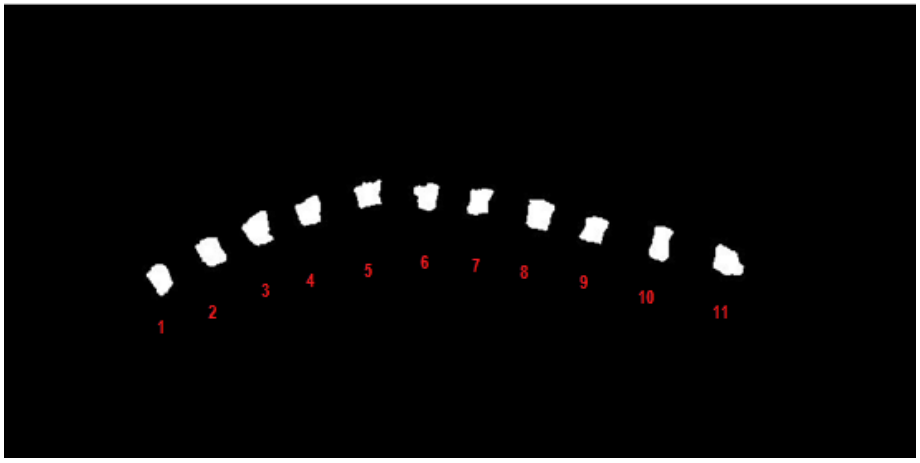

Figure 29. Centroidal locations passing threshold intensity and displayed in B&W.

In order for this to work, a number of dark markings were placed equidistantly along the uniform flexible cylinder's length, between the nose and tail cones. The dark markings have an intensity value lower than the threshold which effectively allows the code to identify the marking's centroidal position per frame, as shown in Figure 30. Thereafter, the centroidal positions are stored in a spreadsheet while the code is running, which allows the data to be post-processed. The centroids are shown in Figure 29, numbered 1 to 11, starting from the nose on the left side, to the tail at the right side of the image.

It has to be noted that the initial plan was to mark the locations using a black permanent marker. Upon trying, it resulted that the ink would not adhere to the silicone material and it was washed away as soon as it was placed in the water. A black non reflective insulation tape was used in the second attempt (on the figure below it is a reflective tape on body #1), however, despite the fact that the tape was not very tight on the cylinder to cause severe behaviour changes such as spring effects, it is acknowledged that the stiffness of the flexible cylinder changed, even if it wasn't visible during the experiments. On a third attempt, in order to minimise any factors that would lead to behaviour change, the following painting approach has been used. A small amount of silicone caulking was placed into a mixing pot with white spirit, black oil-based paint and stirred very well. This led into mixing the silicone with the paint and with the aid of the white spirit to thinning it down to a liquid having low viscosity. With a fine art brush, the black strips were painted on the flexible cylinder. The body left to rest and when the white spirit evaporated from the mixture, the black colour silicone adhered onto the main body.

Since the camera and the flexible cylinder are expected to lie on parallel planes to the bottom of the tank, it can be assumed that by knowing the difference in pixels between the

nose and the tail of the flexible cylinder, in addition to its full scale length, a factor of scaling can be determined. By knowing this scale factor, it is then possible to determine the displacement in time of each marking, as well as to be able to plot each marking's centroid position on the same axis. Finally, the forward distance travelled by the flexible cylinder can also be measured in case it is observed during the experiments.

The ability to plot each marking's centroid position on the same axis from different frames, a midlines figure can be produced which can then be compared with a similar figures obtained while a fish was exhibiting a Von Kármán gait (Figure 38). This comparison allows one to evaluate whether the flexible cylinder was undertaking the specific movement, alongside forward displacement.

Figure 30. Centroids identification by the Matlab® Code.

3.2.2 Code Processing

The code provided in Appendix B can be divided into four processing steps:

Step 1: Accessing the video, setting the parameters and creating the output files: The code creates two spreadsheets, one where the centroids information will be stored and one for the adjacent centroids, as well as the output video where the centroids are marked. The average threshold value can be adjusted and the first frame from which to extract position can be defined.

Step 2: Frame processing the video: The dark regions are identified. This step allows editing of the image such as crop, rotation and removal of any light coloured objects if needed in order to simplify the image. The binary image is extracted.

Step 3: Apply the algorithm to the video: The y-position of the first centroid at which the body is tethered is determined and the layout of the spreadsheet is defined for the data to be stored. The coordinates of the first centroid are detected and then for the rest of the centroids in relation to the centroid before. The total length of the cylinder is calculated in pixels.

Step 4: Visualise the results: Export the processing into the form of a video and spreadsheet data. The video shows the flexible body with the centroids identified using red dots and the spreadsheet has the centroid coordinates, in pixels.

3.2.3 Video Processing Limitations

From the way the code is designed and from the fact that each video needs to be at least one minute long to get a meaningful oscillation, analysing every frame would mean that thousand of frames have to be read and processed. This is a time consuming process.

Furthermore, the code very frequently fails to pick up the appropriate centroid positions, in turn leaving a cell into which the wrong position is written – typically the following centroid position. This error can only be rectified manually, an operation which is extremely time-consuming and repetitive. Therefore, before any further analysis can be carried out, validation on each centroid location in time has to be performed. Thus, in an effort to minimise the number of empty cells, in addition to making sure that the available data for Fourier analysis is as complete as possible, it was decided to resample from 30Hz to 6Hz post Matlab® code processing. Every five centroidal values were re-sampled to one marking. Furthermore, in the odd event that five consecutive positions for the same marking are absent, the two nearest centroidal points to one side of the missing position are treated as points that can be extrapolated linearly to the location of the omitted marking.

It is important to note that given that the Fourier spectra will be developed using an FFT (Fast Fourier Transform) algorithm, the number of input values this algorithm can compute must be n^{th} power of number two, therefore it was decided to take a total of 1024 of the 5-frame averaged samples for each case studied. Should the number of inputs lie between such specific values, what the algorithm does is that it tabs the remaining cells to the next higher power with zeros.

Chapter 4

Experimental Results

The following section presents the results from the experimental analysis that took place in order to investigate the dynamic behaviour of two flexible cylinders in the presence of a bluff body. To the best of the author's knowledge, there are only three published studies [11] [97] [113] that focus on an inanimate object of similar geometry in such a flow. A very good input is also given by the work done in [35]. In this work, the added mass component is different as it is the bluff body with the towed flexible body that are moving in the stationary fluid not the opposite as it is happening during the current project [97]. In [113], the experiment is highly idealised and it has an extremely small scale compared to the current experiment. A series of tests have been run on a very small filament measuring 10x0.15mm, at a 60mm distance behind a bluff body of 4mm diameter. They eventually managed to show that the filament was exhibiting the Von Kármán gait [113]. Finally, in [11], the study uses a euthanatized fish, stiffness and geometry of which constantly changes as it gradually sets into 'rigor mortis' state.

In this chapter, the motion of two flexible cylinders is discussed, analysed and several conclusions drawn. For the first flexible cylinder a defect affected its coupling with the oncoming vortices and therefore the meaningfulness of the data acquired is questioned. A positive outcome was the observation that an upstream motion of the flexible cylinder was observed in these experiments. The second flexible cylinder undertook a full analysis which resulted in very positive conclusions. A qualitative analysis of the shed vortices showed interaction with the flexible cylinder. Through the FFT process, the resonant frequency of the flexible cylinder is found and compared with theoretically obtained results. General conclusions are drawn regarding the coupling quality of the flexible cylinder to the flow. Moreover, the average velocity has been measured in different locations downstream, aiming to characterise the velocity profile

4.1 Preliminary Results Analysis

The following observations took place when a flexible cylinder was immersed in the recirculating channel with flow characteristics as described in Case #1, Table 5, and it was tethered at a distance of $2D_{bb}$ away from the bluff body.

As soon as the footage was taken, an attempt took place to identify whether the experimental vortex shedding frequency matches that predicted by the Strouhal equation. During the very detailed examination of the video, it was noticed that the flexible cylinder had a kink as shown in Figure 31, which could not be a result of the oncoming vortices.

Figure 31. The kink clearly indicated at the second half of the cylinder near the tail.

This discontinuity dominated the flexible cylinder's oscillation. It was acting as an obstacle as it was preventing the cylinder to bend according to the oncoming vortices. Furthermore, it was forcing the flexible cylinder to oscillate on a plane not parallel to the bottom of the flume, having a three-dimensional movement. This made the measurement of the velocity impossible at that point, as the displacement of the body in the vertical plane was unknown. The flexible body was mainly exhibiting an oscillation similar to a pendulum. When it was reaching the maximum points of the motion, it was flipping underwater, completing a full circle motion and making the nose point to the bottom of the flume, thus, leading it out of the desired parallel plane. In order to make an attempt and measure the forward velocity of the flexible cylinder the 3rd dimensional movement had to be restricted or minimised. Therefore, it was decided to pick two points in the flow where the kink was at a lower point than the nose. At that stage, the nose of the flexible cylinder was moving on a plane parallel

to the bottom of the flume and therefore the distance between the two nose displacement points for one second could be approximately measured as show in Figure 32.

Figure 32. Nose displacement of the flexible cylinder for 1s. Top - 11s, Bottom - 10s.

Using Pythagoras' Theorem, between the 10^{th} and 11^{th} second, the velocity with which the flexible cylinder was traveling upstream was calculated to be $0.172\ m/s$. As expected, it is slower than the flow velocity, however, due to the point of inflection and therefore the flexible body not having a proper oscillation, it cannot be considered accurate. Also, since it is not known exactly where the flexible cylinder is placed on the shedding vortex, this value cannot be used to calculate any other characteristics. Despite the fact that the method used to calculate the velocity is partly inaccurate, a forward movement of the flexible cylinder can be observed at a direction opposite that of the direction of the flow and it should still yield to reasonable values provided that the following conditions are satisfied:

i. The flexible object travels upstream by a negligible degree.
ii. It lies in a 2-D plane parallel to the bottom of the tank.
iii. The amplitude of the perturbation (difference in y-displacement) is small compared to the distance between the measuring points.

In general, it was observed that at flow speeds much lower than $0.29\ m/s$, the flexible cylinder was slaloming in the flow without the flow having an impact on the flexible cylinders' oscillation. It is suspected that this might be happening due to the low flow speed.

At 0.29m/s, the cylinder was clearly influenced by the effect of the unsteady flow. There were instances where the flexible cylinder appeared to move upstream in a similar manner to the dead trout by utilising a method that appeared similar to the Von Kármán gait. It is also believed from the motion of the flexible cylinder that the flexible cylinder was not always synchronized with the flow, however this can only be proved with the use of a flow measurement technique such as Particle Image Velocimetry (PIV), to investigate the location of the vortices. Conversely, when the motion of the flexible cylinder appeared to be synchronized with the flow, an upstream motion was observed. Again, this could be verified only with the use of a PIV. Similar incidents were observed during other experiments with a dead trout in unsteady flow [11].

Figure 33 shows the observed motion of the cylinder upstream due to unsteady flow for a one second interval, between the 6^{th} and 7^{th} second. The camera used had a frame rate of 30 frames per second which has been used as a scale. However, at some cases there was no noticeable change in the movement of the flexible cylinder and the frames were not included. The dotted line on the figures represents the flexible cylinder's starting position in the first frame and indicates the forward movement. The fact that the flexible cylinder is moving forward can also be verified by observing the tethering rope at the video which is not tensed while the flexible cylinder is on the forward state, as well as by measuring the distance from the nose of the flexible cylinder to the bluff body.

Once the flexible cylinder moved a few centimetres upstream, it was always dropping back to the initial position to resume its oscillatory motion in the unsteady wake. At this point, it is very important to note that the flexible cylinder was expected to have larger motions upstream, until it gets sucked into the low pressure region behind the bluff body and stay there before dropping back to the initial position. This did not happen and the possible reason was discovered in a later stage. The flexible cylinder had an internal defect at the second half of its body, closet to the tail, which produced an improper oscillation and consequently affected the oscillation frequency. Also, it is suspected that this is the reason for which the flexible body had the discontinuity while oscillating in the water.

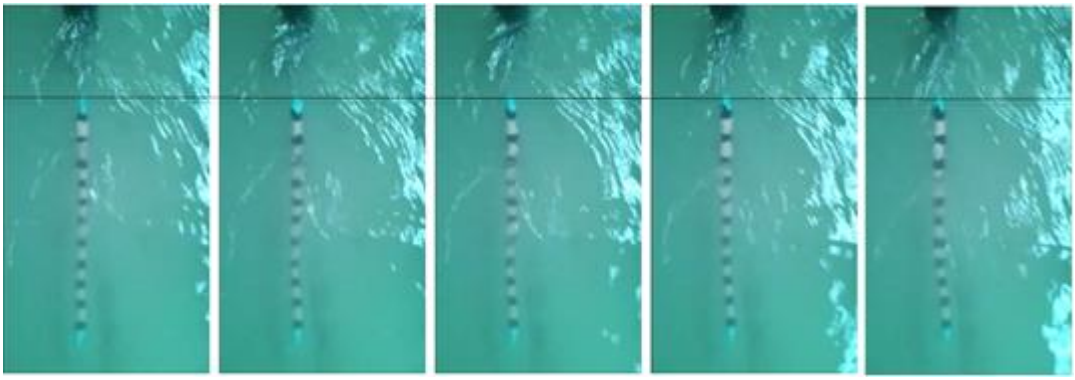

Frames: 1, 2, 3, 5, 7

Time: 0, 33.33, 66.66, 100, 166 (ms)

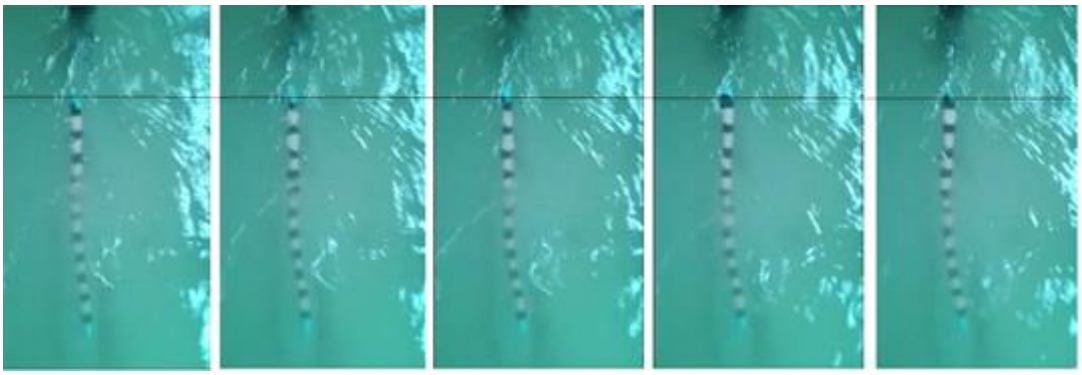

Frames: 10, 12, 13, 15, 16

Time: 200, 333.33, 400, 433.33, 500 (ms)

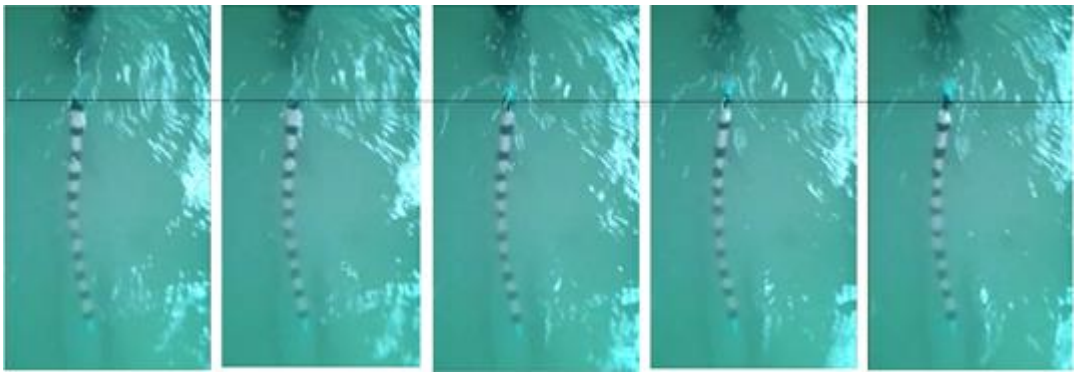

Frames: 18, 19, 21, 23, 24

Time: 533, 600, 633.33, 700, 766 (ms)

Figure 33. The observed upstream motion and the respective time in milliseconds.

4.1.1 Summary and Limitations of Preliminary Results

Despite showing some evidence for a flexible cylinder moving upstream, the results cannot be conclusively proved as it cannot be demonstrated that the cylinder is firstly, adopting the Von Kármán gait and secondly that the upstream movement is not because of the flexible cylinder being sucked into the formation region behind the bluff body. As previously discussed, the size of the formation region is estimated to be approximately $1.75D_{bb}$ for a bluff body with Reynolds number in the order of 26000 and flow velocity $0.29m/s$ [11]. The flexible cylinder in the current report was towed $2D_{bb}$ downstream of the bluff body however due to the relatively low flow speed, the Reynolds number was just below 26000, thus the flexible cylinder was very close to, or at the edge of the formation region which gets bigger with a decrease of Reynolds number, as discussed in section 2.2.1. Furthermore, the use of PIV or LDV (Laser Doppler Velocimetry) imaging is necessary to prove that the cylinder isn't being affected by the low pressure suction region behind the bluff body, as well as to determine whether the motion of the cylinder was using a vortex interception mode or a slaloming mode. Effectively, this would help to explain more conclusively the mechanism causing the cylinder to move upstream.

In general, the experimental results show the importance of having a flexible cylinder performing as a slender body. The assumption of 'slenderness' requires not only that the body geometry is slowly varying in the longitudinal direction, but that its lateral motions do not change rapidly along the same direction; in other words, the wavelength of undulatory body motion must be large compared with the transverse dimensions of the body [114]. The defect has led to stiffness change at that particular point on the body, leading to a different body motion than the expected which has not given any meaning full results for this study. Furthermore, the importance of the body oscillating on the same plane can be seen. Since the experimental setup is consisted by only one overhead camera, the three dimensional motions could not be captured.

4.2 Experimental Analysis

Following the unsuccessful analysis of the first body, a second body was designed with special attention to the manufacture to minimise the risk of a manufacturing defect being produced. The results from the first attempt clearly showed the importance of having a well-designed cylinder since many factors could possibly cause an error as well as the importance of having a very clear video recording.

In this section, a newly designed flexible cylinder has been immersed in the towing tank with flow characteristics as described in Case #3, Table 4, and it was tethered at a distance of $2D_{bb}$ away from the bluff body. It has a total length of 0.676m and 0.022m diameter.

This section is divided into several steps. Starting from a visual analysis of the video footage obtained during the experiments, the flexible cylinder's motion is analysed by describing the interaction of the vortices with the body. Two attempts to estimate the frequency of the flexible cylinder take place using the visualisation. Then, using the Matlab® code, the position of the centroids over time is detected, allowing the amplitude of motion of the flexible cylinder to be found. Through FFT analysis, a power spectrum of the flexible cylinder resonant frequencies has been plotted and discussed.

4.2.1 Water Flow Case #3 Analysis

Figure 34 provides captured images from flow Case #3 and flow footage video #1, with characteristics as described in Table 5 and Table 4 respectively. Red dye has been added to the water upstream of the bluff body to help visualise the flow characteristics. With reference to the flow visualization screenshots as shown in Figure 5, it is clear that although the Reynolds number is higher than most typical studies, the wake consists of an identifiable vortex street as first described by Theodore Von Kármán.

By looking at 16 pictures in Figure 34 (Frames 60 to 135 – spaced equally by five frames) it is noticeable that the flexible cylinder does tend to flex according to the respective vortex passing along its length, in what appears to be a synchronised slaloming mode similar to that shown in Figure 6. This method of swimming where the object mimics the shape of a swimming fish as described in the literature, would be expected to exploit the environment to minimise drag and potentially produce thrust.

Starting from frames 60 – 95 (Figure 35), one can easily note that the dye in the water cannot provide clear vortex identification as it is spread along the cylinder but some of the vortices can still be recognised. This is due an excessive amount of dying in the water at certain occasions. Looking at frame 100, three clearly visible vortices running along the length of the flexible cylinder can be identified. One in the upper part (rotating anticlockwise) of the frame acting on the marking just before the nose, one vortex in the middle of the cylinder (rotating clockwise) and one at the tail of the cylinder (rotating anticlockwise). A sixth of a second later, at frame 105, the clockwise rotating vortex in the middle of the cylinder travels down the length of the flexible cylinder. At the same time, the anticlockwise vortex located at the tail is passing the flexible cylinder (frame 110) and by frame 120, the anticlockwise vortex at the tail of the cylinder is replaced by the clockwise vortex where it reaches maximum displacement. Going back to frames 80 – 95, by observing the motion of the flexible body, it is observed that these motions are repeated again, only this time in the opposite sense to the movement it has just gone through. The flexible cylinder seems to repeat these motions in a periodic manner, following what appears to be the body's interaction with the oncoming vortices. In some occasions, an upstream movement was perceptible but only by a few centimetres.

Frames: 60, 65, 70, 75

Time: 0, 166, 332, 664 (ms)

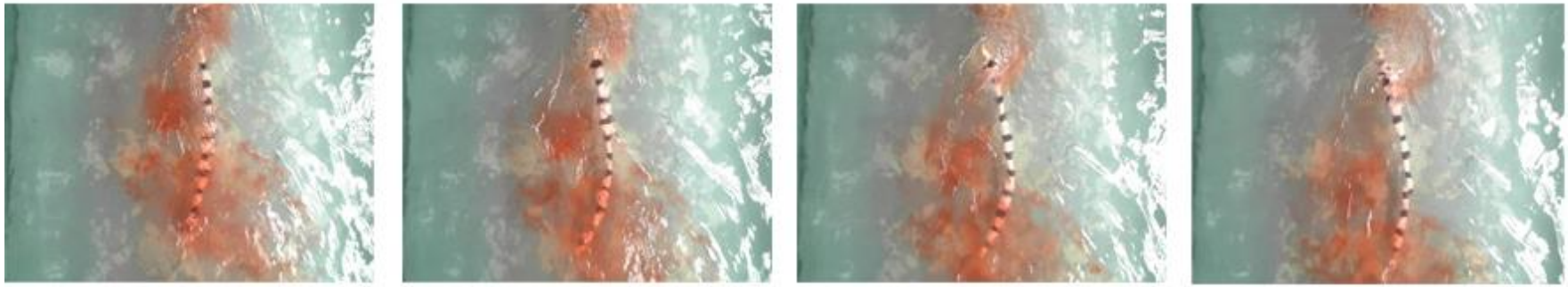

Frames: 80, 85, 90, 95

Time: 830, 996, 1162, 1328 (ms)

Figure 34. Video Footage 1 for flow Case #3 – from left to right (1).

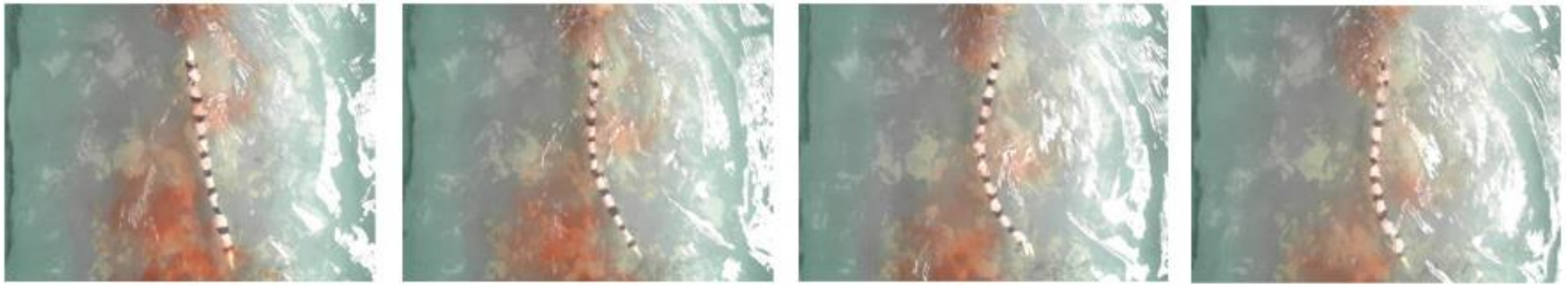

Frames: 100, 105, 110, 115

Time: 1494, 1660, 1826, 1992 (ms)

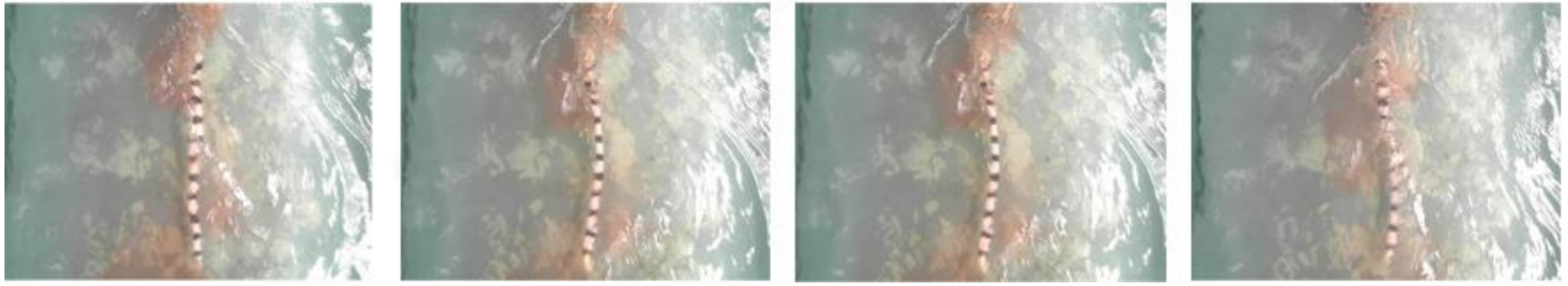

Frames: 120, 125, 130, 135

Time: 2158, 2324, 2490, 2656 (ms)

Figure 33. Video Footage 1 for flow Case #3 – from left to right (2).

As discussed in the literature review, it is known that during the Von Kármán gait, tail beat frequency consistently approaches the rate at which vortices are shed from the cylinder, and the body oscillates laterally with a magnitude similar to the spacing of the vortices. This indicates a phase locking of the swimming kinematics to the vortex wake and thus a potentially passive mechanism of energy conservation in fast, turbulent flows [32]. A careful examination of the flow visualisation footage can identify whether the experimental vortex shedding frequency matches the one predicted from theory, presented in Table 4.

To measure the frequency at which the tail of the flexible cylinder is moving, two random sets of frames were examined as described in Table 12 and Table 13.

	Frame Environment	**Real Environment**	**Units**
Wave wavelength [λ] =	0.045	0.264	m (frame 136)
Distance travelled at 20fps [d20] =	0.024	-	m
Time [t] =	20	30	fps
Distance travelled at 30fps [d30] =	0.036	-	m
Body length [L_{fc}] =	0.115	0.676	m
Velocity [V_{fc}] =	0.036	0.211	m/s
Frequency [f_{fc}] =	-	0.8	Hz

Table 12. Frequency estimation of Flow Case #3: Frames 108 - 128.

	Frame Environment	**Real Environment**	**Units**
Wave wavelength [λ] =	0.055	0.338	m (frame 88)
Distance travelled at 22fps [d22] =	0.032	-	m
Time [t] =	22	30	fps
Distance travelled at 30fps [d30] =	0.004	-	m
Body length [L_{fc}] =	0.11	0.676	m
Velocity [V_{fc}] =	0.044	0.272	m/s
Frequency [f_{fc}] =	-	0.805	Hz

Table 13. Frequency estimation of Flow Case #3: Frames 038 - 060.

Initially, the wavelength has been measured near the respective set of frames to ensure more accuracy. The uneven amount of dye concentration in the water, has resulted in

different vortex sizes in some cases or it was not clear enough to be measured. Also, the difference in pressure at the different points of the vortex makes it even more difficult to measure the wavelength with accuracy. This can be seen in Figure 34. If available and for the best results, PIV could have been used, however, given that the right approximate dimensions are used per set of frames, very good values can be obtained. Next, the distance between the tip of the tail at the initial frame to the last frame was measured. Since the amount of frames passed for the flexible cylinder to move this distance are known, the velocity can be easily found by scaling the number of frames per second needed to 30fps. Then, both the wavelength value and the calculated velocity value were scaled to the real value as described in section 3.2.1.

In Table 12, the analysis of the first set of frames (108-128) can be found. The approximate wavelength is 0.26m (frame 136), with the flexible cylinder having a speed of 0.211m/s, resulting to a natural frequency of 0.800Hz. The analysis of the next set of frames (038-060) in Table 13, showed that the wavelength is 0.32m (frame 88), with the flexible cylinder having a velocity of 0.272m/s, resulting to a natural frequency of 0.805Hz. Comparing the two approximations to the expected range of shed frequencies, to be discussed in section 4.5, it can be seen that some correlation exists. The approximated frequency of oscillation for the tail falls near the lower boundary (0.836Hz) of the expected frequency range 0.891±0.055Hz. As it has already been verified through visualisation earlier, the flexible cylinder oscillates as described in the theory.

Following the estimation of the frequency by extracting and observing frames from the video footage, an assessment of the amplitude of the flexible cylinder was made. The extracted frames were interrogated with edge the detection technique described in section 3.2.1 where information about the instantaneous position of the flexible cylinder have been acquired. The frames depict only the positions of the centroids of the black stripes on the flexible cylinder. This gives a very clear image of how the cylinder is interacting with the flow and it is very easy to visualise the oscillation. It can be assumed that the oscillation of the flexible cylinder is represented by a transverse wave, meaning that the flexible cylinder is displaced in a direction perpendicular to the direction of the flow. In this chapter, the maximum amplitude of the flexible cylinder is the distance from the crest to the trough, instead from the point of rest to the crest or trough, as it is normally. The wavelength is the length of a complete cycle.

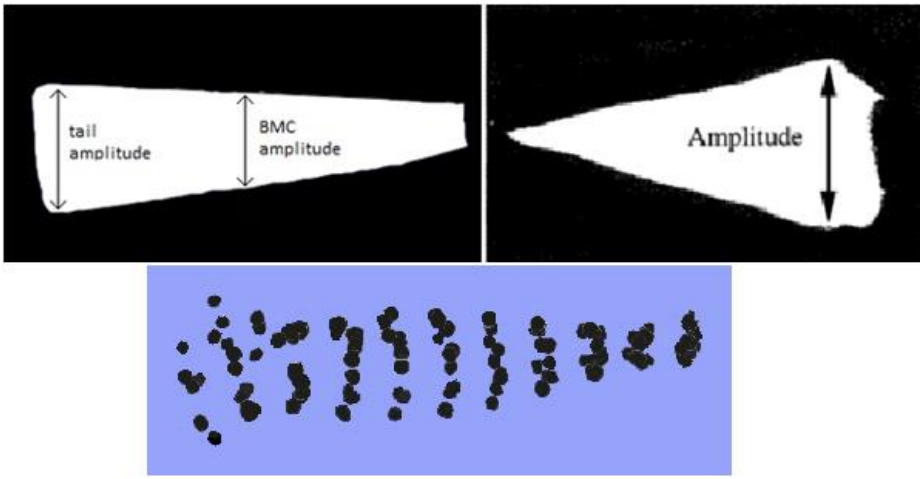

Figure 35. Superposition of flexible cylinder oscillation (top left). Superposition of eel (top right) [5]. Superposition of flexible cylinder centroids on one plot (bottom).

Figure 35 shows superimposed images of the oscillating flexible cylinder over a few cycles, which is used to extract the amplitude of the tail and the cylinder main body for one cycle (Figure 36). The same technique has been used by Allen and Smits to find the frequency and the amplitude of the unsteady shape of the eel [5]. Comparing the superposition image of the flexible cylinder to the one of the eel, there are some expected differences. The area of the nose is sharp because eel's tip is fixed in one place, compared to the flexible cylinder where it is free to move forward and laterally. Furthermore, since the flexible cylinder is free to move, it occupies a larger oscillating area compared to the one that it would if the nose was fixed. Therefore the amplitudes can only be calculated by extracting points for one cycle since the superimposed image contains more than on cycle. Figure 36 shows a sequence of cylinder shapes after using the edge processing technique [5], superimposed on one plot. The maximum amplitude over one cycle of the tail has been found to be $0.26m$ and of the body $0.22m$.

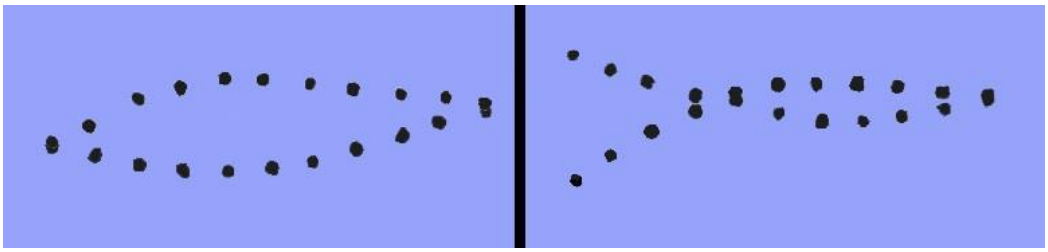

Figure 36. Maximum amplitudes for body (left) and centroid 11 (right) for one cycle. Nose to tail, right to left.

Having established that the flexible cylinder is interacting with the upcoming vortices to an expected degree, an attempt to use the Matlab® code follows. Initially, when attempted to use the Matlab® code as described in section 3.2.1, the results instead of containing data

for 11 centroids, it contained only for eight. Furthermore, the majority of the data were repetition of others because the code was failing to pick the relevant centroids or it was returning empty cells. The reason for which the code was unable to pick the centroids is because it didn't have a clear window towards the flexible cylinder upon video recording. In a human eye, the centroids of the flexible cylinder were visible enough, however as it has been proven, the code needs a clearer visibility. Any reflection from the upcoming vortices passing next to or above the flexible cylinder where the centroids are located, make the code unable to pick the centroids. Given the situation, it was decided not to rectify any data as it would be meaningless.

Instead, it was decided to make some research into image and video manipulation techniques in order to improve the frames' characteristics of the frames. Initially, a polarised filter was applied on the video and with some contrast alterations, the colours of the video were enhanced. The centroids on the video were more visible now but still not enough for the Matlab® code. Therefore, it was decided to extract a number of consecutive frames into pictures where in turn, using Adobe Photoshop®, the centroids were enhanced by applying black colour on them. Then, the frames were put together using a video editing software and turned into a video again. As a final touch, 'mosaic' was applied on the final video, at the sides of the flexible cylinder, in order to cover any light variations or reflections which could possibly picked up by the code which led the code to pick points only from the oscillating area of the flexible cylinder. Consequently, extracting each and every frame from all the footage acquired, would mean over 45 000 frames had to be extracted from the video, analysed and processed, a long and time consuming process. Therefore, a smaller part from Footage flow #1 was chosen to run the Matlab® code and analyse the behaviour of the flexible cylinder. It can be assumed that if any fluid structure interaction periodicity were to exist, it ought to be easily captured in just few seconds of the available footage for the same flow characteristics. Failure to do so would automatically make the alternate footage statistically worthless even if a degree of periodicity does exist in the latter.

In an attempt to further understand the interaction of the flexible cylinder with the upcoming vortices, a plot outlining the behaviour of each of the markings on the body has been generated for the first 12 seconds of Footage flow #1. The numbers of the centroids are shown in Figure 29. Looking at Figure 37, there is a noticeable inclination to have the tail out of phase with the nose. This is believed to be ought to the amount of vortices acting

on the body at those points. Recalling the theoretical value of the wavelength between the vortices of the same rotation is roughly 0.30± 0.05m and looking at the visualisation in Figure 34, it is clear that at different instances as a minimum there are three vortices, supposedly equally spaced, acting along the body at any point in time. It is also believed that at some instances four vortices of different rotations exist, two on each side of the body (frame 130).

Another observation is that in no instance a marking is exhibiting a larger amplitude than any other further downstream to it. Figure 37 below, shows the amplitude values for a sample timeframe. It can be observed that the amplitude of markings increases accordingly from nose to tail. Given that the vortices will decay as they travel downstream, consequently giving rise to an increase in pressure, makes this an expected occurrence. Additionally, this compliments the theory that the 2nd half of the body near the tail should exhibit larger amplitudes compared to 1st half, near the nose. Finally, it has been observed that at some occasions the flexible cylinder exhibits very high amplitudes. In reality this is not what has been happening. The reason is because since the flexible cylinder was moving in the water, the location of the nose was changing, where consequently, the Matlab® code has recorded higher movement at the centroids, especially to those located at the 2nd half of the body.

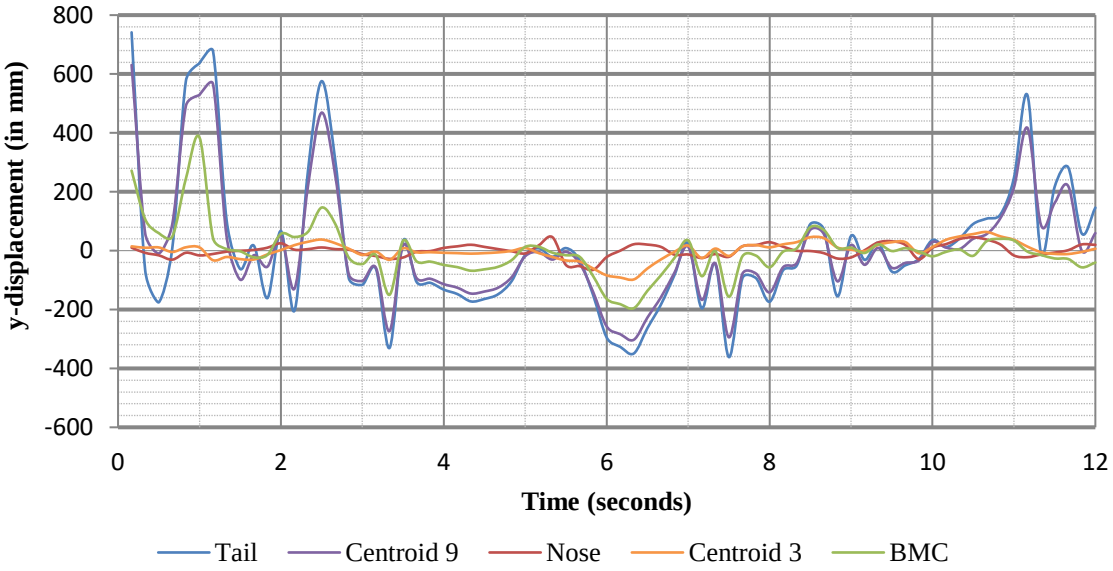

Figure 37. 12 seconds sample of Flow Case #3, Footage 1.

Earlier, through visualisation, the frequency and velocity of the tail were estimated. An attempt to calculate the velocity at a random point on the tail will take place. This will

allow assessing the results as well as the quality of the experimental data and the graph in Figure 37. At the 9.5th second (Frame 285), the BMC (centroid 6) is located at point -1.2776 (y-axis) and few seconds letter at the 10.5th second, it is located at point -17.4306. The tail, during the 10.5th second is located at point 90.5848. Using Pythagoras' Theorem and knowing that distance between two centroids is $56.1mm$, the distance between BMC and tail is $280.5mm$ and the distance over which the vortex travels is $\sqrt{280.5^2 - (90.5648 - 17.4306)^2} = 258.86mm$. The displacement occurred at a time interval of 1s, therefore the velocity of the vortex is approximately 0.258m/s.

Similarly to the preliminary experiment in section 4.1, the procedure used to calculate the velocity of the vortex can be characterised as inaccurate, however it can still provide reasonable values provided that the following conditions are satisfied:

i. The flexible object travels upstream by a negligible degree.
ii. It lies in a 2-D plane parallel to the bottom of the tank.
iii. The amplitude of the perturbation (difference in y-displacement) is small compared to the distance between the measuring points.

Comparing the velocity just found, with the two velocity values found during the visualisation earlier in this chapter, as well as the velocity magnitude contours in section 5.4.2.1 where the flexible cylinder is placed in reality, it is clear that the calculated velocity falls within the expected magnitude. This enhances the validity of the data even more and leads to the final part of the experimental analysis; to plot the power spectrum of the nose, BMC and tail, in order to investigate whether the flexible cylinder is matching with the incidence of the oncoming vortices.

Finally, 30 midlines of the flexible cylinder have been plotted (Figure 40) and compared with those of the trout as shown in Figure 38. It is obvious that they have less curvature. This is because the flexible cylinder has a constant cross section, compared to the significant reduced stiffness in the fish's tail due to the decrease in cross sectional area. Comparing with Figure 39, the midlines show that there is a qualitative similarity not only to a motion of a dead trout but also to how a similar cylinder behaved in experiments with similar conditions, undertaken by other authors. This demonstrates that the cylinder is behaving as expected compared to the literature.

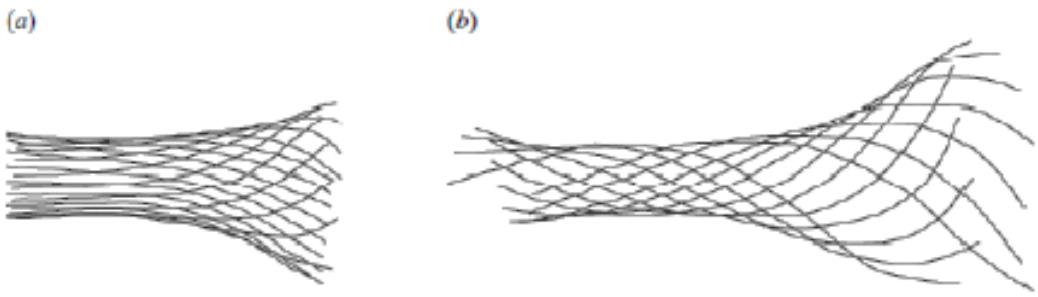

Figure 38. The midlines from a live trout (a) and a dead trout (b) for a cycle of motion of the Von Kármán gait behind a bluff body (taken from [115]).

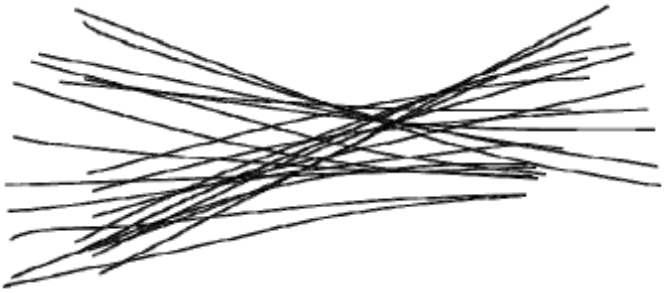

Figure 39. Midlines of a flexible cylinder behind a bluff body (taken from [97]).

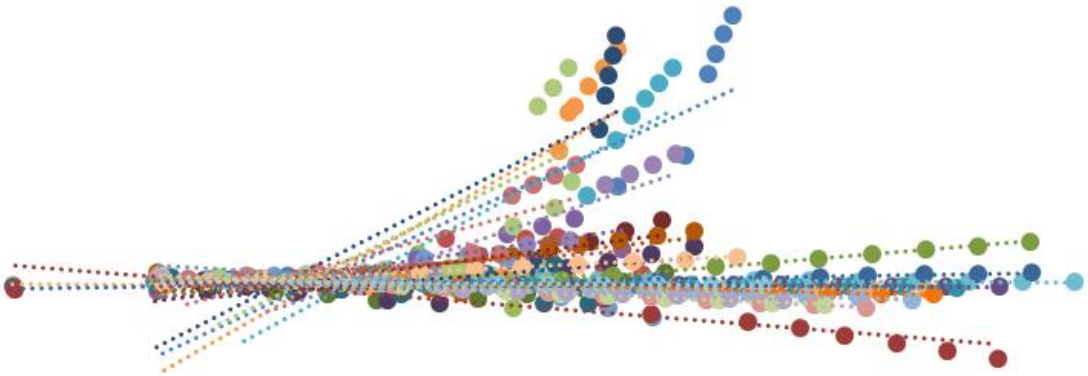

Figure 40. Midlines of the flexible cylinder used in this research.

4.3 Experimental Results Analysis

The following section discusses the results of the experimental analysis conducted to investigate the dynamic behaviour of the flexible cylinder in unsteady flow and then compared with similar work presented in the literature.

In general, it was observed that the flexible cylinder tends to flex in accordance to the respective vortex passing along its length, in what appears to be a synchronised slaloming mode. Furthermore, there were instances where the cylinder appeared to move upstream in a similar manner to a dead trout by utilising a method that appeared similar to the Von Kármán gait, but only by few centimetres. This may be due to it becoming more difficult for the cylinder to synchronise with the flow as the vortex shedding frequency increases. In a similar manner to the findings of a dead trout in an unsteady flow, the motion of the cylinder didn't synchronize with the flow all the time [11]. However, at times the motion of the cylinder appeared to synchronize with the flow; just after these moments when the motion of the cylinder synchronized with the flow a motion upstream was observed.

For the flow arrangement identified in the previous section, periodograms for the nose, BMC (body mean centroid) and tail markings have been generated using Matlab®. Additionally, in an effort to validate the periodogram generated using Matlab®, the three markings have been plotted again using Excel® and then passed through a Fast Fourier Transformation. The resonant frequencies of oscillation of the flexible cylinder were obtained from the videos after applying an FFT on the deformation points. The results can be seen on the periodogram in Figure 41. The frequencies of interest are the following. The frequency of the nose (0.750Hz) and tail (0.656Hz) were found to be lower than the expected shedding frequency range, indicating the motion of the flexible cylinder is generally not fully tuned to the flow. On the other hand, the frequency of the main body (0.838Hz) where centroid 6 is located (BMC), falls within the expected range of frequencies. The predicted natural frequency obtained from the modal analysis in a vacuum was 0.837Hz, it is known that this will reduce due to the damping effect of the surrounding fluid and therefore the observed frequencies of the body obtained experimentally, and given above, fall in the expected range.

The discrepancy between the nose, tail and main body frequencies might be due to the way the flexible cylinder is oscillating, the degree of coupling with the upcoming vortex and

the development of the vortex as it moves downstream. The better the coupling, the closer the oscillating frequency will be to the shed frequency at all points on the cylinder. Furthermore, in some instances, the cylinder appears to change plane and move vertically. This was in some degree expected as the manufacturing of the cylinder has not been done in perfect conditions as well as the experimental environment not providing ideal 2-D flow. Despite all the precautions and detailed manufacturing, this incident was unable to be eliminated completely. In the manufacture of the Moldsil cylinder, a base material is mixed with a hardener which subsequently sets into a rubber cylinder. The properties are thus dependant on the precise mixture of hardener to base which even with the greatest amount of care will vary slightly from cylinder to cylinder. Thus, the elastic modulus is likely to vary slightly from the value calculated through theory; hence, a small discrepancy may arise between the observed results and the theoretical results.

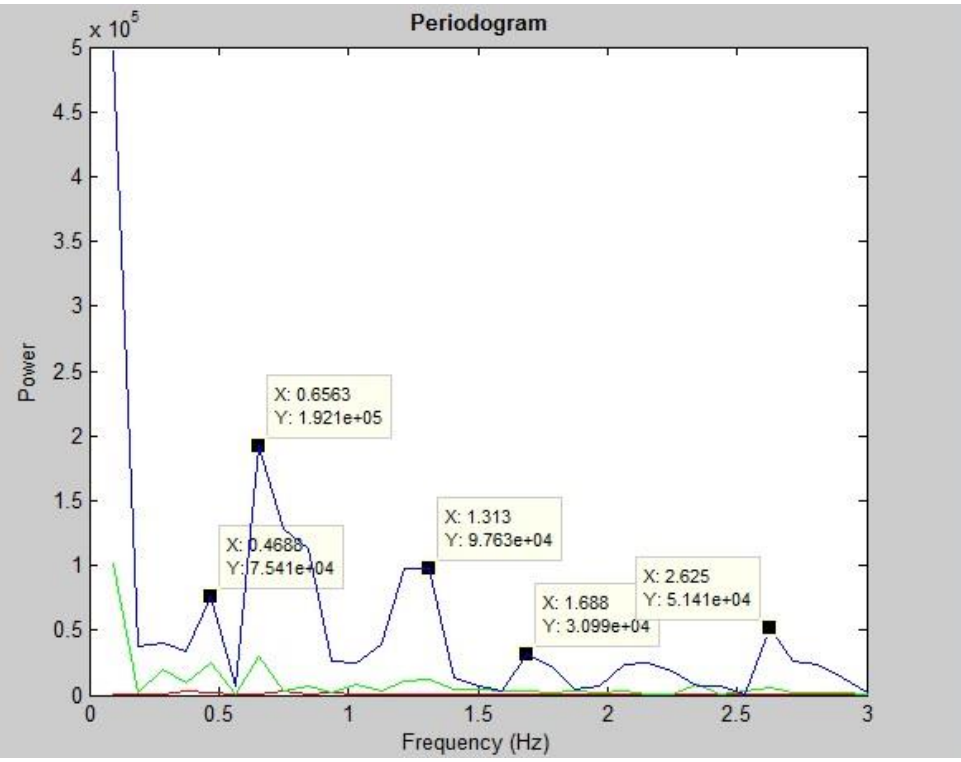

Figure 41. Frequency spectra for nose (red), BMC (green) and tail (blue), Case flow #3 Footage 1.

In comparison with work done from other authors, the flexible cylinder in this report differs in two major areas. The lateral amplitude of the oscillation is much higher and the upstream movement is much less compared to the other research. No more than 2 – 4cm of forward movement has been observed and from the graph in Figure 37, the amplitude of the tail is much larger than then the diameter of the bluff body. The same applies for centroid 9. On the other hand, the nose and centroid 3 and BMC have amplitude no bigger than the

diameter of the bluff body. In the experimentations done in [97], where the experimental velocity was over 0.4m/s, the cylinder was strongly influenced by the effect of unsteady fluid flow. It has been shown that the upstream movement varied from small motions around 1cm to large motions over 4cm, after which the cylinder was drawn into the suction region behind the bluff body and that the lateral displacement was no bigger than the diameter of the bluff body. Not much information is included regarding the lateral displacement of the cylinder, however it is noted that it does not exceed the diameter of the bluff body. During experiments done by other authors, it has been shown that a forward motion of over $15cm$ was possible where the flexible cylinder was tethered up to three times the diameter of the bluff body in front of it (D_{bb} = 9cm), which in turn was sucked into the suction region and back [35]. In this case, the lateral amplitude was higher than the diameter of the bluff body but less than the displacement of the cylinder in this project. In extension, in [35], an experiment is designed with a rigid flexible cylinder, therefore with zero lateral displacement and still forward movement has been observed. This gives the belief that the forward gait is irrelevant of the stiffness of the body, however because it is considered to implement piezoelectric material in the body, there is more interest in the overall deformation of the body and not the forward velocity.

In addition, the author believes that there is a good possibility of being able to extract more energy out of a cylinder that has greater lateral amplitude than a cylinder that has less lateral amplitude with increased upstream movement. This assumption is based on that piezoelectric material will be used where its deformation is directly related to the surface deformation of the flexible body and therefore to the force applied on the body from the oncoming vortex. With this assumption, it can be considered that more energy can be extracted from cylinders with higher lateral amplitude compared to those with less. This will be examined further in chapter 7.

Overall, the results obtained are very interesting and have shown that an inanimate object can be tuned to hold station behind a bluff body and have a natural frequency matched or very close to the shed frequency, resulting in a strong body response to the unsteady fluid flow. The results obtained from this experimental work will be used as verification data for a computational model of the system. The model will allow additional variables to be investigated to aid the design of tuned flexible cylinder to fluid flow.

4.4 Open Channel Velocity Profile Characterisation

In order to further understand the development of the flow, the vertical velocity profile of the water channel has been described, through experimental procedure.

The pumps and the bridge have the same arrangement as Case #3, found in Table 4. The bluff body and the flexible cylinder are not present in the water channel. The water channel was run for 15 minutes for the water to reach a steady flow. Using, the same lightweight, buoyant ball as mentioned in the experimental design, section 3.1, the time and the distance have been measured at two locations to find the average velocity of the flow.

As shown in Figure 42, for Location #1, the measurements have been taken between the four and the 6.5 metre of the water channel length. From a range of ten velocities, the maximum recorded was 0.504m/s and the minimum 0.393m/s. The coefficient of variation between the velocities has been found to be 8.81%. Given the methodology used to measure the velocity and the variation of the water channel flow from the pumps, it is considered a reasonable percentage. The average velocity was found to be 0.442m/s at a water height of 0.49m, as indicated by the water height scale, attached on the walls of the water channel. Using the coefficient of variation, the maximum average velocity found to be 0.481m/s and the minimum 0.403m/s. As it will be explained later in chapter 5, section 5.4.1, the two latter velocities will be used as the upper and lower boundaries to assess the correlation to the velocity profile extracted from the computational model.

Similarly, at Location #2, the measurements have been taken between the 7.5th and the 10th metre of the water channel length. From a range of ten velocities, the maximum recorded was 0.476m/s and the minimum 0.407m/s. The coefficient of variation between the velocities has been found to be 5.19%. The average velocity found to be 0.453m/s at a water height of 0.5m. Using the coefficient of variation, the maximum average velocity found to be 0.467m/s and the minimum 0.421m/s.

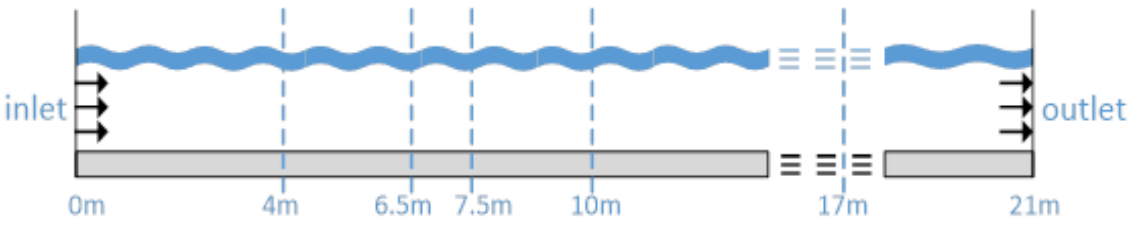

Figure 42. Average velocity measurement at different locations.

On the 17th metre of the channel, an Acoustic Doppler Velocimetry (ADV) has been installed, constantly measuring the averaged cross-section velocity (and discharge) of the water channel, with 1% accuracy. Unfortunately, it was not possible to move it and measure the average velocity at the two previously defined manual measurement locations, however the recordings at the 17th metre have been compared with the ones found upstream, assessing their validity.

The average velocity has been found to be 0.40m/s and the water height 0.52m. Compared to the previous two locations, the average velocity is lower and the water height higher. The average velocity found using the ADV closely matches the minimum velocity recorded at the two other locations, using the lightweight ball. This gives a good confidence in the measurements recorded using the ball.

As discussed, in chapter 2, section 2.3, the velocity profile of the flow is divided into two regions. For each region, empirical equations have been presented, all of them giving an approximation of the vertical velocity profile. If one would like to re-create an accurate vertical velocity profile, one should only use the correct equations for each region. This gives the advantage to predict which equations should give good approximations and which will not, within the outer region. Therefore, if all the equations behave as expected, will give a firm reassurance that the velocity profiles plotted can be used on a later stage to assess the quality of the water channel flow development, in the computational model. Further discussion will follow in chapter 5.

Having obtained the experimental data, it is now possible to use the equations presented in section 2.3.2 and plot the velocity distribution function. Since the area of interest is the outer region of the velocity profile, the analysis will focus only there, excluding any comments related to the inner region and the distribution accuracy of the equations. As seen in Figure 43, the red line represents Coles' wake function. It can immediately be observed that this equation does not represent a correct velocity profile. The shape of the graph does not resemble the expected one as shown in Figure 9 and the average velocity values are outside the experimental range. As discussed, Coles' law is unable to predict the velocity dip-phenomenon in three-dimensional turbulent flows [69] [73], therefore, it shouldn't give any acceptable approximation.

Observing the blue and purple lines, they have a very close approximation along the length of the velocity profile curve, except from near the surface. As it has been discussed, the log-law fails to predict the dip-phenomenon and this is what is observed in Figure 43. According to the semi-empirical equation named the 'dip-modified log-wake' law represented by the purple line, the maximum velocity is 0.543m/s and it is located at a distance of 0.38m from the bed of the water channel. To assess the validity of the location, Equation 17 for the dip-phenomenon location has been used, already presented in section 2.3.2. Two variations of the equation are also presented, shown below as Equation 27 and Equation 28, established by different authors through the years. Since the equations are easy to implement, it was decided to use all three equations and observe the outcome.

$$\xi_{dip} = \frac{1}{1 + 1.2exp\left(\frac{-Ar}{2}\right)}$$

Equation 17. Dip-phenomenon dimensionless location.

$$\xi_{dip} = \frac{C_1 + C_2 \times Ar^{C_3}}{C_4 + Ar^{C_3}}$$

Equation 27. Dip-phenomenon dimensionless location – variation 1.

$$\xi_{dip} = 0.44 + 0.212\left(\frac{z}{h}\right) + 0.05sin\left(\frac{2\pi}{2.6}\frac{z}{h}\right)$$

Equation 28. Dip-phenomenon dimensionless location – variation 2.

Equation 17, introduced earlier in section 2.3.2, uses the channel aspect ratio to calculate the location and gives a dimensionless height of 0.36. Similarly, Equation 27 [116] is applicable at the centreline of the channel ($\frac{W_{channel}}{2}$) and it uses the distance (z) from the wall with a linear trend of sinewave function. It gives a height of 0.34. Equation 28 [69] uses some predefined constants in conjunction with the aspect ratio to calculate the dip position, being 0.33.

Observing the velocity values for the simple dip-modified log-wake law, it can be seen that the maximum velocity of 0.543m/s occurs within a region of 0.04m, from 0.35 – 0.39m distance from the bed, depending on the amount of decimal places taken into consideration. This matches the locations calculated using Equation 17 from the literature and its variations. Having an accurate dip location gives good confidences regarding the accuracy of the experimental data, as well as the validity of the semi-empirical equation used to plot

the velocity profile of the water channel. Equation 16, once plotted, it gives a good approximation of the maximum velocity value at 0.543m/s. Despite the value being an approximation, it is still close to the 0.522m/s velocity found using Equation 13 for U_{max} from the theory. Once again, worth mentioning that the value of Coles' constant which the semi-empirical equation depends on, varies a lot. As aforementioned, many researchers have changed this value to fit their data as clearly stated in published work [69].

For this project, it is sufficient to validate the velocity profile distribution curve as a whole. The semi-empirical equations behave as expected using the experimental data and the fitting process. The 'dip-modified log-wake' law gives a qualitative and quantitative approximation of the velocity profile in the water channel. Having a validated velocity profile graph, Figure 43 will be used as a reference point later in chapter 5, where comparison between the computational velocity profile and the theoretical/ experimental will take place.

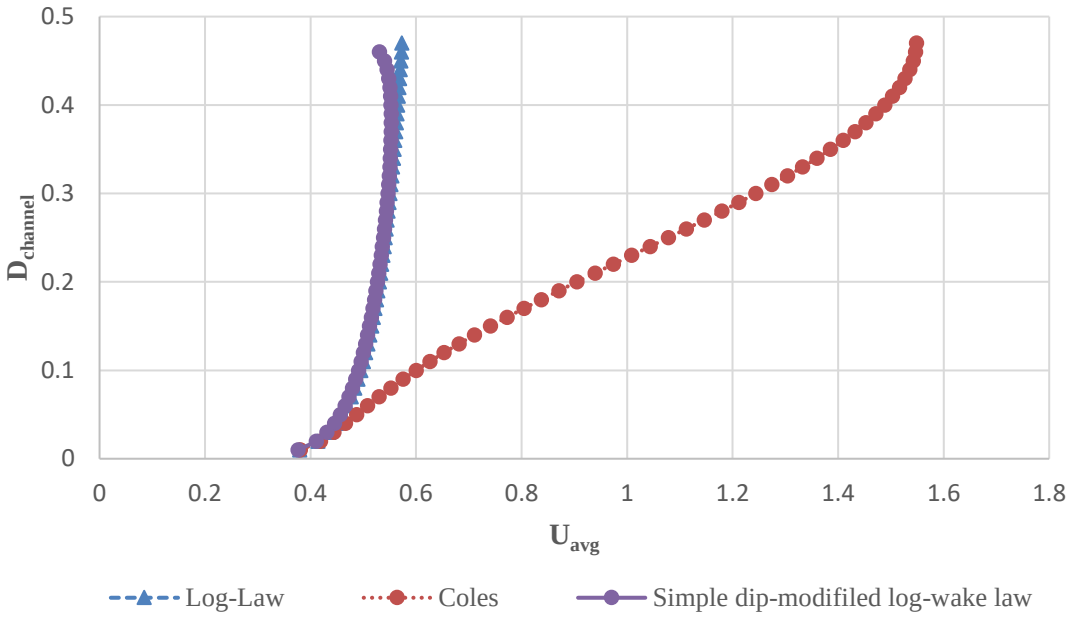

Figure 43. Vertical velocity distribution for Location #1.

4.5 Strouhal Number Sensitivity Analysis

As previously discussed, Equation 7 has been used to predict the Strouhal number of several flow cases, as shown in Table 4. Flow Case #3 has a shed frequency closest to the natural frequency of the flexible cylinder, as determined theoretically in section 3.1.4.

The experiments presented in section 4.3 have shown that the flexible cylinder can exhibit consistent Von Kármán gait and deform in respect to the shed vortices. This shows that the experimental flow velocity and bluff body size can give Reynolds and Strouhal numbers sufficient to excite the flexible cylinder.

This section investigates the sensitivity of the empirical equations presented in section 2.2.2 (Equation 7, Equation 8 and Equation 9) for the prediction of Strouhal number. The aim is to understand the variation between the Strouhal numbers and respective shed frequencies at three different velocities. These will be the maximum, minimum and average velocities measured experimentally, as presented in section 4.4, at the location of the bluff body.

As discussed in the literature, it is not clear which empirical equation to use for the present research, especially given the array of relationships proposed over the years. The reason for undertaking this investigation is to create some reference values for Strouhal number and shed frequency, which will be used in chapter 5 to assess the quality of the computational results.

In addition, by knowing the approximations of the Strouhal number, it will be possible to identify an approximation of the expected drag coefficient by correlating the Strouhal numbers with existing experimental data by other authors. This will give another quantity to assess the computational model results.

Table 14 shows the three velocities mentioned above, with Strouhal and shed frequency numbers for each equation. Firstly, the coefficient of variation between the Strouhal numbers from all three equations, at each flow velocity has been found and compared with the respective coefficient variation of the frequency. As it can be observed, there is approximately 6% difference between the estimated Strouhal numbers, same with the frequencies. This is expected, as it is already indicated by the respective authors that the data within the envelope are accurate within ±5%.

	V_{max} = 0.476m/s		$V_{nominal}$ = 0.453m/s		V_{min} = 0.407m/s	
	Re = 5.4014×10^4		Re = 5.1404×10^4		Re = 4.6185×10^4	
	St	f_{shed}	St	f_{shed}	St	f_{shed}
Equation 7 (Fey)	0.1871	0.88	0.1873	0.839	0.1878	0.756
Equation 8 (Roshko)	0.2119	0.997	0.2119	0.949	0.2119	0.853
Equation 9 (unidentified)	0.1979	0.931	0.1979	0.886	0.1979	0.796
Coeff. Var.	6.26%	6.26%	6.19%	6.19%	6.08%	6.08%
Average	0.1990	0.9360	0.1991	0.8913	0.1992	0.8017

Table 14. Strouhal empirical equations analysis.

Next is to investigate the rate of change of Strouhal number with velocity. By plotting the three Strouhal numbers per equation against flow velocity, it is possible to see each equation's sensitivity against the increase of flow velocity and consequently Reynolds number, by observing the slope of the lines. However because only three points are available, it is difficult to observe the change in the slope. Therefore, the gradient of each line has been found by dividing the difference of two Strouhal points with the difference of the two respective velocity points such that $\frac{St_2-St_1}{U_2-U_1}$. Equation 7, Equation 8 and Equation 9, have gradients -0.01, 0.0001 and 0.0002, respectively. It is observed that the gradient found using Equation 7 is 100 times greater than Equation 8 or Equation 9. This shows that Equation 7 is more sensitive to change than the other two. It also has negative gradient due to the method the author chose when undertaking the experiments, which resulted in this equation.

As discussed in section 2.2.2, there is not an exact value for the Strouhal number but a possible range, enclosed in the envelope presented in Figure 4. Therefore, a range of Strouhal and shed frequency numbers can be identified, where, if any computational results fall within, can be considered acceptable for the needs of this research. Firstly, the averages for Strouhal number and shed frequency per flow velocity have been calculated. Then, since the nominal velocity will be the input velocity of the computational model, the range is created using the later in combination with the coefficient of variation of the Strouhal numbers given by the three equations. Therefore, the accepted range of shed frequency which will be used as the validating guideline for the computational model is 0.891±

6.19%, or otherwise, 0.891± 0.055Hz. The maximum boundary of the shed frequency is 0.946Hz and the minimum is 0.836Hz.

A similar investigation is undertaken for the drag coefficient. In many occasions, in the literature, the drag coefficient of the flow past a cylinder in the Reynolds number of 5.1404×10^4 is considered to be 1.2. However, the author has found that this is not the case. By observing Figure 44, it can be seen that the drag coefficient for the respective Reynolds number varies between 1 – 1.4 [117]. Figure 44 consists of the experimental work undertaken by 47 eminent authors in the field and it is clearly seen that the drag coefficient is not 1.2 as considered by a significant amount of other authors in the literature. Furthermore, the book of Zdravkovich details numerous experiments and flow characterisation past a circular cylinder through all flow regimes. It specifically states that within the TrSL3 regime, the upper transitional regime, where the Reynolds number of this research lies, the Strouhal data vary up to 10% and consequently the respective drag coefficient [9].

Additionally, by looking at other published computational work where the flow around a circular cylinder has been characterised for two and three-dimensional models, the data present in Figure 44 has been used as the validation method of their numerical results [118] and they have considered any drag coefficient values as good results within the range of 1-1.2 [119]. The author believes that the range of 1-1.4 is too large to be considered as a validation method for a computational model. Therefore, given that the majority of the authors in the literature take 1.2 as the reference value, the author has decided that a range of 1-1.2 will be sufficient for the needs of this research.

To sum up, it has been investigated how the three empirical equations change with the change of the flow velocity. It has also been investigated how much difference there is between the Strouhal and shed frequency approximations between the equations at a specific flow velocity. That is 6.2% for the nominal flow velocity, which will be used as input for the computational model. Therefore, the computational model will be considered accurate enough when, after mesh independence is achieved, the shed frequency will be within $\pm 6\%$ of the average shed frequencies show in Table 14, in other words 0.891 ± 0.055, with a drag coefficient value between 1-1.2.

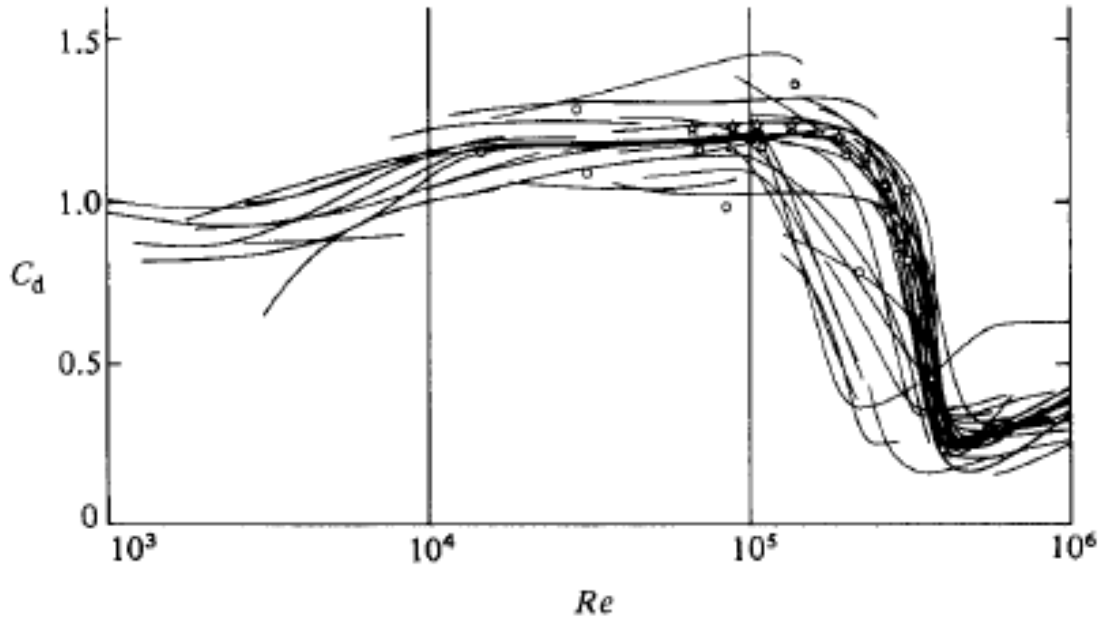

Figure 44. Drag Coefficient results for circular cylinders 100< Re < 100 000 ([117]).

4.6 Further Experimental Analysis

Following the complete analysis of the experimental data at0.453m/s velocity, more tests have taken place at different flow velocities and the behaviour of the flexible cylinder has been recorded. Through the same experimental procedure and analysis method as described in section 4.2, the following data have been extracted:

Velocity (m/s)	Frequency (Hz)			Amplitude (m)	
	Shedding	Body	Tail	Body	Tail
0.400	0.743	0.746	0.853	0.210	0.240
0.423	0.785	0.773	0.88	0.218	0.248
0.453	0.839	0.800	0.800	0.224	0.261
0.460	0.851	0.88	0.720	0.233	0.278
0.503	0.929	1.013	1.280	0.2850	0.360

Table 15. Case #3 testing in various flow velocities.

As it can be seen in Table 15, in order to obtain the frequency at which the flexible cylinder is oscillating, two measurements have taken place, one at the tip of the tail and one at the centre of the flexible cylinder (centroid 6). Similarly to the data acquired from the FFT

analysis as discussed in the previous section, there is a discrepancy between the two set of frequency values per flow velocity. As it will be discussed in future work, the flexible cylinder is expected to have different level of coupling to the flow, according to its natural characteristics. This will give a better coupling between the frequencies or lower match with lower amplitude values as well. Finally, as it has been observed from the experiments, in many occasions during the same frame (moment in time), the flexible cylinder is not coupled to the flow on the same level across its length. Consequently, this will lead to different frequency values and amplitudes between the tail and body. More discussion and analysis between the frequencies and amplitudes will take place in chapter 5, where the computational model of the system will be built.

4.7 Summary

Through visual analysis of the video footage, the flexible cylinder's motion and interaction with the vortices has been discussed. It is very clear that the cylinder has a good coupling with the upcoming vortices and a reasonable good match between the frequency of the flexible cylinder and the shed frequency. Two qualitative attempts to estimate the frequency of the flexible cylinder took place through visualisation. Both give really good approximation to the shed frequency as expected. This has given a lot of value to the data acquired which led to use the Matlab® code which detects the position of the centroids during time. This allowed the measurement of the amplitude of the flexible cylinder by observing the variation of the centroids in time for one cycle. Furthermore, a displacement graph and a power spectrum of the resonant frequencies at the boundary conditions has been produced.

Further experimental analysis has been undertaken where the same model of flexible cylinder has been tested in different velocity regimes. The frequencies and amplitude of each case have been found and will be used in future projects for further scientific research.

A simple quantitative study has taken place aiming to characterise the velocity profile of the water channel. The average velocity of the flow has been measured in two locations and compared with the data obtained from a third location downstream, using an ADV.

The results have shown a good match assuring the quality of the obtained value for the average velocity profile. This can now be used as the input velocity in the computational model presented in chapter 5.

Overall, the results from the experimental analysis give confidence that a bio-inspired inanimate object can be tuned to vibrate in such a manner to hold station with little or no energy input behind a stationary bluff body. In addition, the vibration mode shapes will enable energy to be extracted from its vibration mode shapes, in a specific, or series of, unsteady flow regimes.

Chapter 5

CFD Domain Assessment

In order to model the experimental system described in chapters 2 and 3, ANSYS® Workbench has been used. Finite Element Analysis (FEA), and Computational Fluid Dynamics (CFD) in Fluent, have been combined for the needs of this thesis. The software has been used to create a fully coupled computational model which has been used to predict numerically the amplitude of the flexible cylinder, at a known flow velocity.

The computational work presented in this chapter has been divided into four stages of validation. The first stage investigates the velocity profile and how the flow develops as it moves downstream. It has been found that the velocity profile at the location of the bluff body is underdeveloped, however when a fully developed computational velocity profile has been compared to a fully developed profile using the literature, there is some correlation but still with a noticeable difference.

The second stage presents the work done towards a validated three-dimensional model. Initially, a two- dimensional flow past a bluff body model has been designed. This has helped to understand the required structure of the mesh, to find the correct first layer thickness and understand any limitations that might exist. Good results of drag coefficient and shed frequency have been obtained. Creating the two-dimensional model has given an initial understanding of how the system under study behaves under fluid dynamics. The 2D model was extruded in the third dimension, creating the three-dimensional model. Satisfactory values of drag coefficient and shed frequency have been obtained, independent of the mesh size.

In the third stage, the vortices shed from the bluff body traveling downstream are investigated. Similar patterns were observed compared to those from the experimental work undertaken in this research and in the literature. The Von Kármán vortex street is also visible. Some limitations of the turbulence model used are identified.

In stage four, the inanimate body is introduced in the model. This arrangement represents the energy harvesting system. Due to its complexity, analysis of the system is done separately, in Chapter 6.

Overall, a fully coupled computational model is presented which can be used in the future as a design tool, to predict the amplitude of a flexible cylinder at different flow regimes. This fulfils one of the major objectives of this research, enabling to proceed to the last part of this research study, to develop a system which can harvest energy from vortex induced vibrations.

5.1 Introduction to Computational Fluid Dynamics Work

One of the challenges of this project is to design and validate a computational model which can be used in the future to predict scenarios at different flow velocities and possibly different inanimate body geometries. For this, a fully coupled computational fluid dynamics/finite element model has been created, using the ANSYS® suite.

For this reason, it was necessary to create the experimental flexible cylinder system as a computational model which has then been used to calculate the frequency and amplitudes of the body. The latter are then compared with the experimental and computational work of other authors, assessing the quality of the computational model.

It is worth noting that the same process can be done without computational analysis, especially when the flexible body is of a known simple shape, such as a cylinder, however this will take a vast amount of time as the objects need to be built and then tested in real environment. Furthermore, when it comes down to arbitrary shape objects, this will be very difficult to almost impossible, therefore computational method can be used to analyse these cases.

The work done during the computational analysis can be divided into three main areas:

● Pre-processor: The pre-processor consists of the input of the problem by means of a user interface operator and the subsequent transformation of this input into a form suitable for use by the solver. The region to be analysed is called the computational domain and it is made up of a number of discrete elements called the mesh (or grid) which contain the geometry under analysis. After the mesh generation, the properties of elements and the appropriate boundary conditions are defined [120].

● Solver: The solver calculates the solution of the problem by solving the governing equations. The equations governing the fluid motion are Partial Differential Equations (PDE), made up of combinations of the flow variables (e.g. velocity and pressure) and the derivatives of these variables. Computers cannot directly produce a solution of it. Hence the PDEs must be transformed into algebraic equations [121]. This process is known as numerical discretisation. There are four methods for it as 1) Finite difference method 2) Finite element method and 3) Finite volume method and 4) Spectral method. The finite difference method and the finite volume method both produce solutions to the numerical

equations at a given point based on the values of neighbouring points, whereas the finite element method produces equations for each element independently of all other elements. In the present work ANSYS® Fluent 17.2 has been used which is based on the finite volume method.

● Post-processor: It is used to visualize and quantitatively process the results from the solver part [120]. In a CFD package, the analysed flow phenomena can be presented in vector plots or contour plots to display the trends of velocity, pressure, kinetic energy and other properties of the flow.

5.2 Modelling Assumptions

Initially, the problem has been considered as a flow passing a circle and modelled in two dimensions. Employment of a two-dimensional simulation can reduce computational cost since the dominant vortex shedding mechanism is effectively two-dimensional [122].

It is stated in other studies that the three-dimensionality of the cylinder plays a role when the length to diameter ratio is smaller than 3.8 [123]. In this arrangement, the ratio does not get smaller than 4.09. For this reason, it has been decided to design and study a two-dimensional model and assess its quality and accuracy. A mesh independence study has been carried out where the most preferable 2D model has be extruded into 3D. This has reassured that the structure of the mesh, but not the element number, can produce a correct vortex stream. A final mesh independence test was carried out on the 3D model based on the shed frequency and drag coefficient results.

Since the flow is assumed to be two-dimensional, the bluff body can be represented by a circle as shown in Figure 45. The channel is represented by a rectangular flow domain surrounding the bluff body. The formation of vortices is a purely transient phenomenon, thus all the calculations are performed in a transient model where a moving depiction of the flow passing the bluff body can be observed. Consequently, to enable a stationary result, the transient model is run until the number of time steps shows a periodic steady state solution.

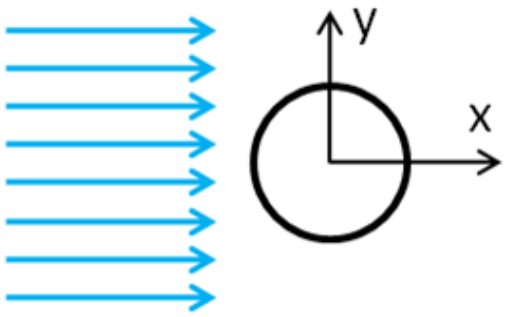

Figure 45. Flow past a cylinder in two-dimensions.

Boundary conditions are applied to the simulation to obtain plots of static pressure, velocity magnitude, and streamlines. The drag and lift coefficients are obtained using the forces exerted by the fluid on the cylinder as computed by the software. The velocity of 0.453m/s has been introduced at the inlet corresponding to a Reynolds number of 5.1404×10^4 according to the theoretical calculations outlined in Table 5. The outlet boundary is defined with an average static reference pressure of 0Pa. The side walls in the 2D model and additionally the bottom in the 3D model have 'no-slip' boundary conditions where velocity increases from zero at the wall surface, to the free stream velocity away from the surface. Zero 'specific shear' has been applied at the top boundary of the 3D model, representing the free surface of the water channel as suggested by ANSYS® Fluent Guidelines [81]. It is recommended for fluid-gas interfaces (i.e. free surface). A 'no-slip' condition has also been used on the bluff body boundary.

Usually the convergence of a CFD-simulation can be assessed via three criteria. The first criterion is set by the magnitude of the residuals of the properties solved by the equations of the turbulence model, most commonly, velocity, continuity (conservation of mass), momentum and kinetic energy. The residual is one of the most fundamental measures of an iterative solution's convergence, as it directly quantifies the error in the solution of the system of equations. In a CFD analysis, the residual measures the local imbalance of a conserved variable in each control volume. Therefore, every cell in the model will have its own residual value for each of the equations being solved. In an iterative numerical solution, the residual will never be exactly zero [124]. However, the lower the residual value, the more numerically accurate the solution is considered to be. It is very important to use the correct residual levels, and it depends on the physics and the whole computational problem that will be simulated. Low residual levels can lead to loosely

converged solutions giving results far from that expected, but at the same time, tightly converged solutions can give a non-physical solution to the problem.

In this project, the value of the residuals are set to be converged at the value of 10^{-3} , as recommended by Fluent for this kind of simulation [81]. This is a guarantee that the converged values of the flow properties will be at least of the order of 10^{-4} , since the solver targets the next lower power as the converged magnitude.

The second criterion is the number of iterations per time step. This criterion ensures that the simulation will not go into an infinite loop in case the solution diverges or if the solution converges slowly. In this project, 300 iterations have been allocated per time step, however due to the good quality of elements and design of the mesh, the time steps have been converging before the end of the 300 iterations.

It should be emphasised that convergence is not guaranteed by solely monitoring the residuals. A low residual does not always mean that the solution is converged, but it does give confidence to the model, alongside very useful information regarding the mesh quality during the model design. That leads to the third criterion which is to compare the answer of the simulation with other similar work or reference values.

In this project, the drag coefficient and the shed frequency are the quantities under investigation. They will be compared with the results of other experimental and computational work. This of course will premise that mesh convergence is achieved. More detailed discussion of the can found in section 5.4.2.1.

5.3 Computational Domain

The computational domain and the planar boundary conditions for the simulation of the flow are shown in Figure 46. The rectangular domain represents the Armfield water channel and the circle represents the bluff body, positioned as described in section 3.1.1.

Step by step guide on how the geometry has been created will not be included in this report since many detailed examples can be found online. The only step worth noting is that after the surface body representing the bluff body was designed, the surface body for the outer boundary was designed as a "frozen body", so that it doesn't merge with the first surface body. Furthermore, a Boolean operation was used to subtract the small surface (bluff body) body from the large surface body (fluid domain). In other words, the surface body of the outer surface has a hole where the bluff body is located.

It is well understood that the larger the computational model, the longer it takes to compute a solution. For this reason, the length of the domain has been cut down to 10.1m, compared to the actual length of the experimental water channel. The distance from the inlet to the location of the bluff body has been kept the same as the experimental work so they can be comparable. The distance from the bluff body to the outlet has been chosen to be 2.6 metres. This is enough distance to accommodate the length of the rope and flexible cylinder, to observe any shed vortices, as well as to avoid having any reversed flow from the outlet. Reversed flow can occur when pressure gradients due to geometry, mean that the flow wants to re-enter the domain at the location where the outlet has been placed. Reversed flow can have an effect on mass-conservation and thus convergence. It is highly recommended that it be minimized or eliminated. Preliminary, shorter versions of the model with low quality, unrefined mesh had “reverse flow” error, however, this been eliminated by allowing the 2.6m distance and increasing the quality of the mesh. Discussion regarding the mesh structure follows in the next section.

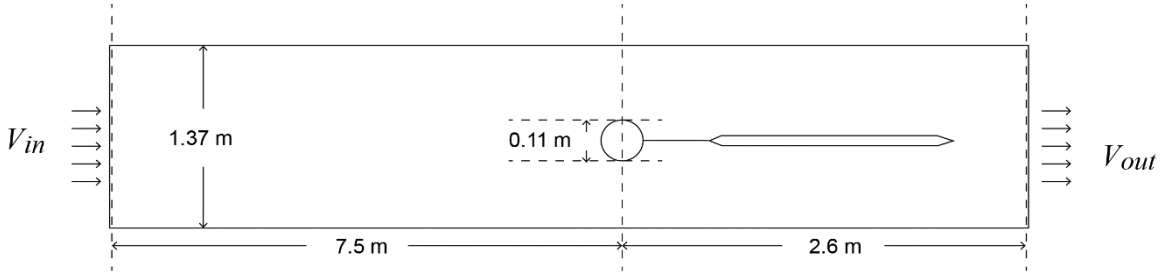

Figure 46. A sketch of the computational domain (not in scale).

5.4 Model Development and Assessment

This section describes the CFD work done to build a 3-D fully coupled fluid-structures interaction model with the goal to imitate the experimental environment, as described in chapter 4. The fluid environment has been divided into four areas of study. In each stage, the results obtained will be compared with theoretical and experimental results where applicable and conclusions drawn. This will assess the quality of the computational model at all four stages justifying any further utilisation of the computational model.

As shown in Figure 47 , the four stages are as follows: Stage 1, the average flow velocity enters the computational domain and the velocity profile begins to build up. Stage 2, the flow is shed from the bluff body, creating the vortices responsible for the excitation of the flexible cylinder further down the domain. At Stage 3, it is investigated whether the vortex field has been established and whether it is able to excite the flexible cylinder present downstream. At Stage 4, the flexible cylinder excitation takes places, where the amplitude of the flexible cylinder is obtained in relation to the input velocity. The amplitude is then used in the next chapter to predict the amount of power that could possibly be harvested using a piezoelectric device.

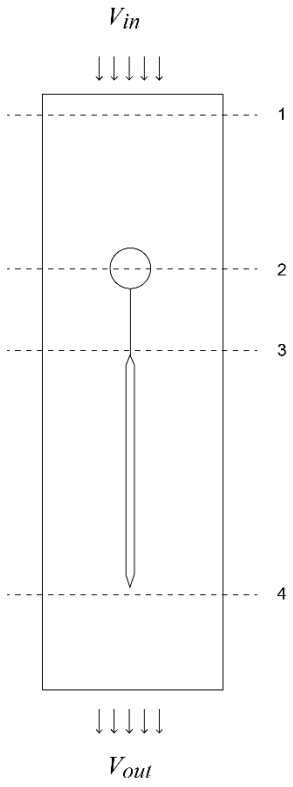

Figure 47. Flow stages in the computational domain (not in scale).

5.4.1 Stage 1: Velocity Profile Examination

The experimental environment, as detailed in Chapter 3, has a length of around 10m. That includes the distance from the water pump outlets up to a metre and a half further down from the tail of the flexible cylinder.

In chapter 2, section 2.3.2 a series of semi-empirical equations have been presented which are used to describe the vertical velocity profile of a fully developed flow in open channels. In chapter 4, section 4.4, a series of experiments have provided the main input parameter for these equations, the average velocity of the flow. In two locations across the channel, the average velocity has been measured and compared with a third location measurements using an Acoustic Doppler Velocimetry (ADV). The measured results have shown good correlation with the data acquired from the ADV.

This section aims to examine the channel flow development in the computational model. To achieve this, the velocity profile found using the semi-empirical Equation 16, as shown in Figure 43 is used as a reference point to compare the velocity profile extracted from the computational model, in two locations. The first location is at 7m, where Location #1 experimental measurements have taken place. The second location was chosen to be 45m downstream, where according to the calculations found in chapter 2, section 2.3.3, at that distance, the flow will be fully developed. At this stage, the bluff body and the flexible cylinder are not present. The water is expected to develop from the inlet and reach the outlet without any obstacles in between. The observations are discussed and quantitative conclusions are drawn regarding the model's ability to create the correct flow downstream, over time.

5.4.1.1 Computational Velocity Profile Examination

Figure 48 depicts three velocity profile cases. The purple line represents the velocity profile of a fully developed flow, created using the 'simple dip-modified log-wake' law. The average input velocity is 0.453m/s, as found from the experiments. The orange line shows the velocity profile of underdeveloped flow taken from the computational model, at a location 7m in the channel. The green line is the velocity profile extracted from the computational model at a channel length of 45m, representing a fully developed flow.

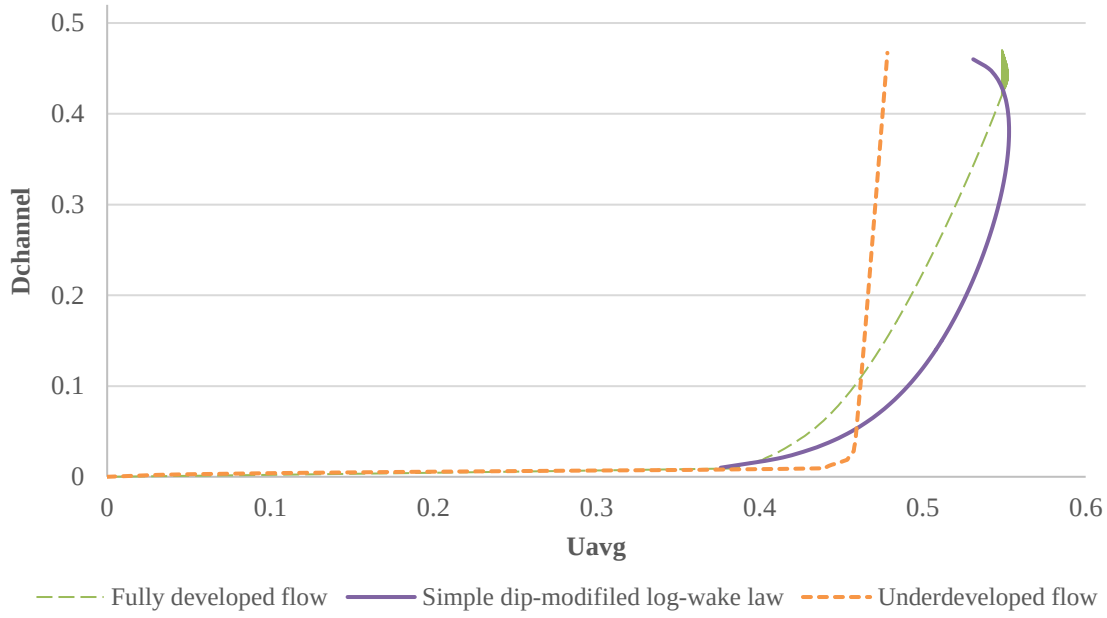

Figure 48. Comparison of vertical velocity profile models.

As it can be observed, the two computational profiles have certain differences when it comes to the shape of the curve. As discussed in chapter 2, section 2.3.2.3, due to the limitations of the experimental environment, it is not possible to undertake the experiments in a fully developed flow. Also, as the flow moves within the experimental region, the velocity profile changes, so that in Location #1 (7m) will be different from the one in Location #2 (10m) or in a location further downstream until it reaches the fully developed state. For that reason, the two fully developed velocity profiles will be compared with each other, the green and purple, as show in Figure 48 and the underdeveloped (orange) will be compared with the data found in Location #1.

For the computational model, from a range of 1200 velocity data, the coefficient of variation found to be 12.35%. Due to the high deviation percentage, it has been decided to

take into consideration only any velocity data falling within the outer region of the flow velocity. The coefficient of variation has dramatically changed to 5.59%. The maximum recorded velocity is 0.552m/s and the minimum 0.456m/s. In chapter 2, Equation 13 has been presented which gives the possibility of calculating the maximum velocity of the flow. At an input velocity of 0.453m/s, the maximum velocity is found to be 0.531m/s. Comparing the computational and theoretical values, there is a reasonable match indicating the computational value to be reasonably accurate.

Moreover, observing the logarithmic shape of the two velocity profiles, there is some obvious difference. This could be due to the mesh density and the value of the parameter the computational model is using to solve the equations. As it has already been discussed, there is a large variation between the proposed constant numbers for the semi-empirical equations, which define the logarithmic shape of the velocity profile. It is worth noting the difference in the dip-phenomenon. In the underdeveloped computational model this is not existent and in the fully developed model it is barely visible. This is because the turbulence model used is not able to solve correctly the boundary layer at the surface of the water channel. Since the surface of the channel is not computed, no dip-phenomenon should be visible.

Comparing the underdeveloped computational model with the measurements in Location #1, it is clear that there is some correlation. The computational model has given an average velocity of 0.463m/s, close to the 0.445m/s measured experimentally. Furthermore, the maximum velocity recorded in the computational model is 0.478m/s and the minimum 0.461m/s. Both values fall within the upper and lower velocity boundaries identified in chapter 4, section 4.4.

Finally, a qualitative comparison of the horizontal velocity profiles of the two computational cases is presented. Figure 49 shows the horizontal velocity profiles at 7m and 45m. The difference in the velocity profile development is clearly visible. Comparing with Figure 11, it can be seen that the developed and under developed profiles are similar. At 7m, the flow is underdeveloped, therefore the plateau of the profile is expected to be more flat, compared to that at 45m, where it is more parabolic since it is fully developed.

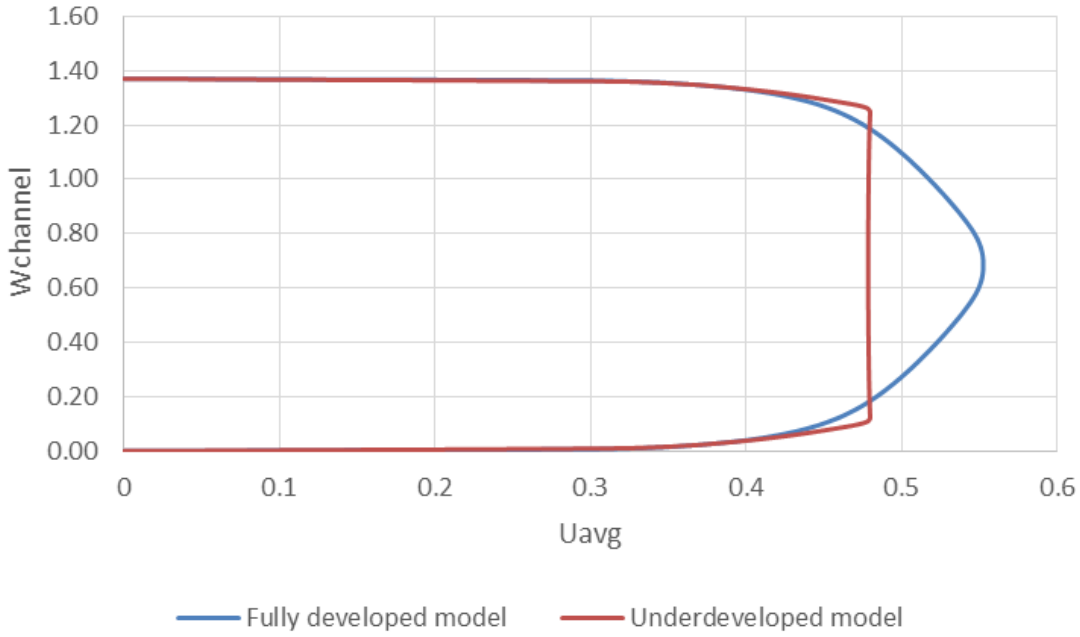

Figure 49. Horizontal velocity profile of developed and underdeveloped flow.

Overall, it has been shown that the velocity profile is developing over the flow domain, during the transient simulation. The discrepancies between the velocity profiles are expected. Firstly, in order to accurately compute the boundary layer near the walls of the water channel, a more dense mesh is required with the appropriate y^+value. Furthermore, since the velocity profile extends throughout the width and height of the mesh, the mesh should consist of significantly more elements in order to allow proper computation of the flow conditions. Similarly, the surface of the channel should have been properly resolved, for example using Volume of Fluid (VOF) method, usually used to compute the free surface.

Having a more accurate velocity profile development, would not add significant value in the current research as the purpose is to fully couple the bluff body with an inanimate object tethered behind, and create a viable design tool that can give results in a reasonable time. However, differences at this stage could manifest themselves later downstream and an understanding of the difference has been shown here.

5.4.1.2 Conclusion

The vertical and horizontal velocity profiles have shown that the velocity profile is developing over the length of the fluid domain. Understandably, the computational graphs do not fitting well with the semi-empirical graphs. This is most probably due to the mesh quality and the y^+ value of the fluid domain over the investigated length. As it will be explained on a later stage, to achieve accurate results, it is important the amount of cells near the walls to be sufficient in order for the turbulence model to resolve the boundary layer. Since there is no mesh refinement at all in the domain except around the bluff body, it is expected that the velocity profile will include a certain amount of deviation in comparison with the one given by the semi-empirical equations. Also, it is known that the semi-empirical equations already have a deviation from the experimental data when they were first developed. The equations give an approximation and do not fit perfectly the velocity profile. This only introduces even more uncertainty compared to the computational one.

In general, this project is focusing on developing the mesh around the bluff body in order to achieve the best possible excitation of the flexible cylinder. Therefore, no mesh refinement work will be undertaken on the fluid domain representing the water channel, but only in the area around the bluff body and the flexible cylinder. Any refinement on the walls of a 10.1m mesh will increase the amount of elements by tens of millions and will increase the computational time tremendously.

Overall, in stage 1, it has been shown qualitatively that the computational model of the water channel can create a velocity profile, which over time, should give a response close to that observed in the experimental apparatus. The velocity profile is developed over time as it moves downstream and will reach the second area of study in the system domain, Stage 2.

5.4.2 Stage 2: Presence of Bluff Body in the Field

In Stage 2, the development of the shed vortices is studied. It is important to ensure that the vortex is developed and shed correctly from the bluff body which in turn will excite the flexible cylinder at a distance of $2D_{bb}$ downstream.

Initially, a two-dimensional model has been created. This has greatly contributed to the understanding of mesh design; to use the right type of mesh, first layer thickness, turbulence model, convergence criteria, etc. This is where most of the mesh development and design has taken place. Expected flow phenomena identified over time during the simulation have given confidence in the quality of the model. The data of lift coefficient over time around the bluff body have been extracted and then, using Fast Fourier Transformation (FFT), a periodogram of the shed frequency has been presented. The results found are compared and discussed with those of other computational and experimental work, where it has been concluded that they are very satisfactory.

The final two-dimensional model has been extruded into a three-dimensional case where another mesh independence test has taken place in order to meet the three – dimensional model mesh requirements. Similar to the two-dimensional model, the shed frequency falls within the expected range. The drag coefficient is an under-prediction, however, as explained by published work of other author, this is a normal occurrence especially in three-dimensional models.

Overall, despite any limitations that might have been identified during the analysis, both two and three-dimensional models have given results that have enabled to proceed further with the research and create a fully coupled model, as it will be presented in a later stage. The goal of this research is not to create the most accurate computational model, but to create and assess a fully coupled model which can be used in the future to predict scenarios of different flow and geometric characteristics, as a design tool.

5.4.2.1 2D Modelling

This section describes the steps and work taken to design a two-dimensional model (Figure 50) which has served as the basis to create the three-dimensional model by extruding in the third axis. Essentially, it contains almost all the work done to create the three-dimensional model of the flow passing a cylinder in a water channel, representing the 2nd stage of the model development. The mesh design subsection describes how the first layer thickness has been calculated, an important value to fulfil the criterion $y^+ \approx 1$. This has reassured that the amount of cells near the bluff body wall are sufficient for the turbulence equations to resolve the boundary layer. As discussed in stage 1, the mesh will only be refined around the bluff body area to save computational time. The settings used in ANSYS® Fluent are discussed where necessary. Mesh independence for the 2D model has reassured that the quantities under investigation are not mesh dependant, allowing comparison with the experimental and computational work of other authors. The model is analysed qualitatively and quantitatively. Flow phenomena over a range of Reynolds numbers are identified and compared with the literature. The drag coefficient and shed frequency results are also assessed by comparing against experimental work from the literature as well as against the acceptable range identified in section 4.5.

Overall, it was possible to assess the model, draw qualitative and quantitative conclusions and to understand any limitations that might exist. The two-dimensional model has shown to produce reliable results and forms the basis of understanding, necessary to develop the three-dimensional model, as it will be discussed at a later stage.

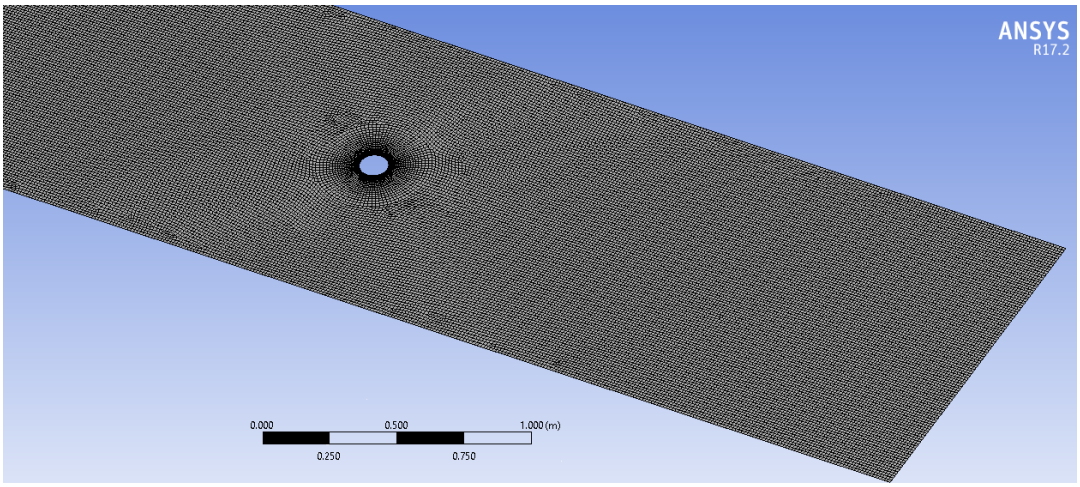

Figure 50. Screenshot of the two-dimensional model.

Mesh Design

In any CFD simulation, the design of the mesh plays an important role in the accuracy and physical representation of a fluid dynamics problem. The size and areas of varying density of elements can have a dramatic effect on both the results and computational effort. This section describes the decisions taken with respect to the design of the mesh in a systematic way. Section 5.4.2.1 describes the mesh independence study and contains further information on the final refined mesh.

The domain has been discretised into a finite number of elements in an unstructured grid. Unstructured grids do not have a direct mapping between where element data are stored in memory and how they connect in the physical space. Unlike structured CFD grids, the cell at location 'n' in memory may have no physical relation to the cell next to it at location 'n+1'. This means that an unstructured solver has to resolve where neighbouring cells are, but it allows for a lot of freedom in constructing a CFD grid. On the positive side, resolution can be added where it is needed and reduced wherever not necessary [125]. Therefore, using this meshing approach, it is possible to have a coarser mesh far upstream and downstream, regions of less importance to this project. It is expected that this will also serve as a positive during the restructuring and reconstruction of the dynamic mesh displacement, in the fully coupled model, improving convergence, at the expense of more computational memory and time.

When modelling the formation of vortices around a cylinder, it is desirable to have a high-cell density at the boundary layer. To achieve this, a structured O-type grid has been used around the bluff body. This is an acceptable and well implemented topology towards flow simulation past a cylinder [27] [126].

An O-type grid has lines of points where the nodes wrap around the object of interest, in this case the bluff body, and meets the first point, such that the grid lines look like the letter 'O' (Figure 52). As it will be presented in Table 17 at a later stage, preliminary work has shown that not only the number of elements around the body of interest, but also the mesh structure are important. The mesh has to follow its geometric shape in order to have accurate drag and lift coefficient. Thus the structured O-type grid around the circular bluff body.

Numerous numerical simulation studies investigating the flow around a body have shown that it is important to have enough elements to fulfil the requirement of the boundary layer around the body. This is directly related to the turbulence model used. Turbulence models like LES and SST k-ω as discussed in section 2.4 require higher numbers of mesh layers within the boundary layer thickness to resolve the wall functions. This is due to the low-Reynolds number that exists in the viscous sublayer. The term 'low-Re' is not to be confused with global Reynolds number, but indicates the low turbulent Reynolds number that exists in the viscous sublayer. Systematic numerical studies of flow over a cylinder for a range of Reynolds numbers between 40 and 10^6, have stated that in order to assure a high level of grid independence, a low-Re approach to meshing should be taken [27]. The y^+ value represents a non-dimensional distance of the first node from a no-slip wall. It links the node distance to shear stress by non-dimensionalsing the value with the fluid properties; density and viscosity. In order to utilise low-Re boundary properties, it is generally accepted that the mesh must achieve first layer thickness equivalent to $y^+ < 1$ for most solvers and turbulence models [127] [128]. However, a study of hull forms in comparably high Reynolds marine flow, concluded that a mesh of $y^+ < 2$ with at least five cells in the boundary layer was sufficient for accurate solution of a number of two-equation turbulence models [129]. In this project, SST k-ω model is used which is a two-equation model [130].

To achieve a mesh within the constraints identified, it is necessary to have a circular mesh around the bluff body, as well as to have sufficient amount of mesh layers to resolve the boundary layer. The process of identifying the appropriate value for the first layer thickness is straight forward and has already been used in the literature [27] [131]. In chapter 2, it has been shown that the law of the wall is represented by Equation 11. The latter can also be written in a non-dimensional form, including y^+ as shown below:

$$U^+ = \frac{1}{k}\ln(y^+) + B$$

Equation 29. y+ form of logarithmic law equation

Therefore, by comparing Equation 29 with Equation 11, $y^+ = \frac{y_h U_*}{\nu}$.

For $y^+ = 1$ as discussed above, the first layer thickness should be y_1=0.0000527m. Furthermore, according to the ANSYS® Turbulence modelling guide, it is important to have a minimum of 10 – 15 layers of cells across the inner region (viscous sublayer, buffer

layer, log-law region) of the velocity profile, to allow the turbulence model to resolve the viscous sublayer. Figure 51, shows a representation of the mesh structure required [81].

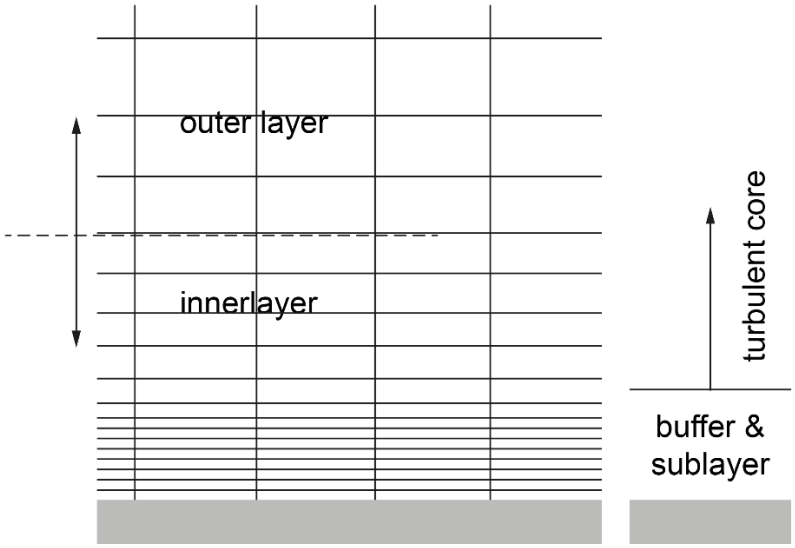

Figure 51. Mesh design requirements of inner region.

To have sufficient layers of cells within the inner region, it is required to choose the right cell growth rate when designing the mesh. A growth rate of 1.2, with 42 layers of inflation and an initial thickness of 0.0000527m, it will give 42 layers of cells within the inner region at a maximum height of $0.0929m$. As shown in Figure 9 in the literature review, the height of the inner region is approximately $0.094m$, therefore there are over 40 layers of cells within the inner region. Figure 52 below shows the O-type structured mesh with the 42 layers of inflation around the bluff body at a growth rate of 1.2.

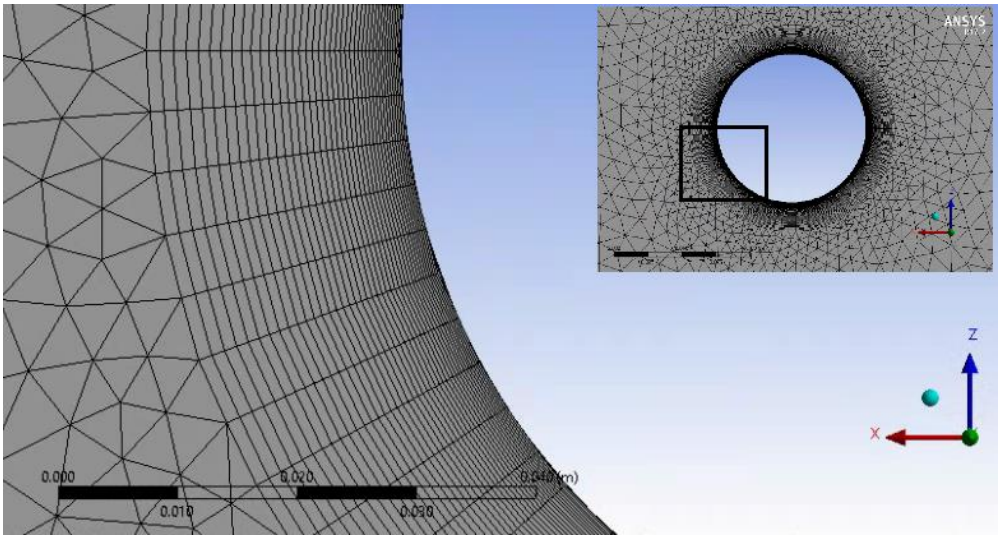

Figure 52. O-type mesh zoomed in on the cylinder boundary.

This method helps to use sufficient amount of elements but also to avoid using excessive computational time for the model. During the design, it has been observed that there were cases whereby decreasing the growth ratio or increasing the inflation layers, hundreds of thousands of additional elements were created. This resulted in over three million elements overall in some cases which in turn will result in excessive computational effort to find a solution.

Considering the representation of a circle in the mesh, the cylinder is effectively represented as a multi-sided polygon. Therefore, it is necessary to find the maximum angle at which the apparent distance between the line defined by a true circle and that of the polygon as defined by the mesh, does not affect the first layer thickness at $y^+ = 1$. This will ensure that the mesh is circular. The method described below was presented in [131] and has been used in the present research.

Geometrical consideration dictates that the maximum difference between a radial line following the surface and that made from polygons is given by,

$$\frac{\partial}{D_{bb}} = \frac{\theta^2}{16}$$

Equation 30. Maximum difference between circle and polygon.

Where ∂ *is* the difference between the circle and polygon in metres and θ is the angle between adjacent radial grid lines in radians [131].

The boundary layer thickness on a cylinder in cross flow as calculated numerically for a range of Reynolds numbers [27], is given by,

$$\frac{\partial u}{D_{bb}} \approx 1.5Re^{-0.625}$$

Equation 31. Boundary layer thickness approximation according to Stringer et al.

Where ∂u is the boundary layer thickness in metres. In this project, the boundary layer thickness is found to be 0.0001875m and as expected, a number larger than the first layer thickness since it represents a higher height.

The relationship between the normal distance from the cylinder's face $y^+$and Reynolds number is given from flat plate theory [27] as,

$$y_h = D_{bb} y^+ \sqrt{74} Re_L^{\frac{-13}{14}}$$

Equation 32. Normal distance relationship with y+ and Re.

Where Re_L is the 'low-Re' discussed previously. For the needs of these calculations, the 'low-Re' will be taken as $0.99U_{avg}$, the maximum velocity that occurs within the boundary layer, which will give the respective max 'low-Re'. The same approach has been used in other studies [27] [132]. Hence, to ensure that the apparent distance between the line defined by a true circle and that of the polygon, as defined by the mesh, does not exceed the boundary layer thickness, Equation 30 and Equation 31 are combined, giving,

$$\frac{\theta^2}{16} \leq 1.5 Re^{-0.625}$$

Equation 33. Relationship between Re and maximum mesh angle in circumferential direction for the boundary layer.

Therefore, the maximum angle value that can be used in order to make the requirement valid is $0.16\ rads$ or 9.48°.

Similarly, to find the apparent distance between the line defined by a true circle and that of the polygon, as defined by the mesh, does not exceed the first normal mesh cell distance corresponding to y^+=1, Equation 30 and Equation 32 are combined, giving,

$$\frac{\theta^2}{16} \leq 8.6 Re^{\frac{-13}{14}}$$

Equation 34. Relationship between Re and maximum mesh angle in circumferential direction for y+=1.

Therefore, the maximum angle value that can be used in order to make the requirement valid is 0.07rads or 4.37°.

In this project, because it is of interest to resolve the boundary layer, an angle of 4° has been chosen during the mesh design around the bluff body. Finally, to ensure that the mesh will be circular, some additional settings have been used in ANSYS® Mechanical. The 'On Curvature' size function has been used which examines the curvature on the edges and faces of the elements, and computes element sizes on these entities such that the size will not violate the maximum size or the curvature normal angle, which has already defined as 4°.

Solver Settings

The numerical solution of the flow is obtained using a commercial CFD code, ANSYS® Fluent 17.2. Discretization is done based on a finite volume approach, in a transient domain, pressure-based solver. The various CFD settings and options are summarised as follows.

A double precision solver has been used to increase the accuracy of the simulation due to the complexity of the unsteady flow modelling. This allows the software to use more RAM to execute the simulations.

The characteristics of the fluid have been set to match those from the experiments. A transient solver has been chosen to simulate the unsteady flow since it is in the interest of this project to see how the flow changes over time and allow for the Von Kármán vortex street to develop. Therefore, another parameter must be considered, the time step size. A smaller time step size allows shedding cycles to be captured and therefore a more accurate representation of the physical flow.

To maintain numerical stability, low Courant number is required and is the product of the average velocity and time step, over the minimum cell width of the mesh under consideration. In CFD simulation, a physical explanation of the Courant number could be that it describes how the fluid is moving through the computational cells. If the Courant number is <=1 fluid particles move from one cell to another within one time step (at most). If it is >1 fluid particles moves through two or more cells at each time step and this can affect convergence negatively. The Courant number was initially estimated at 0.775 using the minimum cell size of the two-dimensional, mesh independent model, at 0.01s time step. Both have been kept constant at all models, two and three-dimensional. From some preliminary work and previous experience, it has been shown that a time step of 0.01s would serve well the needs of the project. This has also been proven correct when investigating the fully coupled model, where a time step of 0.02s wasn't leading to convergence, it was considered to be too large for the mesh displacement and restructuring.

For the solution of the problem, a second order discretization has been selected which refers to the convective terms in the equations; the discretization of the viscous terms is always second-order accurate in ANSYS® Fluent. Second-order discretization generally yields better accuracy whilst first-order discretization yields more robust convergence. In

general, if the second-order scheme doesn't converge, the initial iterations can be started with the first-order scheme and then switch to the second-order scheme. There was no problem in this model, no recommendation for improvements were given by ANSYS® Fluent. SST k-ω turbulence model has been used to perform the mesh independence study and 'Coupling' method for the Pressure-Velocity coupling, as already discussed in section 2.4. The most important ANSYS® Fluent analysis settings are summarised in Table 16 below:

	Solution Setup	**Configuration**
General	Simulation type	2D
	Solver	Double precision, 8-core parallel processing
	Solver type	Pressure-Based
	Time	Transient
	Materials	Water density & viscosity
Boundary Conditions	Inlet	Velocity inlet – 0.453m/s
	Outlet	Pressure outlet
	Bluff body	No-slip wall
	Side walls	No-slip wall
Solution	Pressure-velocity coupling	Coupled
	Gradient	Least Squares Cell Based
	Pressure	Second Order
	Momentum	Second Order Upwind
	Monitors	Drag & Lift coefficients
Run Calculation	Time step size	0.01s
	Number of time steps	Min: 41000, Max: 80000
	Max iterations per time step	300 (convergence at every time step)
Computer Specifications	Processor	AMD FX-8350 Eight-Core Processor
	RAM	32GB DDR-3
	System type	64-bit processor and OS.
	Hard Drive	250GB SSD

Table 16. Final 2D model ANSYS® Fluent settings.

Mesh Independence Study

Grid independency is considered to be achieved when the solution is not affected anymore by the size of the grid. This project is interested in exciting the flexible cylinder behind the bluff body in relation to the shed frequency. Therefore, the drag coefficient and the shed frequency have been taken as the deciding parameters while performing the mesh independence study.

Before the mesh independence study, the quality of the mesh has been evaluated using some criteria given by ANSYS® Fluent. The first is skewness, which evaluated a face or cell and how close it is to being ideal. It is expressed by values in the range of 0 – 1. Highly skewed faces and cells are unacceptable because the equations being solved assume that the cells are relatively equilateral/equiangular. Therefore, the closer to zero, the better the mesh quality.

The second criterion is the element quality. This is expressed by a value in the range of 0 – 1. A value of one indicates a perfect cube or square whilst a value of zero indicates that the element has a high aspect ratio. Therefore, the closer to one, the better the element quality.

In order to improve the initial quality of mesh elements, 'Relevance and Relevance Centre' sizing tools have been used from ANSYS®. These settings apply global refinement or coarsening of the mesh as explained in ANSYS® Global Mesh Controls Guide, shown in Figure 53 [127]. The higher the relevance and the relevance centre, the denser the mesh becomes. This has allowed having a better overall control on the element quality.

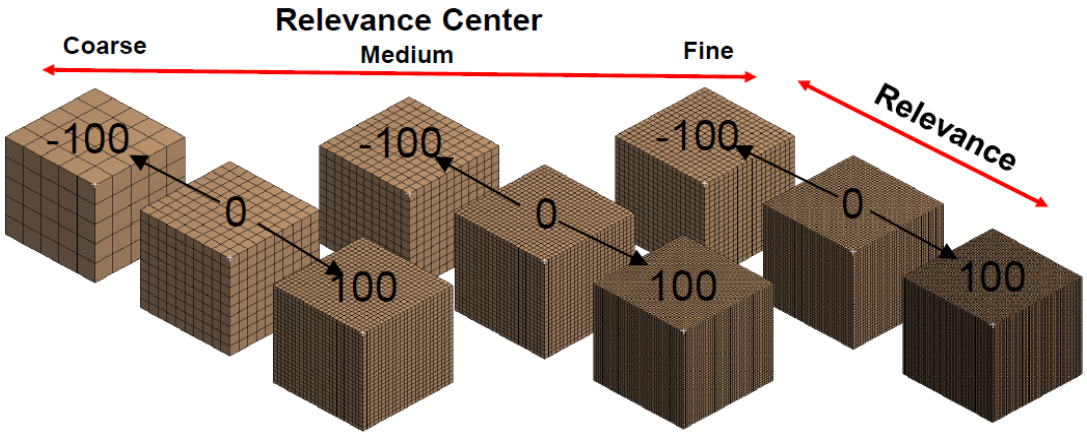

Figure 53. 'Relevance and Relevance Centre' sizing tools for mesh refinement (adapted from [127]).

The models under study have a "Fine" Relevance Centre with zero relevance value. The settings have been chosen such that the mesh is of a high quality and at the same time the number of elements will not dramatically increase, allowing mesh density variation whilst obtaining results within a reasonable time. The mesh design has skewness of 0.026 and element quality of 0.951, both of which are classified as excellent in the ANSYS® Mesh Controls Guide.

Having established that the mesh design has given a domain with high quality elements, a mesh independence study has taken place with an input velocity of $0.453\,m/s$ with a Reynolds number of 5.14×10^4. SST k-ω turbulent model has been used. Table 17 shows the models under investigation. For each model, the Strouhal number, shed frequency and drag coefficient are presented and compared with the respective value of the previous, coarser model. As already discussed, mesh independence will be achieved when the drag coefficient (C_D) and shed frequency (f_{shed}) will not be affected by the size of the mesh. The values presented for drag coefficient are obtained when steady state is reached. Fast Fourier Transformation is used to analyse the lift coefficient values per time step and obtain the frequency of oscillation for each model.

Model #	**Elements #**	**Shed Frequency (Hz)**	**Frequency difference (%)**	**Strouhal number**	C_D	**Cd difference (%)**
1	2283	0.463	-	0.1033	0.343	-
2	12533	0.903	95.03%	0.2014	1.043	204.08
3	19313	0.903	0	0.2014	1.047	0.38
4	26005	0.903	0	0.2014	1.050	0.28
5	38398	0.927	2.65%	0.2068	1.050	0
6	64393	0.927	0	0.2068	1.050	0
7	89907	0.927	0	0.2068	1.050	0
8	140779	0.952	2.69	0.2124	1.050	0
9	516296	1.025	7.66	0.2287	1.11	5.71
10	565123	1.025	0	0.2287	1.10	0.90
11	1788118	0.04	96.09	0.0089	0.76	30.90

Table 17. Mesh Independence study for the two – dimensional model.

Model#1 is the very first mesh created, without any refinement. The mesh is without inflation, unspecified first layer thickness and it does not follow an 'O-type' mesh. As expected the frequency value is well away from the expected range of 0.891 ± 0.055, as presented in section 4.5.

Model #2 represents the first mesh design, including the refinement steps as discussed in section 5.4.2.1. An increase of 448.97% of elements is observed, compared to Model #1. Both drag coefficient and shed frequency have increased, 204.08% and 95.03% respectively. Model #3 compared to Model #2, shows further element increase with further increase in drag coefficient. No change in the shed frequency value is observed, at three decimal places. However, since there is change in the drag coefficient, further refinement is required. Similarly, in Model #4, with more elements, mesh independence is observed in the frequency value, however there is slight change in the drag coefficient value, compared to Model #3. Further mesh refinement has taken place. Model #5 shows same drag coefficient as Model #4, however there is a change in the shed frequency by 2.65%. Model #6 shows that both shed frequency and drag coefficient become independent of the grid size, as no change of the two parameters has been observed. Similarly, Model #7 shows no change in the two parameters. Therefore, it is confirmed that the mesh independence has taken place at the element number of Model #5, 38398 with a shed frequency of 0.927Hz and a drag coefficient of 1.05. The shed frequency falls within the expected range. The drag coefficient is under-predicted by 12.5%, compared to the reference value of 1.2. Models #8,9,10 with further element increase, show changes at both shed frequency and drag coefficient values. Interestingly, Model #11 has failed to compute the flow phenomena as no oscillatory behaviour of the shed frequency and drag coefficient has been observed during the transient simulation, giving non-physical results, followed by a drop in shed frequency and drag coefficient. This is a good example showing that increase of mesh density does not necessarily lead to better results.

Figure 54, represents graphically the mesh independence study, on a logarithmic scale. Starting from the left, at low amount of elements and without any refinement, low values of drag coefficient and shed frequency are observed. With mesh refinement, both quantities increase. Mesh independence for drag coefficient is firstly achieved at 26005 elements up to 140779 elements where it then changes. For the shed frequency at 38398 elements up to 89907. Therefore, a model with element number between 38398 up to around 89907, will fulfil the requirements of this study for the two – dimensional model, as the values of

interest will be mesh independent. It could be possible to investigate further the number of elements between Model #3 - Model #4, and Model #7 - Model #8, to have a more precise element number and therefore to save some computational time, however, because the model is in two-dimensions, the time saved will be insignificant compared to the overall length of the simulation. On the other hand, for the three-dimensional model, smaller mesh element increments will take place since computational time is much higher and any simulation time decrease will really add value.

Achieving mesh independence in the two-dimensional model has given confidence in the overall mesh design as this will be extruded into the three-dimensional. This will also serve as the basis to proceed on the next section where analysis of flow phenomena, drag coefficient and shed frequency is taking place.

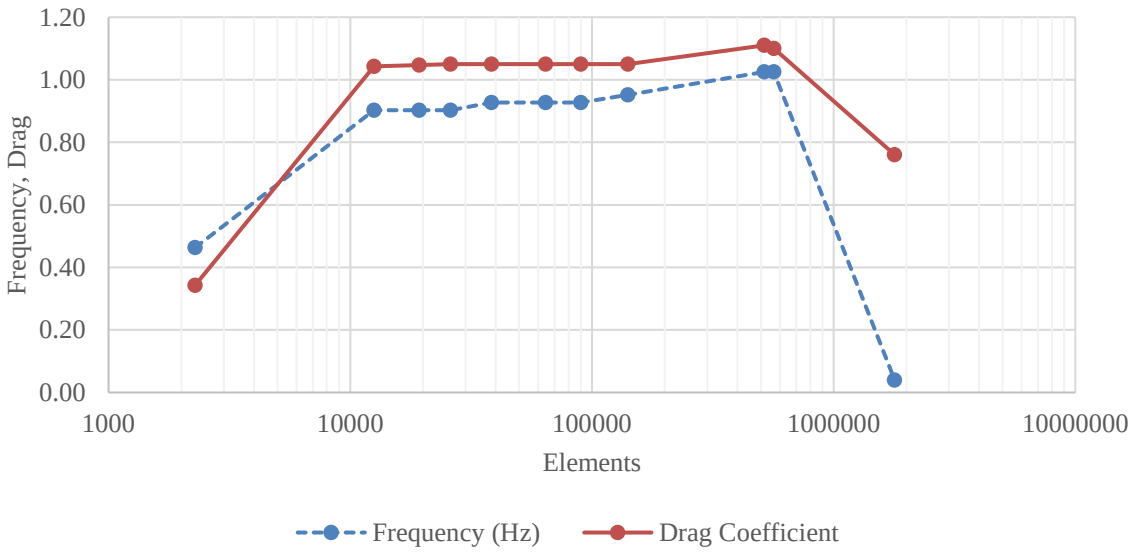

Figure 54. Mesh independence study for the two-dimensional model.

Model Analysis

The previous section has shown that it is possible to have drag coefficient and shed frequency values independent of the mesh density. With this in place, an overall investigation was undertaken with the prime goal of validating the computational model and understand any limitations that may exist. The analysis will firstly investigate the model and identify flow phenomena that occur during the transient simulation and then compare the simulation results to other studies and background literature. The model analysed was Model #5 from the mesh independence study, with 38398 elements as presented in Table 17.

In section 2.2.3, it has been shown that Reynolds number depends on the flow velocity, the diameter of the bluff body and the viscosity of the fluid. Since the viscosity and the diameter are considered fixed at this stage of the research, the only way to change the Reynolds number is to change the input velocity. Thus, to observe flow phenomena at different Reynolds numbers, it will require simulating numerous models at different input velocities, corresponding to the respective flow regimes of interest and run long enough until steady state is reached per simulation so that the phenomenon can be observed. This would also require changing the turbulence model to laminar which is a requirement for low Reynolds numbers, which in turn could possibly require to change other parameters within the model.

However, since a transient simulation is used, meaning the Reynolds number changes around the bluff body over time until it reaches the Reynolds number of the input velocity, all the flow phenomena should still occur, up to and including those occurring during the Reynolds number of the input velocity. Therefore, in an attempt to visually identify flow phenomena over different flow regimes, it was decided to observe the evolution of the Reynolds number with time using the mesh independent Model #5.

As it has been discussed in the literature review (Figure 2), for $40 < Re < 150$, the laminar vortex shedding will be formed behind the cylinder wall as the result of the instability of the region. Furthermore, the vortex street experiences the transition from laminar to turbulent flow and moves toward the cylinder wall as Reynolds number is increased in the range of $150 < Re < 300$. With further increase, the wake region behind

the cylinder wall becomes completely turbulent. The flow regime at this Reynolds number is described as the subcritical region ($150 < Re < 1.4 \times 10^5$).

Thus, several flow phenomena have been identified as part of the assessment of the model at different ranges of Reynolds numbers. In all Figures, the flow direction is from left to right.

Initially, 'Creeping flow' is observed, occurring at $Re < 5$. Figure 55 shows a flow with a very small Reynolds number as already presented in Figure 2(a), in the literature review. The velocity magnitude streamlines are symmetrical not only around the cylinder's upper to lower side, but also around its front to rear. As the Reynolds number increases, the front to rear symmetry disappears and the interval of the streamlines of the cylinder's rear flow widens [133]. Stagnation points (S) are visible at the correct location at $\theta = 0^{\circ}$ downstream of the bluff body and at $\theta = 180^{\circ}$ upstream, with $U_{avg} = 0\ m/s$. Fluid elements passing either above or below the cylinder increase their velocity magnitude (red colour). The velocity at both the top and bottom of the bluff body, near the wall, it is twice the free stream velocity. Velocity along the surface of the cylinder is in a tangential direction, i.e. parallel to the surface of the cylinder [134].

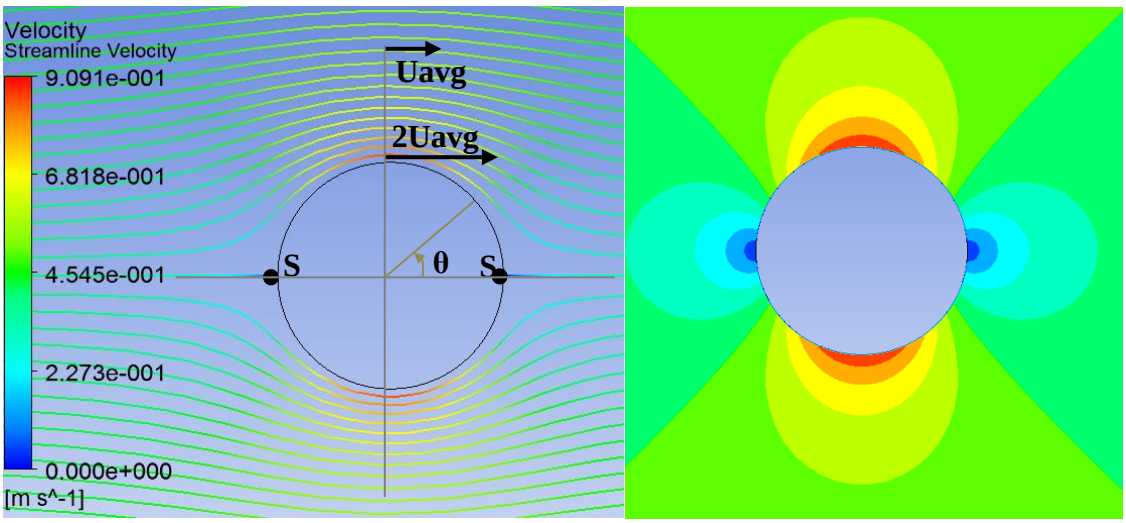

Figure 55. Creeping Flow, velocity magnitude streamlines (left) and velocity contour (right) with stagnation points.

Next, Figure 56 shows stagnant symmetrical vortices occurring at 5 < Re < 40, similar to Figure 2(b). A closed region of the streamline is generated within the cylinder's rear flow. The fluid in the upper half of this region rotates clockwise, and the fluid in the lower half rotates counter clockwise.

The separation points (Sp) are visible in Figure 56. This phenomenon occurs when the boundary layer peels away from the solid surface of the cylinder, as a result of an adverse pressure gradient opposing the flow along it. The angle of separation measures 53°, a very close measurement to various other experimental and numerical studies, where the angle was found to be between 51.2° - 53.6° [27] [135] [136] [137] [138].

Observing the pressure contour, the pressure distribution is as expected, compared to Figure 59, found in the literature. At low Reynolds numbers, the pressure distribution at the top, bottom and downstream the cylinder is negative and on a much higher distribution level compared to upstream where it is positive on a much smaller distribution level.

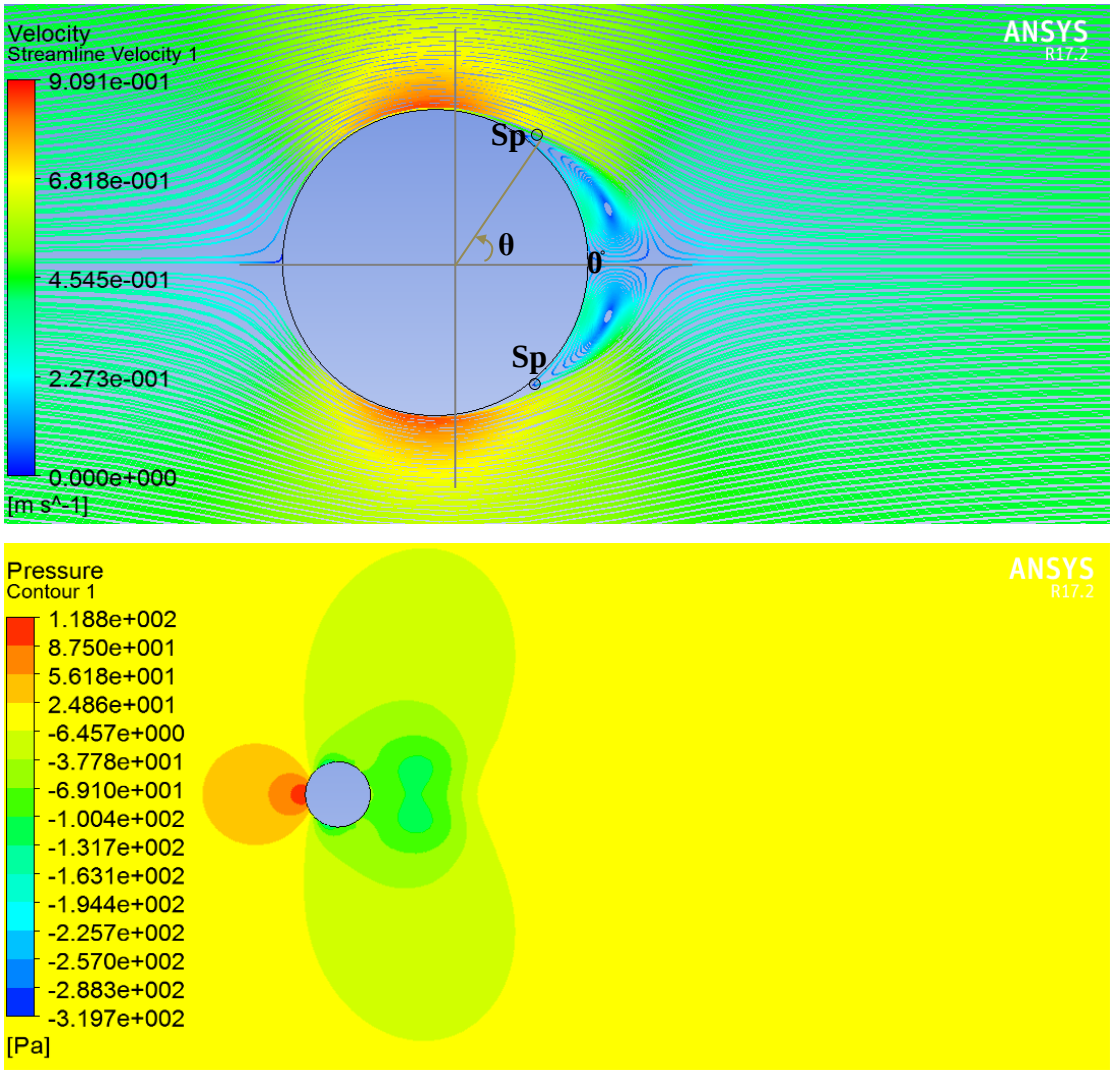

Figure 56. Velocity magnitude streamlines and pressure contour of stagnant symmetrical vortices at 5<Re<40.

As the Reynolds number increases, the length of the vortex increases. When the Reynolds number exceeds 40, the flow downstream becomes unstable as shown in Figure 2(c) in the

literature review and the vortex begins to oscillate in an up-down direction. The fully formed vortex is carried away on the surrounding main flow, and a vortex subsequently occurs on the other side. This vortex then expands before finally dissipating and departing the circular cylinder. In addition to this flow process, every pair of upper and lower vortices behind the cylinder is stored in an alternative regular array to form twin rows of vortices.

During the increase of Reynolds number an increase (measuring from downstream (0º - Figure 56) to upstream (180º - stagnation point) in the separation angle is taking place until it reaches an angle about 80° at Re ≈ 1.4×10^5 and the flow in the wake is becoming turbulent [134]. For higher Reynolds number, the angle drops in accordance to the pressure and drag coefficient drop, observed in the higher Reynolds number region referred to as 'critical' ($3 \times 10^5 < Re < 3.5 \times 10^6$). The reason for the decrease is that the boundary layer on the cylinder experiences a transition to turbulence at this Reynolds number and the separation point decreases from about 80° to about 50° and then to 40° when the boundary layer becomes turbulent.

Figure 57, clearly shows the increase of separation angle from 53° observed in Figure 56, to around 80°, when the Reynolds number is increased. A qualitative measurement of the angle has given a value of about 77.5º-78º. An approximation formula [139] found in the literature has given the value of 78.35º for Re ≈ 5.1404×10^4, reassuring the quality of the model.

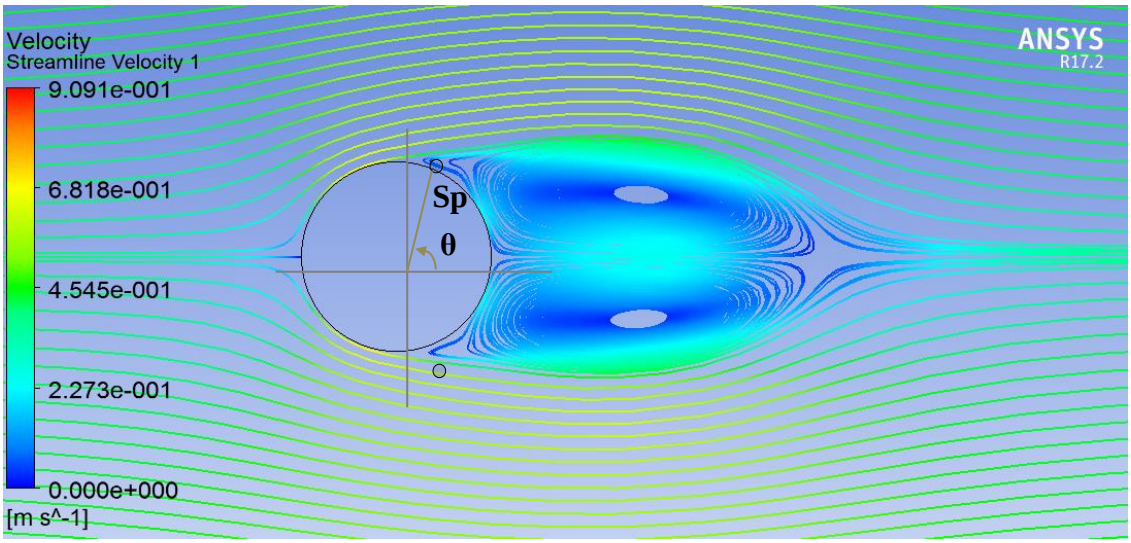

Figure 57. Separation angle increase and wake elongation with Reynolds increase.

While the flow approaching the circular cylinder is in a uniformly steady state (straight lines upstream the cylinder), a periodically varying flow characteristic of the Von Kármán

vortex street appears in the cylinder's rear flow. As the Reynolds number increases into the subcritical regime, the vortices are mixed together, and the flow behind the cylinder (wake) behaves very irregularly on both time and space scales. This is called the turbulent flow state. However, a free stream distant from the wake region maintains a steady state, and the streamlines are held in a regular and smooth shape. This phenomenon is known as laminar flow and are located upstream the cylinder, up to the flow separation points at the top and bottom of the cylinder, where the state of the flow changes to turbulent. The Von Kármán vortex street can be seen in Figure 58, a screenshot of velocity magnitude streamlines and pressure distribution at a Reynolds number of Re ≈ 5.1404 × 10^4, representing the transitional flow.

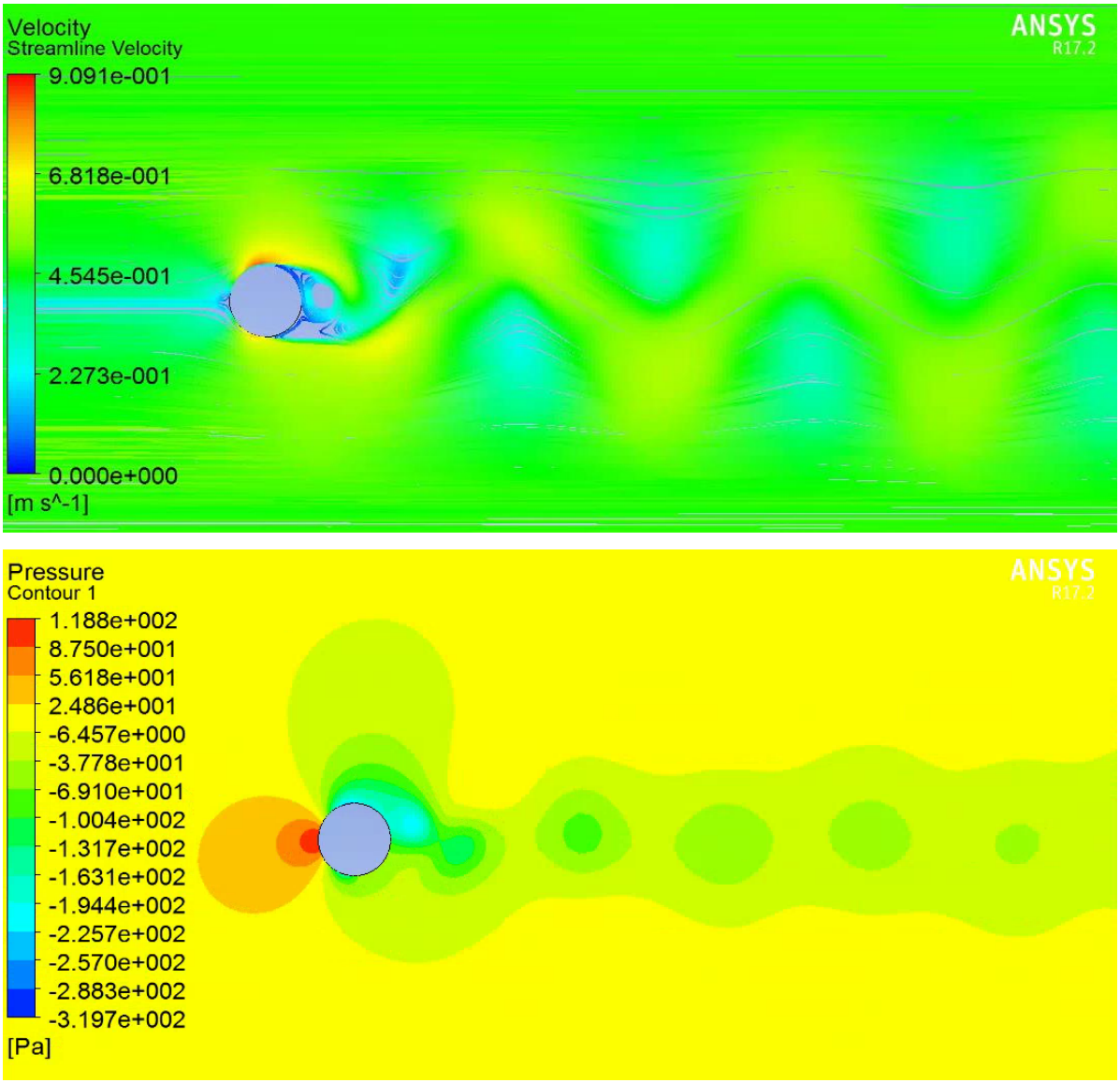

Figure 58. Velocity streamlines and pressure contour describing a Von Kármán vortex street at Re = 5.1404 x 10^4.

Observing the pressure contour in Figure 58, it can be observed that the pressure distribution at the top and bottom of the cylinder started to take the shape of the high Reynolds number pressure distribution, as seen in Figure 59. However, because the Reynolds number of this project is in the subcritical region, it is not considered high enough ($Re < 10^7$) to achieve the exact shape of pressure distribution as presented in Figure 59, however there is still a visible high distribution of negative pressure at the top and bottom and downstream of the cylinder compared to upstream of the cylinder.

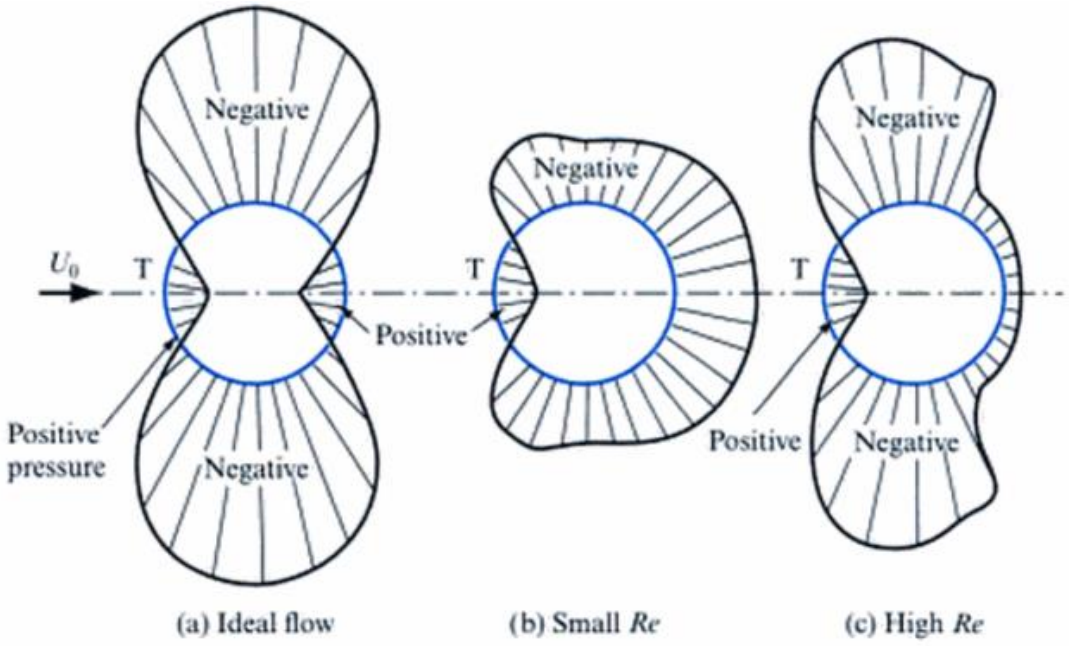

Figure 59. Pressure distribution around a cylinder (taken from [134]).

Up to this stage, it is clear that the numerical model gives a trend similar to that of the experimental data and what has been discussed in the literature. The turbulent flow separation is visible and the eddy currents can be clearly identified. One final analysis has taken place. Figure 60, shows the flow velocity contour at Reynolds number of $Re \approx 5.1404 \times 10^4$ on the 41st second of the simulation. The velocity contour gives a better visualisation of the already developed Von Kármán vortex street. Furthermore, the near walls velocity is zero as expected due to the no-slip condition. It is also clear that the distance between the walls and the bluff body is sufficiently wide so that the flow around the bluff body is not affected by the walls. This reassures that there is no interference in the area from any flow potentially leaving the walls of the channel and entering the recirculation area or any shed vortices come in contact with the walls.

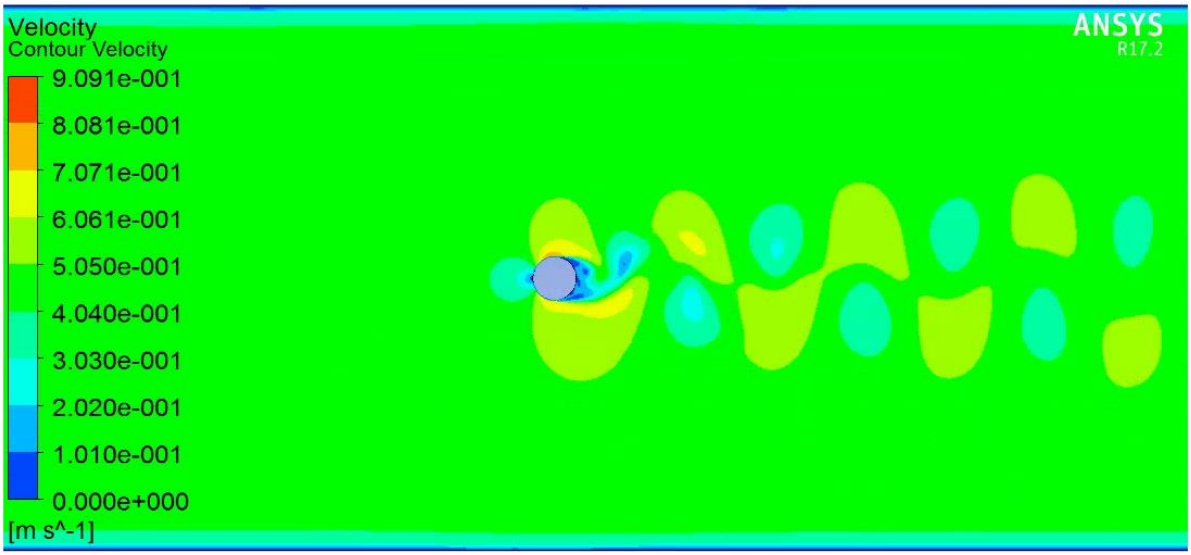

Figure 60. Velocity distribution near channel walls, bluff body and Von Kármán vortex street representation.

The model has indicated that it follows some expected behaviour over a range of Reynolds numbers. However, it is important to assess the parameters of interest acting on and around the bluff body, which in turn create shed vortices and excite the flexible cylinder downstream.

As already discussed, the primary parameter of interest of this project is the shed frequency. The vortices will shed from the bluff body and excite the flexible cylinder located $2D_{bb}$ downstream. The frequency is calculated based on the oscillating frequency of the lift coefficient. The time domain data of the lift coefficient are converted into frequency domain by using the Fast Fourier Transformation (FFT). The frequency of the lift coefficient f_{shed} is then substituted into Equation 2 to get the Strouhal number.

The author, in an attempt to identify which set of data should be used through the FFT, came across an interesting outcome. In some literature, the shed frequency or Strouhal number were found using data through FFT from the 0^{th} second of the simulation up to the limit set by the respective author [140] [26] [141]. That means the authors have used data outside the steady state of the oscillation and then compared with the accepted experimental data in the literature, used as reference values. In some other cases, the data used were free from the bias of the initial transients, meaning only data from the steady state of the oscillation have been used, and still compared with the same reference values [142] [143]. Furthermore, many authors do not give an indication on how they have calculated the drag coefficient. This brings into question the set of data used to find the

drag coefficient. Have they averaged only steady state data or have they also included data from outside the steady state?

It is unclear which method is the correct so that the results of this project are comparable with that in the literature. Therefore, the author has decided, in order to keep some consistency between the data analysed for drag coefficient and shed frequency in this work, solely data from the steady state of the computational simulations will be used. Additionally, the data acquired in this research during the experimental work were during the steady state of the flow. Therefore, in order for the computational data to be comparable with the experimental data acquired, steady state data of the computational work should be analysed. The results are presented in Table 18.

Turbulence models	**Pressure-Velocity Coupling Method**	**Residuals**	**f_{shed} (Hz)**	**St**	**C_d**
SST k-ω (2 equ.)	Coupled	10^{-3}	0.927	0.2068	1.05
SST k-ω (2 equ.)	SIMPLE	10^{-3}	1.025	0.228	1.135
Transition k-kl-ω (2 equ.)	Coupled	10^{-4}	0.854	0.190	1.4
Transition SST (4 equ.)	Coupled	10^{-4}	0.976	0.217	1.68

Table 18. 2D model investigation at different turbulence models.

For the mesh independence study, SST k-ω turbulent model was used. As it has already been presented in Table 17, the shed frequency is 0.927 Hz, and the mean drag coefficient 1.05. The frequency falls within the 0.891Hz ± 0.055 range, identified in section 4.5 as the expected theoretical shed frequency. The frequency magnitude data post Fast Fourier Transformation are presented in Figure 63. The frequency of 0.927Hz gives a Strouhal number of 0.2086, and consequently it falls within the expected Strouhal range. The value of 0.2 is considered in the literature as the reference Strouhal number for the current Reynolds number of 5.1404×10^4. The drag coefficient of 1.05 falls within the expected range of 1-1.2 as identified in section 4.5. There is a difference of 12.5% to the experimental approximated value of 1.2 usually used by other authors. However, as shown in Figure 61, the drag coefficient is a match with the experimental work of Achenbach, with a drag coefficient of 1.05, at a Reynolds number of 5.1404×10^4.

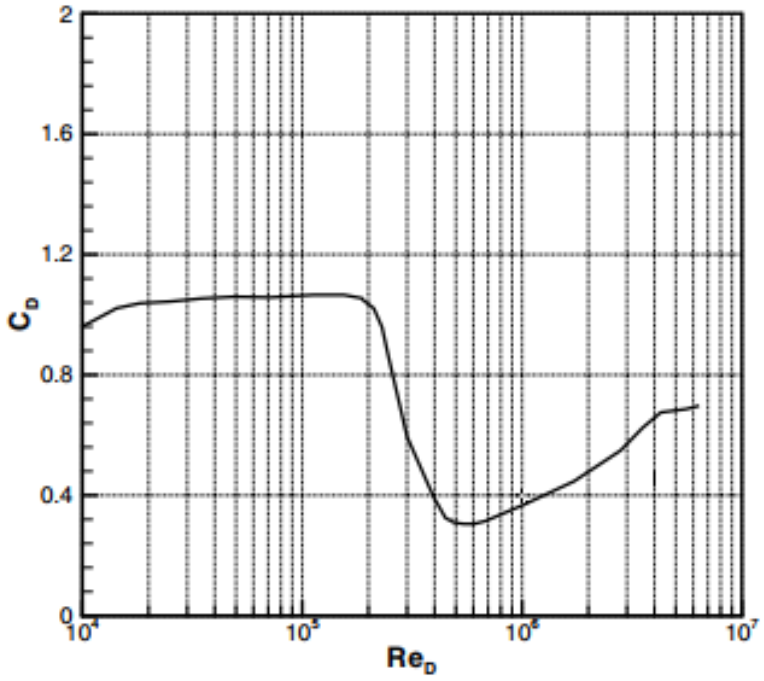

Figure 61. Drag coefficient data of Achenback as a function of Reynolds number (taken from [144]).

Figure 62 below, shows the shed frequency and drag coefficient oscillations.

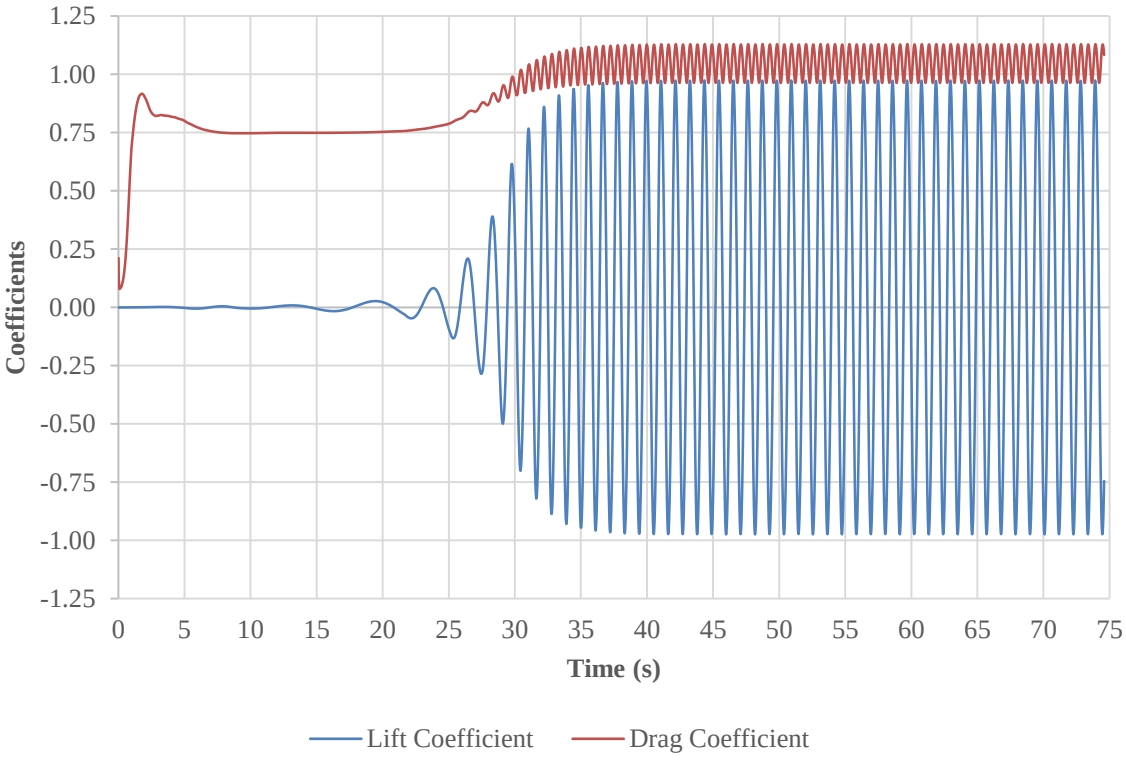

Figure 62. Lift and Drag Coefficients data for two-dimensional Model #5.

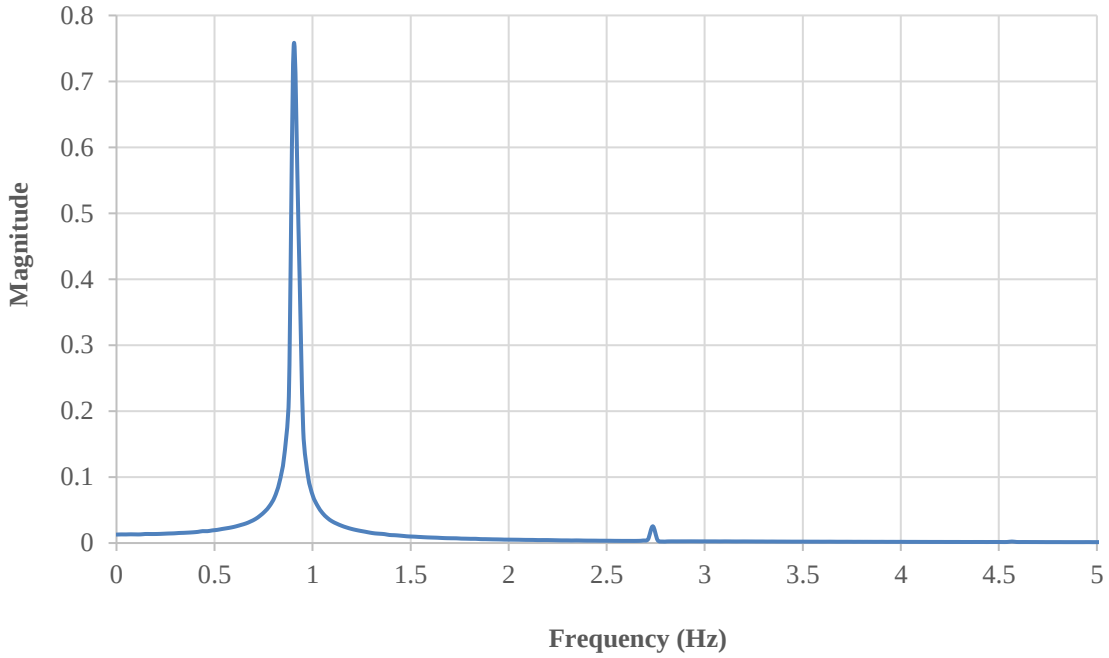

Figure 63. FFT screenshot of Lift Coefficient data for Model #5.

It is considered that changes in drag coefficient may be possible due to changes in modelling parameters. Among others, this could be possible by improving the mesh design, or increasing the amount of elements, or by changing the turbulent model. It is the author's opinion that the mesh design cannot get better due to the detailed design and mesh values used as described in section 5.4.2.1. Mesh independence has already taken place, therefore increasing the amount of elements should not change the results, only to increase the computational time and lead to a non-physical solution. Therefore, it has been decided to use two other turbulent models and a different velocity-pressure coupling method and observe the outcome.

Mesh independence has taken place for every case to have confidence in the results. No discussion will take place regarding the mesh independence study of the new turbulent models, as it is the same process and model design that has already been presented in section 5.4.2.1. Table 19 contains the mesh independence study data for every turbulent model at different mesh size. It was shown that with 38398 elements, all turbulent models show mesh independence at this mesh density. It is important to note that the purpose of using other turbulent models is to gain further understanding on the designed model. The aim is not to take a detailed analysis of different cases but simply to see how the results

behave under certain changes in order to obtain a broader understanding of the overall performance of the computational fluid dynamics modelling.

Turbulence models	**Pressure-Velocity Coupling Method**	**Residuals**	**Model #**	**Amount of Elements**	C_d	f_{shed}	**St**
SST k-ω (2 equ.)	SIMPLE	10^{-3}	1	12533	-	-	-
			2	19313	1.132	1.025	0.228
			3	26005	1.130	1.025	0.228
			4	38398	1.135	1.025	0.228
			5	64393	1.135	1.025	0.228
			6	140779	1.137	1.025	0.2287
Transition k-kl-ω (2 equ.)	Coupled	10^{-4}	1	12533	1.44	0.879	0.1961
			2	19313	1.42	0.854	0.190
			3	26005	1.40	0.854	0.190
			4	38398	1.40	0.854	0.190
			5	64393	1.34	0.854	0.190
			6	140779	1.35	0.854	0.190
Transition SST (4 equ.)	Coupled	10^{-4}	1	12533	1.66	0.976	0.217
			2	19313	-	-	-
			3	26005	1.66	0.976	0.217
			4	38398	1.68	0.976	0.217
			5	64393	1.68	0.976	0.217

Table 19. Additional turbulence models' mesh independence study for the 2D model.

Firstly, for velocity- pressure coupling, 'SIMPLE' has been used instead of 'Coupled', and the SST k-ω turbulent model. This has increased the value of drag coefficient as well as the shed frequency. A value of 1.13 has been obtained for drag coefficient, a 5.83% under-prediction from the reference value of 1.2. This is a closer approximation compared to the drag coefficient value of 1.05, obtained when using the 'Coupled' method. Conversely, the frequency increase falls outside the acceptable range of values, as the maximum accepted frequency is 0.946Hz. A shed frequency of 1.025Hz has been obtained. Interestingly, observing the mesh independence study, it is obvious that the model is less sensitive to mesh density change compare to the 'Coupled' algorithm. The exact reason behind is not in the interest for this research, however it is suspected that it is because the 'SIMPLE' uses a solution algorithm where the governing equations are solved sequentially (i.e.,

segregated from one another) compared to the 'Coupled', where they are solved simultaneously.

Next, the turbulent model has been changed from SST k-ω to transition k-kl-ω with 'Coupled' velocity-pressure method. The residuals convergence has been decreased by one order of magnitude, from 10^{-4} to 10^{-5}.

It can be seen that the application of the transition k-kl-ω turbulent model yields a good agreement with the reference values. The shed frequency is 0.854Hz and it falls within the range. It is a smaller value than the initial value of 0.879Hz, obtained when used the SST k-ω model with the 'Coupled' method. The drag coefficient value has increased significantly as the value of 1.35 has been obtained, however with a 12.5% over-prediction of the reference value of 1.2.

Finally, the transition SST turbulent model has been used where both shed frequency and drag coefficient have been over-predicted, with 0.976Hz and 1.66 respectively.

The results obtained from changing the turbulent model give noticeable differences. This might be caused by the limitations each model has when resolving the momentum, mass and energy equations that are transported by the large eddies in the turbulent flow. Work of other authors will be studied in order to identify whether the differences are an expected occurrence. Understandably, exact comparison with other published work cannot be done because usually is not possible to identify all and the precise settings used to calibrate the simulation software used by the other authors, which also vary a lot in the literature. Thus, it is not possible to have an identical model in that respect. For that reason, the overall design and response of the current model will be assessed by comparing the drag coefficient and Strouhal number values with the computational results of other studies against the reference values of drag coefficient and frequency or Strouhal number.

A very recent study has computed the flow around a circular cylinder for a wide range of Reynolds number, using two prominent commercial and open-source solvers. They stated in their published work that the drag coefficient results they obtained from ANSYS® CFX and OpenFOAM were clearly in agreement with the experimental data. In fact, OpenFOAM was giving values within 10% of the experimental data up to $Re = 10^4$ where the maximum error was approximately 15%. CFX was over-predicting the drag coefficient at Re values of 10^3 and 10^4 reaching maximum error around 30%, showing some recovery

in the critical region ($Re > 10^5$). In general, the majority of drag values were under-predicted by both solvers. They used the same turbulent model as this project, SST k-ω with 'coupled' velocity- pressure coupling method for CFX [27].

Strouhal number, in the laminar range, was captured by both solvers to an accuracy of $\pm 0.1\%$. At Re=1000 both solvers were within $\pm 9\%$ of the best fit of the experimental data. Above this point, the CFX simulations begun to shed vortices at steadily increasing rates, failing to predict the drop at intermediate Reynolds values. OpenFOAM provided matching of Strouhal number at $Re = 10^4$ [27]. Likewise, the model designed for the needs of this research, matched the Strouhal number with the one predicted.

Another study, which focused on viscous flow computations on smooth cylinders with a detailed numerical study with validation, used the same mesh design approach as that in the present research, as described in section 5.4.2.1. They compared their results against some recent experiments [145] as well as classic data from the mid-20th century [51] [146], partly presented in the literature review of this thesis. For a Reynolds number of 9.4×10^4, their computational model under-predicted drag coefficient by 28% and over-predicted Strouhal number by 24%. At Reynolds number of 5.5×10^5, they under-predicted drag coefficient by 100% and over-predict Strouhal by 16% [26]. The 12.5% difference in drag coefficient and the exact match in Strouhal number found in the present research, clearly provide a better approximation to the experimental reference values, compared to those in the literature.

The two and three-dimensional flow past a cylinder in different laminar flow regimes was studied in [140]. They focused on low Reynolds number ($0.1 < Re < 300$), however they have stated that their findings show excellent agreement with the experimental data used to validate their results. They under-predicted Strouhal number by 4% and over-predicted the amplitude and frequency of the oscillating force coefficients for two-dimensional simulation of flow at Re=300.

Numerous studies have tried to predict the flow characteristics past a circular cylinder, using different combinations of computational settings, turbulent models, aspect ratios, residual values etc. All of them have one common outcome. The exact prediction of the experimental values used as references is almost impossible, especially at Reynolds numbers greater than 10^4. A one-model-fits-all Reynolds number, precisely predicting the flow characteristics, does not appear to exist.

Comparing the magnitude of error of the drag coefficient and Strouhal number found in the present study, with the magnitude of error of the aforementioned studies, the author believes that the current model gives very satisfactory results. The mesh design is of a good quality overall, expected physical phenomena are present and the parameters of interest, drag coefficient and shed frequency, are of a good approximation.

Conclusion

Section 5.4.2.1 has a considerable role towards the development of an accurate three-dimensional model. A detailed mesh design has been presented, where all the necessary steps have been discussed in detail. A qualitative investigation of the two- dimensional model has shown that expected flow phenomena are visible and the parameters of interest, the drag coefficient and shed frequency, fall within the expected range and are of a very good approximation to the experimental data used as reference points by other authors in the literature. All the valuable information found while developing the two-dimensional model will be taken into consideration when investigating the three-dimensional model in the next section. SST k-ω turbulent model will be used and given that the results that will be found for the three-dimensional model fall within 12.5% of the reference value of 1.2, they will be considered as acceptable solutions and no other turbulent models will be investigated. It is important to remember that the goal of this research is not to find the most suitable turbulent model and create the most accurate computational model. It is to show that a fully coupled three-dimensional computational model can be developed, where a flexible cylinder behind a bluff can be excited due to the vortices shed from the bluff body, over time. The latter can be used in the future as a design tool in order to predict scenarios of different flow and geometric characteristics.

5.4.2.2 3D Modelling

In the previous section, the design of the computational model has been presented followed by a series of flow phenomena identifications during the transient simulation. The mean drag coefficient and shed frequency were compared against reference values and work of other authors. The results have been very satisfactory and therefore Model #5, presented in Table 17 has been chosen as the basis of the three-dimensional model.

The three-dimensional model has been created by using the 'extrusion' method on the chosen model. This has given an initial 3D model which in turn has been used to undertake a mesh independence study. As it has already been discussed, before proceeding to acquire any results, it is important for the results to be mesh independent, therefore, mesh independence study is presented and discussed in the next section.

In general, the mesh design has been kept the same as it was when first designed in 2D, presented in section 5.4.2.1. Similarly, the solver settings have been kept the same, as already discussed in section 5.4.2.1. No further discussion will take place on these areas.

Figure 64 below shows the three-dimensional model with the bluff body.

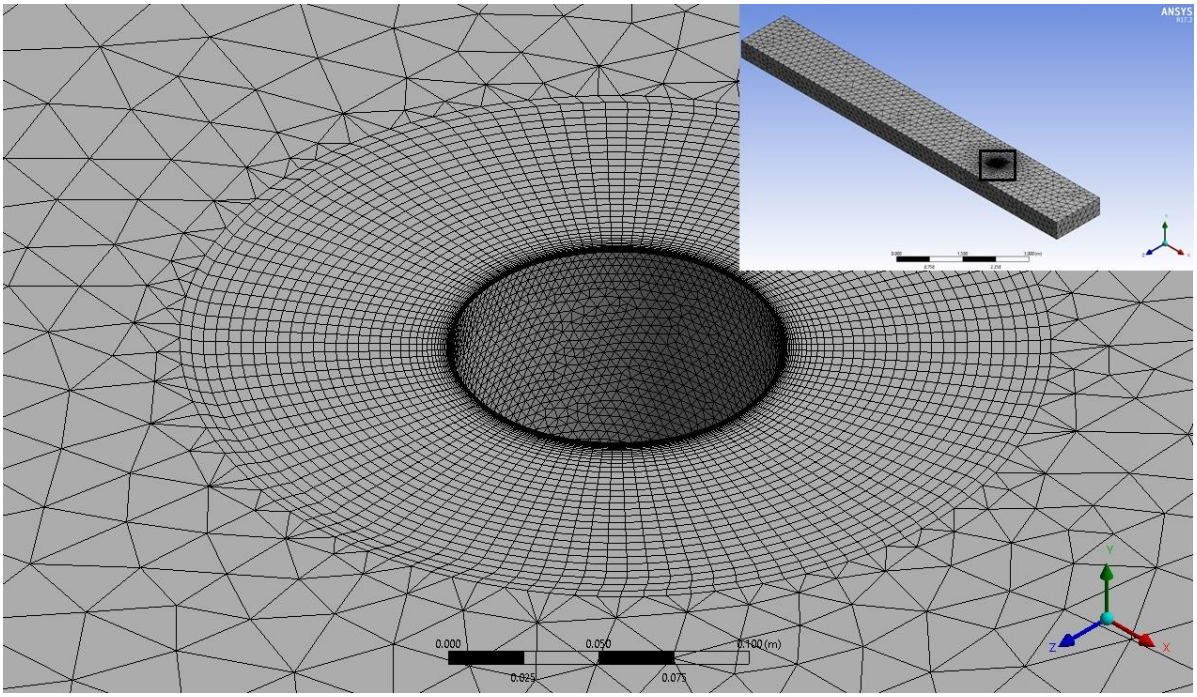

Figure 64. Three-dimensional model of the fluid domain with the bluff body. Flow direction, top left to right.

Mesh Independence Study

As already discussed during the mesh independence study of the two-dimensional model, the prime objective is to determine when the coarseness of the mesh does not influence the solution of the simulation. Keeping the number of cells low reduces the calculation time, a very important factor when it comes to three-dimensional simulation as it requires an excessive amount of computational power and memory.

The mesh quality tools within ANSYS® Fluent have been used before executing the mesh comparison. The 'mesh check' option provides statistics regarding the volume and face area of the mesh cells. Also, any warnings related to mesh quality will appear. The most common error for a three-dimensional mesh is to have "negative volume cells". It means that the elements within the mesh are heavily distorted, large enough to make some vertex, or edges, to penetrate an opposite face resulting in a negative volume. A negative volume will generate unphysical behaviour of equations and most of the times the simulation will not converge and eventually will force the simulation to stop. Since the skewness and the elements are of a high quality and the model has a very good mesh design, no errors have been reported by the software.

The mesh independence study has been performed with an input velocity of 0.453m/s at a Reynolds number of 5.14×10^4. The SST k-ω turbulence model has been used. For each model, the Strouhal number, shed frequency and drag coefficient are presented. Similar to the two-dimensional model, data before the oscillation reaches a steady state will not be taken into consideration, for both drag coefficient and shed frequency. It has been observed by the author that when the FFT is done using the whole range of data, starting from t=0, there is a noticeable change in the parameters of interest. On the other hand, when overlapping segments of data are taken within the steady state only, the change in frequency is marginal. This has given confidence that the frequencies presented later for mesh independence are correct and not biased from the initial transients. To identify the beginning of the steady state, the drag coefficient graph has been observed in the three-dimensional model, instead of the lift coefficient graph, as presented in the two-dimensional model. Being a three- dimensional model, the lift coefficient shows an oscillatory behaviour at a very early stage, compared to the two-dimensional model. As already discussed, it is important to include data only from the steady state, as that is when

the Von Kármán vortices start to shed at a steady frequency. Thus, the drag coefficient graph is observed to identify an approximate time where the steady state begins.

Table 20, presents the meshes created for the needs of this research. Model #0 is the first 3D model created by extruding the two-dimensional Model #5. It has given a frequency outside the expected range and drag coefficient values much lower compared to the 2D model. The introduction of the three-dimensional effects of the flow are already noticeable. Model #0 has given a drag coefficient of 0.766 and a shed frequency of 0.512Hz. Given the very low values, it has been decided to decrease the convergence tolerance by one order of magnitude, from 10^{-3} to 10^{-4} for all the three-dimensional models. The same approach is observed in other studies too, unless the same order magnitude has been used from the beginning of their work [27] [142] [26]. In other work undertaken at low Reynolds numbers (Re<300), 10^{-6} has been used [140]. The author believes that for the Reynolds number of this research, as well as taking into consideration that this is a preliminary design of a dynamic fully coupled model, the convergence criterion smaller than 10^{-5} should be avoided. Problems with mesh deformation and restructuring are likely to occur between the fluid dynamics and the mechanical solver at lower magnitudes of the convergence criterion.

Model #	**Elements #**	**Frequency (Hz)**	**Strouhal number**	C_D
0	1125254	0.512	0.1142	0.766
1	793236	0.952	0.2124	0.950
2	560270	0.952	0.2124	0.921
3	406100	0.805	0.1796	0.850
4	1181467	0.854	0.1905	0.820

Table 20. Mesh independence study for the three-dimensional model.

Starting the mesh independence study, Model #1 has 793236 elements. The shed frequency has been found to be 0.952Hz and the drag coefficient 0.950. With a decrease of 29.36% in elements, Model #2 has given a drag coefficient of 0.921 and a shed frequency of 0.952Hz. No change in the shed frequency has been observed. With further element decrease, Model #3 has given a shed frequency of 0.805Hz and a drag coefficient of 0.850. The number of elements in Model #1 have been increased by 32.86%, creating Model #4. A significant drop in shed frequency and drag coefficient has been observed. This can

possibly indicate that no further increase in elements is possible, as the solution might have begun to diverge. However, this cannot be conclusive since the simulation has been run for 100 seconds and a longer time should be allowed until it is clear that there will be no change in the flow oscillation.

Looking into Model #1 and 2 results, the shed frequency has shown no change despite an element difference of almost 30%. On the other hand, there is a small difference of 3% between the two drag coefficient values. The average drag coefficient between the two models, is 0.935 with a coefficient of variation of 2.19%. With no change observed in the shed frequency and given the very small variation in the drag coefficient, this might indicate mesh independence, however that's still not conclusive.

The shed frequency of 0.952Hz has been over-predicted by 0.6%, compared to 0.946Hz, the upper limit of the reference range 0.891 ± 0.055. The difference can be considered insignificant due to its very small value. The drag coefficient has been under-predicted by 5%, compared to one, the minimum value of the reference range of 1-1.2, as identified in section 4.5. Also, compared to the maximum value of 1.2 which is commonly used in the literature, there is a difference of 20.83%.

The discrepancies in the parameters under investigation are not surprising at all. To begin with, it is very well known in the literature that the forces predicted by the 3D computations, are in general smaller than the ones from the 2D computations. That's due to the three-dimensional effects [26] [147]. Similarly, as stated in a computational fluid dynamics review [148], it is known that for the subcritical regime, in which the Reynolds number of this research lies, for the flow past a circular cylinder, a very large value of the drag force is evaluated from the 2D computation, and the appropriate values can be barely obtained by the 3D computation of the longitudinal vortices in the wake. For that reason, in many published work where three-dimensional models are studied with $Re > 200$-400, it can be observed that the authors are using data extracted only from the component in parallel with the flow, of the parameter under investigation. That leads to results with a better agreement to the reference values. In this research, all three components of the parameters are taken into consideration, which gives a good reasoning for the discrepancies.

Another possible reason for the discrepancies of the computational model can be the turbulence model used. It is also known that different turbulence models give different

results. This has also been observed in the two-dimensional model presented earlier, in section 5.4.2.1.

Furthermore, the crossflow past the cylinder is affected by freestream turbulence, surface roughness, compressibility of the fluid and other factors. For instance, the position of the transition from laminar to turbulent flow in the boundary layer depends on the turbulence level. An increase in the freestream turbulence level leads to an earlier (lower Reynolds number) onset of the critical flow regime (drag crisis) and corresponding changes (dramatic decrease) in the drag coefficient. Surface roughness causes an earlier onset of the critical regime and a higher drag coefficient as well. Thus, the lower value of drag coefficient might well be due to early onset of the critical regime, since the Reynolds number is near the upper boundary of the subcritical with the critical regime. Another common reason that could have led in such discrepancy is caused by different base suction pressure prediction near the leeward side of the cylinder. When less negative pressure is predicted by the turbulence model, it results in lower suction and thus lower drag around this area. The assumption requires further investigation, however it is not within the scope this research to analyse the computational model to such an extent. By qualitatively looking at the pressure contours of the model, the author believes the discrepancy is due to the less negative pressure levels. This is a common occurrence with SST k-ω turbulence model and it has also been seen in other work [149].

In general, there are many cases in the literature where the three-dimensional models under-predict the parameters of interest at Reynolds number of $10^4 - 10^5$. For example, in [142] the flow past a square cylinder at Reynolds number in the range $10^4 - 10^5$ was investigated. They used $k - \varepsilon$ and LES models. Their results under-predicted drag coefficient between 7.31% - 19.41%. They have also validated their mesh designed with a discretisation error estimation method, reassuring mesh independence. In other work, at the same range of Reynolds numbers, the drag coefficient was under-predicted between 11%-39%, at different turbulence models [26].

The author believes that the current mesh design in combination with the turbulence model used have given the best possible results for a Reynolds number of 10^4, despite the differences when compared with the reference values. Additionally, Model #4, a finer version of Model #1, has not given better results. Therefore, it is believed that further mesh refinement of the model will not provide better accuracy.

To assess Models #1,2,3 and to quantify whether the current mesh gives satisfactory results, a discretisation error estimation method has been used. Due to the importance of the three-dimensional model results in this research, it has been decided to use the Grid Convergence Index (GCI), based on Richardson Extrapolation (RE) method for discretisation error estimation. As stated in the American Society of Mechanical Engineers (ASME), Journal of Fluids Engineering, if authors choose to use it, the method per se will not be challenged in the paper review process. This policy from the journal is meant to facilitate CFD publications by providing practitioners with a method that is straightforward to apply, is fairly well justified and accepted, and will avoid possible review bottlenecks, especially when the CFD paper is an application paper rather than one concerned with new CFD methodology. RE is currently one of the most reliable methods available for the prediction of numerical uncertainty and it is 95% accurate [150].

Traditional methods of estimating discretization error, such as Richardson Extrapolation, rely on mesh doubling, i.e. the mesh size changes by a factor of two. Recent development of the GCI [151] [152] provides a discretization error estimate even when the successive mesh refinements are not integer multiples, i.e. doubling the mesh is not required. This is also the case in this research. The meshes are not refined with fixed refinement ratio. The GCI is stated as an error percentage and provides a confidence bound on the estimated error band within which the numerically converged solution will likely lie. GCI error estimates can be used with a minimum of two mesh solutions, but provide a better error estimate when used with three mesh solutions. In this work, the GCI method will be used directly, without any analysis of its origins as it is out of the scope of the research. Further details regarding the method can be found in the respective published work [150] and further literature [152] [153].

Extrapolation-based discretisation error and uncertainty estimates, require a series of solutions. Richardson Extrapolation and all of the uncertainty estimators based on Richardson Extrapolation are applied to a set of solutions where the mesh spacing is varied using systematic mesh refinement [153]. The characteristic variable that is required in this method was chosen to be the average drag coefficient of models #1,2,3, with the respective variables as $\Phi_1 = 0.95$, $\Phi_2 = 0.921$, $\Phi_3 = 0.85$. Since two of frequency values are the same, it is not possible to use the shed frequency as the characteristic variable. Similar approach is observed in other published work [142].

The refinement factor r is defined as the ratio of mesh elements on the finer mesh to coarser mesh,

$$r = (\frac{n_{el1}}{n_{el2}})^{1/d}$$

Equation 35. Refinement factor ratio of fine to coarse mesh.

Where n_{el1} is the number of elements in the fine mesh, n_{el2} is the number of elements in the coarse mesh and d is the grid dimension, three in this case since it is a 3D model.

The most common refinement factor is two because of simplicity. However, requiring a constant mesh refinement ratio over three meshes can become a computational burden, especially for three- dimensional problems. Practical experience has shown that the minimum recommended refinement factor to prevent interference with other numerical errors is 1.1 [152]. Thus, it is necessary to estimate the refinement factor between models #1,2 and 2,3 in order to verify that it is at least 1.1.

Using Equation 35, $r_{21} = 1.1288$ and $r_{32} = 1.1132$, where r_{21} is the refinement factor between the fine and the medium mesh and $r_{32}$is the refinement factor between the medium and coarse mesh. Both fulfil the minimum requirement of $r > 1.1$.

The reliability of all discretisation error estimators require that all solutions used in the estimate are asymptotic, similarly Richardson Extrapolation too. That implies that the error is decreasing with finer mesh. To estimate how asymptotic the solutions are and thus the reliability of the error estimate, an observed order of accuracy ($\hat{p}$) [154] [155] is calculated first using,

$$\hat{p} = \frac{\left|\ln\left(\left(\frac{r_{21}^{\hat{p}} - 1}{r_{32}^{\hat{p}} - 1}\right)\left(\frac{\Phi_3 - \Phi_2}{\Phi_2 - \Phi_1}\right)\right)\right|}{\ln(r_{21})}$$

Equation 36. Observed order of accuracy when more than two solutions are available.

The observed order of accuracy requires three systematically refined meshes and can be calculated only for monotonically converging solutions such that $|\Phi_2 - \Phi_1| < |\Phi_3 - \Phi_2|$ and $(\Phi_2 - \Phi_1)(\Phi_3 - \Phi_2) > 0$. Substituting the respective values, $0.029 < 0.070$ and $0.002059 > 0$. Therefore, the criteria are fulfilled and the chosen meshes can be used

to estimate the observed order of accuracy. Using Equation 36 with the respective values, the observed order of accuracy is $\hat{p} = 8.01956$.

By applying the Richardson extrapolation using the two finest meshes, an extrapolated estimation of the drag coefficient can be obtained:

$$\Phi_{ext}^{21} = \frac{r_{21}^{\hat{p}}\Phi_1 - \Phi_2}{r_{21}^{\hat{p}} - 1}$$

Equation 37. Extrapolated drag coefficient value.

The relative error is defined as,

$$e_a^{21} = \left|\frac{\Phi_1 - \Phi_2}{\Phi_1}\right|$$

Equation 38. Extrapolated relative error.

And the extrapolated relative error is defined as,

$$e_{ext}^{21} = \left|\frac{\Phi_{ext}^{21} - \Phi_1}{\Phi_{ext}^{21}}\right|$$

Equation 39. Extrapolated relative error.

It is important to note that in most practical problems the exact solution is unknown, therefore Equation 37 is used to predict the solution of the problem followed by the implementation of GCI to quantify the accuracy of the solution found from the computational models. GCI is an acceptable and recommended method that has been evaluated over several hundred CFD cases [156] [157] [158] [159].

Using Equation 37, an extrapolated value of 0.956 has been found for the drag coefficient.

Comparing the numerical value of the drag coefficient found in the finest model (Model #1) between the three (Models #1,2,3) and the extrapolated value, Equation 39 gives a 0.0062% error. That implies that the solution found in Model #1 for drag coefficient is almost identical to the predicted value of drag coefficient.

The Grid Convergence Index (GCI) for the fine mesh solution can now be computed. A factor of safety (F_s) of 1.25 is used since three meshes have been used to estimate the observed order of accuracy [150]. When two meshes are used, $F_s = 3$ is used. Thus,

$$GCI_{fine}^{21} = F_s \times \frac{e_a^{21}}{r_{12}^{\hat{p}} - 1} = 1.25 \times \frac{e_a^{21}}{r_{12}^{\hat{p}} - 1}$$

Equation 40. Grid Convergence Index for the fine mesh.

Substituting the respective numbers in Equation 40, $GCI_{fine}^{21} = 0.0090\%$.The safety factor should be thought of as representing a 95% confidence bound on the estimated relative error. Thus, for this project the converged numerical solution lies in the interval of $0.95 \pm 0.009\%$, or 0.95 ± 0.00855, with a 95% confidence level.

Summing up, the implementation of GCI method has reassured that Model #1 has given the best possible answer given the current mesh design, turbulence model and other parameters used. Therefore, it is safe to say that the shed frequency of 0.952Hz and drag coefficient of 0.95 are mesh independent. Model #1 will be used as the basis to create the fully coupled model.

Model Analysis

In an attempt to validate the three-dimensional model with an input velocity of 0.453 m/s and a Reynolds number of 5.1404×10^4, a flow characterisation, visible in a three-dimensional computational model, and beyond those characteristics identified in the two-dimensional model, will be examined.

The transition phenomena in the bluff body wake, particularly for a circular cylinder, have been studied extensively in the past. The low end $(Re \approx 190\ to\ 260)$ of the transition regime is characterised by two distinct discontinuities in the measured wake parameters, as Reynolds number is increased, and can be observed in the Strouhal- Reynolds number relationship as shown in Figure 65. At the first discontinuity, the Strouhal number drops from the laminar shedding curve to a curve for mode-A turbulent vortex shedding. This first discontinuity is hysteretic. At the second discontinuity, there is a jump to a higher Strouhal curve, corresponding to mode-B turbulent vortex shedding. In this case, there is no hysteresis, but instead, a gradual transfer of energy between modes A and B as Reynolds number is increased [160].

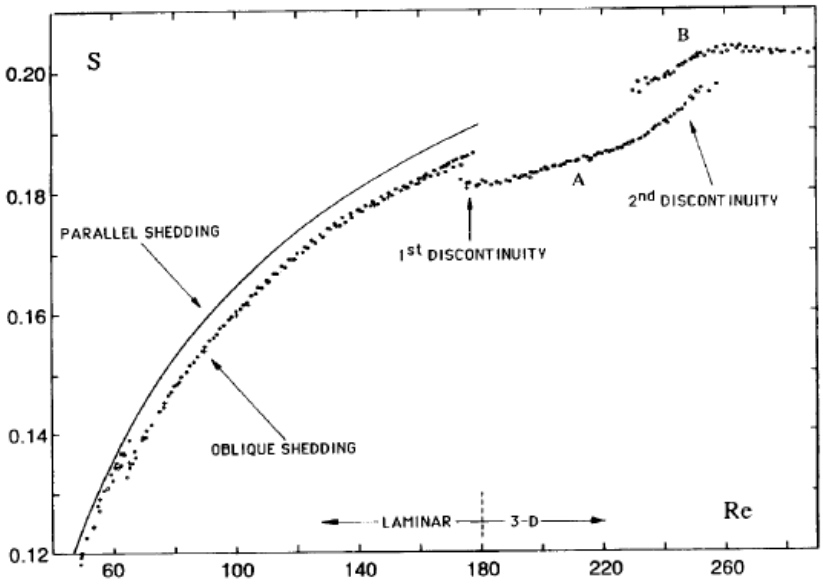

Figure 65. Strouhal- Reynolds number relationship: laminar and three dimensional transition regimes (adapted from [24]).

During this transition, a distinct and intermittent switching of the flow field is visible, similar to that shown in Figure 66. There is a low frequency modulation (marked LD, low drag) in the time-series with the usual shedding mode (marked HD, high drag). The unusual intermittent low frequency modulation phenomenon has been attributed to the formation of large-scale irregularities, namely vortex dislocation. It may be mentioned that vortex dislocation is generated between the spanwise cells due to the out-of-phase movement of the primary vortex in each cell. However, the natural vortex dislocation may appear randomly in space as well as in time.

In this research, Figure 66 below does not represent a low Reynolds number dislocation phenomenon, but spot-like vortex dislocation, studied and presented in [161] and confirmed by other authors [162]. At higher Reynolds numbers (above 1300), there is turbulence formed by the shear-layer instability within the vortex formation region. This instability is basically two-dimensional, but rapidly becomes three-dimensional, causing small-scale turbulent fluctuations. In the present work, the turbulence is somewhat modified from the above. The downstream distortion appears on vortices that have already become three-dimensionally turbulent from within the vortex formation region. In general, it can be said that the vortex dislocation possibly occurs as a result of vortex merging in the spanwise direction or due to phase variation within the large coherent structures, causing a drop in drag and lift forces. These downstream distortions are caused primarily (but not wholly) by vortex dislocation.

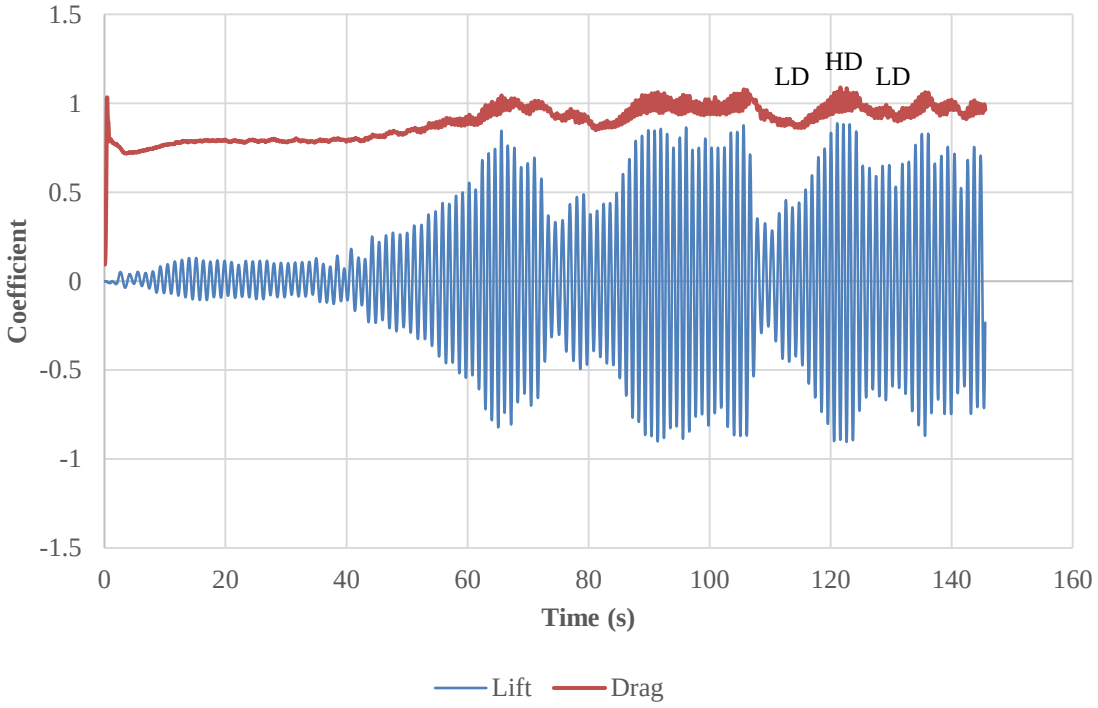

Figure 66. Drag and Lift Coefficient graph for three-dimensional model.

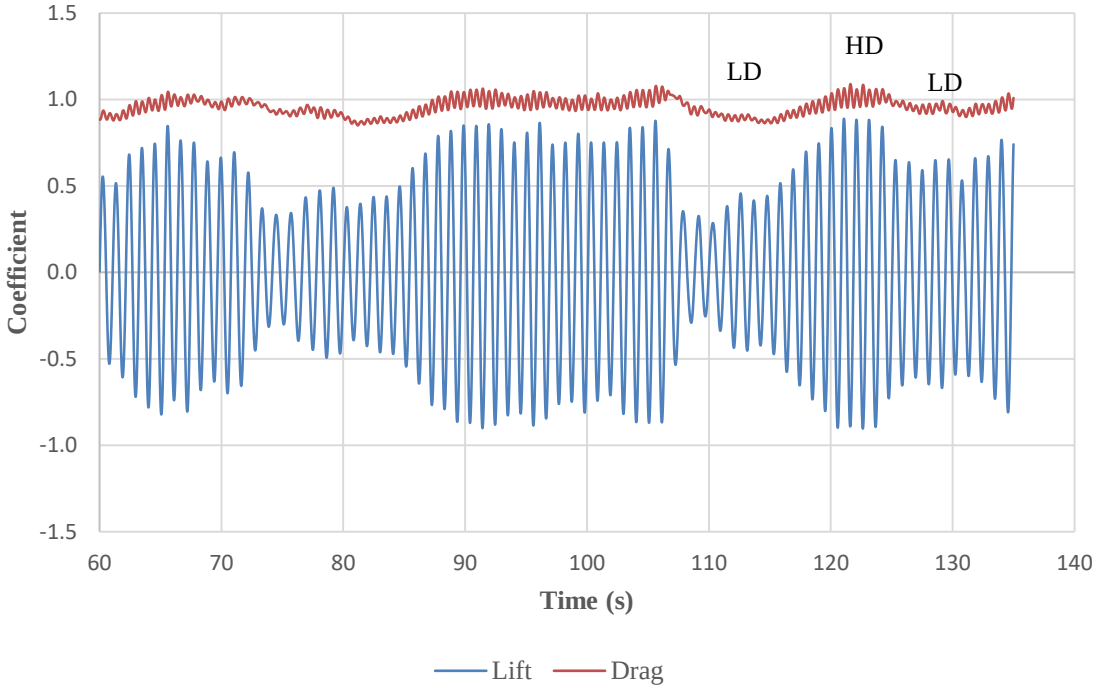

Figure 67. Zoom-in of Figure 66.

Worth mentioning that the numerical results of a study focusing in the investigation of vortex dislocation, has concluded that the change in grid size and the domain size do not change the dislocation and thus dislocation is a physical phenomenon [143].

By observing Figure 67, a zoom-in of Figure 66, the flow past the circular bluff body experiences a dislocation-like phenomenon around the 80^{th} second and the 110^{th} second of the simulation. Similar physical features are present in the drag and lift coefficient data at equivalent Reynolds number found in [141] and other studies [142], however there is no mention of the phenomenon.

Overall, by observing the model has assured that there is three-dimensionality taking place in the flow and vortices are developed and travel downstream which can then excite the flexible cylinder tethered behind the bluff body. As will be discussed further in stage 3, the turbulence model used has limited capabilities thus it is not possible to conduct further analysis, by observing the secondary vortices. In this research, the important conclusion is that vortex dislocation-like phenomena are present, which reassures that the model is able to compute the three-dimensionality of the flow. This is sufficient for the needs of this research. In comparison, by observing the lift and drag coefficient graph of the two-dimensional model (Figure 62), the vortex dislocation is not visible as the model is two-dimensional, which is also correct.

The shedding frequency is the same as the lift force frequency in a steady flow, and it can be obtained by simply observing the graph of lift coefficient. Firstly, the period is found by subtracting as many steady state peaks as possible and then dividing by the number of cycles between them. Frequency equals to the reciprocal of the period. Usually, this method works best for relatively low Reynolds numbers or two- dimensional models, where there is only one dominant frequency and the flow is laminar. However, once the critical Reynolds sets in, many other data are obtained into the lift coefficient signal which end up changing the shape of the graph, making the calculation of the frequency more complex, as observed in Figure 67.

Similar to the two-dimensional model, Fast Fourier Transform (FFT) has been used to analyse the complex signal. The spectral analysis method determines the distribution of vortex energy and average statistics for each vortex frequency by converting the time series of the wave record into a wave spectrum. The time domain data of the lift coefficient are converted into frequency domain when using the FFT. It is very important to extract the

lift coefficient data from the correct axis in Fluent. As it is known from the literature, the lift force is perpendicular to the drag force. The drag force is parallel to the velocity of the flexible cylinder. Therefore, the lift coefficient extracted from Fluent should be recorded from the respective computational axis. Post lift coefficient analysis using FFT, a periodogram has been plotted as seen in Figure 68. It can be observed that there is a dominant frequency peak of 0.952Hz which falls within the expected range as already discussed. There is also a secondary peak, most probably due to the observed phenomenon at 0.879Hz.

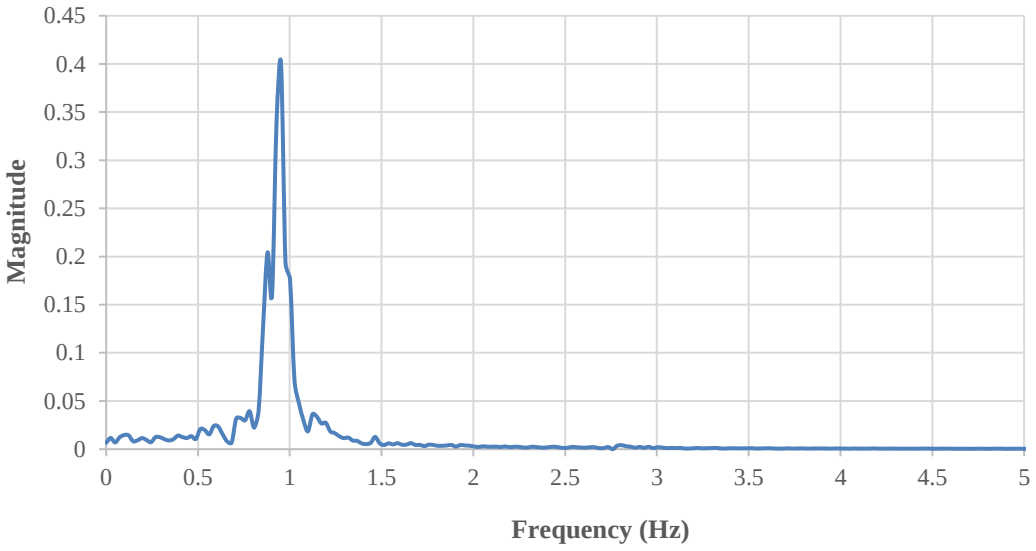

Figure 68. FFT screenshot of Lift Coefficient data for 3D Model #1.

During the two-dimensional model mesh independence study, a very important factor was not taken into consideration. That's the overall time of the simulation. It is known that the denser the mesh, the longer the simulation will take due to the excessive amount of elements. In the two- dimensional model, the amount of elements was relatively low given the available computational power. Therefore, less than a day was sufficient to compute each simulation. On the other hand, in the three-dimensional models, it takes on average six days for around 40s of simulation to compute, using the same computer specifications. The time will further increase when the model is transformed to a dynamic, fully coupled model, where iterations between the fluid dynamics and the mechanical solver will take place.

It is very positive that mesh independence has been achieved in 793236 elements. It gives substantial confidence towards the mesh design combined with the SST k-ω model.

Conclusion

The three-dimensional model has been successfully created and characterised. A 3D phenomenon that should occur in a three-dimensional simulation has been identified and any possible limitations have been identified. The shed frequency of 0.952Hz falls within the expected range identified earlier in section 4.5. The drag coefficient is slightly under-predicted, however this is an expected occurrence in three-dimensional models as already discussed. Overall, the results are satisfactory and persuasive that the final three-dimensional model chosen to proceed and create the fully coupled is Model #1

5.4.3 Stage 3: Established Vortex Field

Stage 3 presents a qualitative investigation of the development of the shed vortices downstream of the bluff body. In the turbulent shear flow, the turbulent structures are often found to be dominated by eddies which preserve a certain spatially organisation and these vertical structures evolve temporally. Many methods to identify and visualise the turbulent structure exist in the literature. Q-criterion [163] has been successfully used to identify the shed vortices. Q represents the local balance between shear strain rate and vorticity magnitude. A positive Q implies that a point in the fluid is dominated by rotation. In Figure 69, the Q iso-surfaces obtained give a clear visual impression of the vortical flow structures in the wake and its three-dimensional character. Furthermore, the breakup of the shear layer and the organisation of the chaotic turbulent eddies into a vortex street is also evident, resembling the observations during the experimental work of this research.

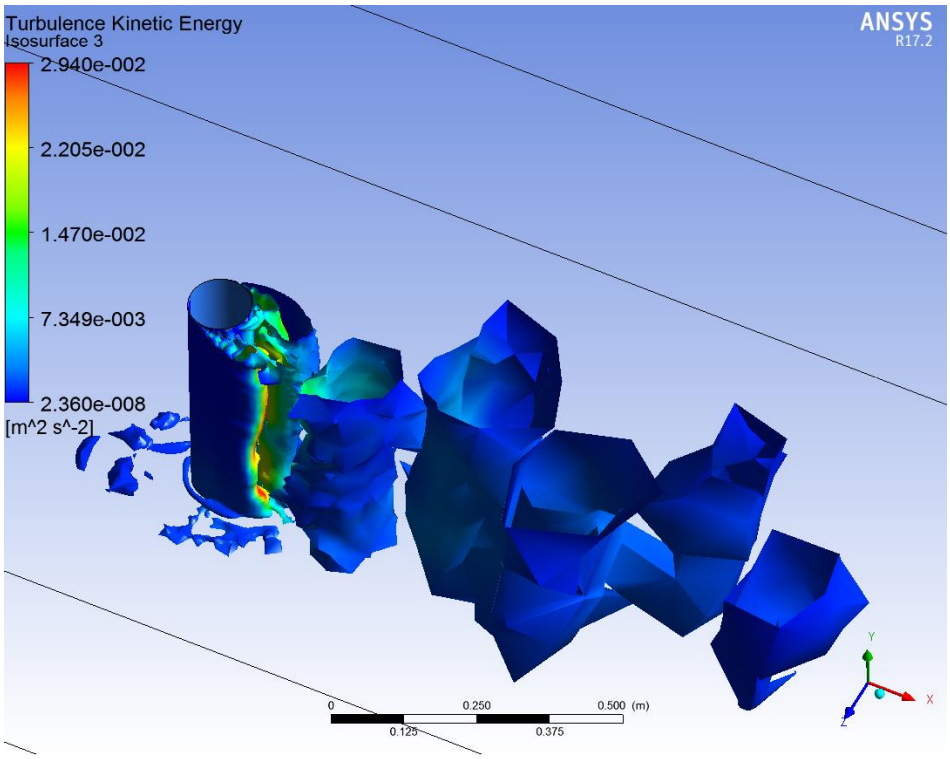

Figure 69. An iso-surface of the second invariant of the velocity gradient Q coloured with turbulence kinetic energy at t=100s

As already discussed in section 5.4.2.2, the three-dimensional flow is characterised by secondary currents. It is known that RANS models have certain limitations as already presented in section 2.4. RANS lack of physical description and are unable to solve the turbulence-induced secondary flows [83]. That is because with RANS, the effect of such

vortices on the flow is fully modelled and translated into an additional turbulent viscosity term in the momentum equation. Therefore, RANS simulate the fluctuating component of the flow regardless the scale of the fluctuations and solve for the Reynolds averaged components. The results are an approximation of the time-averaged flow field. This is the main reason RANS models are much faster than non-RANS. Three-dimensional and unsteadiness effects are still present, but can only be fully captured by more sophisticated turbulence models, in exchange for considerably more computational power and time, limiting their engineering design capability.

As expected, when a plane vertical to the flow was deployed in the CFD analysis, the velocity vectors were in parallel with the domain and no secondary flow was visible. For that reason, despite that it is not the chosen turbulence model, LES has been used for a limited time, just to see how the domain behaves. Figure 70 clearly shows that the secondary currents observed in the computational model of this research, are very similar to those present in a straight open channel [164]. This is a good trade-off example due to computational power limitations. Unfortunately, SST k-ω, like all RANS models cannot reproduce directional effects of turbulent flow such as secondary motions of fluids in the plane normal to the stream wise direction [165] [166]. Being able to observe the existence of the secondary currents, gives confidence that the fluid domain is developed correctly, despite the limitation of the chosen turbulence model.

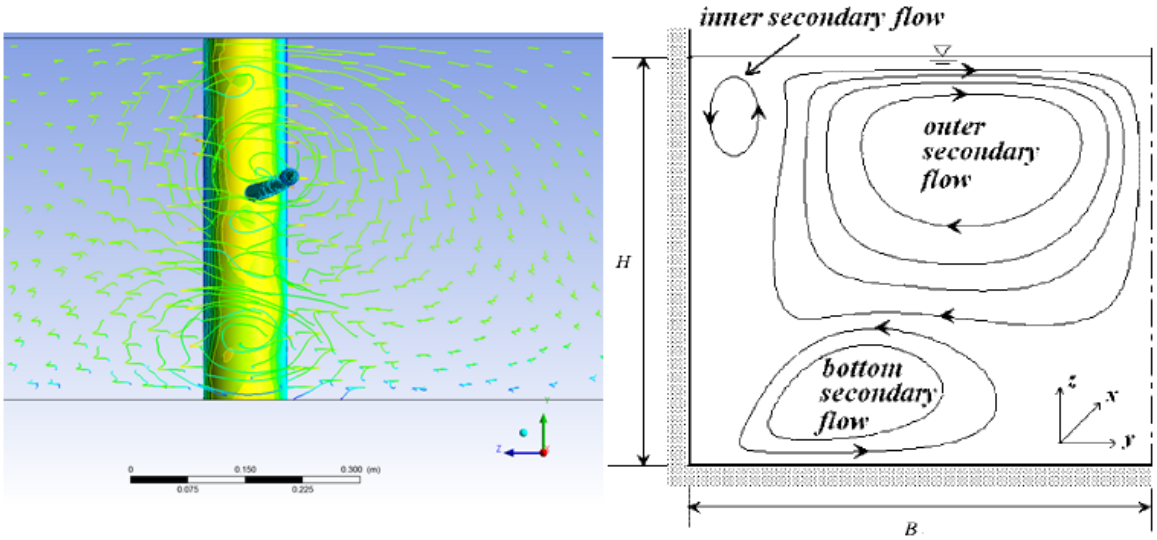

Figure 70. Secondary flows in rectangular open channel (adapted from [164].

On a final note, as previously discussed during the background literature and the experimental work, the level of turbulence has not been measured experimentally. If this was to happen, it could have been used as an input at the computational model. However, in order to use a level of turbulence that would satisfy the needs of this research, the following thinking was considered.

ANSYS® Workbench allows to set the level of turbulence, under the "Turbulence Intensity" settings of the model. A turbulence intensity of 1% or less is generally considered low and turbulence intensities greater than 10% are considered high. The turbulence intensity at the inlet is totally dependent on the upstream history of the flow. If the flow upstream is under-developed and undisturbed, low turbulence intensity can be used. If the flow is fully developed, the turbulence intensity may be as high as a few percent.

According to ANSYS® Fluent Guidelines [81], the turbulence intensity at the core of a fully-developed channel flow is estimated to be $0.16 \times Re_{channel}^{-1/8}$, which gives turbulence intensity of 3.7% given the characteristics of the channel used in this research. Using this as baseline, and because the flow it is not fully developed, a 3.5% turbulence intensity was chosen for the simulations of the computational models.

Understandably, this possibly contains a level of uncertainty, especially when compared to the turbulence levels of the experimental water channel, however, the number is close to the expected turbulence levels of a fully developed flow. In order to have more accurate results, PIV investigation should take place and also to consider the impact of the pump in the flow, which is not possible to implement into the computational model at this stage. Possibly, the pump increases the levels of turbulence, especially during the first seven to ten metres downstream the inlet, where the bluff body and the flexible cylinder are located. Overall, as it will be seen in the next chapter, the results found are of a good agreement with those expected, thus the turbulence intensity chosen is of a satisfactory level.

5.4.4 Stage 4: Presence of Flexible Cylinder in the Field

The analysis of the three-dimensional domain has demonstrated that the computational model with the bluff body, give satisfactory results, similar to computational and experimental work of other authors found in the literature. In stage four, the vortex shedding reaches the flexible cylinder.

As depicted in Figure 71, the surface under investigation in this section is the flexible body, located at a distance of $2D_{bb}$ downstream, from the bluff body. The observed geometry has the same dimensions as the flexible cylinder used during the experimental approach and it has shape of that of a rigid cylinder. The geometry collects the pressure data of the fluid interacting on its surface, which in turn imported in the next process of the simulation, to excite the flexible cylinder. In this section, two methods will be investigated; one-way coupling using a transient CFD/FEA model and a two-way, fully coupled model.

This arrangement represents the energy harvesting system. It is necessary to study and analyse the excitation of the flexible cylinder from the induced vortices, therefore, separate detailed discussion follows in the following chapter.

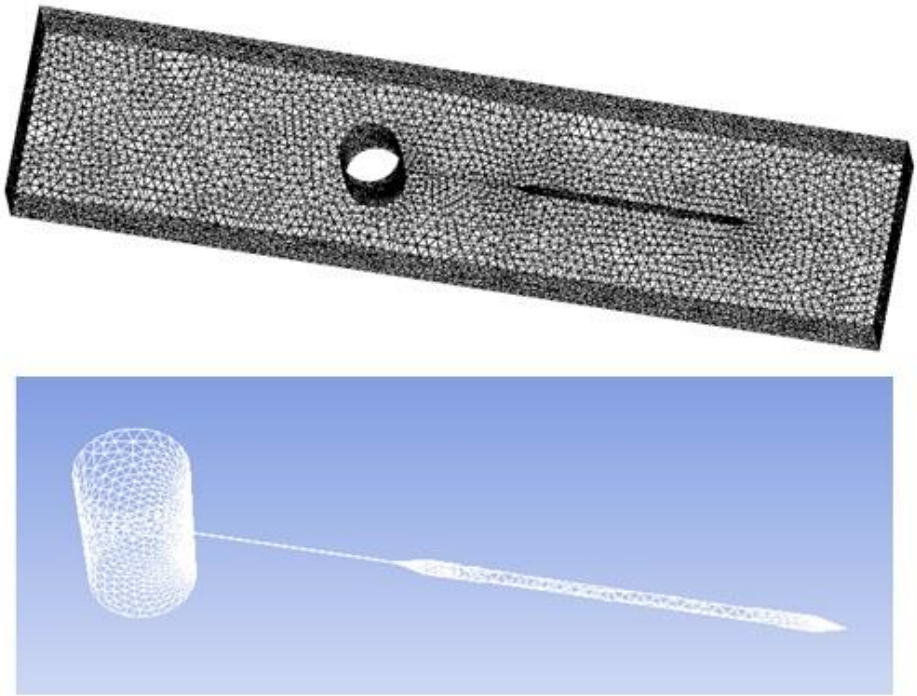

Figure 71. Mesh representation of the water channel, bluff body and flexible cylinder (not in scale).

5.5 Summary

This chapter presents all the work done to validate a fully coupled computational model which will be used in future work to assess further natural characteristics of the flexible cylinder and implement the energy harvesting methodology, presented in chapter 8.

Initially, in Stage 1, the development of the velocity profile in the computational domain has been investigated. It was shown that the flow in the experiment located 7.5m from the inlet pipes, is not a fully developed velocity profile. However, it was shown that the fully developed profile from the model was similar to that obtained from theoretical calculations. This confirms that the model upstream of the bluff body is behaving as expected. To achieve a better fit, further mesh refinement is required, however that would not add any value to the needs of this research, only to increase the computational effort needed to obtain a solution.

In Stage 2, the presence of the bluff body in the field has been examined. Initially, a two-dimensional model has been created. This has greatly contributed to the understanding of mesh design; to use the right type of mesh, first layer thickness, turbulence model, convergence criteria, etc. This is where most of the mesh development and design took place. Expected flow phenomena identified over time during the simulation gave confidence in the quality of the model. The data of lift coefficient over time around the bluff body was extracted and then, using a Fast Fourier Transformation (FFT), a periodogram of the shed frequency has been presented. The results found are compared and discussed with those of other computational and experimental work, where it has been concluded that they are very satisfactory. The two- dimensional model was extruded into the third dimension, creating the three- dimensional model. Satisfactory values of drag coefficient and shed frequency were obtained, independent of the mesh size.

Stage 3, compares the vortices shed from the bluff body and traveling downstream in the computational model with the observations from the experiments. Similar pattern were observed and the Von Kármán vortex street was visible.

Stage 4, shows the final arrangement of the three-dimensional model. The inanimate body is introduced, creating a coupled computational model, representing the energy harvesting system. The model is ready to be used to investigate the frequency and amplitude of oscillation the flexible cylinder.

[This page intentionally left blank]

Chapter 6

CFD Analysis of Energy Harvesting System

This chapter will investigate the presence of the flexible body in the wake of the bluff body in the computational model. Earlier, in section 3.1.4, modal analysis was used to analyse the flexible cylinder characteristics. The results provide values similar to theory, however, since the modal analysis does not take into consideration any damping parameters, viscous damping, the friction between a structure and its surrounding fluid, is not included. Any values found, represent the un-damped characteristics of the flexible cylinder. Modal analysis has served as a validation method towards the flexible cylinder design as a computational model. To find the characteristics of the flexible cylinder taking into account the surrounding fluid, a coupled system can be used, either by using a fully coupled model (two-way coupling) or by inserting the vortex pressure data from CFD into a FEA transient analysis (one-way coupling). Both types of coupling are investigate and the findings are presented in this chapter. From this moment onwards, simulation time begins to play a significant role in the research. As already discussed, the two-dimensional model was giving a solution in under 24 hours. The three-dimensional modal, with the presence of the bluff body only, computes about four seconds of computational time in 24 hours, already a significant increase. To reach the oscillation presented in Figure 66 it was necessary to dedicate just over 30 days. On the other hand, the three-dimensional fully coupled model, computes approximately 1.2s of computational time per day, as it will be discussed later in chapter 6. All the time estimations are based on the computational power available for this research, as presented in Table 16. It is important to note that it was not possible to use the High Performance Computing (HPC) facilities at the University of Southampton due to certain limitations. Each session is limited to 72 hours, where these models require a much longer simulation time. Also, the space given to upload data is very limited to few Gigabytes. The coupled simulations easily exceed 250GBs of data. Finally, an older version of ANSYS® was deployed, limiting the user interaction. Thus, the computer specification as defined in Table 16 has been used to compute the full coupled simulations.

6.1 Transient CFD/FEA Modelling of a Flexible Cylinder in a Flow

In this section, a one-way, pressure coupled CFD/FEA transient model has been developed and tested.

Initially, in ANSYS® Workbench, a transient structural analysis block was added next to the Fluent System, where the CFD simulation of the project took place. The transient structural analysis has as input, the geometry from Fluent, with applied restrictions. Only the flexible cylinder geometry with the rope is active in the transient analysis. This is because it is in our interest to analyse only how the flexible cylinder is oscillating when the pressure is exerted by the fluid. For the 'Setup' input of the transient analysis, the 'Solution' results from Fluent have been used. The transient analysis uses any data produced in the CFD model as the input, in this case the pressure data. This is shown graphically in Figure 72.

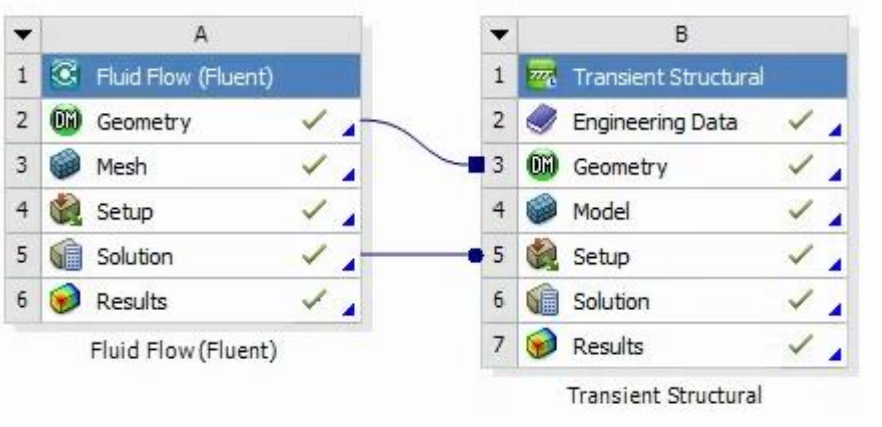

Figure 72. One-way coupling method in ANSYS® Workbench.

Setting-up the transient analysis is relatively straightforward. Firstly, the mesh of the flexible cylinder must be introduced within the geometry in Fluent. That reason is because data should be collected where the surface of the flexible cylinder is, in respect to the location within the mesh. Then, the mesh is inserted from the Fluent geometry into the Transient Structural model, where the bluff body and channel meshes are suppressed, leaving the flexible cylinder and rope meshes visible for analysis. The quality of the mesh has been chosen to be 'medium' on ANSYS® scale and an increase in quality has also been achieved by increasing the 'relevance centre' to 80, splitting each mesh cell to even more parts. Consequently, this has added more nodes and elements on the mesh. Further increase of the mesh density can be achieved when using the 'size function' to 'Proximity

and Curvature'. As it will be discussed later, the last two settings will allow better pressure distribution along the flexible cylinder.

In ANSYS® Workbench, the 'element type' of the mesh is chosen automatically, according to the structure under analysis, contrary to ANSYS® APDL, where most of the details must be predefined manually. For the model under study, by looking at the 'Solution Information' in the analysis tree, it is possible to see that the 'element type' that has been chosen is SOLID186. SOLID186 is a higher order 3-D 20-node solid element that exhibits quadratic displacement behaviour. The element is defined by 20 nodes having three degrees of freedom per node: translations in the nodal x, y, and z directions. The element supports plasticity, hyperelasticity, creep, stress stiffening, large deflection, and large strain capabilities. It also has mixed formulation capability for simulating deformations of nearly incompressible elastoplastic materials, and fully incompressible hyperelastic materials [167].

A 'fixed support' is added at the end of the rope to represent the tethering on the bluff body, as presented during the modal analysis in section 3.1.2. Under 'analysis settings', the time steps of the simulation can be chosen. It is important to choose a transient time step equal to the Fluent time step (input data), otherwise there is a chance that the transient analysis will not be executed. In this case, 0.01s time step has been chosen for both transient and CFD analysis.

Finally, the surface upon which the imported pressure will be acting was selected, i.e. the 'fluid-solid interface'. It is important to select both the flexible cylinder and rope. Any surfaces left unselected, will not be considered during the simulation.

These are the most important settings used for the transient structural analysis. Any other settings have been left at their default values or under 'Program Controlled' function. Table 11 already presented in section 3.1.2 contains in summary the presented discussion.

Figure 73 presents a comparison between a mesh with and without 'advanced size' function. The 'advanced size' function is designed to accurately capture the geometry while maintaining a smooth growth rate between the regions of curvature and/or proximity. In other words, this will give a more detailed mesh with significantly more elements where there is a curve or a joint in the mesh. Consequently, by increasing the elements on the body, the locations where the imported force is applied during the transient analysis are

increased. As seen in Figure 73, the top left model without ‘advance size’ function, has less nodes per surface area, compared to the bottom left model which has a significant amount per surface area. Similarly, the difference in applied pressure can be seen at the right side of Figure 73. There are less pressure arrows on the top model compared to the bottom. Worth pointing out the length of the pressure arrows located on the nodes. This is a good representation of a static pressure image in time, where the shed vortex is exercising different magnitudes of pressure, at different locations on the flexible cylinder. The higher the pressure, the longer the arrows and greater the amount on the nodes. A clearer, full image of the pressure arrows can be found in Appendix C, Figure 122.

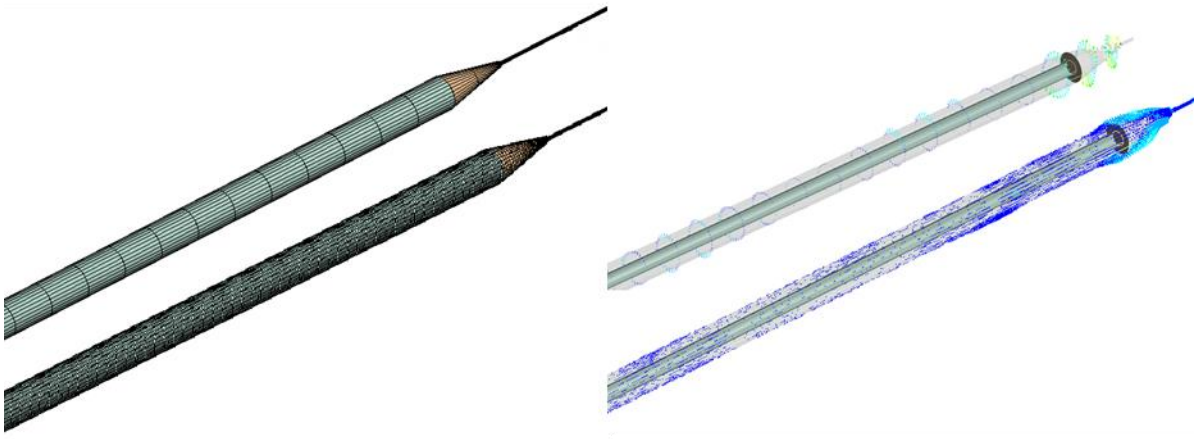

Figure 73. 'Advanced size' function mesh impact and pressure contours.

6.1.1 Transient Results Analysis

A transient dynamic analysis was used to determine the response of the flexible cylinder subjected to a time-dependent loading considering inertia and damping effects. For this analysis, the verified geometry from modal analysis section was used, but now imported in a transient time domain. The boundary conditions are already set. Fixed rope in one end and the flexible cylinder free to oscillate in the other end. The input load is the pressure created by the shed vortices behind the bluff body, where the flexible cylinder is located. The geometry of the flexible cylinder is collecting the pressure data and the latter are inserted in Mechanical transient, which in turn simulates the interaction of the vortices on the flexible cylinder, producing deformation on the flexible cylinder geometry. The ANSYS® Mechanical takes around 30 hours to compute 20s of computational time data for the one-way coupled model. Initially, the drag and lift coefficients on the bluff body have been plotted as seen in Figure 74, for the first 20 seconds of the longer simulation shown in Figure 66.

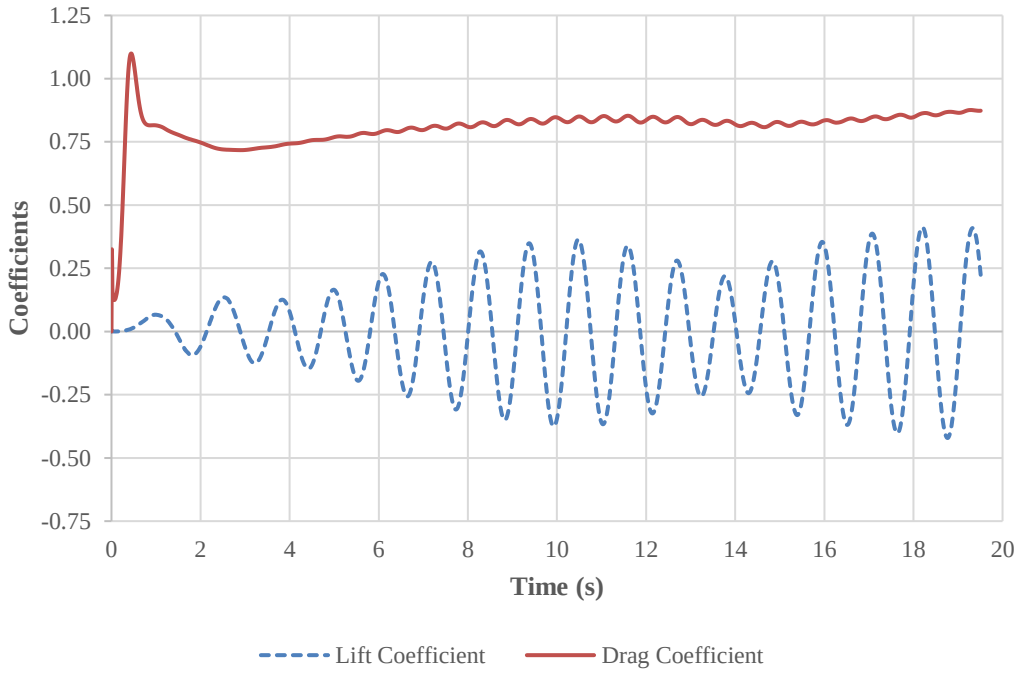

Figure 74. Bluff body drag and lift coefficients with the presence of flexible cylinder.

The coupled model has given an average drag coefficient of 0.80 for the first 20 seconds of the simulation. In comparison, as observed in Figure 75, the same model without the flexible cylinder and the rope, as presented in section 5.4.2.2, has given a drag coefficient of 0.76. The presence of the rope in the wake of the bluff body is already noticeable.

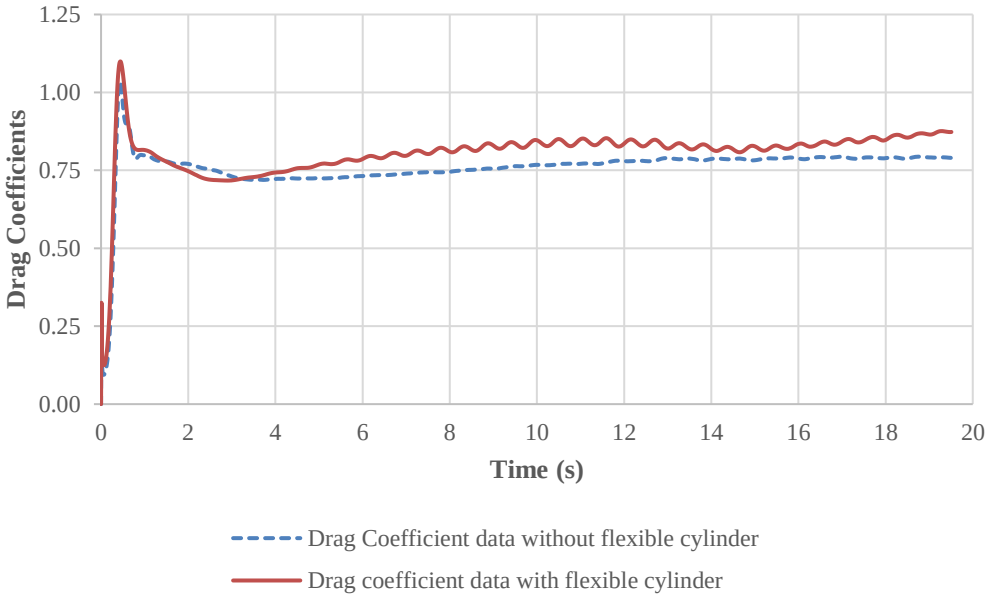

Figure 75. Drag coefficient comparison with and without the flexible cylinder.

Similarly, the one- way coupled model has given a shed frequency of 0.928Hz. The same model, without the flexible cylinder has given a shed frequency of 0.830Hz, for the same period of time and amount of data. Interestingly, one of the secondary frequencies is the same at both models, at 0.635Hz.

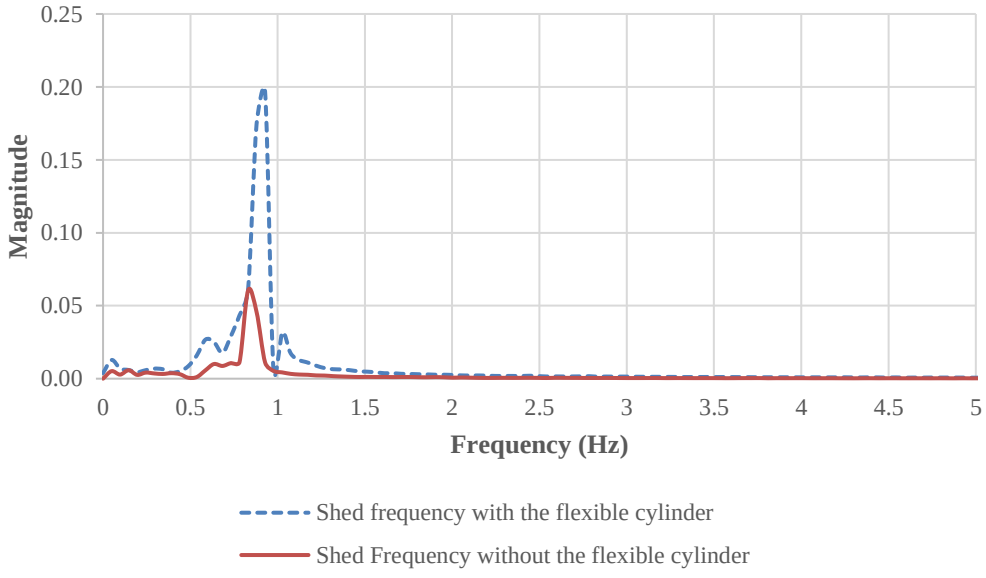

Figure 76. Shed frequencies with and without the flexible cylinder (one-way).

Furthermore, a significant difference in the frequency magnitude is observed. This might be due to the presence of the rope in the wake. It is known that the presence of an object

in the wake can influence the development of the flow. This can initiate transition earlier, therefore the vortices are developed earlier in time, compared to when not present.

The flexible cylinder's frequency of oscillation has been found by applying FFT on the lift data extracted from the transient analysis. As shown in Figure 77, the flexible cylinder has a dominant frequency of 0.156Hz. A secondary peak is also present with a frequency of 0.941Hz, same as the shed frequency.

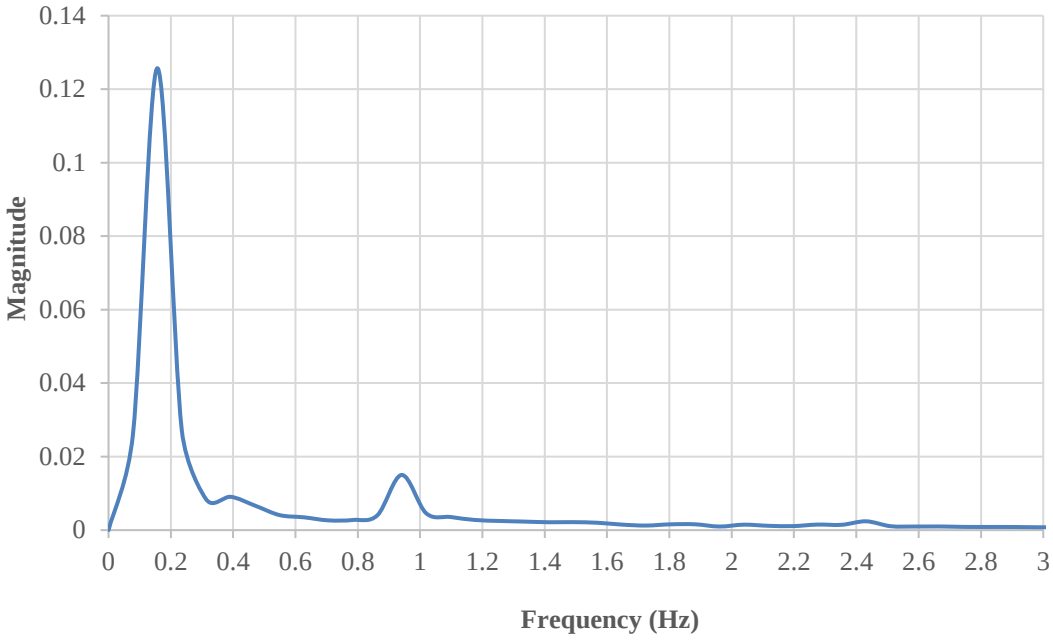

Figure 77. Flexible cylinder frequency for the one-way coupled model.

In general, it can be seen that the flexible cylinder in the one-way coupled model is oscillating due to the upcoming vortices. However, it is under-excided. A similar study [168] has found that when the shed frequency was at a distance from the natural frequency of the flexible body, the one-way coupled model was giving very inaccurate results and it was not in comparison at all with the two-way coupled model, in terms of displacement magnitude or frequency of oscillation. The author believes that the natural frequency of the flexible cylinder with the rope (0.837Hz) and the shed frequency (0.941Hz) are close, therefore this cannot be the case.

Further examination has taken place, by inspecting the deformation contours of the flexible cylinder. The amplitude of oscillation has been measured similarly to the experimental procedure, in parallel with the bottom of the water channel. This required ANSYS® Mechanical to run approximately 30 hours to compute 20s of computational time pressure

data. The results of the simulation were adjusted to run at true scale. The animation settings have been set to 100 frames and 10-second intervals. By observing the flexible cylinder, it can be seen that the first half of the cylinder (nose to centre) is oscillating in a different frequency and displacement magnitude compared to the second half (centre-tail). This is what it has been observed during the experimental results as well. This also explains why there are two peaks in the frequency spectrum in Figure 77.

It is also observed that the flexible cylinder does exhibit an oscillation where mode 0, mode 1 and modes 2 are present, as shown in Figure 28, however these are not as clear as one would expect, especially when compared with the experimental results. Thus, by observing the motion of the flexible cylinder does not give a clear bending moment like that observed during modal analysis as depicted in Figure 26. During the majority of the oscillation, the flexible cylinder has a model shape close to zero, instead of one, as depicted in Figure 78.

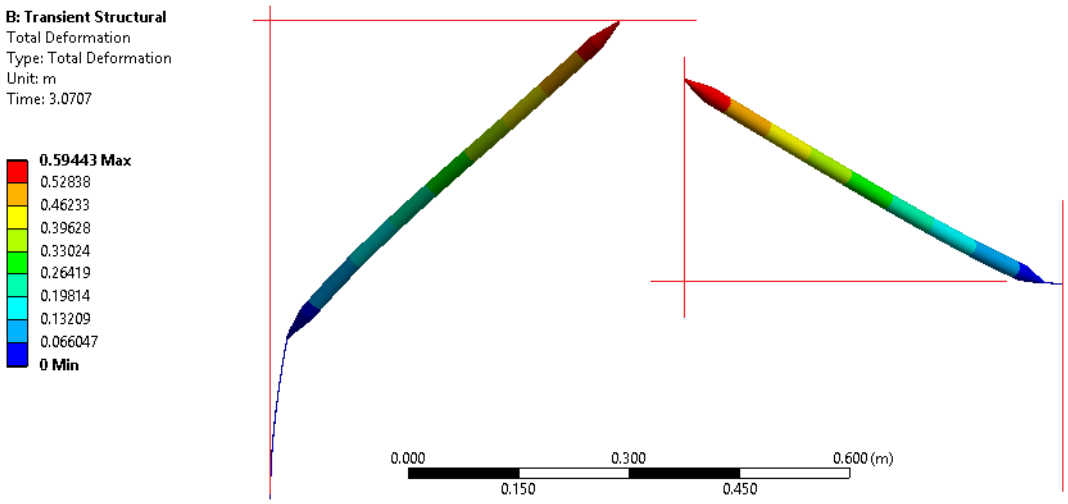

Figure 78. Amplitude examination of one-way coupled model. Left: plane parallel with the bottom of the channel, right: plane vertical to the bottom of the channel.

Considering that the flexible cylinder had mode 0 shape in some occasions during the experimental results, the amplitude of the tail has been measured, in respect to the centre line, passing through the rope and the flexible cylinder at rigid body mode, when t=0s. This is shown on the left flexible cylinder, in Figure 78. The measurement has taken place likewise the experimental work, in a plane parallel to the bottom of the channel.

It has been found that the distance from the centre line looking from the top is 0.44m, which means the double amplitude, as measured in the experimental work, it should be 0.88m. That is almost 4 times larger than the amplitudes measured in the experiments. Furthermore, by looking at the flexible cylinder on the right side in Figure 78, it can be

seen that the tail was pushed by the applied force much higher than the point where it is tethered and where it should be oscillating, given that it is neutrally buoyant. This also explains the significant displacement measured by ANSYS® Mechanical as shown on the contour, as well as the measurement of 0.44m, taken by the author.

Finally, it is important to note that in the time interval of the first 20s, the oscillation might be under- excided, therefore, outside the steady state. That means the presented results might change after longer simulation time. The results were presented in order to show that there is a difference between the parameters of interest when the flexible cylinder and the rope are present in the model. That is why data from the same time interval were used. For the reason, the results of the one- way model will not be compared with the two- way, because the oscillation of interest is when the flow is fully developed and Von Kármán vortex street is present.

Overall, it can been seen that having a one-way coupled model does not give very accurate results, especially related to the modes of oscillation and the amplitude of the flexible cylinder, which are of a primary importance for the needs of this research. Similar studies have also concluded that one and two way models give different results [168] at a certain degree of difference. It is expected that a two- way, fully coupled model should eliminate some of the limitations observed in the one-way coupled model, however in exchange of significant amount of simulation time.

6.2 Fully Coupled Computational Fluid Dynamics Model

As observed in the previous section, the one-way model is limited. This is due to the method of which the data between the mechanical and fluid solver, Fluent, are exchanged. Figure 79, depicts the one-way data exchange process clearly. In Fluent, the fluid field is solved until the convergence criteria are reached. Then, the calculated forces at the structure boundaries are transferred to the structural solver. The structure side is calculated until convergence criterion is reached. Then the fluid flow for the next time step is calculated to convergence. The solution finishes when the desired number of time steps is reached. This method of data exchange does not take into consideration the deformation of the flexible cylinder which has occurred in the mechanical part back into the fluent. In other words, the fluid domain is not affected by the presence of the flexible body, as of its deformation.

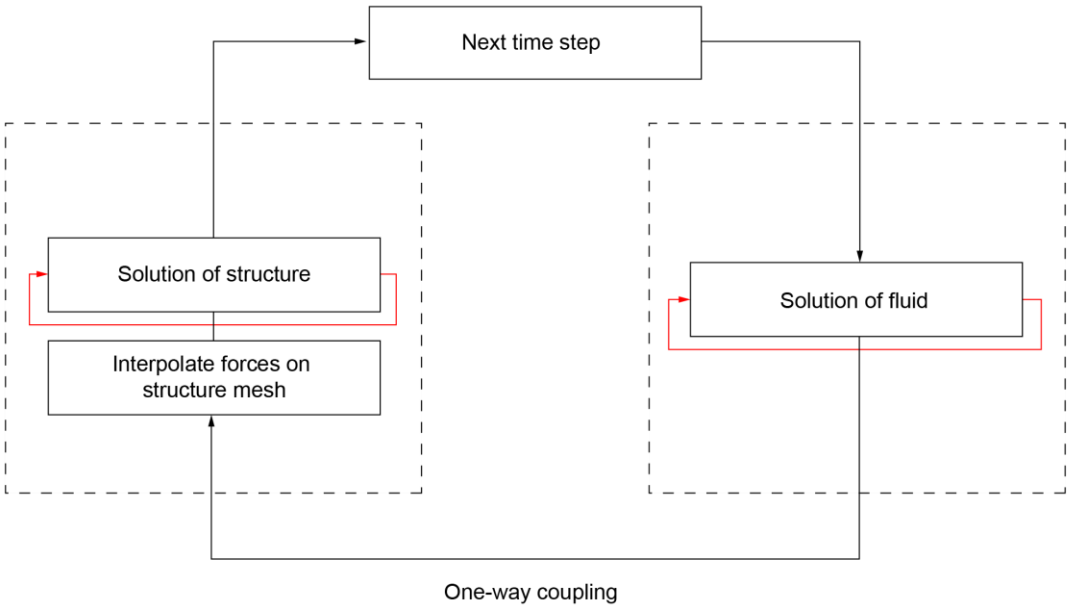

Figure 79. One-way coupling diagram.

On the other hand, for a fully coupled (two-way) model, as shown in Figure 80, all the motions are taken into consideration. Within one time step during transient simulation, a converged solution for the flow field is required to provide the forces acting on the body. Then, forces from the fluid mesh are passed to the surface mesh of the structure, where a solution is attempted under the acting forces. If convergence is achieved, the response of the structure mesh will be a displacement of the grid nodes. The displacement at the boundary between structure and fluid are interpolated to the fluid mesh which leads to its deformation. This is one loop and the whole process is repeated until the desired time step

is reached. Therefore, since the deformation of both the flexible cylinder and the flow in the same moment in time are taken into consideration, it makes the two-way coupled model, more realistic than the one-way.

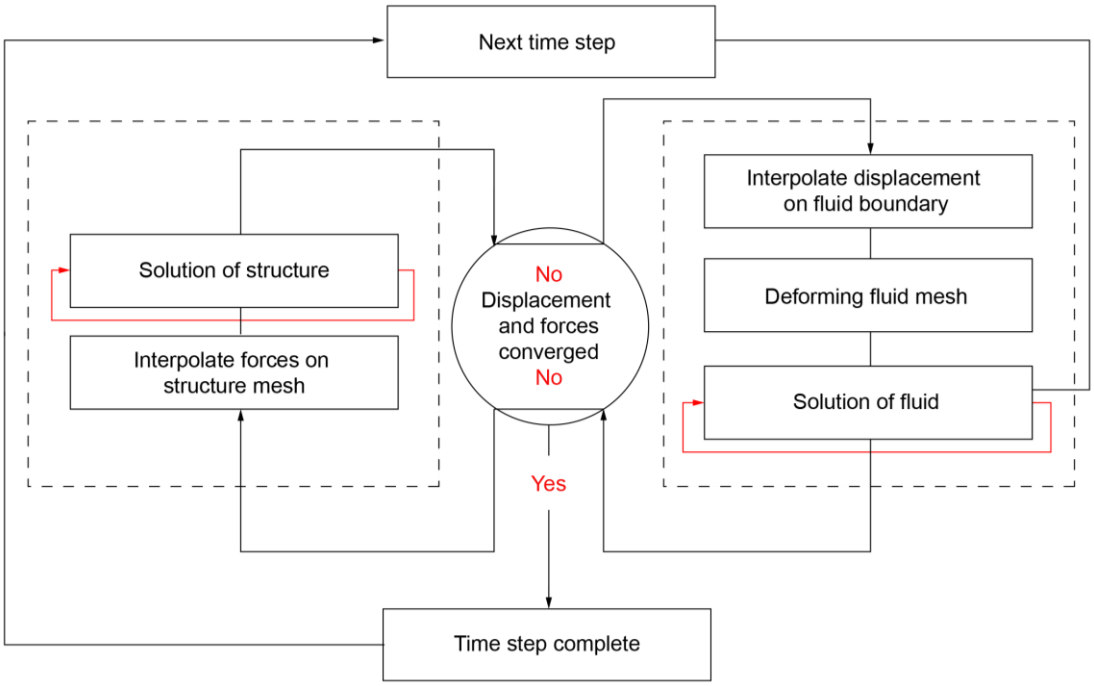

Figure 80. Two-way coupling diagram.

The process is also clear by observing the block connection in ANSYS® Workbench, shown in Figure 81. The fluid and structural domains are both connected in the system coupling domain.

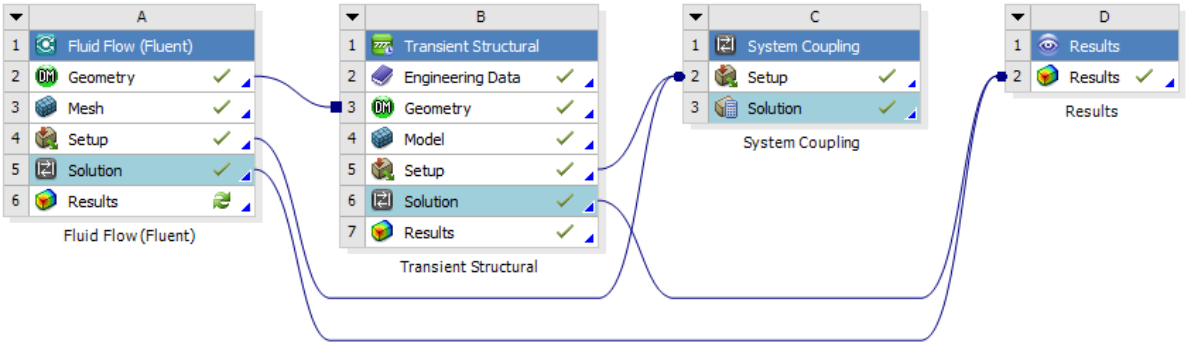

Figure 81. Two- way coupled model ANSYS® Workbench schematic.

The fully coupled model has taken significant time to simulate. It was estimated that 1.2s of computational time were computed in 24 hours. In total, 120s of simulation is presented in this section, which required just over three months to produce.

Initially, the drag and lift coefficients on the bluff body have been plotted as seen in Figure 82. The average drag coefficient for the steady state is 0.838.

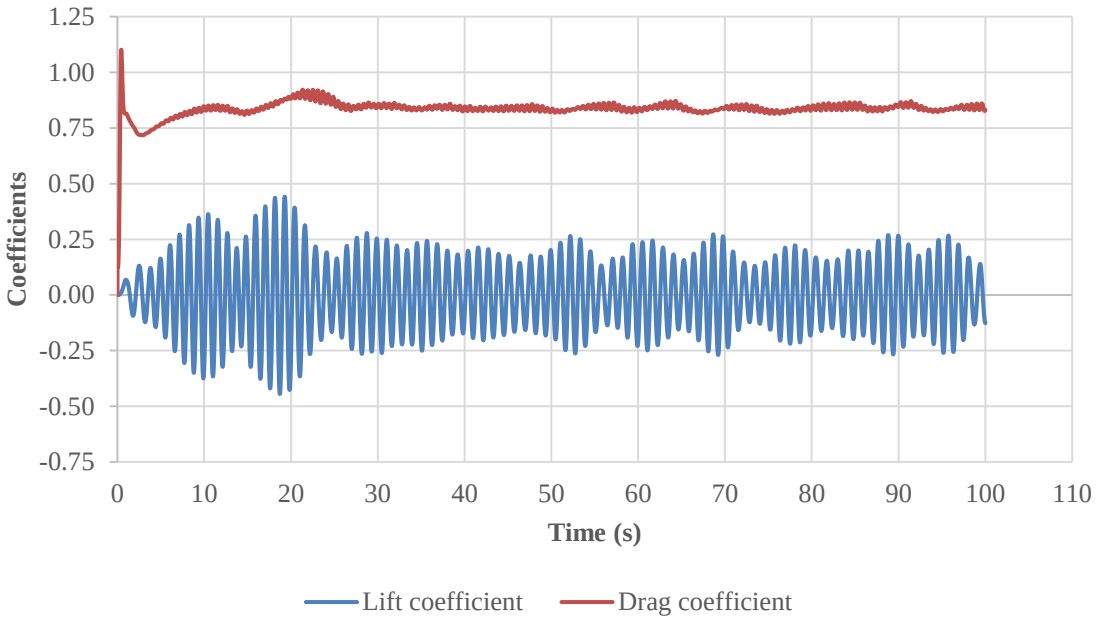

Figure 82. Bluff body lift and drag plot with the presence of flexible cylinder.

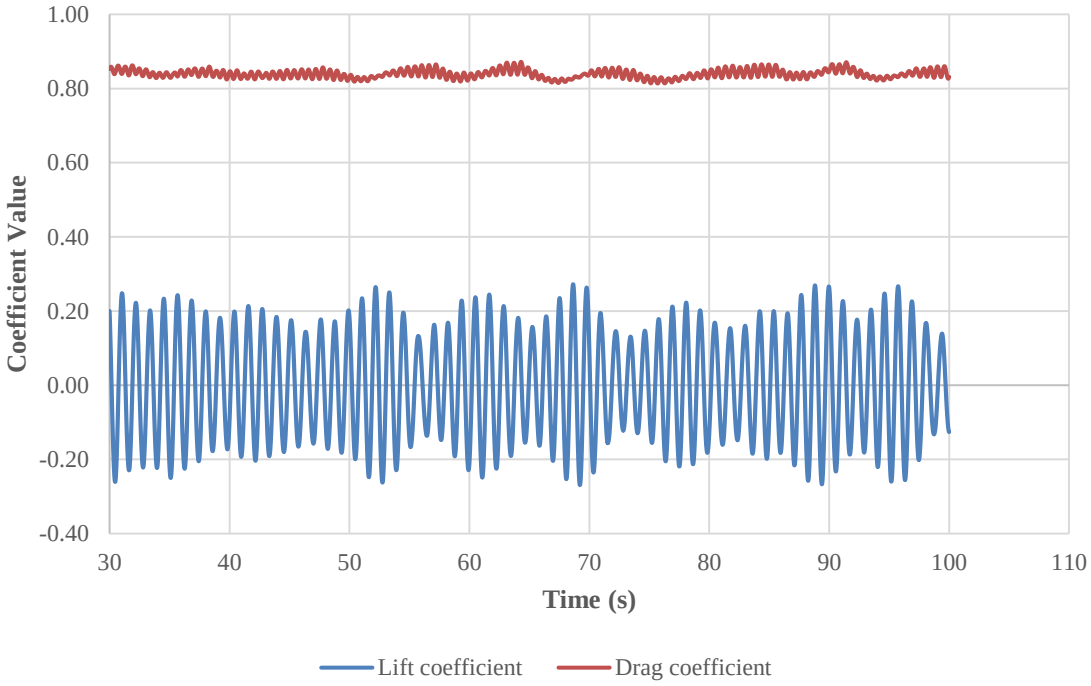

Figure 83. Zoom-in of Figure 82.

Figure 83 shows a zoom-in of Figure 82, making to easier to investigate the values of the two coefficients.

The dominant shed frequency of the two- way coupled model is 0.854Hz as shown in Figure 84. Two secondary shed frequencies are also present, at 0.927Hz and 0.732Hz. The existence of secondary frequencies can also be observed from the lift coefficient data in Figure 82. The oscillation between the 50th to the 55th second is similar to that between the 65th to the 75th. Also, the 55th to the 64th is similar to that at 75th to 85th seconds. From the 85th second onwards, the oscillation is slightly different than before. A detailed investigation is required to say with more confidence what is happening and potentially a longer simulation. The presence of the secondary frequencies can also be related to the vortex dislocation-like phenomena, as discussed in section 6.2.

The presence of the rope and the flexible cylinder in the flow should change the drag coefficient and frequency values and cannot be compared directly to the boundaries set earlier in this research, as discussed in section 4.5. However, the observation made is that the primary and the highest secondary frequency fall within the range of 0.891±0.055. In an attempt to compare the one and two- way models, it is observed that the drag coefficient and frequency values are different between the two coupled models. The author believes that this is expected because the exchange of data between the mechanical and fluid solvers is different but also because the data used are from different locations in time. For the one-way model, data from the first 20 seconds of the simulation were used, compared to the two- way where data after the 50th second were used. Therefore, comparing the results of the two coupled models will not be appropriate in first place.

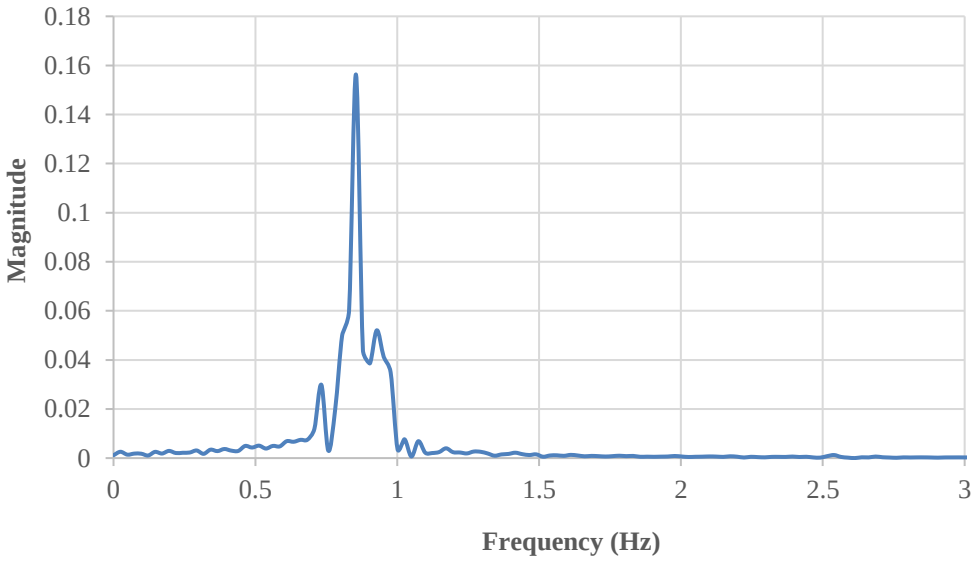

Figure 84. Bluff body shed frequency for the two- way coupled model.

The drag and lift coefficients of the flexible cylinder are presented in Figure 85. The most striking observation is that the lift is larger than the drag. As observed previously in the two and three-dimensional models, the drag is always larger. The increase in lift indicates that the perpendicular forces acting by the fluid on the flexible cylinder are much larger compared to the thrust of the drag forces. This will indicate that the shed vortices excide the flexible cylinder significantly.

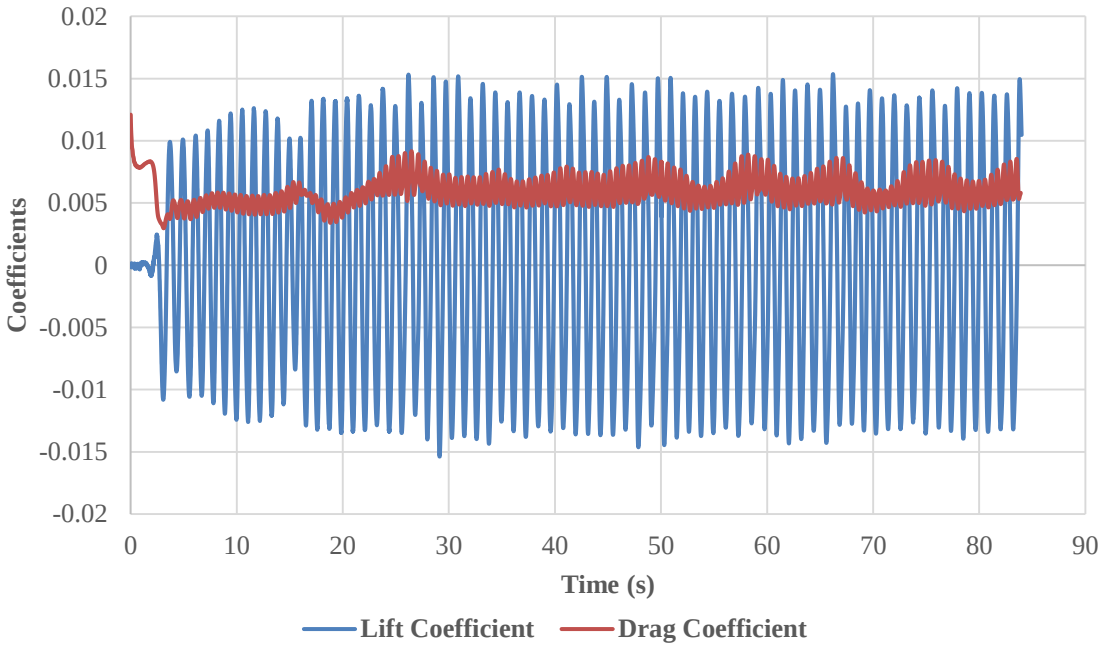

Figure 85. Flexible cylinder drag and lift for the two- way coupled model.

By observing Figure 86, a zoom-in of Figure 85, the average drag coefficient of the flexible cylinder is 0.006, significantly smaller than the drag of the bluff body. This is expected since the flexible cylinder exercise less resistance to the upcoming flow, compared to the bluff body.

The flexible cylinder's frequencies of oscillation were found and presented in Figure 87. A dominant frequency was observed at 0.836Hz, followed by 0.959Hz and 0.738Hz. Comparing the dominant and shed frequencies, there is a 2% difference, thus very close approximation. This implies that, most of the time, the flexible cylinder is 97.89% coupled with the shed vortices. Also, quantitatively comparing the shape of the flexible cylinder frequency periodogram with that of the bluff body, it is clear that there is a strong similarity.

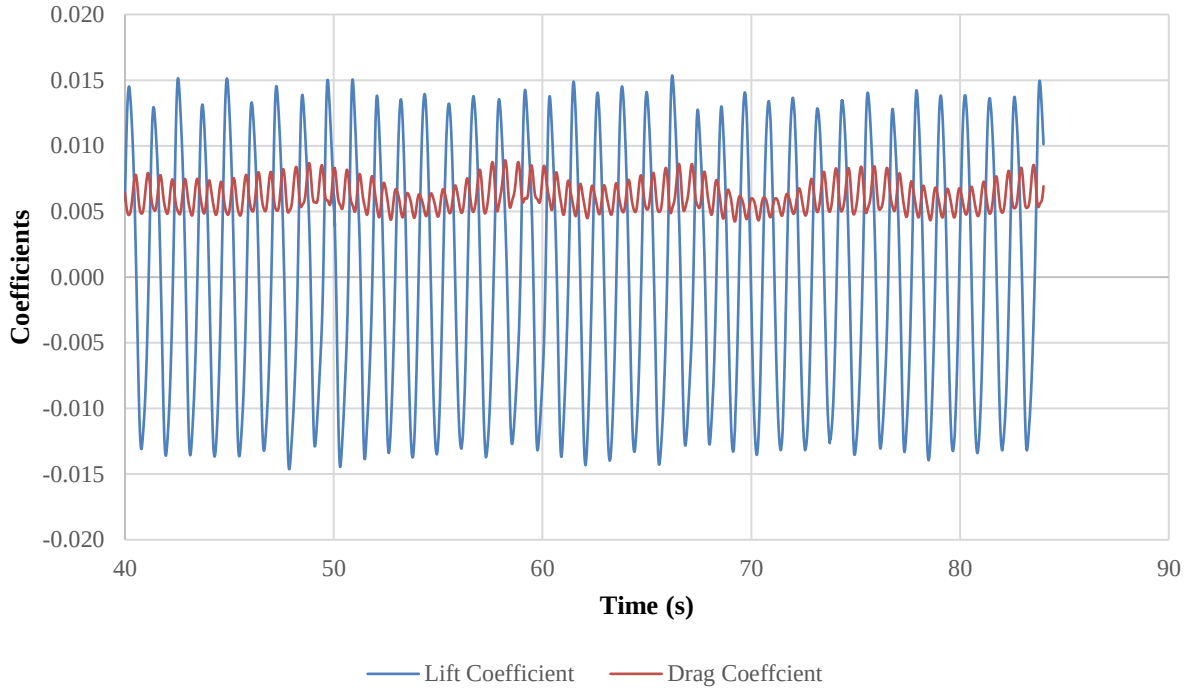

Figure 86. Zoom-in of Figure 85.

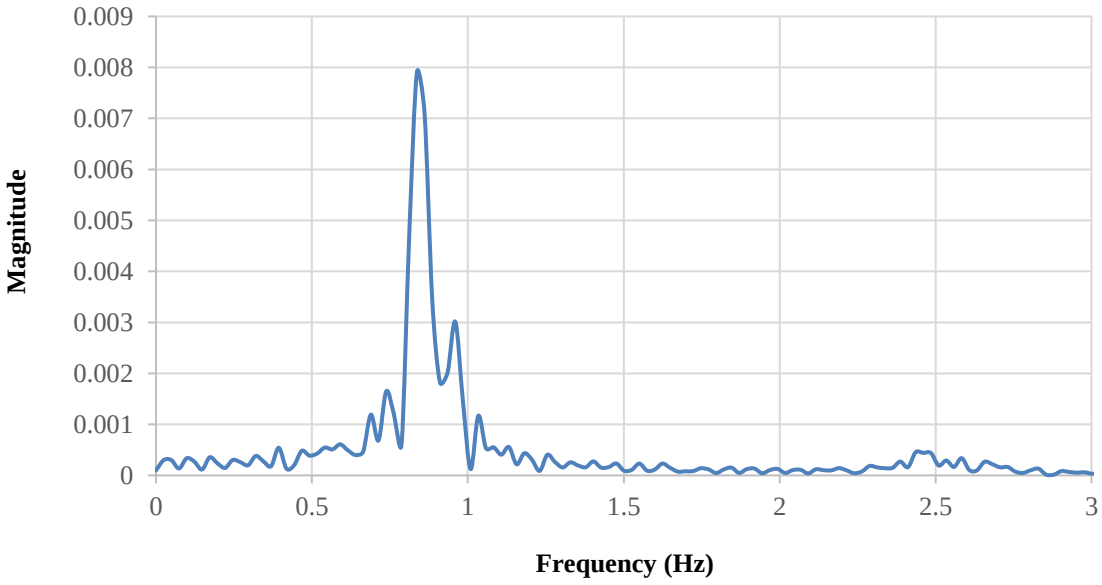

Figure 87. Flexible cylinder frequency for the one-way coupled model.

The analysis of the drag and lift data of the bluff body and flexible cylinder have shown that excitation of the flexible cylinder is taking place. Next is to investigate the development of the flow around the bluff body in three- dimensions, aiming to identify the same flow phenomena, already discussed in section 5.4.2.1, for the two-dimensional model. No axes were used on the screenshots included in following analysis, due to graphical restrictions. It shall be assumed that the direction of the flow always starts from

the backside of the bluff body and moving towards the front, reaching the flexible cylinder, and not the other way round. This has allowed the author to take screenshots at different angles and perspectives without clarifying the direction of the system every time. The fluid is depicted using the Q-criterion = 1, coloured with the velocity contour.

At t=0s, 'creeping flow' is observed, occurring at Re<5. The velocity magnitude streamlines are symmetrical not only around the cylinder's upper to lower side, but also around its front to rear Figure 88(a).

At t=0.36s, with the increase of Reynolds number ($5 < Re < 40$), a closed region of the streamline is generated within the cylinder's rear flow. The fluid in the upper half of this region rotates clockwise and the fluid in the lower half rotates counter clockwise. The separation points become visible as shown in Figure 88(b).

At t=0.5s, the increase of the separation angle is visible, with the increase of Reynolds number. Further development of the vortices takes place during the $5 < Re < 40$ regime, shown in Figure 88(c).

As the Reynolds number increases over time, the length of the vortex increases. When the Reynolds number exceeds 40, the flow downstream becomes unstable as shown and the vortex begins to oscillate in an up-down direction. Figure 88(d) shows that the vortex rotating clockwise started to detach from the bluff body and is moving downstream.

At t=2.5s, Figure 88(e) shows the fully formed vortex carried away on the surrounding main flow, while the counter clockwise rotating vortex on the other side has fully developed, forming the twin vortex that will follow the first. Subsequent of the vortex detachment from the bluff body, is the formation of a new, baby vortex and it is visible between the two large vortices.

(a) t=0s

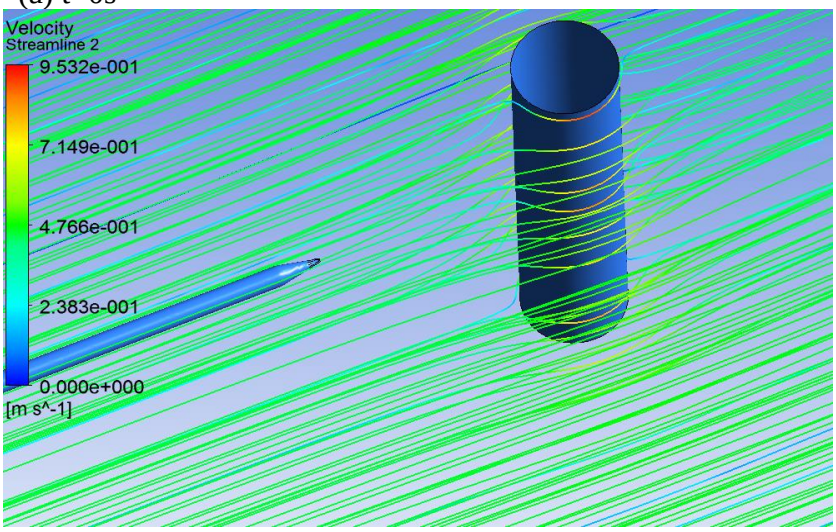

(b) t=0.36s

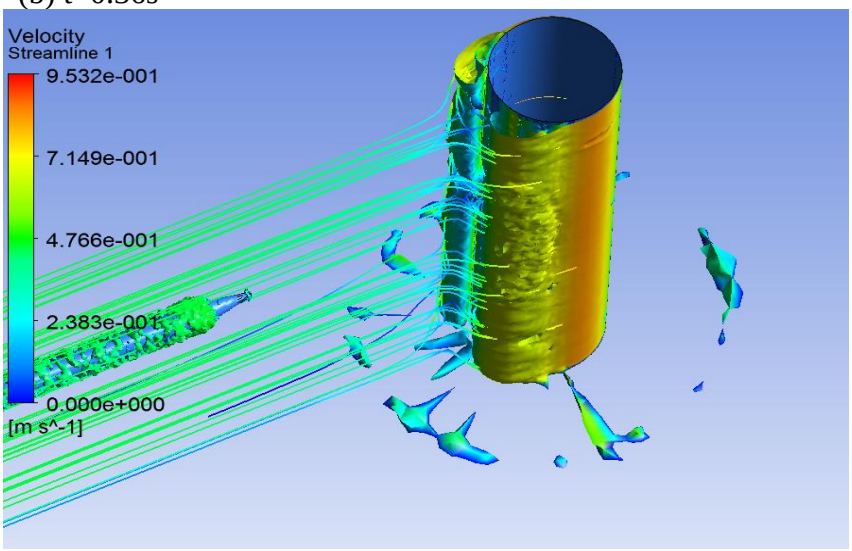

(c) t=0.5s

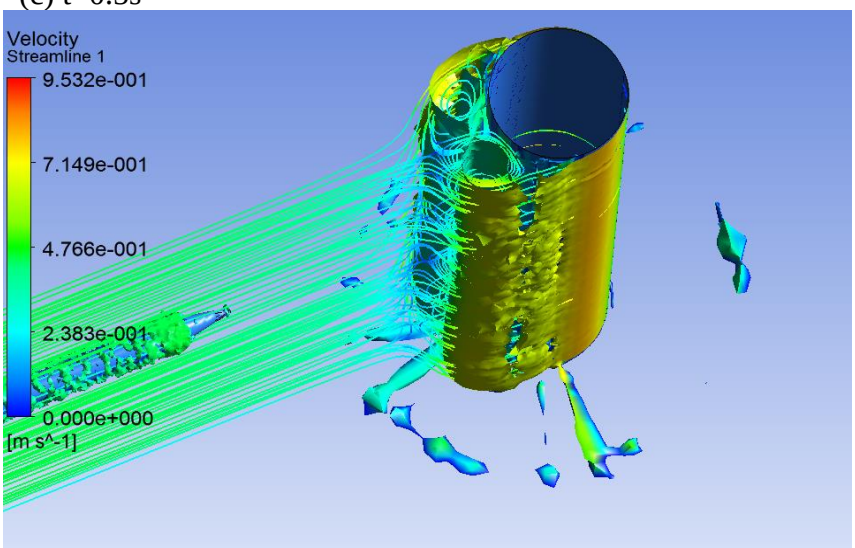

Figure 88. Flow development around the bluff body in three- dimensions.

(d) t=1.03s

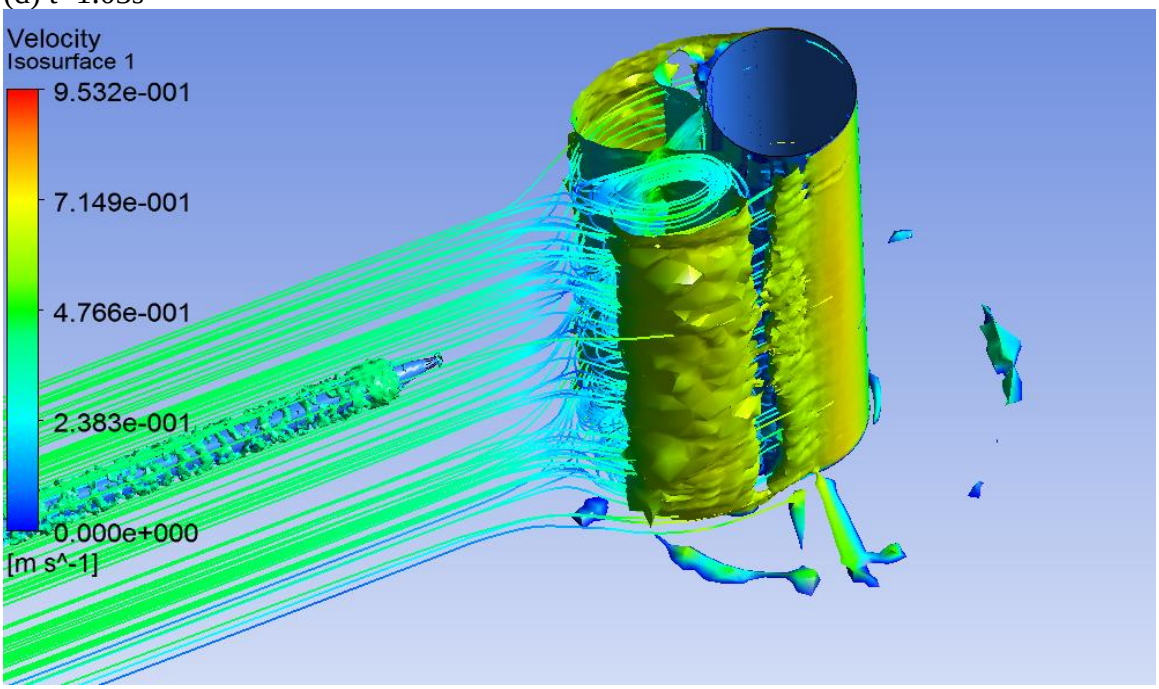

(e) t=2.5s

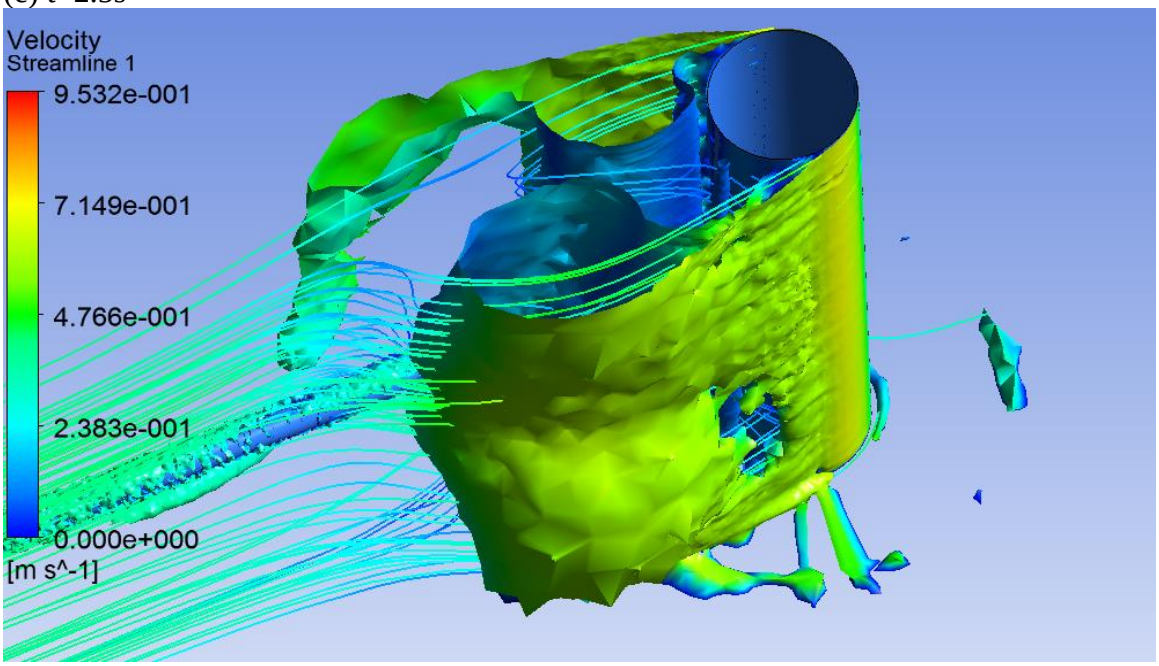

Figure 88. Flow development around the bluff body in three- dimensions.

The next step is to investigate the oscillatory motion of the flexible cylinder in respect to the vortices. To achieve this, the structural deformation of the flexible cylinder was inspected in the mechanical solver and compared with the fluid environment in CFD Post, the ANSYS® post-processing suite. Figure 89 shows the oscillation trace of the flexible cylinder as computed by the mechanical solver. The plot represents the maximum deformation of the flexible cylinder in time, in respect to the neutral axis (rigid body). Most of the time, if not always, the displacement represents that of the tail in respect to the neutral axis in any of the three directions. Thus, in contrary of the experimental results, it is not the deformation of the flexible cylinder from a plane in parallel to the bottom of the water channel.

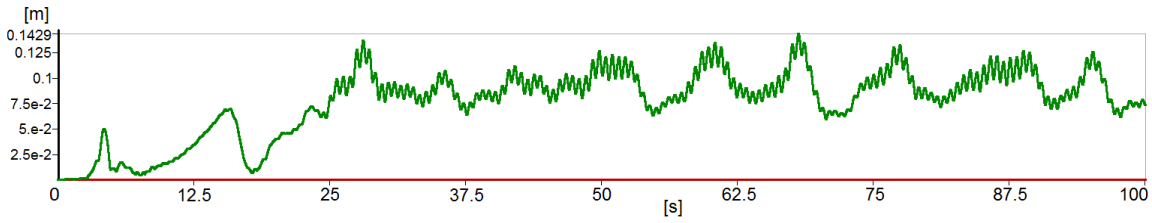

Figure 89. Flexible cylinder oscillation trace in the two-way model.

Observing the first few seconds of the oscillation, no significant displacement of the flexible cylinder is visible. As already observed in Figure 88(e), the first vortex shed from the bluff body had not reached the flexible cylinder until the 2.5th second. When zooming in the mechanical suite (structural), it is possible to observe that the flexible cylinder tail is moving in the order of micrometres, most probably due to the disturbance of the flow by the upcoming vortex and the flowing fluid, from inlet. However, since this is negligible, it can be assumed that there is no displacement. The positive from this observation is that this might be useful when designing a senor application.

At the 2.9th second, the first measurable deformation is initiated. As observed in Figure 90 (top), the first-ever shed vortex has reached the flexible cylinder located at the first half. The flexible cylinder started deforming in the order of millimetres, thus still not identified on the deformation contour since it is in meters. The pair vortex traveling on the other side of the flexible cylinder is located between the rope and the nose, justifying the displacement of the nose from the neutral axis. It is also possible to observe the change of the velocity around the BMC of the flexible cylinder due to the deformation caused by the vortex.

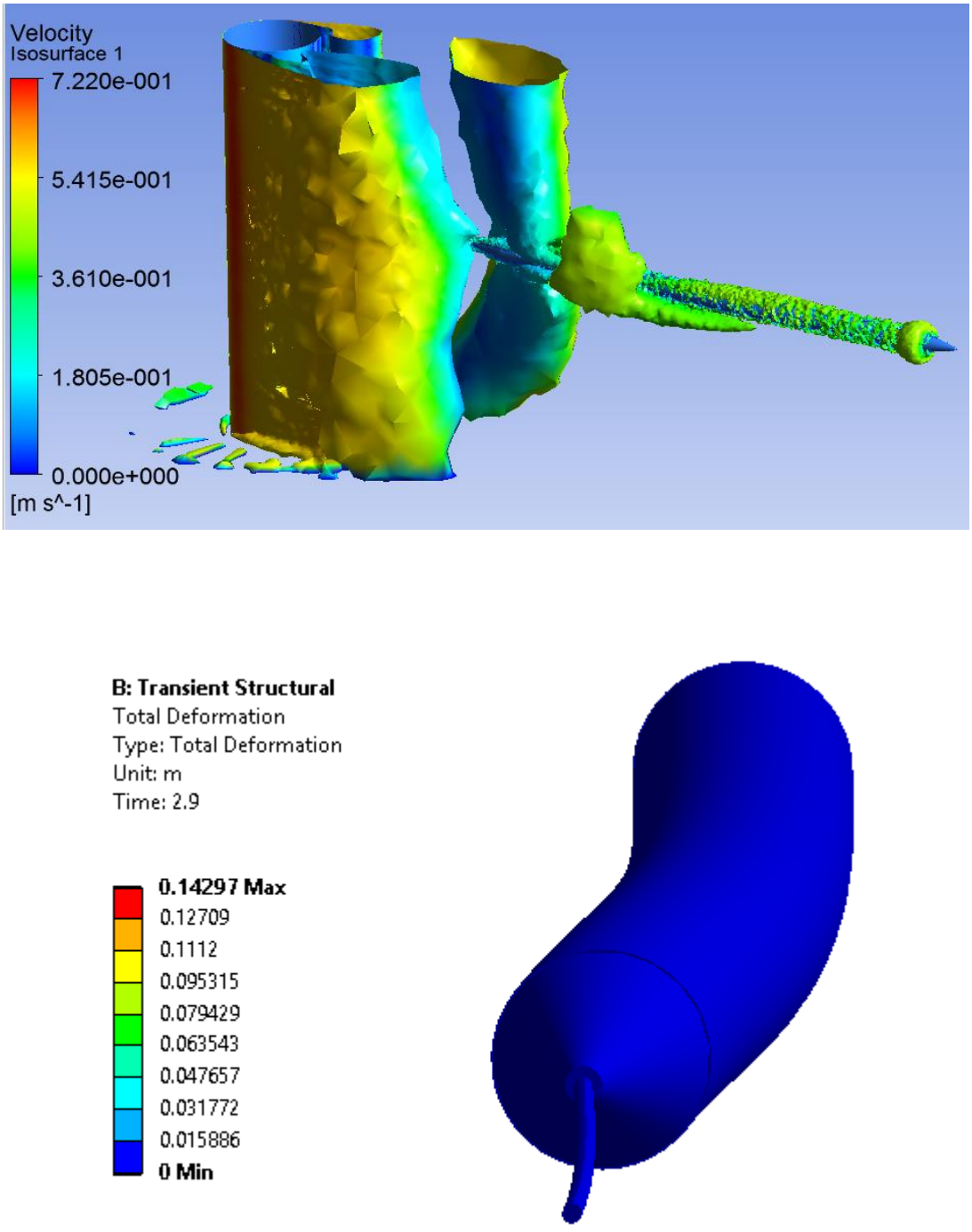

Figure 90. Investigation of flexible cylinder deformation at 2.9s.
Top: CFD Post | Bottom: ANSYS® Mechanical

At the 3.5th second, the first vortex located in the first half, on the right side of the flexible cylinder is moving downstream. Its pair vortex, previously located between the rope and nose, has not moved downstream and deformed the flexible cylinder, as shown in Figure 91. From the size of the first and second vortices, it can be observed that the second vortex carries more kinetic energy than the first vortex. This has also be confirmed by changing the Q-criterion colouring from velocity to kinetic energy. It can also be confirmed by looking at the deformation of the flexible cylinder, being at the location of the second vortex and not any more where the first one is located.

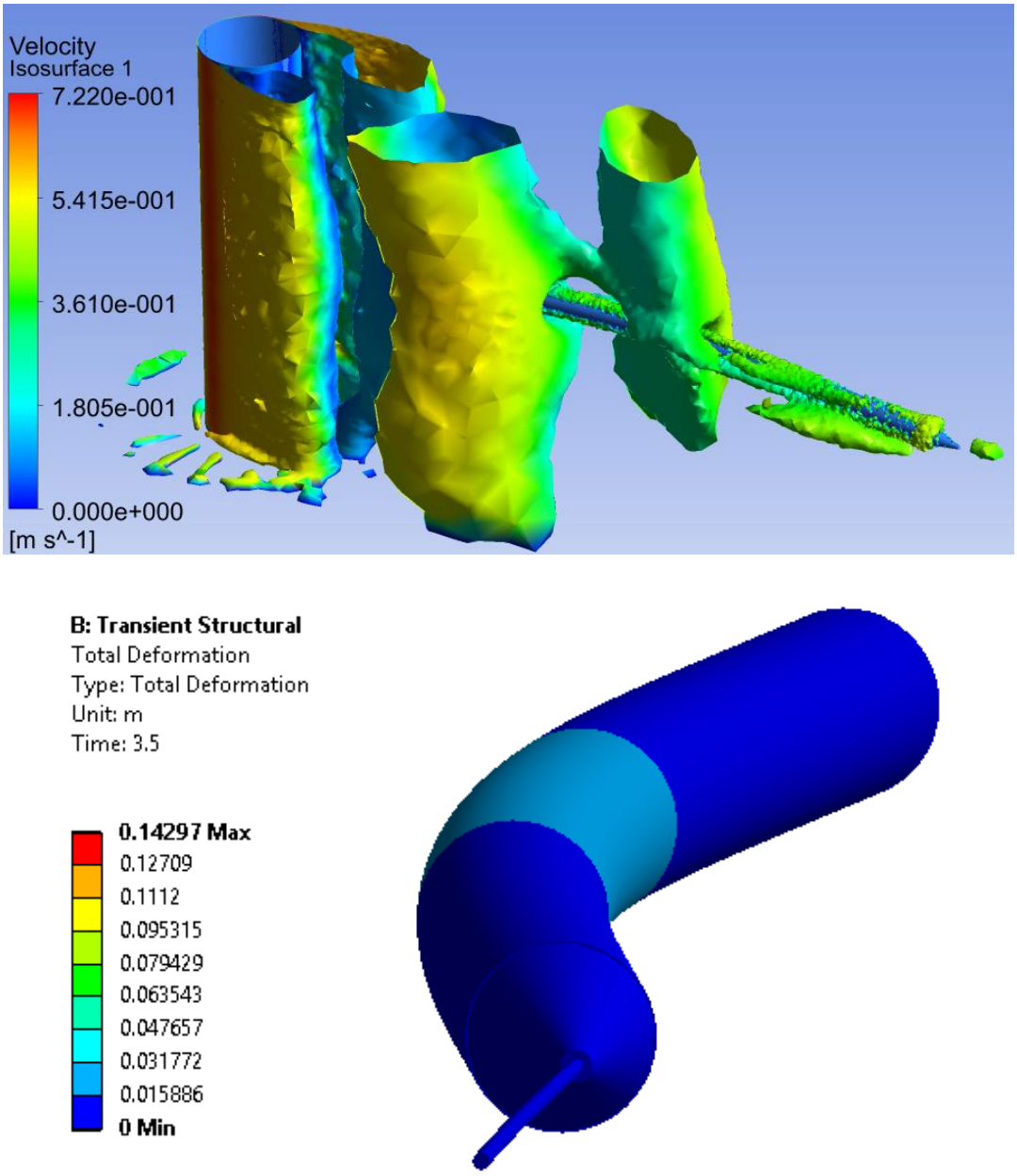

Figure 91. Investigation of flexible cylinder deformation at 3.5s.

Figure 92 and Figure 93 show the vortex development during the 14th to the 17th where significant deformation takes place, as shown second in Figure 89. The Q-criterion has changed to 0.25 to capture more details. It is clear that the second half of the flexible cylinder is moving upwards by the shed vortices until around the 16th second. Then, by the 17th second, the second half of the flexible cylinder has moved near the neutral axis. Figure 94 shows the deformation of the flexible cylinder tail, reaching around 8cm.

t=14s

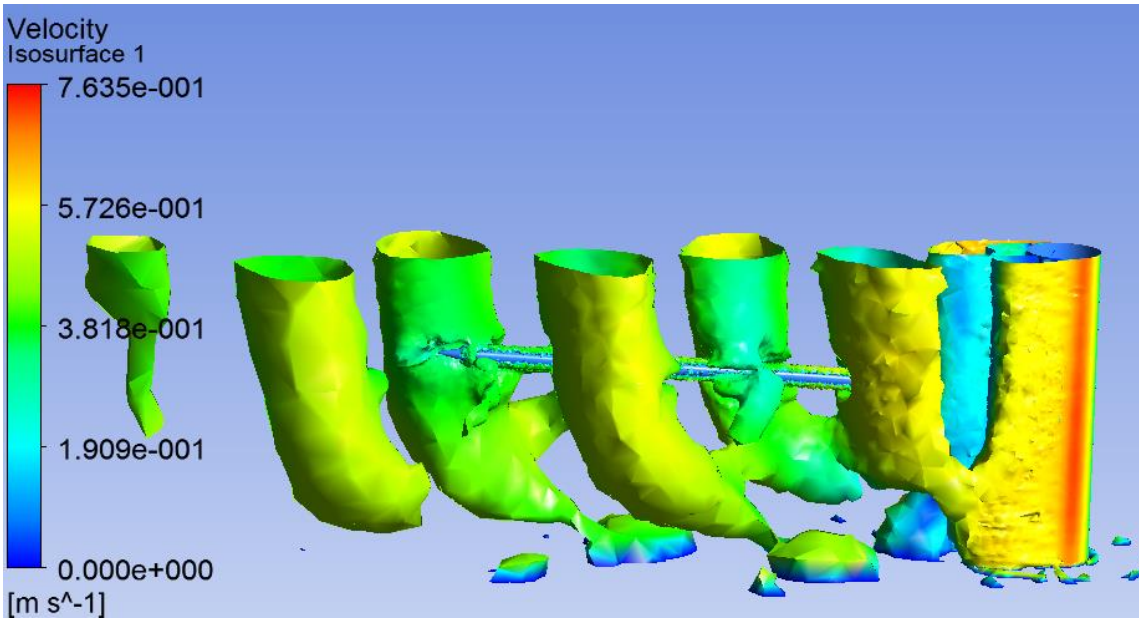

t=14.5s

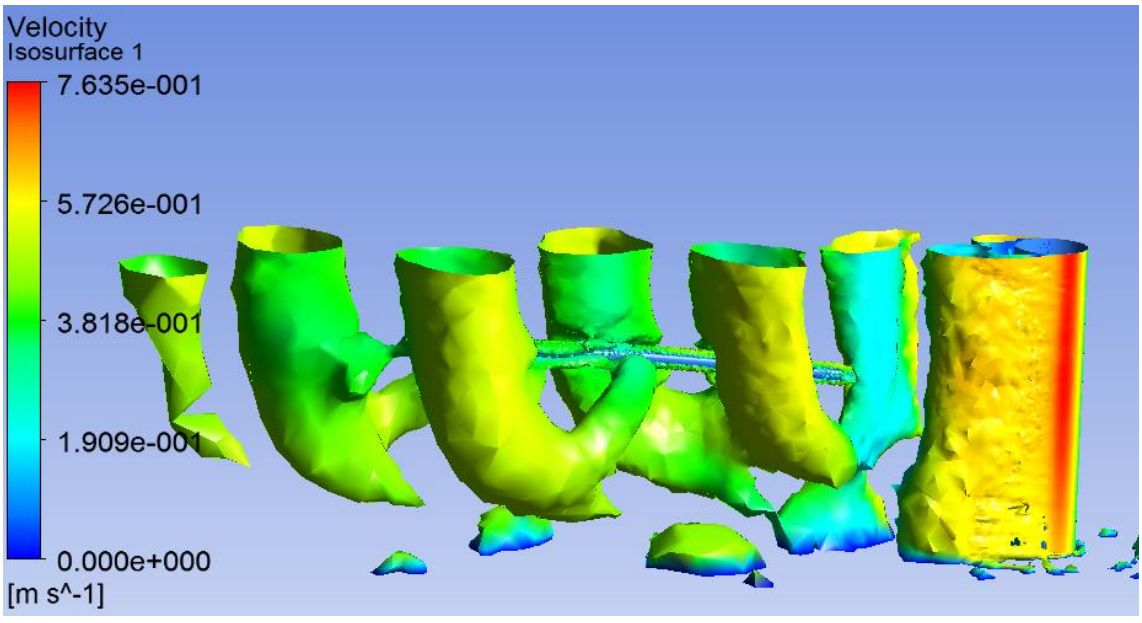

Figure 92. Investigation of flexible cylinder deformation between 14-14.5s

t=15s

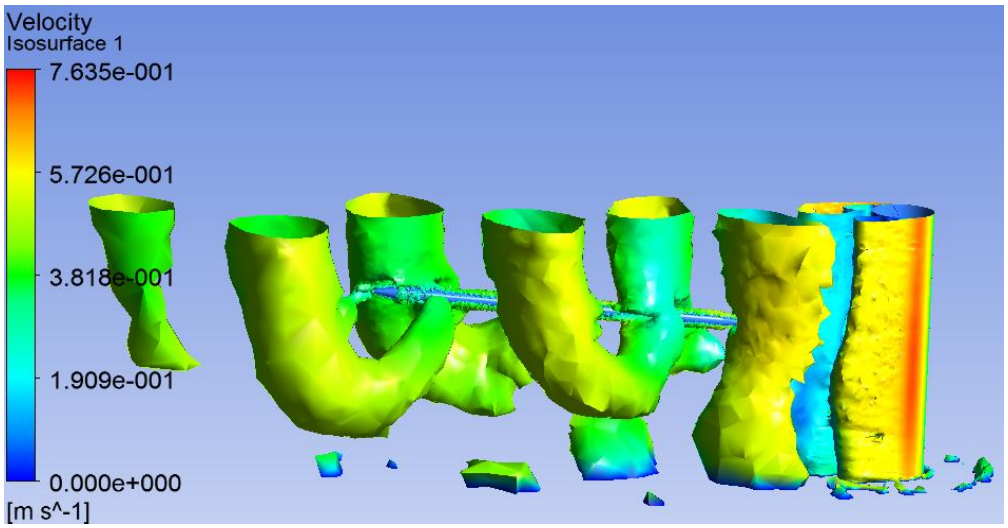

t=15.5s

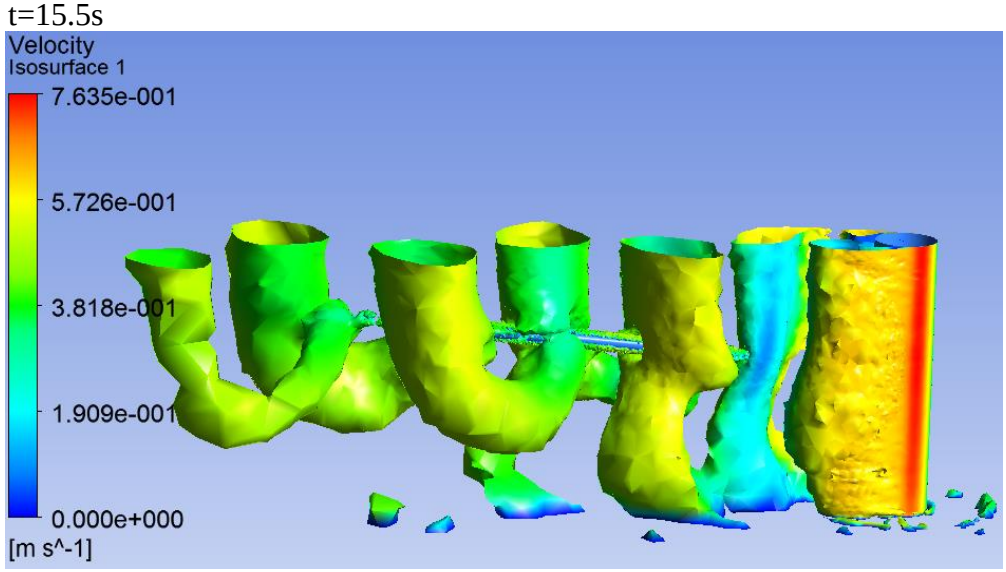

t=17s

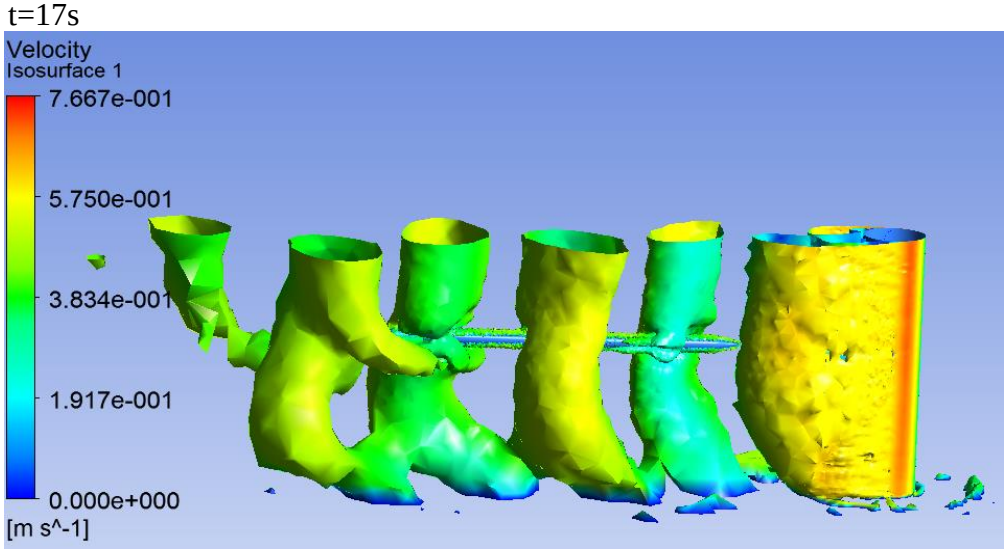

Figure 93. Investigation of flexible cylinder deformation between 15-17s.

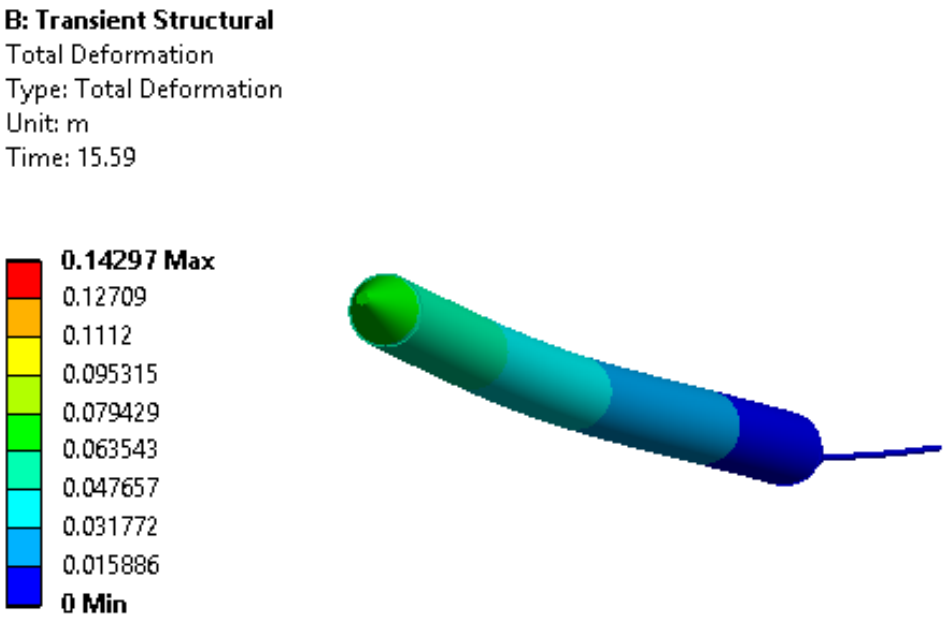

Figure 94. Investigation of flexible cylinder deformation at 15.59s

Another interesting observation is the tail behind the head of the vortex. It resembles a tornado. This tornado-effect is due to the no-slip condition applied at the bottom of the domain, in contrast with the zero shear boundary condition at the top of the domain (free surface).

In section 5.4.2.2, it has been discussed that during transition, a distinct and intermittent switching of the flow field is visible. There is a low frequency modulation in the time-series with the usual shedding mode. The unusual intermittent low frequency modulation phenomenon has been attributed to the formation of large-scale irregularities, namely vortex dislocation. It may be mentioned that vortex dislocation is generated between the spanwise cells due to the out-of-phase movement of the primary vortex in each cell. However, the natural vortex dislocation may appear randomly in space as well as in time. In the aforementioned figures, and more clear in Figure 95, there are instances that the vortices have shape that of a sausage, crossing the flexible cylinder and connect with their pair vortex. It is believed to be due to the dislocation-like phenomenon, however further investigation required to draw certain conclusions. Unfortunately, such kind of investigation is outside the scope of this research. Potentially, this can be a question, for a new research topic.

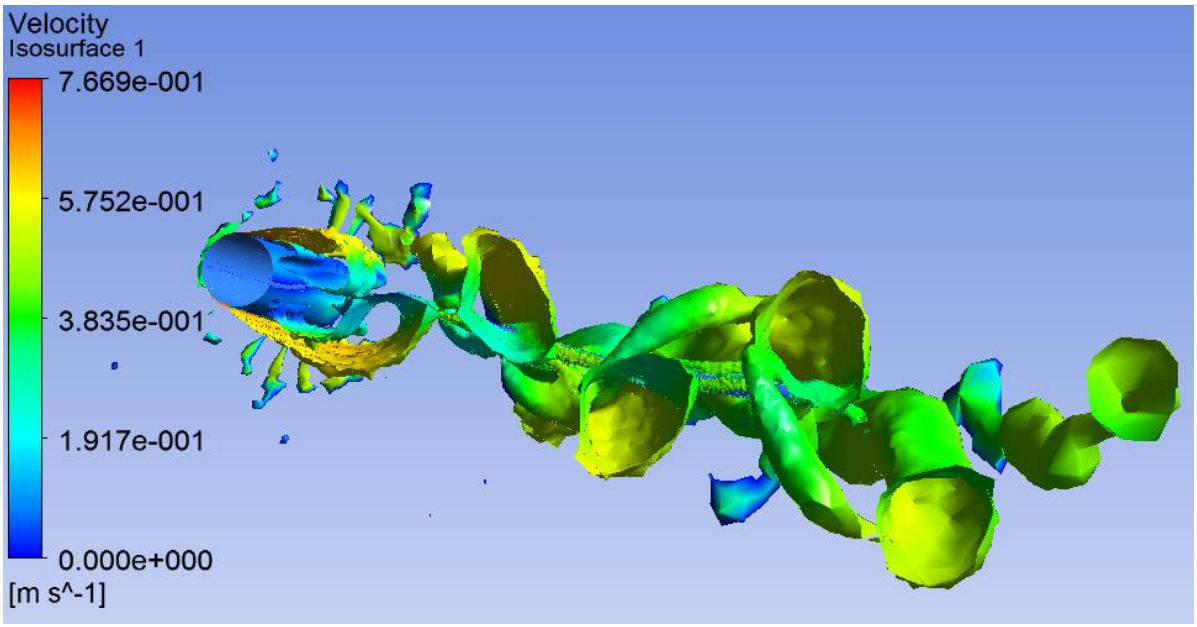

Figure 95. Investigation of flexible cylinder deformation at 77.25s

Finally, set of data were combined on one graph for observation, shown in Figure 96. It can be observed that there is a distinctive correlation of oscillation between the flexible cylinder's displacement and drag coefficient data and bluff body's lift coefficient.

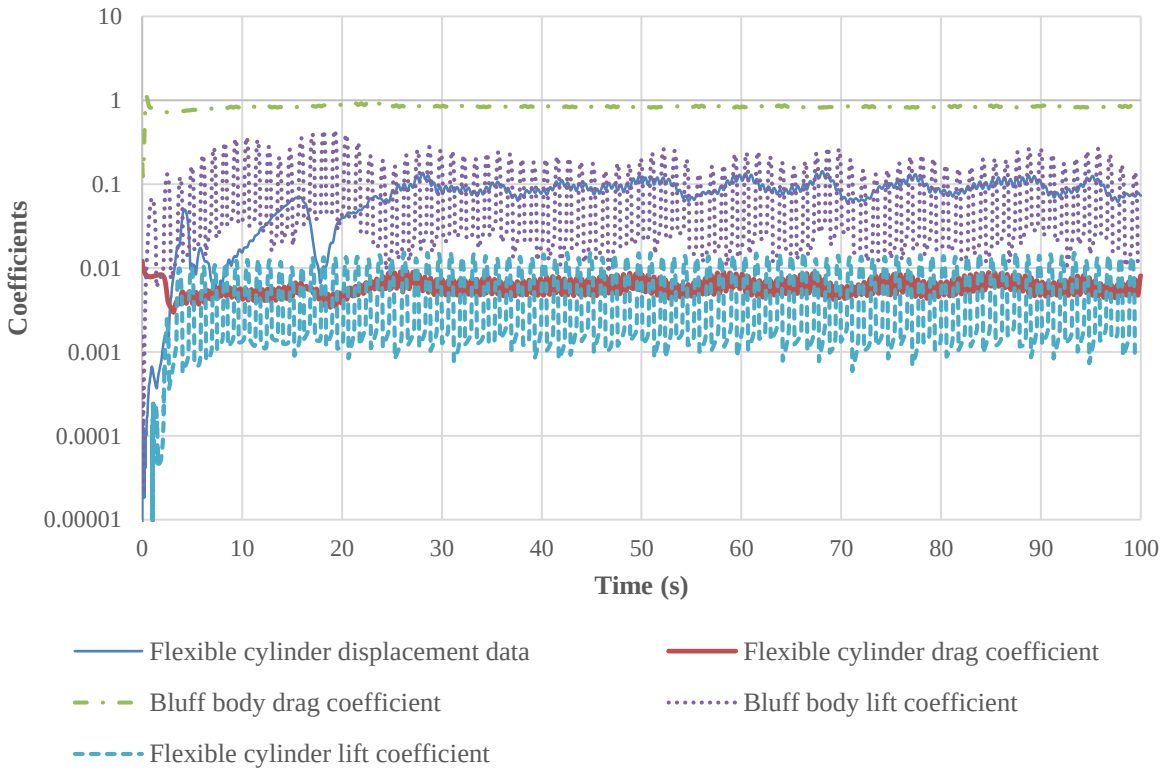

Figure 96. Overall observation of bluff body and flexible cylinder response.

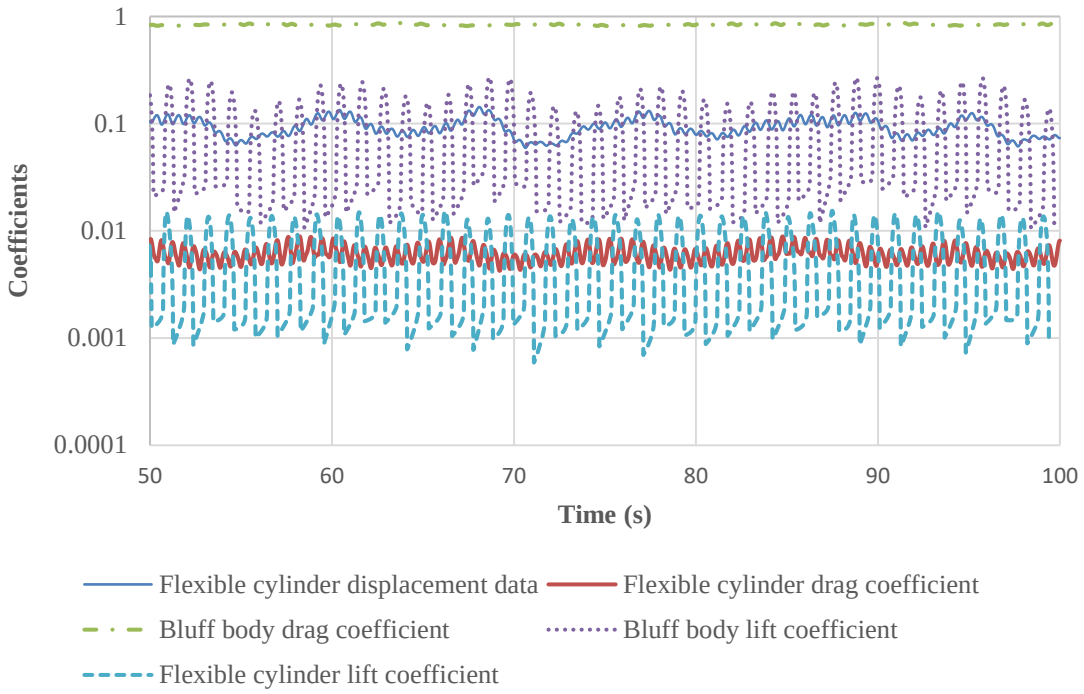

Figure 97. Zoom-in of Figure 96.

Figure 97, a zoom-in of Figure 96, puts all data in perspective, allowing a clearer comparison.

A qualitatively comparison between the experimental observations in chapter 4, Figure 34 and the computational model follow and presented side by side in Figure 98. At computational time t=37.25s, three clearly visible vortices running along the length of the flexible cylinder can be identified. One in the upper part (rotating anticlockwise) of the frame acting on the marking just before the nose, one vortex in the middle of the cylinder (rotating clockwise) and one at the tail of the cylinder (rotating anticlockwise). At t=38.5s, the clockwise rotating vortex in the middle of the cylinder travels down the length of the flexible cylinder. At the same time, the anticlockwise vortex located at the tail is passing the flexible cylinder (t=38.50s) and by t=38.75s, the anticlockwise vortex at the tail of the cylinder is replaced by the clockwise vortex where it reaches maximum displacement.

Furthermore, similarly to the experimental observations, modes 0, 1 and 2 are present in the oscillation of the computational model, as presented in Figure 28.

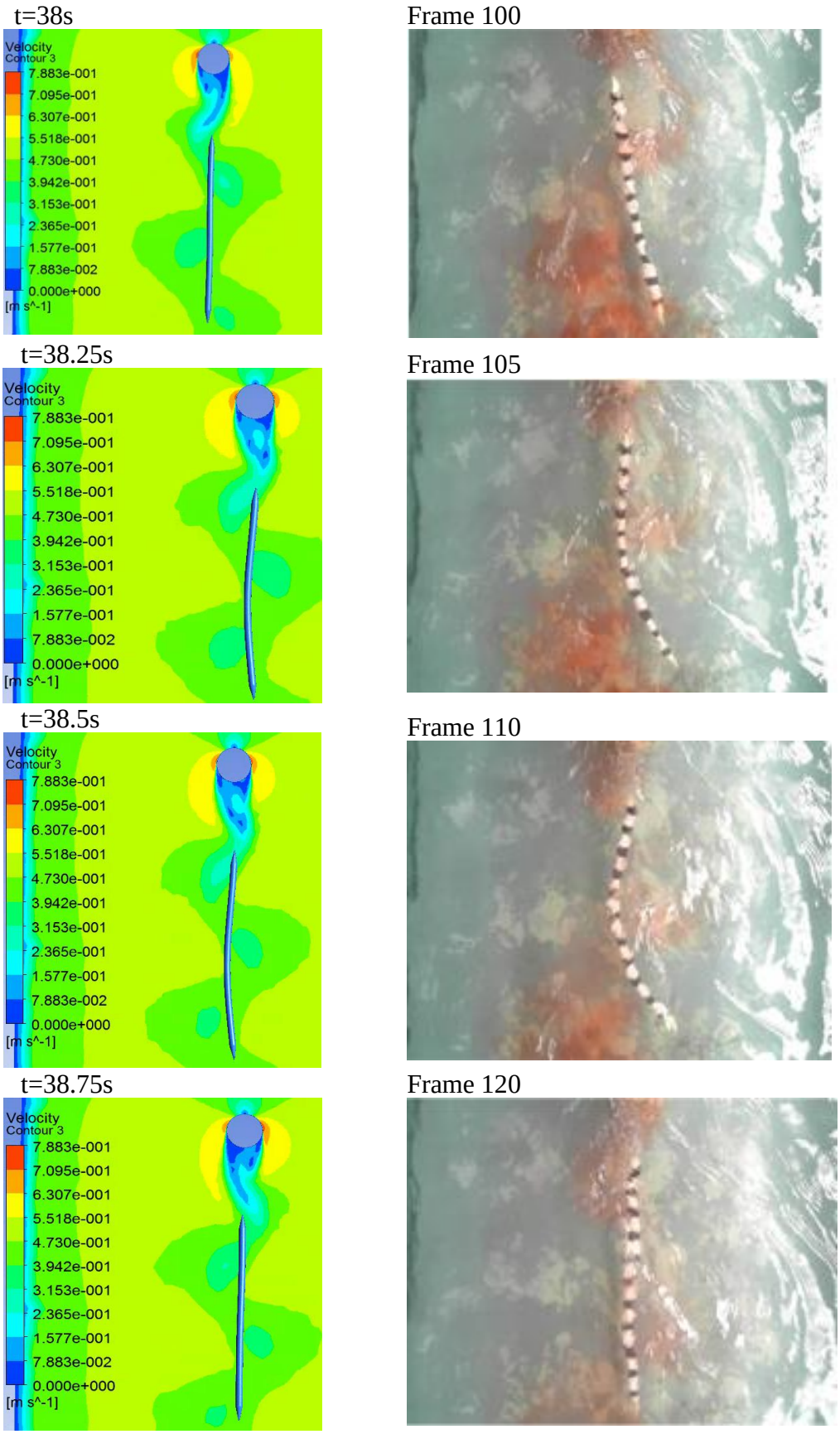

Figure 98. Qualitatively comparison of experimental and computational flexible cylinder oscillation.

In general, it can be said with certainty that the flexible cylinder does tend to flex according to the respective vortex passing along its length, in what appears to be a synchronised slaloming mode similar to that shown in Figure 6, in the literature review. This method of swimming, where the object mimics the shape of a swimming fish, as described in the literature, would be expected to exploit the environment to minimise drag and potentially produce thrust, only to enforce the ultimate goal of this research, to investigate whether there is potential of energy harvesting from this system arrangement.

To measure the amplitude of the oscillation, the directional deformation investigated, in the axis in parallel with the bottom of the channel. The results of the simulation adjusted to run on 'true scale 1.0' on the respective measuring scale. Similarly to the one- way model, the animation settings have been set to 100 frames and 10 seconds interval. The same methodology has been used as the experimental procedure, presented in Figure 36. The amplitude values are average of four measurements with standard deviation of 3.5%.

The maximum amplitude over one cycle of the tail has been found to be 0.22m and of the body 0.19m. Despite the small difference, the approximation found is of a reasonable degree of difference. The computational model simulates a much more ideal environment compared to the experimental one. The turbulence model also contributes in a large extend to the obtained results. Discrepancies of this magnitude, and especially for a fully coupled simulation are expected.

Finally, the exact same two- way coupled model analysed earlier at a velocity of 0.453m/s, was run at a different velocity. The aim of this test was to see whether the model is sensitive to velocity changes. The new velocity was 0.503m/s. Figure 99 shows the lift and drag coefficient graphs for the two velocities. As expected, there is difference in the drag coefficients. Since drag force is proportional to the square of the velocity, the drag at 0.503m/s should be greater than the 0.453m/s. In regards to lift coefficient, further analysis is required, therefore, no conclusions can be drawn at this stage.

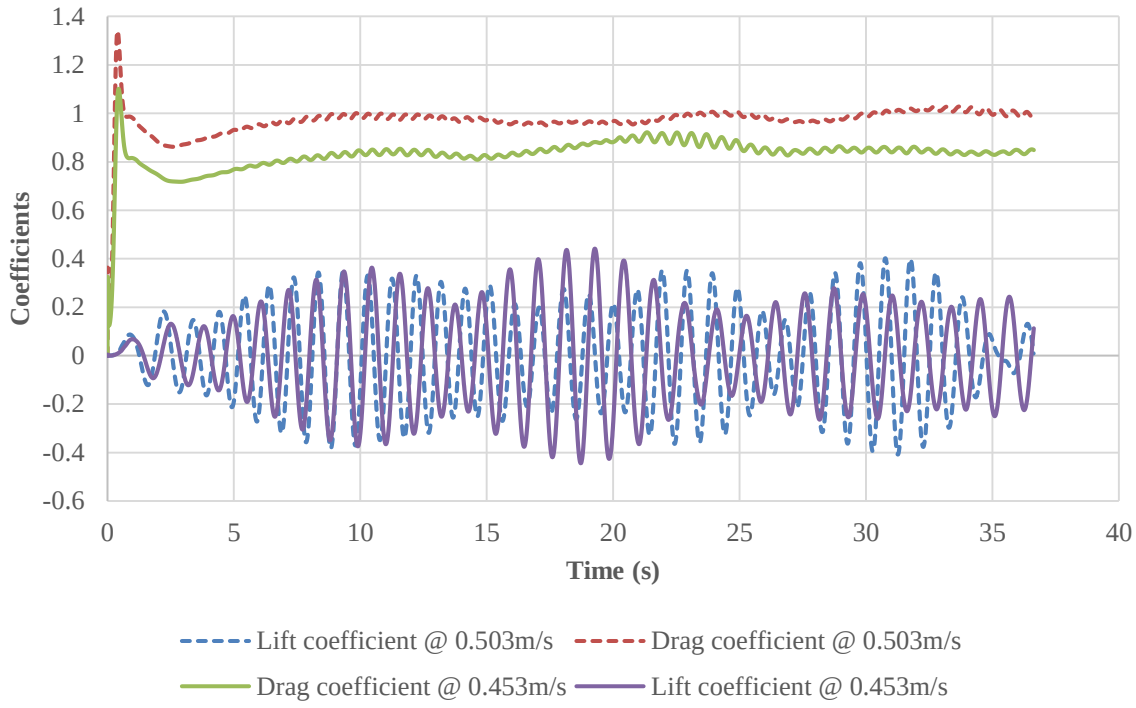

Figure 99. Drag and lift coefficients for 0.503m/s in comparison with 0.453m/s.

6.2.2 Conclusion

The author openly admits that the two- way computational model produced is very data rich and it is not possible to present all the possibilities of investigation in this research. The fully coupled model has been analysed and expected flow phenomena identified. The frequencies of oscillation and the amplitude are very satisfactory. In future research topics, the model and the design methodology used can be used to simulate a range of flow velocities, different diameters and lengths of the flexible cylinder and bluff bodies. This will give trends on how the system will behave at different natural characteristics.

6.3 Summary

The second objective of this research is to determine the amplitude and frequency tuning of an inanimate object to a specific, or series, of unsteady flow regimes, from where, in the future, energy extraction would be possible. For this, a flexible cylinder has been designed and built, where the natural characteristics have been found through theoretical, experimental and computational analysis.

The natural frequency of the flexible cylinder and amplitude are found using one and two way coupling computational models. Both models are investigated and their limitations are discussed. It was found that the one-way, transient CFD/FEA model does not fulfil adequately the expectations of this research. The frequency of oscillation and the amplitude of the flexible cylinder were underdeveloped. This is due to the one-way coupling because this method of data exchange does not take into consideration the deformation of the flexible cylinder occurring in the structural part of the model and does not pass this information to the fluid model. In other words, the fluid domain is not affected by the presence of the flexible body, or its deformation. Therefore, a fully coupled, two-way fluid-structure interactions model has been created. The results found are very satisfactory. Quantitatively and qualitatively analysis has taken place, where flow phenomena were identified over time. The flexible cylinder frequencies of oscillation and amplitude are found to be of good agreement with the experimental results. Observation of the vortex development and excitation of the flexible cylinder are the same as the experimental analysis.

Overall, chapter 6 has validated the computational system in four different stages, using experimental, theoretical and computational results. Any limitations have been identified which will be considered at a later stage during this research, if necessary. The work done has proved that the, fully coupled, three- dimensional model is sufficiently robust and can be used for simple engineering applications to predict scenarios at different flow velocities and possibly different inanimate body geometries. Having a computational model, qualitatively and quantitatively validated fulfils the third objective of this research and allows to proceed towards the completion of this research with the purpose of harvesting energy out of vortex induced vibrations on a flexible cylinder in the water.

Chapter 7

Development and Assessment of Energy Harvesting Device

When a piezoelectric material is strained, an electric charge is generated [169] and this feature is widely exploited in sensors and energy harvesters. Piezoelectric energy harvesters are the most widely researched form of energy harvester with considerable effort spent on improving piezoelectric material properties and harvester performance. This research is investigating the feasibility of such a piezoelectric device, when integrated into the flexible cylinder described earlier, will be able to harvest energy from the shed vortices.

Initially, a step-by-step methodology for fabricating and polarising a flexible piezoelectric device is presented. Then, the piezoelectric device is integrated into the flexible cylinder with the aid of a custom designed apparatus. This has transformed the flexible cylinder to an active energy harvester.

To test the response of the flexible cylinder with the integrated piezoelectric device, a test machine for material characterisation is used, where the frequency and amplitude of oscillation can be predefined. The biggest challenge during the experiment setup was to set the boundary conditions such that they represent the boundary conditions of the experimental investigation in the water. It is important that the oscillatory motion of the flexible cylinder on the test machine is as close as possible to the excitation of the flexible cylinder due to shed vortices.

Finally, the experimental results are presented and analysed. It has been found that a flexible cylinder with integrated piezoelectric device could potentially be used as an energy harvesting device as well as a sensor, always subjected by the nature of application and the energy needs.

7.1 Experimental Design

This section describes the work undertaken to create an in-house flexible piezoelectric device which has then being encapsulated into the flexible cylinder. The research presented in this chapter has built upon the experimental work presented in chapter 3 as well as previously published investigations into the formulation of low temperature screen printable piezoelectric composites carried out at the University of Southampton. A previously defined and best performing piezoelectric formulation [170] has been taken and used to reproduce the piezoelectric film following the necessary process, as presented in section 7.1.1. Section 7.1.2 presents the method of encapsulating the piezoelectric device into the flexible cylinder, including a discussion on difficulties and limitations faced.

7.1.1 Method for Creating the Piezoelectric Device

This section presents all the steps undertaken in order to fabricate the piezoelectric device used in this research. A graphical representation can be seen in Figure 100. To begin with, the structure of the piezoelectric device is designed. The device consists of three layers which will be printed one on top of the other on the substrate. To print each layer, it is necessary to manufacture a screen-printing mesh with the respective dimensions. Each layer will be printed and then cured in the oven at the predefined temperature. When the screen-printing and curing process is complete, the piezoelectric device undergoes a poling process, polarising the piezoelectric film after which the piezoelectric coefficient, $d_{33,}$ is measured.

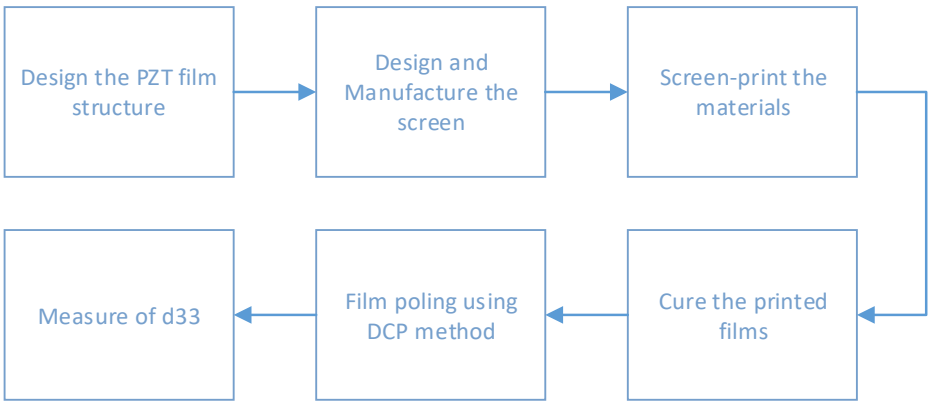

Figure 100. Experimental plan of piezoelectric device manufacturing and poling.

Material deposition can be divided into two categories depending on the thickness of the deposited layers, that is, thin or thick depositions. Thick films usually have thickness between $1\mu - 200\mu$ [171], thus the piezoelectric film in this research can be classified as thick, as it will be discussed later. Thick film technology is a deposition method that is capable of depositing/printing films with greater thickness in one deposit /print. This allows for an increase in production at reduced time and cost.

There are a number of types of printing methods, such as inkjet printing [172] [173] and screen printing. This research has used the screen printing method. Screen-printing is the technique of depositing materials by forcing inks with different compositions and rheological characteristics through a pre-patterned screen onto a substrate surface [174].

Initially, the piezoelectric film structure was designed. To investigate the piezoelectric properties (d_{33}) of the material, it requires the device to be in a capacitor structure. As the mechanical force is in the 3rd direction, on the top electrode, the charge extraction will be also be in the 3rd direction and will be collected using top and bottom electrodes, as discussed in section 2.5.1. The capacitor structure requires two electrodes with the piezoelectric material sandwiched between them, as shown in Figure 101. This capacitor structure will enable contact poling of the piezoelectric material and straightforward connection to the electrodes for the measurement of d_{33} and in actual use.

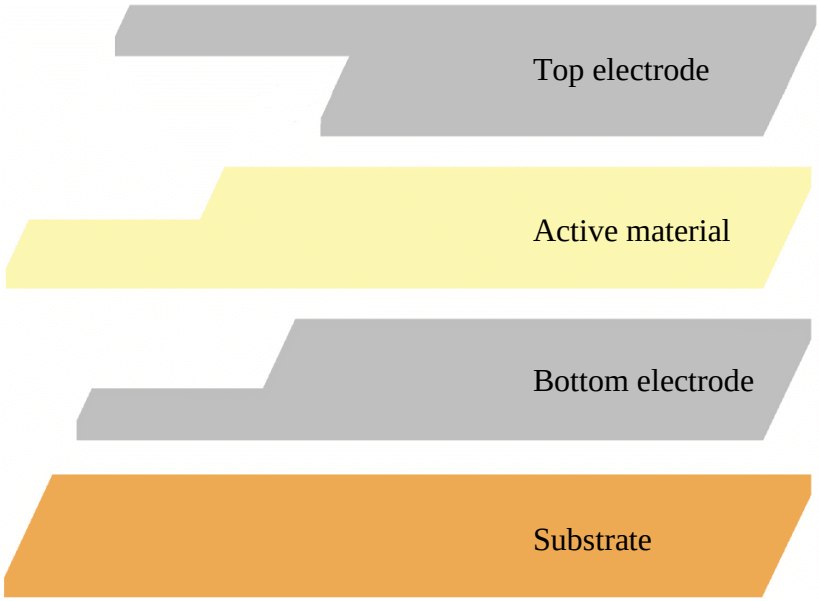

Figure 101. Screen-printing capacitive structure on flexible substrate.

The printed device layers shown in Figure 101 were drawn in Tanner L-Edit, a two-dimensional CAD drawing software. The layouts (Gerber file) were then sent to MCI

Precision screens Ltd, a screen manufacturer based in the UK. Figure 102 shows the layouts to be printed on top of each other in order to fabricate the capacitive structure of the piezoelectric device. To create such a structure, the three layers shown in Figure 102 have been manufactured on a stainless steel mesh, as seen in Figure 103. The screen consists of a mesh of 250 lines per inch with 15 micron emulsion thickness at a 45 degrees angle. This is a standard mesh used for this kind of screen printing process.

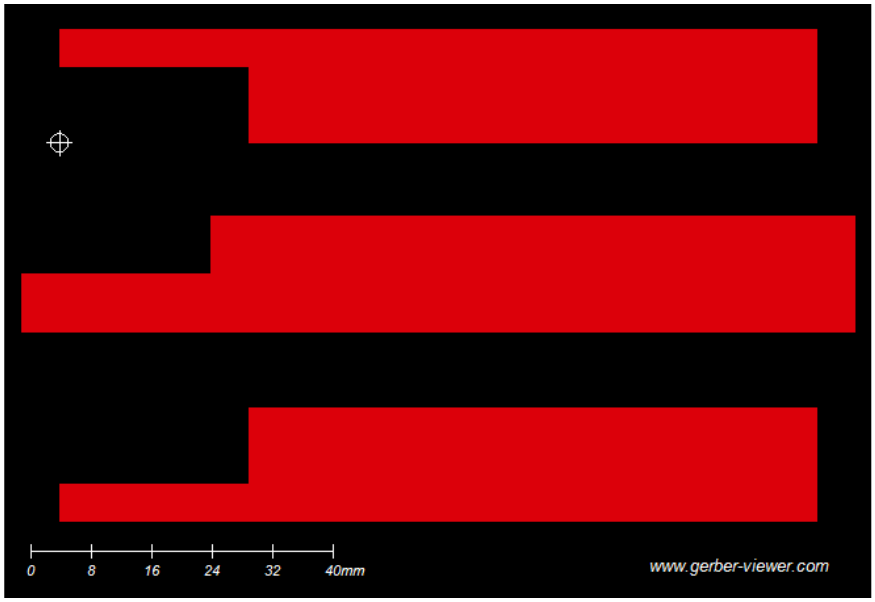

Figure 102. L-Edit designs.

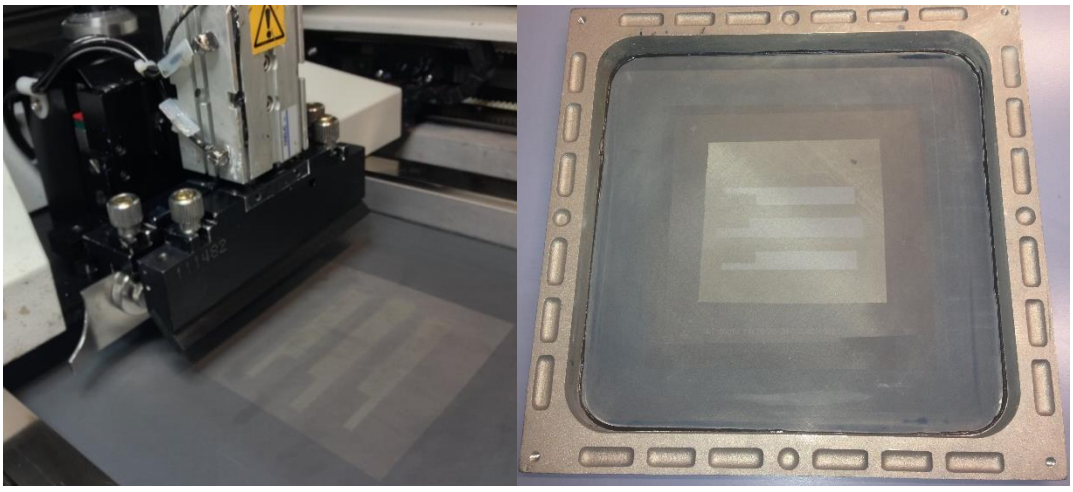

Figure 103. Screen-printing steel mesh secured in place.

The electrodes were printed using silver polymer ink from DuPont (DuPont 5000). The dimensions of the printed electrodes used in this study were 100mm wide, 14mm deep. The printing area for the piezoelectric paste was 110mm wide and 15mm deep in order to fully cover the surface of the bottom electrode so that no contact would be possible

between the two electrodes. Each printed layer is approximately 10μm thick. A printed sample of the sandwiched piezoelectric film printed on a flexible substrate used in this research is shown in Figure 104. The paste was screen-printed on flexible Kapton polyimide 300HN (KATCO), of 75μm thickness.

A mixture of piezoelectric ceramic particles and polymeric binder was used to formulate the piezoelectric composite paste. The exact composition of the paste cannot be revealed for commercial reasons. More information can be acquired from the technical datasheet provided by Smart Fabric Inks [175], a University of Southampton spinoff company.

Figure 104. Printed sample of capacitive structure piezoelectric film on Kapton.

The machine used for screen-printing is a semi-automatic DEK 248 screen-printer, as shown in Figure 105. It consists of many parts that need to be controlled to help either align the substrate to the screen or achieve the screen-printing process. The main parts used have already been summarised in [91] and are briefly presented below:

- Squeegee: It is a rubber-edged blade that forces the printed ink to go through the open meshed areas in the screen.
- Substrate holder: The substrate holder is located on the substrate table. The holder is the place where the substrate is held firmly in place. The substrate holder can be changed according to the size and geometry of the substrate placed on it.
- Screen-printing area: This area is where the screen is fixed and the actual screen-printing process is achieved after the substrate table with the screen holder goes beneath the screen.
- Control interface: The control interface is represented by DEK 248 screen-printer software, which controls the alignment and the substrate holder position in the x-y-z axes. In addition, it controls the speed of the squeegee during printing and the number of deposits printed for the printed layer. The control also specifies the limits of the squeegee during printing. The printing gap, which also influences the

thickness of the printed device, and the force applied by the squeegee on the screen, can also be adjusted by the control system.

- Alignment cameras: The cameras are dedicated to controlling the alignment of the substrates to the screens when needed.

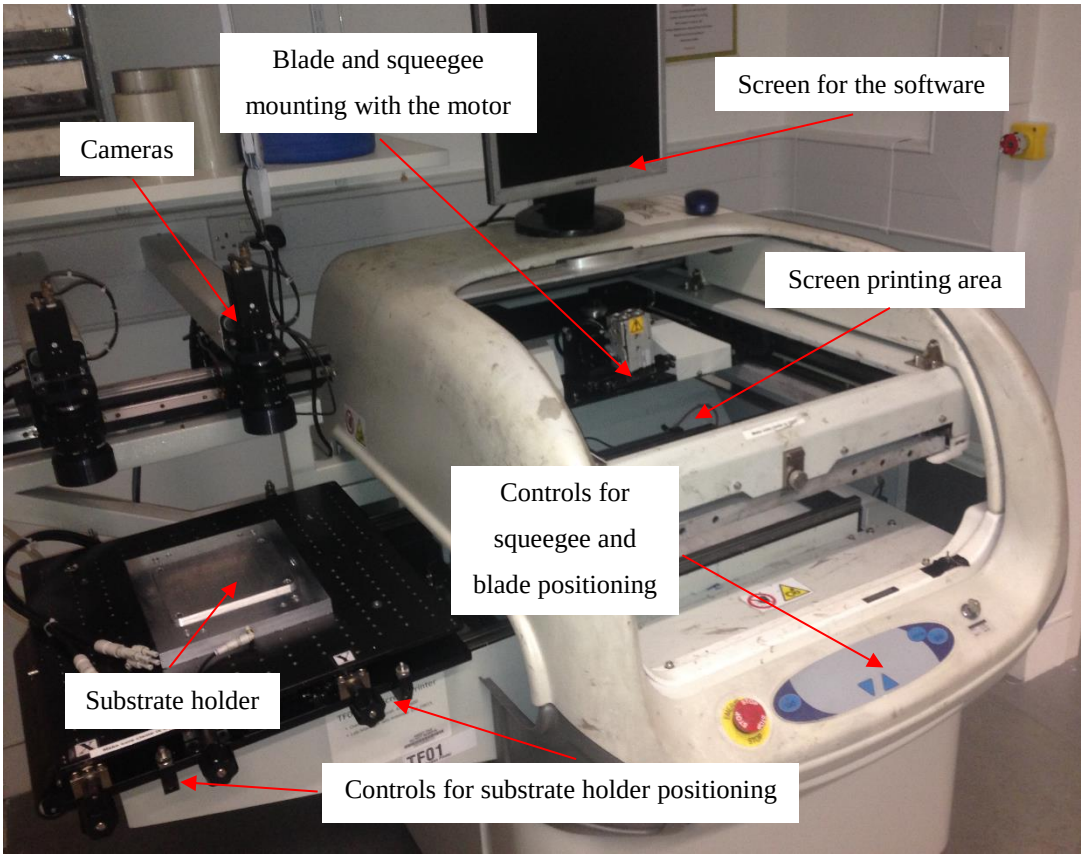

Figure 105. DEK 248 semi-automatic screen printer.

The printing process is as follows:

The screen is placed and secured on the printer as shown in Figure 103. The Kapton is cut and placed on the substrate holder, having sufficient size to print the layers. Then, the software is loaded, through which the position of the substrate holder is calibrated against the bottom of the screen, in x, y and z-axes. Approximately 1mm gap is left between the substrate and the screen. This will allow enough space to deposit the printed materials. The gap height has already been investigated by [91] and it has been found that 1mm will print the layers sufficiently. Then, the position of the blade and the squeegee is calibrated such that both pass over the desired layout on the screen. The paste is placed just before the mesh area of the layer to be printed. The first layer to be printed was the bottom electrode, therefore, silver paste was used. Next, when the settings within the software are checked, the printing begins. Firstly, the blade moves forward pushing the paste evenly over the

respective layer and then moves back to the initial position. Then, the squeegee passes over the same layer and pushes the paste through the mesh, depositing the paste on the Kapton. The exact thickness of each layer cannot be predefined through the software.

When the layer is printed, the printing is cured in a box oven. Then, the mesh is removed from the printer, cleaned thoroughly so that the new paste can be used to print the next layers. The mesh cleaning is repeated every time a different paste is used e.g. between electrode (silver) and active material (PZT). Table 21 presents the printing attempts that took place during the fabrication of the piezoelectric film.

Sample #	PZT layers	Printing method	Outcome
1	2	1 print	Short circuit
2	4	2 prints	Short circuit & pinholes
3	8	4 prints	Successful

Table 21. PZT film printing attempts.

Two layers of silver have been printed for each of the electrodes for all cases, followed by curing in the box oven at 120ºC for 10 minutes. Looking at Table 21, one print represents two layers of the respective material followed by curing at 120ºC. Thus, looking at Sample #3, which was the final PZT film used during the experimental work presented in section 7.2, it is consisted of eight layers of PZT, where curing was taking place for every two layers printed. The first three PZT prints of sample #3 were cured at 110ºC for 2.5 minutes each, where the 4^{th} print (last two PZT layers) were cured at 120ºC for 10 minutes. . Overall, including electrodes with PZT paste prints, sample #3 consists of 12 layers of printed material and it is approximately 175μm thick, including Kapton. The active area is 1050mm^2 (75 x 14mm).

To activate the piezoelectric properties, the material undergoes a poling process. The poling process is achieved by applying an electric field across the piezoelectric film at elevated temperatures for a certain time. The electric field aligns the dipoles and the heating provides the energy for the dipoles to realign. For poling the printed films, the direct-contact method (DCP) has been used which involves applying an electric voltage across the piezoelectric film with the aid of the bottom and top electrodes. The electric field can be calculated according to the thickness of the film by $E = V/d_{PZT}$, where E, V

and d_{PZT} are the electric field (V/m), voltage (V) applied across the electrodes and the thickness (m) of the piezoelectric film, respectively [170]. A Polatron 2006/AC turbo has been used for the poling process, as seen in Figure 106. It is consists of a polarisation box, a hot plate used for heating up the sample, a power supply and a mustimeter. A thermocouple is used to measure the temperature on the surface of the hot plate, and then adjusted as required. The top and bottom electrodes of the devices are connected to the power supply and the applied electric field is adjusted as required.

Figure 106. Polatron 2006. Left: thermocouple, top right: polarisation box, bottom right: hot plate with a sample.

Poling is a lengthy and timely process and it requires systematic systematic tests between the three parameters (E, V, time). Three sets of tests are required where in each test, two of the three parameters are kept constant and the third one is varied in fixed intervals. The d_{33} coefficient is measured for each combination. The poling process aims to find the value for each parameter that gives the highest d_{33} and when all three are combined, to give the highest possible d_{33} value from all the tests.

The d_{33} coefficient was measured using the PIEZOTEST PM300 Piezometer, as shown in Figure 107. The PM300 uses the Berlincourt method to obtain the d_{33} measurements. The key principle is that the test frequency is low compared with any likely system or sample resonances, yet high enough that a conclusive measurement can be made in a few seconds [176]. It adopts the dynamic method by applying an oscillating force (0.25N) to the sample with the aid of a built-in electromagnetic transducer placed at the bottom probe, as shown

at the bottom of Figure 107. The produced charge is estimated with the aid of a differential amplifier to obtain the d_{33} value. A 5% measurement error has been confirmed when the sample is over or under-constricted [170].

Figure 107. Top: PIEZOTEST PM300 set. Bottom: Sample clamping area.

This research builds upon previously published investigations into the formulation of a low temperature screen printable piezoelectric composite carried out at Southampton. This work takes the most flexible PZT-polymer composite from a series of formulations [170] [177] to fabricate the piezoelectric film. In [170] has been found that the chosen material had an initial d_{33} of 22pC/N and following optimisation of the poling parameters, a d_{33} of 27pC/N. Any value between the two can be considered sufficient for the needs of this research. Worth noting that the material used is not on its optimum form. Further research has improved its composition which has led to a d_{33} of 40pC/N.

Initial tests have shown that there is a minimum amount of layers required in order to allow film polarisation. As already discussed in Table 21, sample #1 with one print, meaning two layers of PZT followed by curing, has shown that it is too thin to be polarised. By using a multimeter, it was possible to measure current flowing from the bottom electrode through the PZT layer, to the top electrode. Similarly, sample #2 with 2 prints, or four layers of PZT, was not sufficient either to isolate the two electrodes. In sample #2, pinholes were identified. These are air voids created during the printing. As a ‘quick fix’, voltage (100-

500 V) can be applied to the sample in small increments. This causes the voids to burn, leaving a hole through the electrodes and the piezoelectric layer. The film is still operational, however the amount of pinholes affect the overall performance of the film, decreasing d_{33} dramatically. An example of a film with an excessive amount of small and large size pinholes can be seen in Figure 108. A more appropriate method to reduce or even eliminate any possible air voids in the printed piezoelectric film, is to use a Cold Isostatic Pressing (CIP) machine, just after the printing. The sample is placed in a cylindrical chamber that is filled with a hydraulic fluid. An external force pressurises the hydraulic fluid which then applies a homogenous pressure across the sample, removing any air trapped in the layers [178] In this research, it was not necessary to undergo this process as sample #3 has been printed and polarised successfully, with eight layers of PZT without the presence of any pinholes.

Figure 108. Piezoelectric film with small and large pinholes.

Looking at the work done in [170], it has been possible to identify some possible initial conditions for the poling process of this research. It has been decided to start the investigation with the electric field, at initial poling conditions of 160ºC and 10min for temperature and time respectively. The d_{33} has been measured in four different places along the centreline of each sample for further accuracy. The average was taken as the final value. Figure 109 shows that the d_{33} increased with increasing electric field and reached 26pC/N at an electric field of 3.75MV/m. There was no further significant change in the d_{33} values above 4MV/m with the same poling conditions. A d_{33} of 26pC/N has been achieved which can be deemed acceptable for this research. It is worth noting that more than one parameter combination, for example applying very high voltage in a very short period of time can lead to optimum polarisation, for example, when poling process in oil. However, the length of time the device will remain polarised is dependent on the method/ process chosen for polarisation. For example, the commercial PZT products are designed at a higher d_{33} and

then they are stored for 3-6 months. During that period the d_{33} value drops and reaches the advertised value.

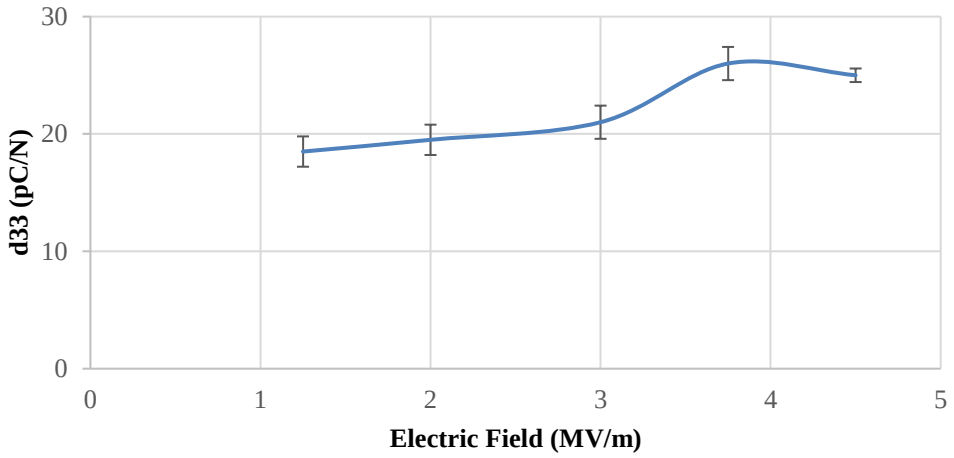

Figure 109. Electric field poling optimisation.

Having identified the optimum poling conditions, three devices with sample #3 printing specifications have been fabricated and poled as shown in Table 22.

Device #	d_{33} measurement location				Average d_{33}
	Far left	1/3 of the length	2/3 of the length	Far right	
1	25	25	26	28	26
2	24	24	25	27	25
3	24	25	25	26	25

Table 22. Poling process measurements for sample #3.

Overall, the polling process is successful and two observations in this research compare with those in similar research. Firstly, it has been identified that low thickness Sample #1 and #2 will lead to a complete short-circuit. This has also been identified by [91] where the same PZT-polymer composite was investigated. Their samples under 100μm thickness have shown the same results. A thickness of 100μm has been set as the minimum threshold of this material. Secondly, it was found that at temperatures higher than 225ºC, sparks would appear while poling. Similarly, in [170] and [91], they have noted that beyond this temperature their samples were found to become short circuited.

7.1.2 Method for Integrating the PZT Film with the Flexible Cylinder

For the experiments conducted in this chapter, a new flexible cylinder has been manufactured with the method described in section 3.1.2. The length of the new flexible cylinder has one quarter of the original length. As it has been observed during the experimental work, the flexible cylinder is oscillating either at mode shape 1 or 2, as shown in Figure 28. Therefore, a quarter of the cylinder can represent either half or one quarter of the overall mode shape of oscillation, respectively. Understandably, this is only an approximation of the mode shape oscillation. It has also been observed from the experimental work that the flexible cylinder does not exhibit mode 1 and mode 2 oscillations at all times, but a mixture of these, and sometimes something in between, where only half the flexible cylinder is excited by the shed vortex. Therefore, there is no unique curvature or amplitude value that the flexible cylinder takes which can be used as the basis to design and conduct a test that replicates an exact oscillation. Therefore, by using a quarter of the cylinder as the length under investigation with the encapsulated piezoelectric device, should give reasonable approximation of the flexible cylinder oscillation observed experimentally.

An addition to the manufacturing process has taken place in order to integrate the piezoelectric film. As depicted in Figure 110, a mounting base has been manufactured to hold the piezoelectric film in place in such a way that it is in parallel with the rod in the middle of the flexible cylinder mould, used earlier. It is important to place the film in such a way that the two edges of its depth would touch the arc of the outer radius. This will allow maximum compression and tension exercised on the film, when the flexible cylinder bends. The outer radius of the cylinder is 11mm and the depth of the piezoelectric film is 15mm. Using the fact that an isosceles triangle is formed and with Pythagorean theorem, it was calculated that the film should be placed at a distance of 8mm from the centre of the cylinder. The film was placed half millimetre closer to the centre of the cylinder, to ensure that there is enough space around the piezoelectric device such that when the silicone is poured into the mould, it encapsulates the piezoelectric device fully.

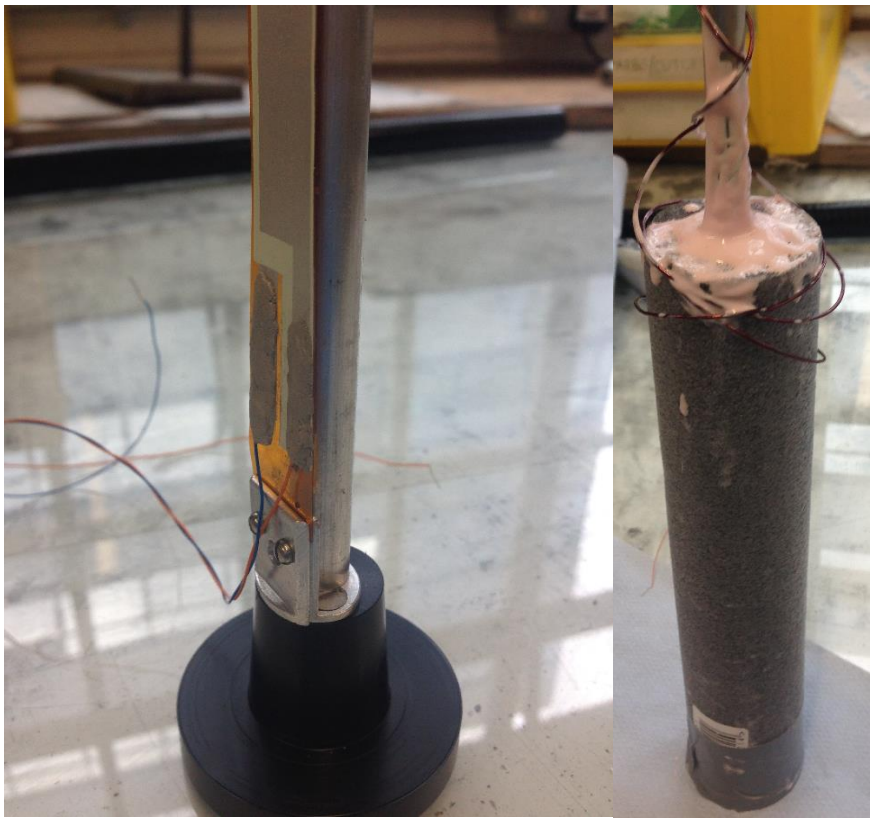

Figure 110. Left: PZT device mounting base. Right: Moulding cylinder.

The piezoelectric device has been successfully encapsulated into the flexible cylinder, however during the attempt to remove the rod from the middle of the flexible cylinder, the force applied was excessive, resulting in catastrophic damage to the piezoelectric device, shown in Figure 111. A release agent was applied on the rod just before moulding the silicone, however it has not been proven useful. This can be accounted as the main limitation of the moulding process used.

Figure 111. Catastrophic damage to the piezoelectric film.

The film has been removed from the flexible cylinder by cutting the part of the flexible cylinder covering the film, leaving a flat surface on the flexible cylinder, where the film was previously located. It has been found that Kapton does not adhere permanently on the silicone. The piezoelectric device was replaced with a new one, covered with silicone and placed into the cylindrical mould so it takes the cylindrical shape while drying out. This

should not affect the experiment since the already cured silicone can become one part with silicone added at a later stage and bond like both parts were created at the same time. This setback has also proven useful since now it is certain that the film is encapsulated in the flexible cylinder and that there is no space around it. If any gaps were present around the edges of the film, the latter would slide under tension or compression, defying the purpose of the experiment.

Overall, a method for encapsulating the piezoelectric device into a flexible cylinder has been presented and any limitations have been identified. The outcome is satisfactory and it shown in Figure 112, in section 7.2.

7.2 Experimental Setup

This section describes the design of the experimental apparatus used to perform experiments on the deflection behaviour of the flexible cylinder. For the purpose of this test, an Instron Electropuls 1000 test machine was used, equipment designed to evaluate the mechanical properties of materials and components. It is possible to predefine the frequency and amplitude of oscillation at which the actuator will move and consequently the flexible cylinder.

Given the material from which the flexible is made, the smallest available load cell has been used, $2\text{Kg} \approx 20N$. Depending on the load cell, the machine can provide different ranges of force. The idea behind the test is to investigate the output power of the system at different frequencies and amplitudes. Therefore, during the tests, one of the two parameters is kept constant, while the other one is changed at fixed intervals.

From the experimental work, it has been observed that the first three modes of oscillation can be present, shown graphically in Figure 28. At mode 0, the flexible cylinder behaves as a rigid body. At mode 1, there is one crest or one trough in the oscillation of the flexible cylinder. At mode 2, there will be one crest and one trough at all times. At mode 3, there will be either two crests and one trough or one crest and two troughs. The amount of crests and troughs that a flexible cylinder will have depends on the flow velocity and the length of the cylinder. The flow velocity must be strong enough in order to be able to exert enough lift force on the flexible cylinder at such a level where the frequency of the shed vortex

will match the resonant frequency of the flexible cylinder at all times. As it can be seen during the experiments, there were occasions where the flexible cylinder had different levels of coupling to the upcoming flow at one area, compared to another area further downstream. Regarding the length of the flexible cylinder, this must be long enough so that it will be able to flex and match the wavelength size of the shed vortices. The most common experimental case observed is in mode 2, however, as it has been seen in some rare occasions, three vortices are acting on the flexible body developing into a mode 3 oscillation, nevertheless, not a complete one.

Due to the limited testing area (0.3m x 0.3m) and maximum displacement range (0.06m) of the test machine, as well as the boundary conditions, it was decided that it would be better to conduct the tests using a quarter of the flexible cylinder. This should still give a good approximation to the oscillation of the flexible cylinder observed experimentally.

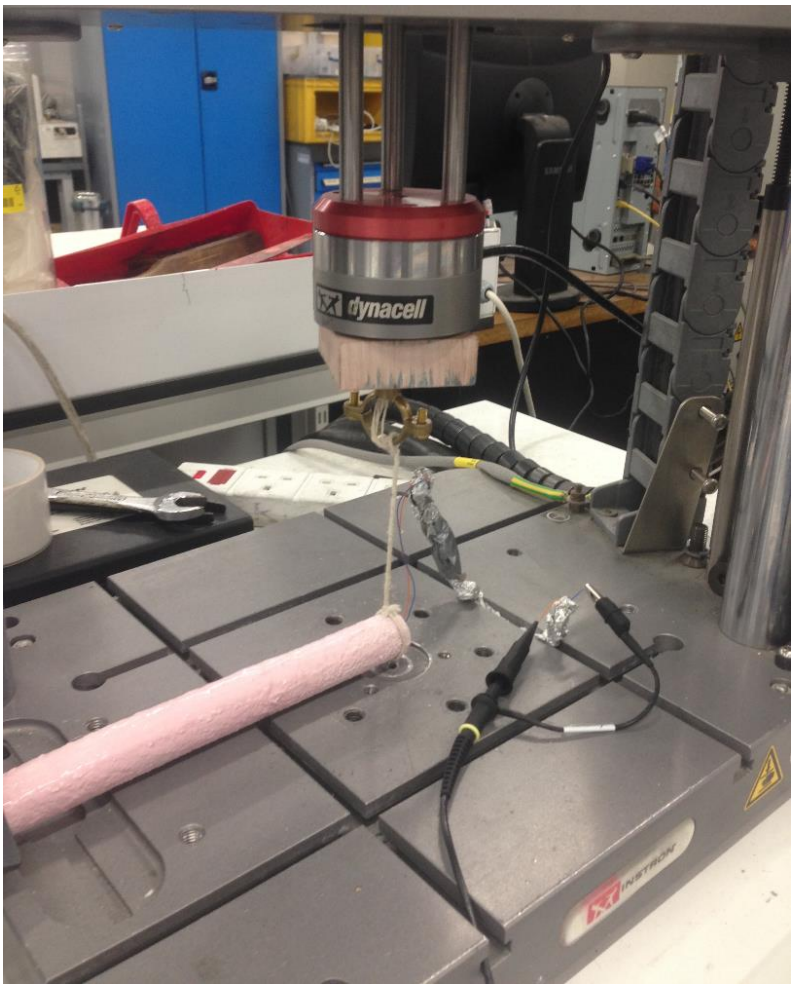

Figure 112. Test machine setup with one of the boundry conditions.

The biggest challenge during the experiment setup of the test machine was to set the boundary conditions such that they represent the boundary conditions of the experimental investigation. Given that the experiments have been carried in water and in an uncontrolled environment, it is impossible to replicate the exact boundary conditions. Also, as it has already been discussed in section 3.1.4, the flexible cylinder was not always behaving in a specific manner. Looking at the mode shapes of oscillation, it can be seen that it is possible to take a quarter of the sinusoidal-like oscillation and extract the boundary condition observed, creating an approximation of the observed oscillation. It can be assumed that the end of the flexible cylinder which is near the centre line (rigid body), thus no displacement, can be replicated by clamping on the testing area of the machine. This can represent one side of the quarter of the flexible cylinder. The other side can be assumed to be the part of the cylinder moving, resulting in the sinusoidal-like oscillation. Initially, this side was clamped on the actuator, however it has been found that this introduced further tension on the flexible cylinder during oscillation since the flexible cylinder was clamped on both sides. Therefore, the oscillatory side of the cylinder has been tethered on a rope, where it has been allowed to slide and rotate slightly, decreasing any additional forces that might have been introduced while clamped directly on the actuator. This can be seen in Figure 112.

Understandably, the chosen boundary conditions might not represent exactly what has been observed experimentally, however conducting the experiments in the air instead of water, it is believed that the boundary conditions chosen are still suitable and represent sufficiently those observed experimentally and the needs of this research.

Undertaking this experimental work, it will be possible to obtain a correlation between the applied frequency, amount of deformation and amount of produced voltage and power. Then, the amount of deformation can be compared to the respective values obtained from the computational model and experimental work conducted in the water channel and draw conclusions. The experimental set-up will allow the assessment of changes in the amplitude and frequency of oscillation of the flexible cylinder than may occur due to; changing flow characteristics or geometric changes to the flexible cylinder.

7.3 Output Power Measurement

As discussed in the previous section, the experiment has been designed to mimic the oscillation of the flexible cylinder in the water. The dynamic motion of the test machine on the flexible cylinder deforms the encapsulated piezoelectric device. The output voltage of the device was observed and recorded using a Tektronix MDO4054B-3 oscilloscope.

The purpose of the experiment is to characterise the piezoelectric device in terms of peak output power. Knowing the maximum power of the device is not so much a means of analysis, as it is an aid to the design of a system for a specific application.

The peak power is given by,

$$P_{peak} = \frac{V_{peak}^2}{R_L}$$

Equation 41. Peak output power of the piezoelectric device.

Where V_{peak} is the instantaneous peak voltage and R_L the applied resistive load.

The energy is calculated by the sum of power over a specific time range and is given by,

$$\int_{t_1}^{t_2} \frac{V(t)^2}{R_L} dt$$

Equation 42. Equation of energy.

The experimental work aims to correlate the peak power of the piezoelectric device with the frequency and amplitude of oscillation of the flexible cylinder. For this, a series of tests have been conducted as follows:

- Open-Circuit Voltage (OCV) with fixed amplitude and variable frequency. This test will identify how the voltage changes with frequency.
- OCV with fixed frequency and variable amplitude. This test will identify how the voltage changes with amplitude.
- Close-Circuit Voltage (CCV) with the presence of resistive load. This test will study the response of the device when a series of resistive loads are present in the system. The peak output power will be examined.

7.4 Experimental Results

To characterise the response of the piezoelectric material integrated in the flexible cylinder, a series of tests have been undertaken. During the tests, either the frequency or the amplitude of oscillation were kept constant, such that the response of the system can be characterised. Initially, OCV tests were conducted, where maximum potential difference produced by the piezoelectric device when the circuit is not closed. The tests enabled to identify the maximum voltage that can possibly be produced by the system, within the range of amplitudes and frequencies investigated.

Figure 113 shows the OCV of the device at a fixed amplitude of 56mm. The error bars represent the standard deviation between the recorded data for each test. It is a clear indication that with the increase of frequency, there is an increase in the peak voltage. The graph also shows that the device is sensitive enough to capture small changes in frequency, as can be seen for the small changes in frequency of 0.8Hz, 0.84Hz, 0.9Hz and 0.95Hz.

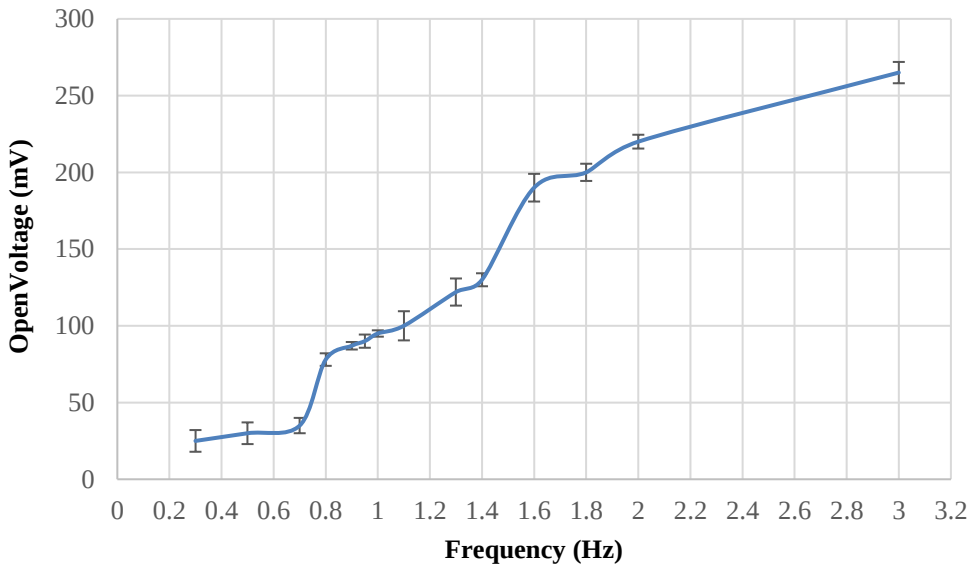

Figure 113. Investigation of peak voltage with varying frequency at 56mm amplitude.

The initial test established that peak voltage increases with the increase of frequency. To investigate how the amplitude influences the peak voltage, four tests have been conducted, presented in Figure 114. The lowest frequency of 0.84Hz, has a similar trend to that of 0.95Hz with maximum peak voltages of 80mV and 87mV respectively. Increasing the frequency to 1.4Hz, the peak voltage increases at low amplitudes (16-20mm) followed by a small drop of peak voltage at medium amplitudes (22-26mm), however still larger than

the lower frequencies. At maximum amplitude, a maximum peak voltage of 140mV is recorded. Finally, at a higher frequency of 2Hz, a smaller peak voltage is observed at lower amplitudes, compared to the 1.4Hz frequency. Continuing, with the increase of amplitude, there is an increase in the peak voltage, reaching 220mV at 56mm of amplitude. Comparing the maximum peak voltages in Figure 114, with that in Figure 113, it can be seen that in some cases the results do not match exactly, but there might be a difference of ±5-10mV. Since this research is not studying the exact output of the device and only aims to characterise the response of the system, the results are acceptable. Finally, the peak voltages represent the average of different tests, therefore a degree of deviation (~7-10%) exists between the measurements.

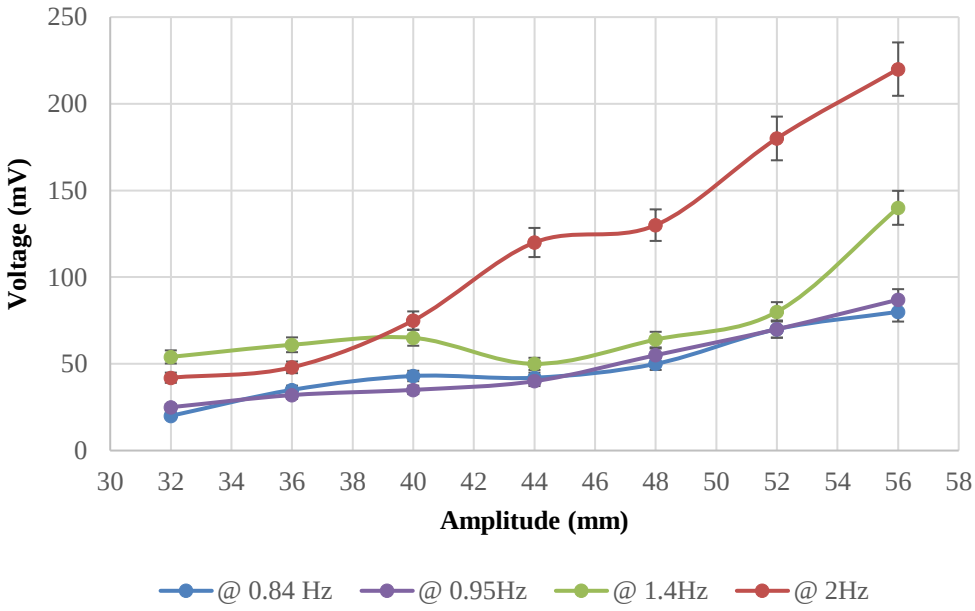

Figure 114. Investigation of open- circuit peak voltage with varying amplitude.

Further experimental work has investigated the response of the piezoelectric device while separately applying resistive loads ranging from 10MΩ to 80MΩ. The peak voltage values were recorded and the peak power was found using Equation 41. The peak voltage values represent an average of three to five consecutive peaks and when necessary, data from more peaks were used in order to keep the standard deviation less than 10% for each peak voltage value. Figure 115 shows the change of peak voltage for one bending cycle, at different resistive loads. Four frequencies at maximum amplitude were investigated. As expected, and according to Ohms law, voltage increases with the increase of resistance, as they are proportional.

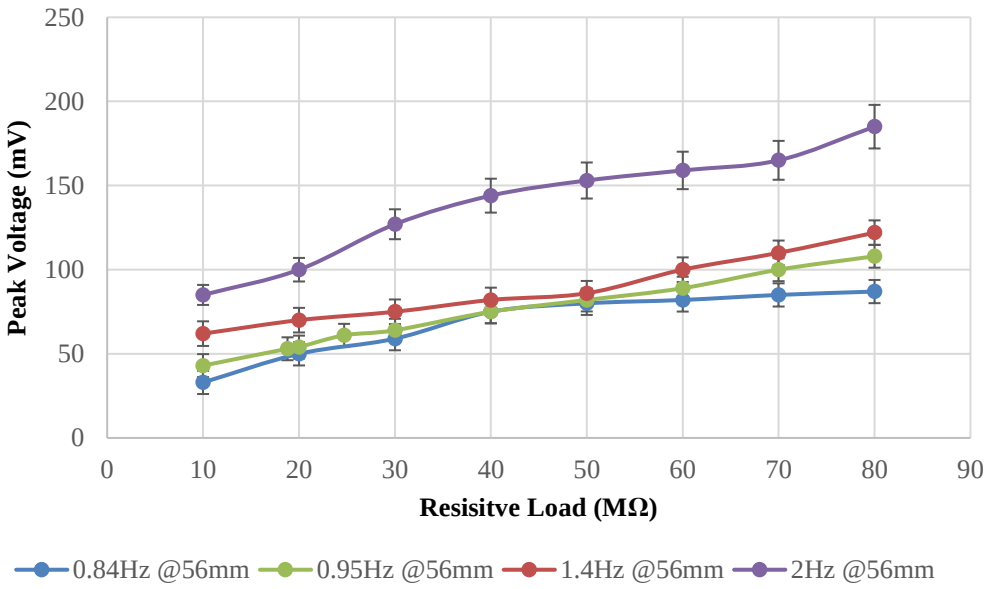

Figure 115. Investigation of peak voltage at different resistive loads.

Figure 116 shows the variation of the resistive load and peak power as a function of frequency. At the lowest frequency and highest resistive load, the least power is produced. At the highest frequency and smallest resistive load used, the most power is produced. From this experimental work it can be observed that with the increase of frequency and decrease of resistive load, there is increase in power. Further tests at lower resistances would have made this observation more clear, but these tests were not conducted. Similar observation have been made in other work [179].

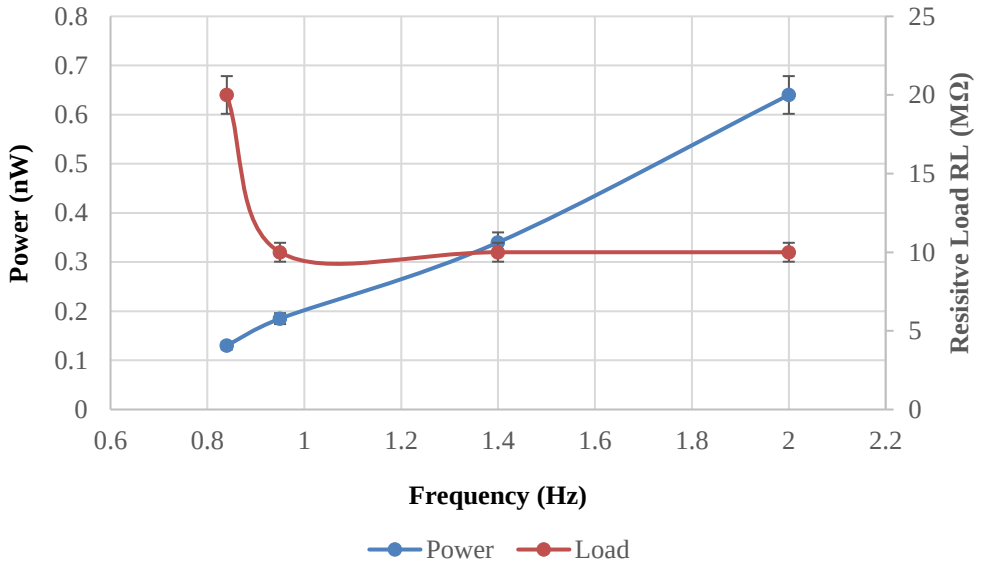

Figure 116. Resistive load and peak power variation as a function of frequency.

Figure 117 complements the previous observation. At three of the four frequencies there is a decay of power with the increase of the resistive load. This implies that the optimum resistive load has not yet been found and that it will be less than 10MΩ. Subsequent to obtaining these results, the internal impedance of the piezoelectric device has been measured using the LCR400 Precision Bridge from THURLBY THANDAR Instruments. The bridge provides fast, convenient and accurate means of measuring inductance, capacitance, and resistance of a device. The capacitance and resistance have been measured at 100Hz and 10kHz. The capacitance was approximately 13pF. The internal resistance at 100Hz test was estimated around 1.3MΩ and at 10kHz, around 7.7kHz. Since the operating frequencies in this research are under 100Hz, 1.3MΩ can be considered the best approximation. The maximum power transfer theorem states that, the maximum amount of power will be dissipated by a load resistance when that load resistance is equal to the total resistance of the source [180] [181]. If the load resistance is lower or higher than the equivalent resistance the source network, its dissipated power will be less than maximum. Therefore, it is expected that the maximum output power will occur around 1.3MΩ.

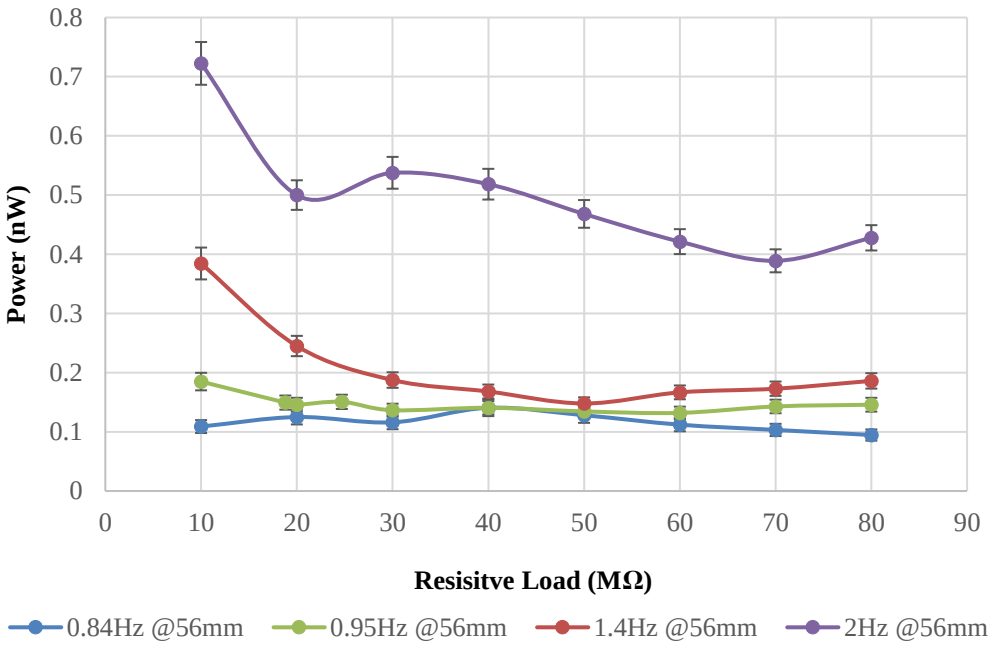

Figure 117. Investigation of peak power at different resistive loads.

Finally, the energy produced by a half cycle, one upwards movement, has been found using Equation 42. Initially, the voltage data of the upward motion were separated from the downward motion data. For the integration, Simpson's Rule was used. Figure 118 shows the energy produced for one half cycle at different frequencies with a resistive load of

10MΩ. The higher the frequency, the higher the energy. It is expected that the maximum output energy per half cycle (upwards movement) will be produced at maximum power at optimum resistive load.

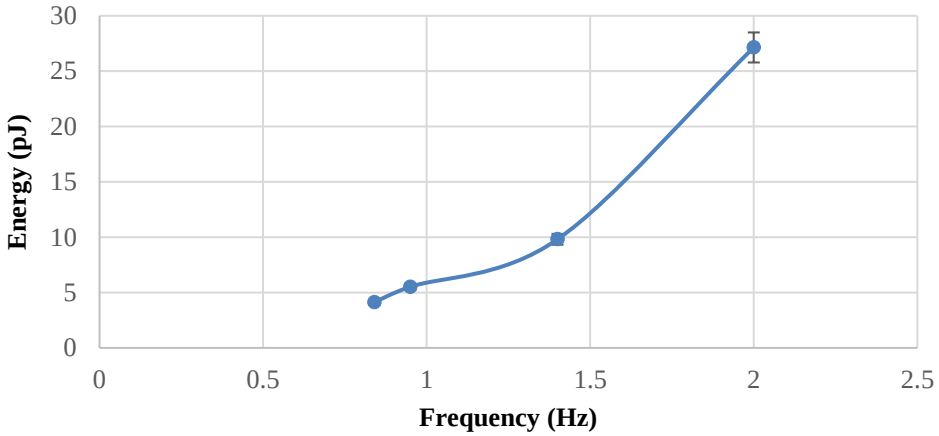

Figure 118. Half cycle output energy at different frequencies with 10MΩ load.

Further observations were made. Figure 119 is a magnified screenshot of six cycles at a frequency and amplitude of 2Hz and 56mm respectively, with 10MΩ resistive load. It can be observed that there are spikes on a regular interval during the oscillation. These are caused by the triboelectric effect. This effect is a type of contact electrification on which certain materials become electrically charged after they come into frictional contact with a different material [182]. Positive and negative charges on the two dissimilar surfaces are generated. Research in the field of flexible triboelectric (TENG) – piezoelectric devices is trying to exploit the two phenomena, by designing hybrid nanogenerators. Further work in the area can be found in [182] [183] [184]. In an attempt to further understand the impact of triboelectric effect shown in Figure 119, the latter is compared with some of the findings presented in [183], focusing on a hybrid energy harvesting device and the results are briefly presented in Figure 120. Graphs (a) and (c) in Figure 120 represent the open circuit output voltage of the hybrid system as a function of frequency, under a force of 5N. It is clear that the output voltage is an order of magnitude larger with the triboelectric effect taken into account. Comparing with the results in Figure 119, the triboelectric peaks have higher magnitude than the actual output waveform. Understandably, the triboelectric peaks in this research are instantaneous, therefore the output power and energy is very small compared to that produced from the half cycle as a whole. Graph (b) represents a magnified view of the data corresponding to 4Hz shown in (a). The transition between the two states, compression and release, are characterised by a sawtooth waveform. A similar observation

can be made in the results of this research, during bending (moving upwards) and releasing (moving downwards) of the flexible cylinder.

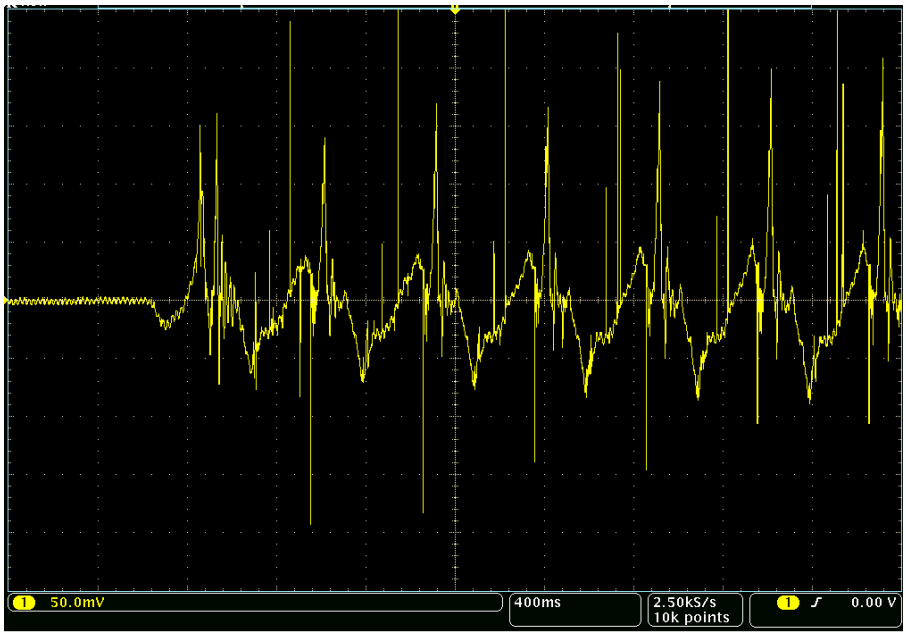

Figure 119. Magnified output voltage over time at 2Hz with 10MΩ load.

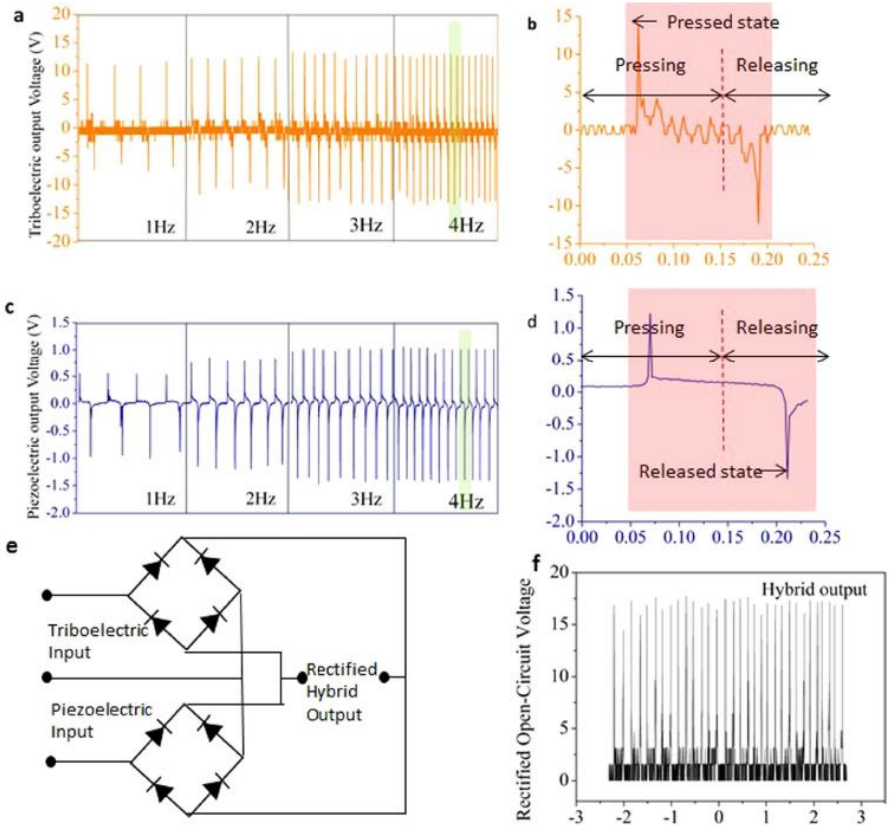

Figure 120. Triboelectric-piezoelectric hybrid nanogenerator (taken from [183]).

To better understand the magnitude of the output voltage of the piezoelectric device used in this research and consequently the output power and energy, a compression test was conducted. According to [183], a human fingertip force can range between 2-5N. With this in mind, the flexible cylinder has been placed on a straight surface and the open-voltage has been measured using the oscilloscope, while the author was taping the surface of the flexible cylinder. The test might have not been scientifically designed, however interesting results have been obtained. It has been found that with a 'press' (compression) the output voltage would reach an average of 3.5V, whereas a 'release' would reach an average output voltage of 2.5V. The results are at least 10 times larger than the recorded open-circuit voltage, presented in Figure 114. Furthermore, by qualitatively observing the shape of the waveform in Figure 121, it has similar shape to that presented in Figure 120 (d).

Schematic (e) in Figure 120 shows a circuit diagram of the hybrid output where the piezoelectric and triboelectric outputs are combined in parallel, using a rectifying bridge made of diodes. A similar arrangement could potentially be created for the device in this research, with or without taking into consideration the triboelectric effect. The rectifying bridge is a configuration that provides the same polarity of output for either parity of input. This will increase and almost double the output voltage, as shown in Figure 120 (f).

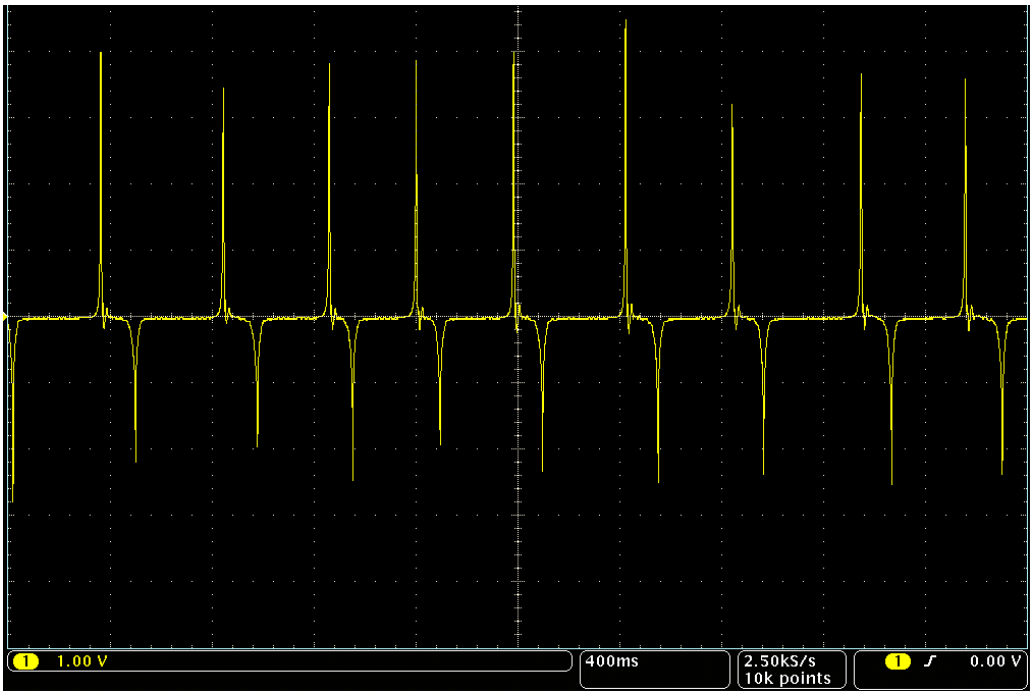

Figure 121. 'Press' and 'release' test screenshot.

The last observation demonstrated that there is a significant difference between the force applied on the flexible cylinder when compressed, compared to when bent. With this in mind, further investigation has taken place. At the half cycle test, the upward motion of the flexible cylinder could reach a maximum displacement of 56mm. However, since the displacement was taking place on the tethered side of the cylinder (right side boundary condition), a difference in curvature has been observed compared to the left side (clamped boundary). At the left half of the flexible cylinder, where two thirds of the piezoelectric device were located, the curvature was larger compared to the right half, where one third was located. This is a clear indication that only a part of the piezoelectric device bent, where approximately one third stayed unchanged. Consequently, this decreased the amount of the harvested energy dramatically. It has also been observed that the radius of curvature was large, resulting to low curvature and subsequently to smaller bending. On a separate note, the piezoelectric coefficient d_{33} of the piezoelectric device is low compared to that of other devices, decreasing the output even more.

It is clear that the experimental apparatus has certain limitations, however the points identified earlier can also exists during a natural, uncontrolled environment. Under a control environment, the system can be designed with more precision and more accurate prediction of the harvested energy can take place.

Concluding, as discussed during the experimental work in section 4.3 and the computational work in chapter 5 and 6, the flexible cylinder at frequencies close to 0.84-0.95Hz is expected to have average tail and body amplitudes of 0.13m and 0.11m respectively. Comparing these values with the experimental results in this section, it is safe to say that there is potential of harvesting energy from the system when a piezoelectric device is integrated into the flexible cylinder, since the tests in this chapter were at a smaller amplitude. The device can also act as a form of sensor, since it has been shown that its output is sensitive to the frequency changes.

7.5 Summary

This chapter has conducted the experimental work necessary to investigate whether there is the potential for energy harvesting when a flexible cylinder with an integrated piezoelectric device, is tethered and placed behind a bluff body, in flowing water.

Initially, the methodology for fabricating and polarising a flexible piezoelectric device is presented. It has been found that there is a limited amount of active material layers that must be printed in order to have a working device. The d_{33} of the material falls within the expected range, however enhanced piezoelectric material could be used in the future, to increase the piezoelectric coefficient value.

Integrating the piezoelectric device into the flexible cylinder has been a challenge since initial trials were unsuccessful, leading to the destruction of a sample. For future work, it is advised that a mass production encapsulation method should be developed.

A laboratory representation of the motion of the flexible cylinder in water was successfully developed using a quarter of the body with the capability to apply representative amplitudes of deformation at representative frequencies.

Testing a quarter of the flexible cylinder in the test machine was conducted systematically, it was found that with an increase of frequency and amplitude, there is an increase in output voltage. By applying several resistive loads, it was found that at low frequency and large load, the output power is low, whereas, at higher frequency and smaller load, the output power is higher.

The output voltage, power and energy are in the order of mV, nW and pJ respectively. They can be considered very small as an energy harvesting application, however as it will be discussed in the next chapter, a system optimisation will give higher output. Also, the lab based tests conducted were of a very small amplitude compared to the real displacement in the water. Finally, it has been found that the system is sensitive to small frequency changes, thus making it suitable in sensing applications.

Overall, it has been shown that a flexible cylinder tethered behind a bluff body with integrated piezoelectric device, has potential of energy harvesting and sensing applications. With this in place, the overall research work is completed and it has created the potential for further research in this area.

Chapter 8

Discussion and Conclusions

8.1 Discussion

The purpose of this research is to investigate whether the mechanisms used by a fish to extract energy from unsteady flow can be applied to a flexible inanimate object in order to harvest energy with the potential to provide power at a sensing system.

During the experimental work, three methodologies were developed that can be used in order to design an experiment for assessing energy harvesting from unsteady fluid flow. Firstly, a method of creating an unsteady flow environment at a specific flow velocity and Reynolds number is described (chapter 3.1.1). Secondly, a method to design a neutrally buoyant flexible cylinder is presented (chapter 3.1.2). Finally, the manufacturing method of the flexible cylinder is described, with all the necessary details and steps that need to be taken into consideration (chapter 3.1.3).

From the experimental results, it was found that when the motion of the flexible cylinder was synchronised with the unsteady flow, a motion upstream was observed that appears similar to that of a trout swimming in the Von Kármán gait. The values of frequency and amplitude of the flexible cylinder have been measured and they are in agreement with the theory and the computational results.

The image obtained from the experimental tests were analysed using the Matlab® motion assessment algorithm. This extracted the position of markings on the flexible cylinder which have been used to assess the amplitude of the motion, but also via a FFT, the frequency of oscillation of the flexible cylinder. The analysis concluded that the frequency of oscillation measured experimentally was close to the shed frequency from the bluff body from theory, but the sparse data used may have affected the results. This was partially due to difficulties in using the motion assessment algorithm due to poor lighting and visibility

issues. Qualitatively, the motion of the body is as expected compared to the literature and can therefore be used to verify the computational models.

A fully coupled, computational model has been designed and assessed in four stages. The incoming velocity profile, the shedding of vortices from the bluff body, the creation of a Von Kármán vortex street and finally the response of an inanimate body to the vortex street.

In Stage 1, it was shown that the flow in the experiment located 7.5m from the inlet pipes, is not a fully developed velocity profile. It has also been found that the computational graphs of the velocity profile do not fit well with the semi-empirical graphs. This is mostly due to the mesh quality being focused on assessing the mid-stream of the water channel and not on predicting the velocity profile at the boundaries. Overall, it has been shown qualitatively that the computational model of the water channel can create a velocity profile, which over time, should give a response close to that observed in the experimental apparatus.

In Stage 2, the flow around the bluff body was examined, firstly in two-dimensions and then in three-dimensions. It was also found that the computational shed frequency falls within the expected range of shed frequencies and therefore the Strouhal number, as predicted by the semi-empirical equations, available in the literature. Identification of flow phenomena have further validated the area around the bluff body and it is expected with confidence that the shed vortices will be simulated and travel downstream to reach the flexible cylinder.

In Stage 3, a qualitative comparison between the computational fluid domain and the experimental vortices observed using dye was conducted. It is visible that the creation and movement of the shed vortices in the computational model resemble those observed experimentally, moving downstream towards the flexible cylinder.

In Stage 4, the work done and presented in chapter 6, has proved that a fully coupled, three-dimensional model is sufficiently robust and can be used for simple engineering applications to predict scenarios at different flow velocities and possibly different inanimate body geometries. Firstly, a transient CFD/FEA analysis demonstrated some good correlation with the experimental and theoretical findings, however being computationally simpler, it was not providing adequate results for design purposes.

The next stage of the research was to use the experimentally and computationally derived results to demonstrate that there is potential of energy harvesting.

The first part of this research area has described in detail the steps to fabricate, polarise and integrate a flexible piezoelectric device into the flexible cylinder. The second part has conducted the experimental work necessary to investigate whether there is the potential for energy harvesting when a flexible cylinder with an integrated piezoelectric device, is tethered and placed behind a bluff body, in flowing water. Using a quarter of the flexible cylinder, a laboratory representation of the motion of the flexible cylinder in water was successfully developed with the capability to apply representative amplitudes of deformation at representative frequencies. The output obtained can be considered small for an energy harvesting application, however a system optimisation will give higher output, making it more suitable. The system is sensitive to small frequency changes, thus making it suitable in sensing applications.

The outlined research areas have successfully been completed with significant amount of investigation, discussion and contribution to the area. This research work has created further research questions and they will be presented in chapter 9.

8.2 Conclusions

The overall aim of this research was to investigate whether a suitably tuned inanimate object has the potential to harvest energy when excided by an unsteady underwater fluid flow.

All the objectives were fulfilled through chapters 3-7 and the outcomes are presented below:

- It was shown that it is possible to excite a flexible silicone cylinder tethered behind a bluff body, using unsteady fluid flow.
- It was shown that the inanimate object can be tuned to vibrate in such a manner to hold station behind the bluff body and have a natural frequency matched or be very close to the shed frequency.
- A fully coupled computational model was designed and validated using experiments and theory. In addition, quantitative analysis of the model has shown that the model is very data rich allowing one to undertake a significant investigation of the vortices shed from the bluff body and their interaction with the flexible cylinder.
- A flexible piezoelectric device was designed, fabricated, polarised and successfully integrated into the flexible cylinder.
- A laboratory representation of the motion of the flexible cylinder in water was successfully developed and investigated. It has been found that there is potential of energy harvesting or sensor application.

Overall, it can be said with confidence that a flexible cylinder tethered behind a bluff body with an integrated piezoelectric device, has the potential to harvest low levels of energy and/or act as a sensing device.

8.3 Specific Contributions to the Subject

The aim of this thesis was to investigate whether an inanimate object can be tuned to respond to an unsteady flow field and whether the motion of the inanimate object is sufficient to act as an energy harvesting device or sensor. The work of this thesis has uniquely contributed to the area of fluid-structure interactions modelling and energy harvesting with sensing in the following areas:

- The use of quantitative experimental data obtained from a novel image analysis technique as the basis for the validation of the fluid-structure interactions model.
- For the first time a fully coupled, three dimensional, fluid structure interactions model of an inanimate object tethered behind a bluff body has been created, with the capability to act as a design tool.
- The development of a novel imbedded piezoelectric sensor with energy harvesting capabilities, within the physical constrains of the experimental environment.

The image analysis technique used in this research has shown that it is possible to measure the motion and interaction of an object underwater with the shed vortices, by detecting the position of known centroids with respect to time. Using this method, a relatively simple experimental monitoring system was developed, without requiring complex equipment.

Computational modelling is one of the initial design steps before the implementation of a system in a real environment. Specific variables within the system can be adjusted and by observing how the changes affect the outcomes, researchers can make predictions about what will happen in the real system. Modelling can expedite research by allowing scientists to conduct thousands of simulated experiments computationally in order to identify the actual physical experiments that are most likely to help find appropriate solutions. Having a robust model which is validated by theoretical and experimental data will enable actions like this in the case of an inanimate object tethered behind a bluff body, in water. Through this research a validated fully-coupled model was developed that provides realistic structural and fluid responses when compared to experimental observations.

This research has shown that a piezoelectric device can be embedded into a flexible, silicone cylinder and act as an energy harvesting and sensor device, within the physical constraints of the experimental environment. This allows one to further investigate the optimisation of the overall device towards specific real-world applications.

[This page is intentionally left blank]

Chapter 9

Further Work

9.1 Possible Areas for Improvement

The present research has highlighted a number of areas that require further research. These can be divided into five main areas:

1) Experimental data image acquisition technique.
2) Computational modelling.
3) Optimisation for energy harvesting and sensor applications.
4) Real environment Fluid- Structure Interactions testing.

9.1.1 Experimental Data Image Acquisition Technique

This research has presented a novel image analysis technique to investigate the motion of an inanimate object underwater, which does not require complex infrastructure. Improvement of this technique can take place by improving the overall tracking algorithm such that it gives data that are more robust and possibly the use of underwater cameras provided they do not disturb the vortex field but eliminate the need to look through the free surface. For example, some part of the code could assess the level of lighting received by the camera and adjust the contrast between the flexible cylinder and the water around it. This should improve significantly the data acquisition process.

9.1.2 Computational Modelling

The fully coupled model has proven to exceed expectations by providing detailed insight into the fluid structure interaction behaviour through being very data rich, however it takes significant amount of time with an average computer to undertake the desired simulations.

With this been said, the turbulence model used is still much faster than other, more complex turbulence models which will need more time to compute.

A possible improvement is to undertake more experimental measurements which will allow to decrease the size of the current computational model. For example, using pressure gauges at different locations around the water channel, will provide data which can then be inserted into the computational model, creating a better representation of the experimental channel, at a much smaller mesh design. Also, having more information about the flow development at different stages, it will allow to assess the model in much greater depth. Additionally, in cases that only the displacement of the inanimate object is of interest, the pressure around the latter can be recorded, and used as direct input in a significant smaller model, without the need of the water channel simulation. Further measurements could relate to the drag and lift coefficients. Potentially, the drag at the bluff body can be found experimentally and compared to that found using the computational model.

Overall, improvements in the efficiency of the model would be very beneficial. It will allow exploring further the fluid environment and the flexible cylinder interaction. For example, the influence of geometric variation on the flexible cylinder and the bluff body and different flow velocities could be investigated.

The fully coupled computational model can also allow to explore further the piezoelectric insertion in the system. Several techniques can be used in order to integrate a piezoelectric device or piezoelectric material in to the flexible cylinder. Any of these will affect differently the vibrational characteristics of the flexible cylinder. By adding extra mass, the flexural rigidity of the body changes which is similar when extra damping is inserted into the system. Consequently, adding the new material will affect not only the frequency of oscillation but also the transverse and lateral amplitudes of motion, alongside other parameters. Also, the output energy can be predicted as well, if the ANSYS® piezoelectric suite is used, within the fully coupled model.

9.1.3 Optimisation for Energy Harvesting and Sensor Applications

A flexible piezoelectric device has been successfully integrated in to the flexible cylinder. It is vital to undertake specific study to optimise the piezoelectric device itself, addressing

the requirements of a specific application. Among others, optimising the piezoelectric charge coefficient, the substrate flexibility and take into consideration the effect of triboelectricity to optimise the output power.

Identifying the best piezoelectric material and arrangement for energy harvesting depends on many different parameters. The ultimate purpose is to harvest as much energy as possible from any kind of arrangement; however, the author believes that the same piezoelectric arrangement would not be the most appropriate for all the flexible cylinder systems because each system will have different natural characteristics. Therefore, it might be possible to divide the system arrangements into categories where different piezoelectric materials could possibly be used to achieve maximum energy harvesting in each case.

As found in the experimental results, it is known that similar to the fish, the flexible cylinder exhibits larger amplitudes towards the second half of its body compared to the first half. This can be treated as a case where two piezoelectric materials can be used to harvest energy. In theory, and up to a specific point, if the same piezoelectric material is inserted everywhere in the flexible cylinder, the one found at the second part of the object will produce more energy compared to the first half. This is also given that the length of the cylinder is long enough to allow the object to have at least one mode of oscillation. If longer, two modes might be possible, therefore the cylinder could be divided into two areas, where two different piezoelectric arrangements could potentially be used. The piezoelectric material arrangements can include either piezoelectric material with different properties or with different arrangement of the piezoelectric crystals.

In order to be able to reach such a level of innovation, where different piezoelectric arrangements are inserted in the flexible cylinder, it is essential understand how the flexible cylinder behaves under one type of piezoelectric material. Subsequently, further studies can take place to find multiple piezoelectric materials that would be most appropriate for every section of the cylinder. Finally, it is important to understand that at certain flow velocities, there is a good possibility of not being able to harvest any measurable amount of energy from the first half or even from the whole flexible cylinder due to small levels of deformation.

9.1.4 Real Environment Fluid- Structure Interactions Testing

Given representative deformation of amplitude and frequency, the piezoelectric sensor integrated within the flexible cylinder is capable of energy harvesting. However, this demonstration occurred in a laboratory environment. The system needs to be designed and placed underwater, at a real fluid- structure interactions environment.

9.2 Potential Applications

In general, it can be said that the presented system has certain characteristics. Due to the tethering, it can self-align to the direction of the flow. Since it is an energy harvesting device, it can be self-powered when designed and optimised for a specific application. This also allows deployment at great depth, where the light from the sun cannot reach, compared to other sensors which may use the light of the sun to operate. It can trickle- charge an already charged power bank.

Compared to other energy harvesting devices, it is a very simple structure, it has no rotating parts, thus making it more robust and less maintenance is required. Finally, it is fish friendly since it looks and moves like a fish!

9.2.1 Fluid- Structure Interactions Energy Harvesting System

This research has shown in the lab that there is potential of energy harvesting from the system. A large scale deployment of the system could allow an array of many flexible cylinders. This will multiply the output power significantly. Also, larger scale deployment could include a larger flexible cylinder with larger integrated piezoelectric devices, increasing the output power.

For example, looking at the legs of an oil rig jacket, these can be used as the bluff bodies, where arrays of flexible cylinders could be tethered on each leg. Arrangements of bluff bodies in a fluid has been extensively studied to date, thus information from there can be used to investigate the implementation of the energy harvesting system.

In addition to large-scale applications, it is possible to deploy the system at a smaller scale, for example in rivers, where the depth of the water is much smaller. This has also been verified experimentally in this research, since the flexible cylinder was oscillating at 30cm depth.

9.2.2 Fluid- Structure Interactions Sensor Application

The system can also be used as a sensing device while is being used as an energy harvester. As it has been found, the flexible cylinder is sensitive in frequency changes, thus can provide a signal when a threshold is reached.

For example, it can be used as a force-mapping sensor. The sensor does not need energy to operate as it can be only activated when a force is applied at the piezoelectric elements. The data of the sensor is the output voltage at different amplitude, at different locations on the flexible cylinder. The data can be extracted using an interface circuit, interpreted and transmitted using a microcontroller and low-power transmitter. The microcontroller and the transmitters can be powered with either a pre-installed power supply or by the harvester, in case it is chosen to operate as a harvester and as a sensor. A possible application is to detect or predict potential development of tsunami, since their development initiates underwater and could be detected due to the associated pressure waves.

[This page is intentionally left blank]

Appendices

Appendix A

A.1 Flow Cases

A1.1 Case #3 Water Channel Flow Characteristics

Location #1:				
Time (s)	**Velocity (m/s)**	**Recordings**		**Units**
5.68	0.440	**Distance travelled:**	2.5	m
5.13	0.487	**Average velocity:**	0.44	m/s
4.96	0.504	**Maximum velocity:**	0.50	m/s
5.01	0.499	**Minimum velocity:**	0.39	m/s
6.06	0.412	**Coefficient of variation (CV):**	8.81	%
5.55	0.450	**Max velocity with CV:**	0.48	m/s
5.86	0.426	**Min velocity with CV:**	0.40	m/s
5.73	0.436			
6.16	0.405			
6.35	0.393			
5.68	0.440			

Table 23. Location 1 measurements.

Location #2:

Time (s)	Velocity (m/s)	Recordings		Units
5.68	0.440	**Distance travelled:**	2.5	m
5.13	0.487	**Average velocity:**	0.44	m/s
4.96	0.504	**Maximum velocity:**	0.50	m/s
5.01	0.499	**Minimum velocity:**	0.39	m/s
6.06	0.412	**Coefficient of variation (CV):**	8.81	%
5.55	0.450	**Max velocity with CV:**	0.48	m/s
5.86	0.426	**Min velocity with CV:**	0.40	m/s
5.73	0.436			
6.16	0.405			
6.35	0.393			
5.68	0.440			

Table 24. Location 2 measurements.

A.2 Buoyancy Evaluation Tool

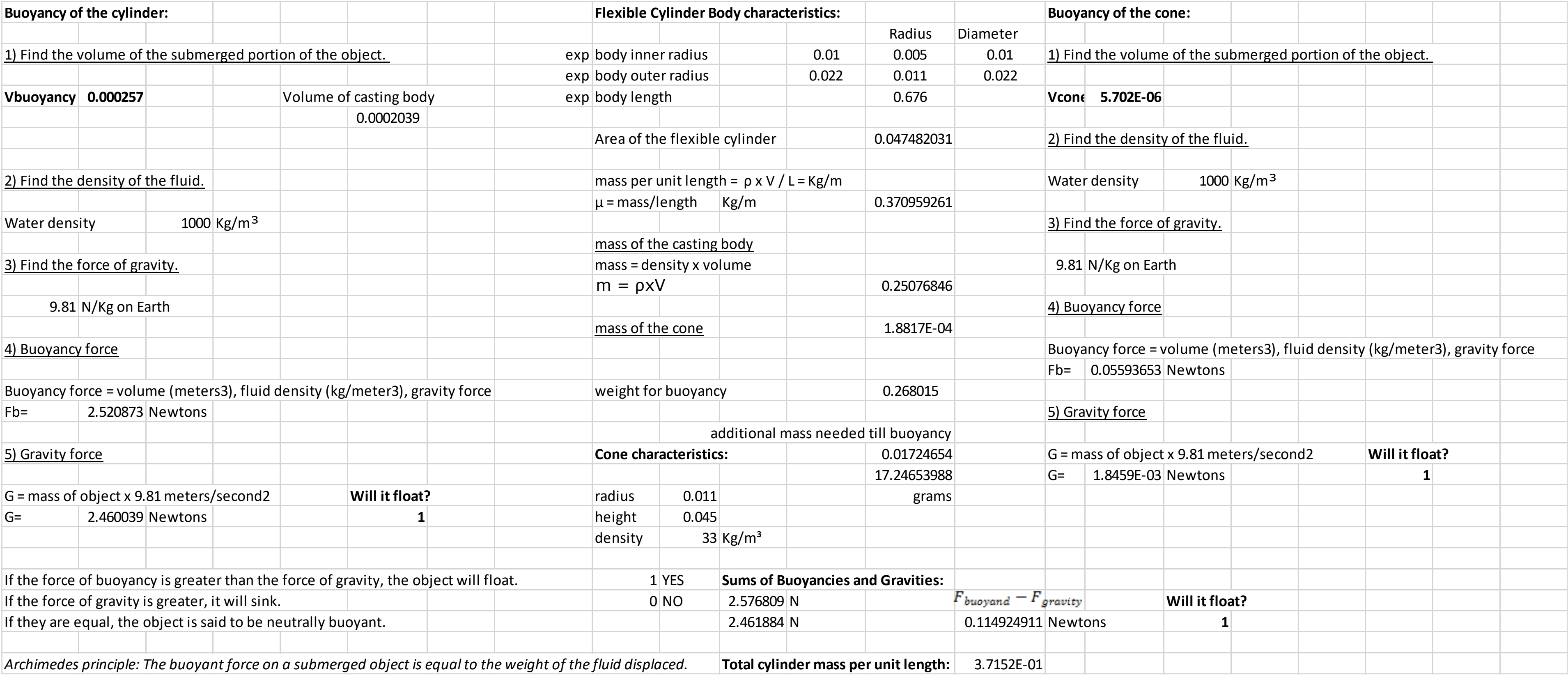

Buoyancy of the cylinder:								**Flexible Cylinder Body characteristics:**						**Buoyancy of the cone:**							
												Radius	Diameter								
1) Find the volume of the submerged portion of the object.							exp	body inner radius			0.01	0.005	0.01	1) Find the volume of the submerged portion of the object.							
							exp	body outer radius			0.022	0.011	0.022								
Vbuoyancy	**0.000257**			Volume of casting body			exp	body length				0.676		**Vcone**	**5.702E-06**						
					0.0002039																
								Area of the flexible cylinder				0.047482031		2) Find the density of the fluid.							
2) Find the density of the fluid.								mass per unit length = ρ x V / L = Kg/m						Water density		1000	Kg/m³				
								μ = mass/length		Kg/m		0.370959261									
Water density		1000	Kg/m³											3) Find the force of gravity.							
								mass of the casting body													
3) Find the force of gravity.								mass = density x volume						9.81	N/Kg on Earth						
								m = ρxV				0.25076846									
9.81	N/Kg on Earth													4) Buoyancy force							
								mass of the cone				1.8817E-04									
4) Buoyancy force														Buoyancy force = volume (meters3), fluid density (kg/meter3), gravity force							
														Fb=	0.05593653	Newtons					
Buoyancy force = volume (meters3), fluid density (kg/meter3), gravity force								weight for buoyancy				0.268015									
Fb=	2.520873	Newtons												5) Gravity force							
												additional mass needed till buoyancy									
5) Gravity force								**Cone characteristics:**				0.01724654		G = mass of object x 9.81 meters/second2					**Will it float?**		
												17.24653988		G=	1.8459E-03	Newtons			**1**		
G = mass of object x 9.81 meters/second2					**Will it float?**			radius	0.011			grams									
G=	2.460039	Newtons			**1**			height	0.045												
								density	33	Kg/m³											
If the force of buoyancy is greater than the force of gravity, the object will float.								1	YES	**Sums of Buoyancies and Gravities:**											
If the force of gravity is greater, it will sink.								0	NO	2.576809	N		$F_{buoyand} - F_{gravity}$			**Will it float?**					
If they are equal, the object is said to be neutrally buoyant.										2.461884	N		0.114924911	Newtons		**1**					
Archimedes principle: The buoyant force on a submerged object is equal to the weight of the fluid displaced.										**Total cylinder mass per unit length:**			3.7152E-01								

A.3 Flow Characteristics

Tank Characteristics (Armfield Water Channel):				
Length [L] =	23.000	m	(23.00m max)	
Width [W] =	1.370	m	(1.50m max)	
Depth [D] =	0.470	m	(0.60m max)	
Perspex width [P_w] =	0.600	m		
Perspex level from tank bottom [P_l] =	0.460	m		
Nominal flow velocity [Vnom $_{exc}$] =	0.453	m/s	(excludes perspex - Taken from Run Details.xlsx - Test 2)	
Nominal flow velocity [Vnom $_{inc}$] =	0.457	m/s	(includes perspex)	
Reynolds no. water channel [$Re_{channel}$] =	1.1980E+05	122040	(rectangular channel)	
Entrance length [E_{length}] =	30.893			
Actual flow velocity [V_{actual}] =	0.493	m/s	(accounting for flow constriction near the cylinder due to solid blocking effects)	
Kinematic viscosity [v] =	1.054000E-06	m^2/s	(at 18°C)	
Air density [ρ_{air}] =	1.205E+00	kg/m^3	(at 20°C)	

Bluff body dimensions and respective characteristics:				
Diameter [D_{bb}] =	0.1100	m	$St = St^* + m/\sqrt{Re}$	
Reynolds no. [Re] =	5.1404E+04			
Strouhal no. [St] =	1.873E-01		Roshko	2.1195E-01
Exp. vortex shedding frequency [f] =	0.839	Hz		
Downsteam vortices spacing [λ] =	5.401E-01	m	(excluding perspex)	
Downsteam vortices spacing [λ] =	5.452E-01	m	(including perspex)	

Re Range					St*	m
47	<	Re	<	180	0.2684	-1.0356
180	<	Re	<	230	0.2437	-0.8607
230	<	Re	<	240	0.4291	-3.6735
240	<	Re	<	360	-	-
360	<	Re	<	1300	0.2257	-0.4402
1300	<	Re	<	5000	0.204	0.3364
5000	<	Re	<	2.00E+05	0.1776	2.2023

Flexible body dimensions:						
Tapered Ends (given f)			Uniform Cylinder Section			
Nose f_1 =	0.222222222	Hz	Outer Diameter [D_{outer}] =	0.022	m	
Nose length =	0.045	m	Inner Diameter [D_{inner}] =	0.010	m	
Nose Volume =	5.70199E-06	m^3	Lcasting/D_{outer} =	26.63636364		
Nose mass =	1.8817E-04	kg	Length casting [$L_{casting}$] =	0.586	m	
Tail f_2 =	0.222222222	Hz	Volume of hollow casting body =	0.000176733	m^3	
Tail length =	0.045	m	Volume of inner cylinder =	0.000046024	m^3	
Tail Volume =	5.70199E-06	m^3	Second moment of area [I] =	1.101E-08	m^4	$I_0 = \frac{\pi}{4}(r_2^4 - r_1^4)$
Tail mass =	1.8817E-04	kg	Reynolds no. [Re_{fc}] =	2.738E+05		

End to end flexible body length [L_{fc}] =	0.676	m	(incl. uniform section + nose + tail lengths)
Young's Modulus [E] =	790000	N/m^2	
Moldsil Flexural Rigidity [EI] =	8.696E-03	Nm^2	
Moldsil S.G. =	1.23		
Density Dow Floormate 300a=	33	Kg/m^3	
Mass per unit length [μ] =	0.37170	kg/m	(incl. nose + tail ends mass but lumped therefore pul only of uniform cylinder section)
Total water volume displaced =	2.342E-04	m^3	
Displaced water mass =	2.342E-01	kg	
Mass ratio [m*] =	9.302E-01		(total mass of flexible body divided by displaced water mass)
added mass [m_{added}]=	0.316072747		$m_{added} = \rho\pi L_{fc} R^2_{outer}$
Damping (added mass per unit length) [C_{fc}] =	0.467563235		$C_{fc} = \frac{m_{added}}{L_{fc}}$
added mass coefficient	0.001260417		

A.4 Video Footage

4.1 Flow Cases Video Footage

4.1.1 Flow Case #3

Video footage:				
	Distance tethered away from Bluff Body			
Footage	$2D_{bb}$	$3D_{bb}$	Units	Notes
#1	00:01:10 – 00:01:19:23		h:m:s:ms	v.2 – 30fps
	Footage time range			

Table 25. Video footage of flow, Case#3.

A.5 Open Channel Velocity Profile

5.1 Vertical Velocity Profile Fitting Calculations

FITTING OF VERTICAL VELOCITY PROFILE

Note: Data used from experiments in Jun 2016.

Water depth	Dchannel	0.47
Hydraulic radius:	Rh	0.278744589
Open channel Reynolds number:	$\frac{Uavg\ x\ Rhydrolic}{\nu}$	119801.9912
rougness Reynolds number:	< 5	smooth bed
no-slip distance:	$y_o = \frac{\nu}{9u_*}$	5.67314E-06
	$u_* = \sqrt{\tau/\rho}$	0.0206
shear velocity:	$\frac{V - U_{max}}{u^*} = 3.66$	0.0211

Calculation using different variables to see the difference between the equations.

von Karman constant:	k	0.41
shear stress near the wall:	$\tau_{bed} = \rho u_*^2$	0.425
	$\tau_o = \frac{f}{8}\rho U^2$	0.421

Calculation using different variables to see the difference between the equations.

Location #1 experimental measurements:

time	distance	velocity
5.68	2.5	0.440140845
5.13		0.487329435
4.96		0.504032258
5.01		0.499001996
6.06		0.412541254
5.55		0.45045045
5.86		0.42662116
5.73		0.436300175
6.16		0.405844156
6.35		0.393700787
		0.445596252

	0.012040153		
friction factor:	0.016997459	$f = (100Re)^{-1/4}$	Blasius formula (friction factor f)
Reference: Lecture_no3_Turbulent flow_modelling.pdf			
umax:	0.522861671	$U_{max} \approx V(1 + 1.33\sqrt{f})$	
Reference: Open Channel Flow Resistance -Ben Chie Yen, J.o.Hydr.Eng.2002			
good approximation to the computational model's max value 0.55m/s			
constant α:	0.301073249	$\alpha = 1.3e^{\left(\frac{W_{ch}}{2D_{ch}}\right)}$	
Reference: Velocity Distribution in Open Channels:Combination of Log-law and Parabolic-law			
constant B:	5.5	Table with references in the thesis	
Coles constant (Π):	0.2	Ref in the thesis	

Dimensionless dip-phenomenon location:

Equ. 13: Value #1	0.768596235	$\xi_{dip} = \frac{1}{1 + 1.3\exp\left(\frac{-Ar}{2}\right)}$	Reference: # 69
Equ. 13.1: Value #2	0.730942526	$\xi_{dip} = 0.44 + 0.212\left(\frac{z}{h}\right) + 0.05\sin\left(\frac{2\pi}{2.6}\frac{z}{h}\right)$	Reference: # 87
Equ. 13.2: Value #3	0.71805119	$\xi_{dip} = \frac{C_1 + C_2 * Ar^{C_3}}{C_4 + Ar^{C_3}}$	Reference: # 64

Real location of Umax from the bed:

Value #1:	0.36124023	m
Value #2:	0.343542987	m
Value #3:	0.337484059	m

aspect ratio:

C1=	42.4
C2=	1
C3=	4.2
C4=	94.7

A_r = 2.92553191

$z = \frac{W_{channel}}{2}$

5.2 Vertical Velocity Profile Coordinate Points

	Log: smooth	Coles function	simple dip-modified log-wake
	$\frac{U_{avg}}{U_*} = \frac{1}{k} ln \frac{y_h U_*}{\nu} + B$	$\frac{U_{avg}}{U_*} = \frac{1}{k} ln \frac{y_h U_*}{\nu} + B + w(\xi)$	$\frac{U_{avg}}{U_*} = \frac{1}{k}\left[ln\left(\frac{y_h}{y_0}\right) + 2\Pi\, sin^2\left(\frac{\pi}{2}\xi\right) + \propto ln(1-\xi)\right]$
Height from the bed (yh)	**Velocity values (Uavg)**		
0.01	0.379353927	0.380443255	0.376185601
0.02	0.414267169	0.418619614	0.410832925
0.03	0.434690106	0.444464885	0.431027044
0.04	0.449180411	0.466512521	0.445324786
0.05	0.460419964	0.487410652	0.456406967
0.06	0.469603348	0.508310721	0.465466882
0.07	0.477367789	0.529797625	0.473140251
0.08	0.484093653	0.552190443	0.479805719
0.09	0.490026286	0.575664549	0.485706694
0.1	0.495333206	0.600309116	0.491008544
0.11	0.5001339	0.626157263	0.495828396
0.12	0.50451659	0.653203211	0.500251908
0.13	0.508548274	0.681412737	0.504343306
0.14	0.51228103	0.710729935	0.508151702
0.15	0.515756144	0.741081825	0.51171521
0.16	0.519006895	0.772381648	0.51506375
0.17	0.522060506	0.804531354	0.518220984
0.18	0.524939527	0.837423541	0.521205707
0.19	0.527662848	0.870943052	0.524032858
0.2	0.530246448	0.904968326	0.526714263
0.21	0.532703968	0.939372575	0.529259201
0.22	0.535047142	0.974024853	0.531674828
0.23	0.53728614	1.008791029	0.533966498
0.24	0.539429832	1.043534699	0.536138016
0.25	0.541486002	1.078118046	0.538191813
0.26	0.543461516	1.112402664	0.540129087
0.27	0.545362465	1.146250343	0.541949886
0.28	0.547194272	1.179523824	0.543653154
0.29	0.548961793	1.212087535	0.545236738
0.3	0.550669385	1.243808294	0.546697347
0.31	0.552320981	1.274555984	0.548030456
0.32	0.553920136	1.304204211	0.549230149
0.33	0.555470079	1.33263093	0.55028887
0.34	0.556973748	1.359719041	0.551197059
0.35	0.558433826	1.385356961	0.55194261
0.36	0.559852769	1.409439162	0.552510069
0.37	0.561232832	1.431866679	0.552879431
0.38	0.56257609	1.452547583	0.553024265
0.39	0.563884453	1.471397419	0.552908726
0.4	0.56515969	1.48833961	0.552482529
0.41	0.566403436	1.50330582	0.551671997
0.42	0.56761721	1.516236279	0.550362865
0.43	0.568802421	1.527080067	0.54836361
0.44	0.569960384	1.535795362	0.545314999
0.45	0.571092323	1.542349634	0.540410117
0.46	0.572199382	1.54671981	0.53107312
0.47	0.573282631	1.548892387	#NUM!
0.48	0.574343074	1.548863502	
0.49	0.57538165	1.546638961	
0.5	0.576399243	1.542234221	
	Umax		
	0.572199382	1.54671981	0.553024265

[This page intentionally left blank

Appendix B

B.1 Flexible Cylinder's Motion Assessment Tool (Matlab® code)

```
%% Detecting flexible object motion

clear all;

%% Step 1: Access Video with MMREADER - Use |mmreader| to access the
video and get basic information about it

filename = ('C:\Users\am506\Documents\MATLAB\VID_20131021_145518.mp4');
% name of the avi from which to extract data
flexibleObj = mmreader(filename);

excelname1 = 'Centinfo_0583.xls';
% excel sheet in which to store centroid information
excelname2 = 'Centtobo.xls';
% excel sheet in which to store data between adjacent centroids
outputvide = 'VID_20131021_145518.avi';
% video output in which centroids are tagged

LightValue = 40;
% Specify the average pixel value as the threshold
sedisk = strel('disk', 1);

framexposcrop = 0;
frameyposcrop = 50;
bretocrop = 640;
heitocrop = 320;
rotateby = 0;

pixelmaxno = 150;

meaninitframe = 1050 - 900;
% identify first frame from which to extract position
secondstomean = 5;
% identify for how long initial data shall be extracted in order to
determine mean values of cylinder centroids
secondsmeanon = 240;
% identify for how long to read data after initial data extracted
lastmeanframe = floor(meaninitframe + (get(flexibleObj, 'FrameRate') *
secondstomean));

%% Step 2: Frame processing in the video

LightPart = rgb2gray(read(flexibleObj, meaninitframe));
% representative frame from the video and for which the algorithm is
developed on
DarkPart = imextendedmin(LightPart, LightValue);
% identify dark regions

figure, imshow(LightPart);
% display the grayscale image
```

```
figure, imshow(DarkPart);
% display the binary image

% Remove small structures
noSmallStructures = imopen(DarkPart, sedisk);
figure, imshow(noSmallStructures);

% Crop as needed
noSmallStructures = imcrop(noSmallStructures, [framexposcrop
frameyposcrop bretocrop heitocrop]);
figure, imshow(noSmallStructures);

% Rotate if necessary
noSmallStructures = imrotate(noSmallStructures, rotateby);
figure, imshow(noSmallStructures);

% Remove any structure containing less than max no of allowable pixels
noSmallStructures = bwareaopen(noSmallStructures, pixelmaxno);
figure, imshow(noSmallStructures);

% Remove any extraneous objects that exist on the border of the image
noSmallStructures = imclearborder(noSmallStructures);
figure, imshow(noSmallStructures);

% Fill any holes that lie within the area
noSmallStructures = imfill(noSmallStructures, 'holes');
figure, imshow(noSmallStructures);

%% Step 3: Apply the Algorithm to the Video

I = read(flexibleObj, 1);

noofdistances = 11;     %
markallowance = 6;     % used for the cases when extraneous objects
still result

initxpos = zeros((noofdistances + markallowance), 4);
% fourth column to be used to keep track of row no. in excel sheets
topbotbc = zeros((noofdistances + markallowance), 2);
% columns used to represent top and bottom distances between centroids
respectively

maxabovebelow = zeros(2, 2);
% used to store the furthest pixel position above and below of each
centroid

initypos = 0;
% determine y-position of first centroid at which body is tethered
yposrefgivenx1 = zeros(1, floor(get(flexibleObj, 'FrameRate') *
secondstomean));
initxpos(:, 1) = 1;
initxpos(:, 4) = 4;
% column that shall be used to keep a counter of the excel rows for
every centroid

%% to read the first 15 seconds in order to determine the means

for f = meaninitframe : lastmeanframe - 1
    singleFrame = read(flexibleObj, f);
```

```
    singleFrame = imcrop(singleFrame, [framexposcrop frameyposcrop
bretocrop heitocrop]);
    singleFrame = imrotate(singleFrame, rotateby);
% when movie needs rotating

% Convert to grayscale to do morphological processing.

    I = rgb2gray(singleFrame);

    DarkPart = imextendedmin(I, LightValue);
% identify dark regions

% Remove small structures
    noSmallStructures = imopen(DarkPart, sedisk);
    noSmallStructures = bwareaopen(noSmallStructures, pixelmaxno);
    noSmallStructures = imclearborder(noSmallStructures);
    noSmallStructures = imfill(noSmallStructures, 'holes');

    stats = regionprops(noSmallStructures, {'Centroid'});

    if ~isempty([stats.Centroid])
        if f > meaninitframe

       % IMP: TO DETERMINE POSITION OF THE FIRST CYLINDER CENTROID IN
       % RELATION TO THE BLUFF BODY HAD THE CYLINDER BEEN IN ITS
       % EQUILIBRIUM POSITION UPON NO CROSS FLOW ACTING. THE IMPORTANCE
OF
       % THE BELOW LIES IN THE FACT THAT IRRESPECTIVE OF THE POSITION
OF
       % THE CAMERA, ONE CAN STILL DETERMINE THE POSITION OF THE
CYLINDER

            yposrefgivenx1(1, (f - meaninitframe + 1)) =
stats(1).Centroid(2);

            if (stats(1).Centroid(1) > (initxpos(1, 2) - 0.5)) &&
(stats(1).Centroid(1) < (initxpos(1, 2) + 0.5))
                initxpos(1, 1) = initxpos(1, 1) + 1;
                initxpos(1, 2) = stats(1).Centroid(1);
                initxpos(1, 3) = initxpos(1, 3) + initxpos(1, 2);
            end

       % IMP: TO DETERMINE THE MAX POSITION OF THE FOLLOWING CENTROIDS
IN
       % RELATION TO THEIR PREVIOUS CENTROID, THUS GIVING THE POSITION
OF
       % THE CENTROIDS HAD THE FLEXIBLE CYLINDER BEEN STATIONARY

            for n = 2 : (numel([stats.Centroid]))/2
                centdist = hypot((stats(n).Centroid(1) - stats(n -
1).Centroid(1)), (stats(n).Centroid(2) - stats(n - 1).Centroid(2)));
                if (centdist > (initxpos(n, 2) - 0.5)) && (centdist <
(initxpos(n, 2) + 0.5))
                    initxpos(n, 1) = initxpos(n, 1) + 1;
                    initxpos(n, 2) = centdist;
% used temporarily to establish max distance between centroids
                    initxpos(n, 3) = initxpos(n, 3) + initxpos(n, 2);
                end
            end
```

```
        else
            initxpos(1, 2) = stats(1).Centroid(1);
            initxpos(1, 3) = initxpos(1, 2);
            for n = 2 : (numel([stats.Centroid]))/2
                centdist = hypot((stats(n).Centroid(1) - stats(n -
1).Centroid(1)), (stats(n).Centroid(2) - stats(n - 1).Centroid(2)));
                initxpos(n, 2) = centdist;
                initxpos(n, 3) = initxpos(n, 2);
            end
        end
    end
    clearvars singleFrame I DarkPart noSmallStructures;
end

%% to determine the y-position of the stationary object

histox = yposrefgivenx1;
histoy = min(yposrefgivenx1):((max(yposrefgivenx1) -
min(yposrefgivenx1))/secondstomean):max(yposrefgivenx1);
[~, bar] = max(hist(histox, histoy));
initypos = histoy(bar);

%% to determine the total length of the flexible cylinder in pixels
assuming there is no cross flow

initxpos(1, 2) = initxpos(1, 3)/initxpos(1, 1);
initxpos(1, 3) = initxpos(1, 2);
xlswrite(excelname1, initxpos(1, 2), 'Init Positions', 'C6');
xlswrite(excelname1, initxpos(1, 2), 'Init Positions', 'C7');
xlswrite(excelname1, initypos, 'Init Positions', 'C2');

for g = 2 : (numel(initxpos)/4)
    initxpos(g, 2) = initxpos(g, 3)/initxpos(g, 1);
    initxpos(g, 3) = initxpos(g, 2) + initxpos(g - 1, 3);    %
establish x-position of respective centroid
    xlswrite(excelname1, initxpos(g, 2), 'Init Positions',
sprintf('%c%i', 'B' + g, 6));
    xlswrite(excelname1, initxpos(g, 3), 'Init Positions',
sprintf('%c%i', 'B' + g, 7));
end

clearvars yposrefgivenx1 histox histoy bar;

%% Step 4: export the processing into the form of a video and
spreadsheet data

aviobj = avifile(outputvide, 'compression', 'IYUV');
aviobj.quality = 70;
aviobj.fps = get(flexibleObj, 'FrameRate');

for k = lastmeanframe : (lastmeanframe + floor(get(flexibleObj,
'FrameRate') * secondsmeanon) - 1)
    singleFrame = read(flexibleObj, k);
    singleFrame = imcrop(singleFrame, [framexposcrop frameyposcrop
bretocrop heitocrop]);
    singleFrame = imrotate(singleFrame, rotateby);
% when movie needs rotating 180 degrees

    % Convert to grayscale to do morphological processing.
```

```
    I = rgb2gray(singleFrame);

    DarkPart = imextendedmin(I, LightValue); % identify dark regions

    % Remove small structures.
    noSmallStructures = imopen(DarkPart, sedisk);
    noSmallStructures = bwareaopen(noSmallStructures, pixelmaxno);
    noSmallStructures = imclearborder(noSmallStructures);
    noSmallStructures = imfill(noSmallStructures, 'holes');

    stats = regionprops(noSmallStructures, {'Centroid', 'PixelList'});

    disp(k);    % display frame no. being analysed

    if ~isempty([stats.Centroid])
        for n = 1 : (numel([stats.Centroid]))/2
            initxpos(n, 4) = initxpos(n, 4) + 1;

            xlswrite(excelname1, k, sprintf('Centroid %i', n),
sprintf('%c%i', 'A', k));
            xlswrite(excelname1, stats(n).Centroid(1),
sprintf('Centroid %i', n), sprintf('%c%i', 'C', k));
            xlswrite(excelname1, stats(n).Centroid(2),
sprintf('Centroid %i', n), sprintf('%c%i', 'D', k));

            width = 2;
            row = (floor(stats(n).Centroid(2)) -
width):(floor(stats(n).Centroid(2)) + width);
            col = (floor(stats(n).Centroid(1)) -
width):(floor(stats(n).Centroid(1)) + width);

            singleFrame(row, col(1, 3), 1) = 255;
            singleFrame(row(1, 3), col, 1) = 255;
            singleFrame(row, col(1, 3), 2) = 0;
            singleFrame(row(1, 3), col, 2) = 0;
            singleFrame(row, col(1, 3), 3) = 0;
            singleFrame(row(1, 3), col, 3) = 0;

        end
    end

    aviobj = addframe(aviobj, singleFrame);

    clearvars singleFrame I DarkPart noSmallStructures;
end

aviobj = close(aviobj);
```

Appendix C

C1. Computational Analysis Pressure Distribution

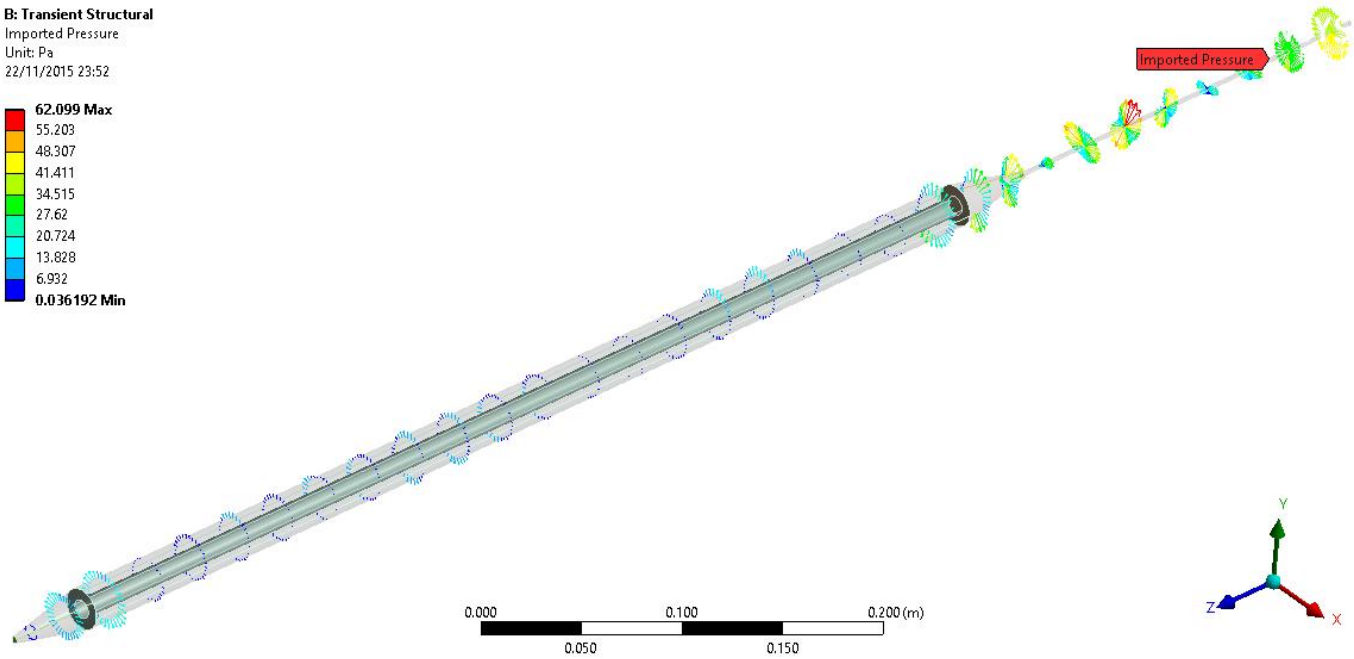

Figure 122. Pressure distribution example on the mesh nodes in transient analysis.

References

[1] I. F. Akyildiz, D. Pompili and T. Melodia, "Underwater acoustic sensor networks: research challenges," *Ad Hoc Networks,* vol. 3, no. 3, pp. 257-279, 2005.

[2] "Underwater Sensing, Communication, Networking and Systems," *Sensor Networks - Special Issue,* vol. 19, 2019.

[3] Y. Junku, "Design and Control of Autonomous Underwater Robots: A Survey," *Autonomous Robots,* vol. 8, no. 1, pp. 7-24, 2000.

[4] Z. Dibin, S. P. Beeby, M. J. Tudor, N. M. White and N. R. Harris, "Novel Miniature Airflow Energy Harvester for Wireless Sensing Applications in Buildings," *IEEE Sensors Journal,* vol. 13, no. 2, pp. 691-700, 2013.

[5] J. J. Allen and A. J. Smits, "Energy Harvesting Eel," *Journal of Fluids and Structures,* vol. 15, pp. 629 - 640, 2001.

[6] J. D. Anderson, "Computational fluid dynamics," Singapore, 1995).

[7] B. R. Munson, A. P. Rothmayer and H. Theodore, Fundamentals of Fluid Mechanics, Ames, Iowa: John Wiley &Sons, Inc, 2013.

[8] J. C. Liao, "A review of fish swimming mechanics and behaviour in altered flows.," *Philosophical transactions of the Royal Society of London. Series B, Biological sciences,* vol. 362, no. 1487, pp. 1973-93, 2007.

[9] M. M. Zdravkovich, Flow around circular cylinders, Oxford: Oxford University Press, 1997.

[10] D. R. Blevins, Flow induced vibration, Malabar: Krieger Publishing Company, 1990.

[11] D. Beal, F. Hover, M. Triantafyllou, J. Liao and G. Lauder, “Passive propulsion in vortex wakes,” *Journal of Fluid Mechanics,* no. 549, pp. 385-402, 2006.

[12] J. M. J. Journée and W. W. Massie, Offshore Hydromechanics, Delft University of Technology, 2001.

[13] A. B. Phillips, J. I. Blake, B. Smith, S. W. Boyd and G. Griffiths, “Nature in engineering for monitoring the oceans: towards a bio-inspired flexible autonomous underwater vehicle operating in an unsteady flow,” *Proceedings of the Institution of Mechanical Engineers, Part M: Journal of Engineering for the Maritime Environment,* vol. 224, no. 4, pp. 267-278, 2010.

[14] C. Norberg, “Effects of Reynolds number and a low-intensity freestream turbulence of the flow around a circular cylinder,” Chalmers University of Technology, Göteborg, 1987.

[15] U. Fey, . M. Konig and E. Eckelmann, “A New Strouhal-Reynolds Number Relationship for a Circular Cylinder in the Range 47<Re<1x10^5,” *Physics Fluids,* vol. 10, no. 7, pp. 1547-1549, 1998.

[16] D. Gerich and H. Eckelman, “Influence of end plates and free ends on the shedding frequency of circular cylinders,” *Journal of Fluid Mechanics,* vol. 122, pp. 109 - 121, 1982.

[17] B. H. Awbi, Ventilation of Buildings, Londno: Spon Press, 2003.

[18] A. Chadwick, J. Morfett and M. Borthwick, Hydraulics in Civil and Environmental Engineering, Fourth Edition, London: Spon Press, 1986.

[19] T. S. A., “Vortex shedding from groups of three and four equispaced cylinders situated in a cross flow,” *Journal of Wind Engineering and Industrial Aerodynamics,* no. 4, pp. 213-221, 1990.

[20] S. C. Tapia-Siles and R. Chellali, “Simple Von Kármán vortex street model,” in *OCEANS 2010 IEEE,* Sydney, 2010.

[21] J. H. Lienhard, “Synopsis of Lift, Drag, and vortex frequency data for rigid circular cylidners,” Pullman, Washington, 1966.

[22] P. W. Bearman, “Vortex shedding from oscillating bluff bodies,” *Annual Review of Fluid Mechanics,* vol. 16, pp. 195-222, 1984.

[23] A. Roshko, “Perspectives on bluff body aerodynamics,” *Journal of Wind Engineering and Industrial Aerodynamics,* vol. 49, no. 1-3, pp. 79-100, 1993.

[24] C. H. K. Williamson, “Three-Dimensional Vortex Dynamics in Bluff Body Wakes,” *Experimental Thermal and Fluid Science,* no. 12, pp. 150-168, 1996.

[25] C. H. K. Williamson, “Vortex Dynamics in the cylinder wake,” *Annual Review of Fluid Mechanics,* vol. 28, pp. 477-539, 1996.

[26] G. Vaz, C. Mabilat, R. van der Wal and P. Gallagher, “Viscous flow computations on smooth cylinders: A detailed numerical study with validation,” in *26th International Conference on Offshore Mechanics and Arctic Engineering*, San Diego, California, USA, 2007.

[27] R. M. Stringer, J. Zang and A. J. Hillis, “Unsteady RANS computations of flow around a circular cylinder for a wide range of Reynods numbers.,” *Ocean Engineering,* no. 87, pp. 1-9, 2014.

[28] Y. Cao and T. Tamura, “Large-eddy simulations of flow past a square cylinder using structured and unstructured grids.,” *Cumputers and Fluids,* no. 37, pp. 36-54, 2016.

[29] J. C. K. Cheung, “Effects of surface roughness on a circular cylinder in supercritical turbulent flow.,” in *12th Australian Fluid Mechanics Conference*, Sydney, 1995.

[30] “PipeFlow.com,” [Online]. Available: http://pipeflow.com/pipe-pressure-drop-calculations/pipe-roughness. [Accessed 24 04 2019].

[31] A. Fage and J. Warsap, “The effects of turbulence and surface roughness on the drag of circular cylinder,” *Aeronautical Research Committee: Reports and Memoranda No. 1283,* October 1929.

[32] J. C. Liao, “Neuromuscular control of trout swimming in a vortex street: implications for energy economy during the Von Kármán gait,” *Journal of Experimental Biology,* no. 207, pp. 3495-3506, 2004.

[33] S. Vogel, Life in moving fluids: the physical biology of flow, New Jersey: Princeton University Press, 1994.

[34] J. Liao, D. Bea, G. Lauder and M. Triantafyllou, “The Kármán gait: novel body kinematics of rainbow trout swimming in a vortex street,” *Journal of Experimental Biology,* vol. 206, no. 6, pp. 1059-1073, 2003.

[35] J. Schembri, “MSc Maritime Engineering: Investigation of a flexible cylinder in unsteady flow,” Southampton, 2010.

[36] C. H. K. Williamson and R. Govardhan, “Vortex-induced vibration,” *Review of Fluid Mechanics Annual,* vol. 36, pp. 413-455, 2004.

[37] J. Dahl, *Vortex-Induced Vibration of a Circular Cylinder with Combined In-line and Cross-flow motion.,* Massachusetts: MIT, 2008.

[38] T. Sarpkaya, “Vortex-induced oscillations. A selective review,” *ASME Journal of Applied Mechanics,* vol. 46, no. 2, pp. 241-258, 1979.

[39] O. M. Griffin and S. E. Ramberg, “Some recent studies of vortex shedding with application to marine tubulars and risers,” *ASME Journal of Energy Resources Technology,* vol. 104, no. 1, pp. 2-13, 1981.

[40] G. V. Parkinson, “Phenomena and modeling of flow-induced vibrations of bluff bodies,” *Progress in Aerospace Science,* vol. 26, pp. 169-224, 1989.

[41] T. Barnard, R. Durrans, S. Lowry, M. Meadows, T. Walski and B. Whitman, Computer Applications in Hydraulic Engineering, Canada: Bentley Institute Press, 2013.

[42] J. Southard, "Chapter 4," in *Introduction to Fluid Motions, Sediment Transport, and Current-Generated Sedimentary Structures*, Massachusetts, MIT, 2006, pp. 83 - 156.

[43] J. Nikuradse, "Laws of flow in rough pipes," *Translation in National Advisory Committee for aeronautics, Technical Memorandum,* vol. 1292, p. 62, 1950.

[44] M.I.T., "Basics of Turbulent flow," [Online]. Available: http://www.mit.edu/course/1/1.061/OldFiles/www/dream/SEVEN/SEVENTHEORY.PDF. [Accessed 24 04 2019].

[45] H. Schlichting and K. Gersten, Boundary-layer Theory, Springer, 2000.

[46] Wikipedia, "Law of the Wall," 12 September 2016. [Online]. Available: https://en.wikipedia.org/wiki/Law_of_the_wall. [Accessed 14 September 2016].

[47] H. Chanson, Applied Hydrodynamics: An Introduction to Ideal and Real Fluid Flows, Leiden, The Netherlands: CRC Press, Taylor & Francis Group, 2009.

[48] T. von Kármán , "Mechanical Simulitude and turbulence (Reprint from Nachrichten von der Gessellscharft de Wissenschaften zu Gottingen)," National advisory committee for aeronautics, Washington, 1930.

[49] T. Von Kármán, "Mechanical similitude and turbulence," in *Techincal memorandums national advisory committee for aeronautics*, Washington, 1930.

[50] J. Nikuradse, "Laws of flow in rough pipes," *Translation in National Advisory Committee for aeronautics, Technical Memorandum,* no. 1292, p. 62, 1950.

[51] H. Schlichting, Boundary layer theory, New York: McGraw-Hill, 1979.

[52] P. Bradshaw, T. Cebeci and J. Whitelaw, Engineering calculation methods for turbulent flow, London: Academic Press Inc, 1981.

[53] P. Steffler, N. Rajaratnam and A. Peterson, “LDA measurements in open channel flow,” *Journal of Hydraulic Engineering ASCE,* vol. 111, no. 1, pp. 119 - 130, 1985.

[54] I. Nezu and W. Rodi, “Open channel flow measurements with a laser Doppler anemometer,” *Journal of Hydraulic Engineering ASCE,* vol. 111, no. 1, pp. 335 - 355, 1986.

[55] A. Cardoso, W. Graf and G. Gust, “Uniform flowin a smooth open channel,” *Journal of Hydraulic Research,* vol. 27, no. 5, pp. 603 - 616, 1989.

[56] S. Kirkgöz and M. Ardiclioglu, “Velocity profiles of developping and developed open channel flow,” *Journal of Hydraulic Engineering ASCE,* vol. 115, no. 11, pp. 1099 - 1105, 1997.

[57] H. Kudela, “Lecture no3 - Turbulent flow Modelling,” Search Results, [Online]. Available: http://www.itcmp.pwr.wroc.pl/~znmp/dydaktyka/fundam_FM/Lecture_no3_Turbulent_flow_Modelling.pdf. [Accessed 16 09 2016].

[58] B. C. Yen, “Open Channel Flow Resistance,” *Journal of Hydraulic Engineering,* vol. 128, no. 1, p. 20, 2002.

[59] T. Cebeci, Analysis of turbulent flows, Oxford: Elsevier Ltd, 2004.

[60] I. Nezu and H. Nakagawa, Turbulence in open-channel flows, Balkema, Rotterdam NL., 1993.

[61] X. Li, Z. Dong and C. Chen, “Turbulent flows in smooth-wall open channels with different slope,” *Journal of Hydraulic Research,* vol. 33, no. 3, pp. 333 - 347, 1995.

[62] D. Coles, “The law of the wake in turbulent boundary layer,” *Journal of Fluid Mechanics,* vol. 1, pp. 191 - 226, 1956.

[63] J. Hinze, Turbulence, New York: McGraw-Hill, 1975.

[64] I. Nezu and W. Rodi, “Experimental study on secondary currents in open channel flow.,” in *Proceedings of the 21st IAHR Congress*, Melbourne: IAHR, 1985.

[65] N. Afzal, “Scaling of power law velocity profile in wall-bounded turbulent shear flows,” in *43rd AIAA Aerospace Sciences Meeting and Exhibit*, Reno, Nevada, 2005.

[66] O. Castro-Orgaz, “Hydraulics of developing chute flow,” *Journal of Hydraulic Research,* vol. 47, no. 2, pp. 185 - 194, 2009.

[67] J. Francis, “On the cause of the maximum velocity of water flowing in open channels being below the surface,” *Transcripts ASCE,* vol. 7, no. 1, pp. 109 - 113, 1878.

[68] F. Stearns, “On the current meter, together with a reason why the maximum velocity of water flowing in open channel is below the surface,” *Transcripts ASCE,* vol. 7, pp. 331 - 338, 1883.

[69] H. Bonakdari, F. Larrarte, L. Lassabatere and C. Joannis, “Turbulent velocity profile in fully-developed open channel flows,” *Enviromental Fluid Mechanics,* vol. 8, pp. 1 - 17, 2008.

[70] S. Kirkgoz, “Turbulent velocity profiles for smooth and rough open channel flow,” *Journal of Hydraulic Engineering,* vol. 115, no. 11, pp. 1543 - 1561, 1989.

[71] “www.hymetrics.com,” Hymetrics Limited, [Online]. Available: http://www.hymetrics.com/Pages2_Flow_Measurement.htm. [Accessed 24 04 2019].

[72] R. Absi, “An ordinary differential equation for velocity distribution and dip-phenomenon in open channel flows,” *Journal of Hydraulic Research,* vol. 49, no. 1, pp. 82 - 89, 2011.

[73] R. Absi, “Analytical methods for velocity distribution and dip-phenomenon in narrow open-channel flows,” in *International Workshop on Environmental Hydraulics*, Valencia, 28th - 29th October 2009.

[74] Y. Shu-Qing, T. Soon-Keat and L. Siow-Yong, “Velocity Distribution and Dip-Phenomenon in Smooth Uniform Open Channel Flows,” *Journal of Hydraulic Engineering,* vol. 130, no. 12, pp. 1179 - 1186, 2004.

[75] S. Kundu and K. Ghoshal, “Velocity Distribution in Open Channels: Combination of Log-law and Parabolic-law,” *International Journal of Mathematical, Computational, Physical, Electrical and Computer Engineering,* vol. 6, no. 8, 2012.

[76] S. Q. Yang, S. K. Tan and S. Y. Lim, “Velocity Distribution and Dip-Phenomenon in Smooth Uniform Open Channel Flows,” *Journal of Hydraulic Engineering,* vol. 130, no. 12, pp. 1179 - 1186, 2004.

[77] . Y. Goswami and F. Kreith, Handbook of Energy Efficiency and Renewable Energy, New York: CRC Press, Taylor & Francis Group, 2007.

[78] D. A. Jones and D. B. Clarke, “Simulation of flow past a sphere using the Fluent code,” Maritime Platforms Division, DSTO Defence Science and Technology Organisation, Australia, 2008.

[79] “Wikipedia,” 23 9 2015. [Online]. Available: https://en.wikipedia.org/wiki/Filter_(large_eddy_simulation). [Accessed 24 04 2019].

[80] D. C. Wilcox, Turbulence modeling for CFD, California, 2004.

[81] ANSYS, “ANSYS Turbulence modelling guide,” 2015.

[82] H. K. Versteeg and W. Malalasekera, An introduction to computational fluid dynamics : the finite volume method, Harlow: Pearson/Prentice Hall, 2007.

[83] S. Wasserman, “Engineering.com,” November 2016. [Online]. Available: http://www.engineering.com/DesignSoftware/DesignSoftwareArticles/ArticleID/13743/Choosing-the-Right-Turbulence-Model-for-Your-CFD-Simulation.aspx. [Accessed 18 10 2017].

[84] “CFD Online,” [Online]. Available: https://www.cfd-online.com/Wiki/SST_k-omega_model. [Accessed 24 04 2019].

[85] J. Curie and P. Curie, “Development by pressure of polar electricity in hemihedral crystals with inclined faces,” *Bulletin del Societe Chimique de France*, vol. 3, p. 90, 1880.

[86] R. Patel, M. Kermani and M. Moallem, “Applied vibration suppression using piezoelectric materials.,” *Nova Science Publishers,* 2008.

[87] R. C. Dorf, “The electrical engineering handbook,” *CRC Press IEEE Press*, 1997.

[88] G. Lippmann, “Principe de la conservation de l'electricite,” *Ann de Chemie e de Physique*, vol. 5, p. 145, 1881.

[89] C. Galassi, M. Dinescu, K. Uchino and M. Sayer, Piezoelectric Materials: Advances in Science, Technology and Applications, Dordrecht: Springer Netherlands, 2000.

[90] D. Damjanovic, The science of hysteresis: Hysteresis in piezoeelctric and ferroelectric materials, G. Bertotti and I. Mayergoyz, 2005.

[91] A. Almusallam, “Screen-Printed Low Temperature Piezoelectric Thick Films for Energy Harvesting on Fabrics,” PhD Thesis, Southampton University, 2016.

[92] “Sparkler piezoceramics: General information,” Sparkler Ceramics PVT LTD.

[93] P. Shashank, “Modeling of Electric Energy Harvesting using Piezoelectric Windmill,” *Applied Physics Letters,* vol. 87, no. 18, 2005.

[94] W. Robbins, M. Dustin, I. Marusic and T. Novak, “Wind-Generated Electrical Energy using Flexible Piezoelectric Materials,” *American Society of Mechanical Engineers,* pp. 581-590, 2006.

[95] H. Sun, Z. Dibin, N. M. White and S. P. Beeby, “A Miniature Airflow Energy Harvester from Piezoelectric Materials,” *Journal of physics conference series 476: 012057,* 2013.

[96] K. Streitlien and G. Triantafyllou, “Efficient Foil Propulsion Through Vortex Control,” *American Institute of Aeronautics and Astronautics Journal,* vol. 34, no. 11, pp. 2315 - 2319, 1996.

[97] B. J. Smith, J. I. R. Blake and S. W. Boyd, “The development of a Bio-inspired method to recover energy from Unsteady flow,” School of Engineering Sciences - Ship Science Reprt No:146, University of Southampton, 2009.

[98] G. W. Taylor, J. R. Burns, S. M. Kammann, W. B. Powers and T. R. Welsh, “The Energy Harvesting Eel: A Small Subsurface Ocean/River Power Generator,” *IEEE Journal of Oceanic Engineering,* vol. 26, no. 4, p. 539 - 548, 2001.

[99] H. D. Akaydin, N. Elvin and Y. Andreopoulos, “Wake of a cylinder: a paradigm for energy harvesting with piezoelectric materials,” *Experiments in Fluids,* vol. 49, p. 291 – 304, 2010.

[100] A. Khalak and C. H. K. Williamson, “Dynamics of a hydroelastic cylinder with very low mass and damping,” *Journal of Fluids and Structures,* vol. 10, pp. 455-472, 1996.

[101] H. J. P. Keighley, F. R. McKim, A. Clark and M. J. Harrison, Archimedes’ Principle and Flotation. In Mastering Physics, London: Macmillan Master Series, 1984.

[102] W. R. Hawthorn, “The Early Development of the Dracone Flexible Barge,” *Proceedings of the Institution of Mechanical Engineers,* vol. 175, pp. 52 - 83, 1961.

[103] M. P. Païdoussis, “Dynamics of Flexible Cylinders in Axial Flow. Part 1 Theory,” *Journal of Fluid Mechanics,* vol. 26, no. Part 4, pp. 717 - 736, 1966a.

[104] J. L. Lopes, M. P. Paidoussis and C. Semla, “Linear and Non Dynamics of Cantilevered Cylinders in Axial Flow, Part 2: The Equations of Motion,” *Journal of Fluids and Structures,* vol. 16, no. 6, p. 715 – 737, 2002.

[105] M. P. Païdoussis and B. K. Yu, “Elastohydrodynamics and Stability of Towed Slender Bodies of Revolution,” *Journal of Hydronautics (AIAA),* vol. 10, p. 127 – 134, 1976.

[106] M. J. Hannoye and M. P. Païdoussis, “Instabilities of Tubular Beams Simultaneously Subjected to Internal and External Flows,” *Journal of Mechanical Design (ASME),* vol. 100, pp. 328 - 336, 1978.

[107] R. D. Blevins, Formulas for natural frequency and mode shape, New York: Van Nostrand Reinhold, 1979.

[108] Silex, “www.acc-silicones.com,” ACC Silicones Europe, [Online]. Available: http://www.acc-silicones.com/content/products/mm913.ashx. [Accessed 2014 07 30].

[109] A. K. Chopra, “Modal Analysis of linear dynamic systems: Phisical interpretation,” *Journal of structural engineering,* no. 517, 1996.

[110] P. Lisy and P. Perun, “Natural Frequencies of Small Cylinders and Tubes,” *Problems of Mechatronics, Armament, Aviation, Safety Engineering,* vol. 2, no. 20, pp. 7-20, 2014.

[111] AlephZero, “ansys-modal-what-does-the-deflection-result-represent,” 19 06 2015. [Online]. Available: https://www.physicsforums.com/threads/ansys-modal-what-does-the-deflection-result-represent.728097/.

[112] MathWorks, “Detecting Cars in a Video of Traffic,” [Online]. Available: http://www.mathworks.co.uk/help/images/examples/detecting-cars-in-a-video-of-traffic.html#zmw57dd0e3064. [Accessed 03 08 2014].

[113] S. Y. Wan, L. B. Jia and X. Z. Yin, “Kinematics and forces of a flexible body in Kármán vortex street,” *Chinese Science Bulletin,* vol. 54, no. 4, pp. 556-561, 2009.

[114] J. N. Newman and T. Y. Wu, “A generalized slender-body theory for fish-like forms,” *Journal of Fluid Mechanics,* vol. 57, no. 4, pp. 673-693, 1973.

[115] J. C. Liao, D. N. Beal, G. V. Lauder and M. S. Triantafyllou, “Fish Exploiting Vortices Decrease Muscle Activity,” *Science,,* vol. 302, p. 1566-1569, 2003b.

[116] X. Wang, Z. Y. Wang, M. Yu and D. Li, “Velocity profile of sediment suspensions and comparison of log-law and wake-law,” *Journal of Hydraulic Research,* vol. 39, no. 2, pp. 211 - 217, 2001.

[117] B. Cantwell and D. Coles, “An experimental study of entrainment and transport in the turbulent near wake of a circular cylinder,” *Journal of Fluid Mechanics,* vol. 136, pp. 321-374, 1983.

[118] R. Orselli, J. R. Meneghini and F. Saltara, “Two and Three-Dimensional Simulation of Sound Generated by Flow Around a Circular Cylinder,” in *15th AIAA/CEAS Aeroacoustics Conference* , Miami, Florida, 2009.

[119] C. Reichel and K. Strohmeier, “Application of Models for Laminar to Turbulent Transition to Flow Around a Circular Cylinder,” *Fluid Structure Interaction,* vol. 4, pp. 7-11, 2005.

[120] H. K. Versteeg and W. Malalasekera, An introduction to computational fluid dynamics, Glasgow: Prentice Hall, 2007.

[121] D. C. Wilcox, Turbulence modeling for CFD, California: DCW Industries, 2004.

[122] C. J. Roy, L. J. DeChant, J. L. Payne and F. G. Blottner, “Bluff-Body Flow Simulations using Hybrid RANS/LES,” *American Institute of Aeronautics and Astronautics Journal (AIAA),* pp. 2003-3889, 2003.

[123] H.-C. Lim and S.-J. Lee, “Flow Control of Circular Cylinders with Longitudinal Grooved Surfaces,” *American Institute of Aeronautics and Astronautics Journal (AIAA),* vol. 40, no. 10, pp. 2027-2036, 2002.

[124] M. Kuron, “Engineering.com,” 06 January 2015. [Online]. Available: http://www.engineering.com/DesignSoftware/DesignSoftwareArticles/ArticleID/9296/3-Criteria-for-Assessing-CFD-Convergence.aspx. [Accessed 12 08 2017].

[125] “Innovative-CFD.com,” 01 11 2012. [Online]. Available: http://www.innovative-cfd.com/cfd-grid.html. [Accessed 24 04 2019].

[126] S. J. Karabelas, B. C. Koumroglou, C. D. Argyropoulos and N. C. Markatos, “High Reynolds number turbulent flow past a rotating cylinder,” *Applied Mathematical Modelling,* no. 36, pp. 379-398, 2011.

[127] ANSYS®, “ANSYS® Global Mesh Controls Guide,” 2014.

[128] A. C. Benim, M. Cagan, A. Nahavandi and E. Pasqualotto, “RANS Predictions of turbulent flow past a circular cylinder ver the critical regime.,” in *Proceedings of the 5th Iasme/Wseas International Conference on Fluid Mechanics and Aerodunamics*, 2007.

[129] P. Jagadeesh and K. Murali, “Application of low-Re turbulence models for flow simulations past underwater vehicle hull forms,” *Journal of Naval Architecture and Marine Engineering,* vol. 2, pp. 41-54, 2009.

[130] I. ANSYS, “ANSYS FLUENT 17.0 User's Guide,” SAS IP, Inc, Canonsburg, PA, 2013.

[131] P. Arnold, “CFD validation of high Reynolds number flow past a circular cylinder,” Minerva Dynamics, Bath, UK, 2014.

[132] G. P. Arnold, “The Reactions of The Plaice (Pleuronectes Platessa L.) to Water Currents,” *Journal of Experimental Biology,* no. 51, pp. 681-697, 1969.

[133] M. Sato and T. Kobayashi, “A fundamental study of the flow past a circular cylinder using Abaqus/CFD,” in *SIMULIA community Conference*, Providence, RI, 2012.

[134] J. F. Douglas, Fluid Mechanics, Pearson Education, 2005.

[135] M. N. Linnick and H. F. Fasel, “A high-order immersed interface method for simulating unsteady compressible flows on irregular domains,” *Jounral of Computational Physics,* vol. 1, no. 204, pp. 157-192, 2005.

[136] K. Herfjord, “A study of two-dimensional separated flow by a combination of the finite element method and Navier-Stokes equations,” Norwegian Institute of Technology, Department of Marine Hydrodynamics, Trondheim, Norway, 1996.

[137] D. Russel and Z. J. Wang, “A Cartesian grid method for modeling multiple moving objects in 2D incompressible viscous flow.,” *Journal of Computational Physics*, no. 191, pp. 177-205, 2003.

[138] S. Xu and Z. J. Wang, “An immersed interface method for simulating the intercation of a fluid with moving boundaries,” *Journal of Computational Physics*, vol. 2, no. 216, pp. 454-493, 2006.

[139] C. Dalton, “semanticscholar.org,” University of Houston Fundamentals of vortex-induced vibration. [Online]. Available: https://pdfs.semanticscholar.org/a988/6c90c89adb1e5bec3d12cbfb4bcef9c8e13c.pdf. [Accessed 08 09 2017].

[140] B. N. Rajani, “Numerical simulation of laminar flow past a circular cylinder,” *Applied Mathematical Modelling,* no. 33, pp. 1228-1247, 2009.

[141] K. Kakuda and N. Tosaka, “Finite element simluation of 3D flow around a circular cylinder,” *International Journal of Computational Fluid Dynamics,* no. 20, pp. 193-209, 2006.

[142] B. A. Younis and A. Abrishamchi, “Three - dimensional turbulent vortex street shedding from a surface-mounted square cylinder,” *Journal of Fluids Engineering,* vol. 136, 2014.

[143] A. K. Saha, G. Biswas and K. Muralidhar, “Three-dimensional study of flow past a square cylinder at low Reynolds numbers,” *International Journal of Heat and Fluid Flow,* no. 24, pp. 54-66, 2003.

[144] P. Catalano, M. Wang, G. Iaccarino and P. Moin , “Numerical simulation of the flow around a circular cylinder at high Reynolds numbers,” *International Journal of Heat and Fluid Flow ,* no. 24, pp. 463-469, 2003.

[145] J. J. Wilde and R. Huijsmans, “Experiments for High Reynolds NUmbers VIV on Risers,” in *ISOPE 2001 Proceedings*, Stavenger, Norway, 2001.

[146] A. Roshko, “Experiments on the flow past a circular cylinder at very high Reynolds numbers,” *Journal of Fluid Mechanics,* no. 10, pp. 345-356, 1961.

[147] Y. Constantinides and O. Oakley, “Numerical Prediction of Bare and Straked Cylinder VIV,” in *OMAE 2006 Proceedings*, Hamburg, 2006.

[148] M. Hafez and K. Oshima, Computational Fluid Dynamics Review, World Scientific, 1998.

[149] K. Liaw, “Simulation of flow around bluff bodies and bridge deck sections using CFD,” University of Nottingham, Nottingham, 2005.

[150] I. B. Celik, U. Ghia, P. J. Roache, C. J. Freitas, H. Coleman and P. E. Raad, “Procedure for Estimation and Reporting of Uncertainty Due to Discretization in CFD Applications,” *Journal of Fluids Engineering,* vol. 130, no. 7, 2008.

[151] P. J. Roache, “Perspective: A Method for Uniform Reporting of Grid Refinement Studies,” *ASME Journal of Fluids Engineering,* vol. 116, 1994.

[152] P. J. Roache, Verification and Validation in Computational Science and Engineering, Albuquerque: Hermosa Publishers, 1998.

[153] T. S. Phillips, “Extrapolation-based Discretization Error and Uncertainty Estimation in Computational Fluid Dynamics,” Virginia Polytechnic Institute and State University, Blacksburg, VA, 2012.

[154] P. J. Roache, “Verification of Codes and Calculations,” in *26th AIAA Fluid Dynamics Conference,* San Diego, California, 1995.

[155] “Verification of Codes and Calculations,” *AIAA Journal,* vol. 36, no. 5, pp. 696-702, mAY 1998.

[156] J. H. Ferziger and M. Peric, “Further Discussion of Numerical Errors in CFD,” *International Journal of Numerical Methods in Fluids,* no. 23, pp. 1263-1274, 1996.

[157] L. Eça, M. Hoekstra and P. J. Roache, “Verification of Calculations: an Overview of the 2nd Lisbon Workshop,” in *AIAA Computational Fluid Dynamics Conference,* Miami, 2007.

[158] L. F. Richardson and J. A. Gaunt, “The Deferred Approach to the Limit,” *Philosophical Transactions of the Royal Society of London A,* no. 226, pp. 299-361, 1927.

[159] B. L. Broadhead, B. T. Rearden, C. M. Hopper, J. J. Wagschal and C. V. Parks, “Sensitivity- and Uncertainty-Based Criticality Safety Validation Techniques,” *Nuclear Science Engineering,* no. 146, pp. 340-366, 2004.

[160] C. H. K. Williamson, “The Existence of Two Stages in the transition to Three-Dimensionality of a cylinder wake,” *Physics of Fluids,* no. 31, p. 3165, 1988.

[161] C. H. K. Williamson, “The natural and forced formation of spot-like 'vortex - dislocations' in the transition of a wake,” *Journal of Fluid Mechanics,* no. 243, pp. 393-441, 1992.

[162] T. Wei and C. R. SMITH, “Secondary vortices in the wake of circular cylinders,” *Journal of Fluid Mechanics,* vol. 169, p. 513, 1986.

[163] J. C. R. Hunt, A. A. Wray and P. Moin, “Eddies, stream, and convergence zones in turublent flows.,” Centre for Turbulence Research Report, CTR-S88.193-208, 1988.

[164] H. Kang and C. Sung-Uk, *International Journal for numerical methods in fluids,* vol. 1334, no. 51, p. 1319, 2006.

[165] G. Pezzinga, “Velocity distribution in compound channel flows by numerical modeling,” *Journal of Hydraulic Engineering,* vol. 120, no. 10, pp. 1176-1198, 1994.

[166] D. Cokljat D and B. Younis, “Second-order closure study of open channel flows,” *Journal of Hydraulic Engineering (ASCE),* vol. 121, no. 2, pp. 94-107, 1995.

[167] A. J. Petrella, “http://inside.mines.edu/,” Inside.mines, 2012. [Online]. Available: http://inside.mines.edu/~apetrell/ENME442/Documents/SOLID186.pdf. [Accessed 23 November 2015].

[168] F.-K. Benra, H. J. Dohmen, J. Pei, S. Schuster and B. Wan, “A Comparison of One-Way and Two-Way Coupling Methods for Numerical Analysis of Fluid-Structure Interactions,” *Journal of Applied Mathematics,* vol. 2011, p. 16, 2011.

[169] S. Beeby, G. Ensell, M. Kraft and N. White, MEMS Mechanical Sensors, Boston: Artech House, 2004.

[170] A. Almusallam, N. R. Torah, K. Yang, J. Tudor and S. P. Beeby, "Flexible Low Temperature Piezoelectric Films for Harvesting from Textiles," in *PowerMEMS,* Atalanta, USA, 2012.

[171] S. Priya, J. Ryu, C. S. Park, J. Oliver, J. J. Choi and D. S. Park, "Piezoelectric and magnetoelectric thick films for fabricating power sources in wireless sensor nodes," *Sensors,* vol. 9, pp. 6361-6384, 2009.

[172] Y. Liu and T. Cui, "Polymer-Based rectifying diodes on a glass substrate fabricated by Ink-Jet printing," *Macromolecular Rapid Communications,* vol. 26, pp. 289-292, 2005.

[173] J. Windle and B. Derby, "Ink jet printing of PZT aqueous ceramic suspensions," *Journal of Material Science Letters,* vol. 18, pp. 87-90, 1999.

[174] J. Birnstock, J. Blassin, A. Hunze, M. Scheffel, M. Stobel and K. Heuser, "Screen-printred passive matrix displays based on light-emitting polymers," *Journal of Applied Physics,* vol. 78, p. 39053907, 2001.

[175] "Smart Fabric Inks," [Online]. Available: www.fabinks.com. [Accessed 24 04 2019].

[176] "Piezotest.com," Piezotest Ltd, [Online]. Available: http://www.piezotest.com/d33piezometer.php. [Accessed 24 04 2019].

[177] A. Almusallam, R. N. Torah, D. Zhu, J. M. Tudor and S. P. Beeby, "Screen-printed piezoelectric shoe-insole energy harvester using an improved flexible PZT-polymer composites," in *PowerMEMS,* London, 2013.

[178] A. Almusallama, Z. Luob, A. Komolafea, K. Yang, A. Robinson, R. Torah and S. Beeby, "Flexible piezoelectric nano-composite films for kinetic energy harvesting from textiles," *Nano Energy,* vol. 33, pp. 146-156, 2017.

[179] S. J. Priya and K. Uchino, "Modeling of Piezoelectric Energy Harvesting Using Cymbal Transducers," *Japanese Journal of Applied Physics,* vol. 45, no. 7, p. 5836–5840, 2006.

[180] Physics & Astronomy - Georgia State University, “Norton's Theorem,” Hyperphysics, [Online]. Available: http://hyperphysics.phy-astr.gsu.edu/hbase/electric/Norton.html. [Accessed 24 04 2019].

[181] Physics & Astronomy - Georgia State University, “Thevenin's Theorem,” Hyperphysics, [Online]. Available: http://hyperphysics.phy-astr.gsu.edu/hbase/electric/thevenin.html. [Accessed 24 04 2019].

[182] Q. Zheng, B. Shi, Z. Li and Z. L. Wang, “Review on Recent Progress on Piezoelectric and Triboelectric Energy Harvesters in Biomedical Systems”.

[183] X. Wang, B. Yang, J. Liu, Y. Zhu, C. Yang and Q. He, “A flexible triboelectric-piezoelectric hybrid nanogenerator based on P(VDF-TrFE) nanofibers and PDMS/MWCNT for wearable devices,” *Nature: Scientific Reports*, vol. 6, no. 36409, 2016.

[184] J. Zhonga, Q. Zhonga, F. Fan, Y. Zhang, S. Wang, B. Hua, Z. L. Wang and J. Zhoua, “Finger typingdriventriboelectric Q2 nanogenerator and itsuseforinstantaneouslylightingupLEDs,” *Nano Energy,* vol. 2, no. 4, pp. 491-497, 2013.